Merve Şansaçar

Ph.D. Thesis

AGU 2025

INVESTIGATION OF SH2 DOMAINS OF SPLEEN TYROSINE KINASE ENZYME FOR TARGETING ACUTE MYELOID LEUKEMIA USING BOTH *IN SILICO* AND *IN VITRO* STUDIES

Ph.D. THESIS
SUBMITTED TO THE BIOENGINEERING
AND THE GRADUATE SCHOOL OF ENGINEERING AND SCIENCE
OF ABDULLAH GUL UNIVERSITY
IN PARTIAL FULFILLMENT OF THE REQUIREMENTS
FOR THE DEGREE OF
DOCTOR OF PHILOSOPHY

By
Merve Şansaçar
August 2025

INVESTIGATION OF SH2 DOMAINS OF SPLEEN TYROSINE KINASE ENZYME FOR TARGETING ACUTE MYELOID LEUKEMIA USING BOTH *IN SILICO* AND *IN VITRO* STUDIES

A THESIS
SUBMITTED TO THE DEPARTMENT OF BIOENGINEERING
AND THE GRADUATE SCHOOL OF ENGINEERING AND SCIENCE OF
ABDULLAH GUL UNIVERSITY
IN PARTIAL FULFILLMENT OF THE REQUIREMENTS
FOR THE DEGREE OF
DOCTOR OF PHILOSOPHY

By
Merve Şansaçar
August 2025

SCIENTIFIC ETHICS COMPLIANCE

I hereby declare that all information in this document has been obtained in accordance with academic rules and ethical conduct. I also declare that, as required by these rules and conduct, I have fully cited and referenced all materials and results that are not original to this work.

Name-Surname: Merve Şansaçar

Signature :

REGULATORY COMPLIANCE

Ph.D. thesis titled 'Investigation of SH2 domains of Spleen Tyrosine Kinase enzyme for targeting acute myeloid leukemia using both *in silico* and *in vitro* studies' has been prepared in accordance with the Thesis Writing Guidelines of the Abdullah Gül University, Graduate School of Engineering & Science.

Prepared By

Merve Şansaçar

Advisor

Assist. Prof. Emel Başak Gencer Akçok

Head of the Bioengineering Program

Assist. Prof. İsmail Akçok

ACCEPTANCE AND APPROVAL

Ph.D. thesis titled 'Investigation of SH2 domains of Spleen Tyrosine Kinase enzyme for targeting acute myeloid leukemia using both *in silico* and *in vitro* studies' and prepared by Merve Şansaçar has been accepted by the jury in the Bioengineering Graduate Program at Abdullah Gül University, Graduate School of Engineering & Science.

28/08/2025

JURY:

Advisor : Assist. Prof. Emel Başak GENCER AKÇOK…….…….....

Member : Assist. Prof. Şerife AYAZ GÜNER……..

Member : Assist. Prof. Melis KARTAL YANDIM…….....

Member : Assist. Prof. İsmail AKÇOK…….....

Member : Assoc. Prof. Yusuf SÜRMELİ…….....

APPROVAL:

The acceptance of this Ph.D. thesis has been approved by the decision of the Abdullah Gül University, Graduate School of Engineering & Science, Executive Board dated ….. /….. / …….. and numbered ……..……. .

…….. /…….. / ……..

(Date)

Graduate School Dean
Prof. İrfan ALAN

ABSTRACT

INVESTIGATION OF SH2 DOMAINS OF SPLEEN TYROSINE KINASE ENZYME FOR TARGETING ACUTE MYELOID LEUKEMIA USING BOTH *IN SILICO* AND *IN VITRO* STUDIES

Merve Şansaçar
Ph.D. in Bioengineering
Advisor: Assist. Prof. Emel Başak Gencer Akçok
August 2025

Acute Myeloid Leukemia (AML) is a clonal malignancy characterized by genetic and epigenetic abnormalities and one molecule that has emerged as a potential therapeutic target in this complex disease is Spleen Tyrosine Kinase (Syk) which consists of two SH2 domains at its amino terminus followed by a catalytically active kinase domain. Recent studies in cancer treatment methods to prevent the activation of abnormal proteins that lead to cancer have revealed that SH2 domains are also important targets in addition to active kinase domains. In this study, candidate inhibitors were identified through in silico studies by screening two libraries, COCONUT and ENAMINE. In vitro binding tests were then conducted for two candidate inhibitors selected from the ENAMINE library (Z260816155 and z2155444005), and binding was confirmed *in vitro* in HEK293 cells using FRET technology and Differential Scanning Fluorimetry Assay (DSF). Finally, the aim was to investigate the biological activities of inhibiting protein-protein interactions by targeting the SH2 domains of Syk on AML cells. The candidate inhibitors used decreased cell viability at low micromolar concentrations (1-25 μM) in THP-1 and HL-60 cells and, in a correlated manner, induced apoptosis and caused cell cycle arrest cells compared to control cells. Furthermore, they modulated the gene expression of TNF-α and IL-1β and effectively suppressed the anti-apoptotic proteins Bcl-2 and Bcl-xL.

Keywords: Spleen Tyrosine Kinase, SH2 (Src Homology 2) domain, Molecular Docking, Protein-Protein Interactions, Acute Myeloid Leukemia

ÖZET

AKUT MİYELOİD LÖSEMİYİ HEDEFLEMEK İÇİN *İN SİLİCO* VE *İN VİTRO* ÇALIŞMALAR KULLANILARAK DALAK TİROZİN KİNAZ ENZİMİNİN SH2 ALANININ ARAŞTIRILMASI

Merve Şansaçar
Biyomühendislik Anabilim Dalı Doktora
Tez Danışmanı: Dr. Öğretim Üyesi Emel Başak Gencer Akçok
Ağustos 2025

Akut Miyeloid Lösemi (AML), genetik ve epigenetik anormalliklerle karakterize klonal bir malignitedir ve bu karmaşık hastalıkta potansiyel bir terapötik hedef olarak ortaya çıkan moleküllerden biri, amino terminalinde iki SH2 alanı ve bunu takip eden katalitik olarak aktif bir kinaz alanından oluşan Dalak Tirozin Kinaz'dır (Syk). Kansere yol açan anormal proteinlerin aktivasyonunu önlemek için kanser tedavi yöntemlerinde yapılan son çalışmalar, aktif kinaz alanlarına ek olarak SH2 alanlarının da önemli hedefler olduğunu ortaya koymuştur. Bu çalışmada, aday inhibitörler, COCONUT ve ENAMINE olmak üzere iki kütüphanenin taranmasıyla *in silico* çalışmalar yoluyla tanımlanmıştır. Daha sonra ENAMINE kütüphanesinden seçilen iki aday inhibitör (Z260816155 ve z2155444005) için *in vitro* bağlanma testleri yürütülmüş ve bağlanma, FRET teknolojisi ve Diferansiyel Taramalı Florimetri Testi (DSF) kullanılarak HEK293 hücrelerinde in vitro olarak doğrulanmıştır. Son olarak, amaç, AML hücrelerinde Syk'nin SH2 bölgelerini hedef alarak protein-protein etkileşimlerini inhibe etmenin biyolojik aktivitelerini araştırmaktır. Aday inhibitörler, THP-1 ve HL-60 hücrelerinde düşük mikromolar konsantrasyonlarda (1-25 μM) hücre canlılığını azaltmış ve kontrol hücrelerine kıyasla ilişkili bir şekilde apoptozu indükleyerek hücre döngüsünün durmasına neden olmuştur Ayrıca, TNF-α ve IL-1β gen ekspresyonunu modüle etmiş ve anti-apoptotik proteinler Bcl-2 ve Bcl-xL'yi etkili bir şekilde baskılamışlardır.

Anahtar kelimeler: Dalak Tirozin Kinazı, SH2 (Src Homology 2) alanı, Moleküler Kenetleme, Protein-Protein Etkileşimleri, Akut Myeloid Lösemi

Acknowledgements

First, I extend my profound gratitude to my advisor, Assist. Prof. Emel Başak GENCER AKÇOK, for her extraordinary encouragement, keen insights, expert guidance, extraordinary patience, and unwavering support.

I am deeply thankful to my thesis monitoring committee members, Assist. Prof. Şerife AYAZ GÜNER and Assist. Prof. Melis KARTAL YANDIM They have followed my research and have always improved my research with their valuable questions and suggestions. I also would like to thank my defense committee members, Assist. Prof. İsmail AKÇOK and Assoc. Prof. Yusuf SÜRMELİ for separating their valuable time to evaluate my studies and improve my academic career.

I would like to thank Hüseyin GÜNER, Assist. Prof. İsmail AKÇOK, Ceyhun SARI and Muhsin Samet YÜCEL for their valuable contributions to the *in-silico* studies. I also thank flow cytometry expert Esma SARAYMEN for her invaluable technical support for the flow cytometry experiments.

I would like to thank EBGA Lab, AŞ Lab, and FİDAN Lab members for their valuable friendships, help, cooperation and support not only in the laboratory, but also in my life.

I would also like to thank Izmir Institute of Technology Biotechnology and Bioengineering Research and Application Center, Assist. Prof. Şerife AYAZ GÜNER and her master students Fatma FINDIK and Ghazi AL ALİ their invaluable technical support for the protein purification experiments.

I would like to thank the Scientific and Technological Research Council of Turkey (TUBITAK) and Health Institutes of Turkiye (TUSEB) for their financial support. This thesis was funded by TUBITAK (Grant ID: 124Z119) and TUSEB (Grant ID: 22905).

I express my appreciation to my dear friends Büşra Acar, Nihan Aktaş Pepe, Seray Zora Tarhan, Sümeyye Özuzun, Nur Şebnem Ersöz, Atiyye Zorluer, Nazendenur Bayram, Hatice Kılıç, Mehmet Burak Yiğit, Ferhan Yenisert, Seda Arıcı, Canan Çil and Sultan Şahin Keskin for their absolute love, belief, support and tremendous encouragement.

Finally, I express my very profound gratitude to my family members Serap ŞANSAÇAR İlhan ŞANSAÇAR, Muhammed İbrahim ŞANSAÇAR, Furkan Samed ŞANSAÇAR and Duygu KAYA ŞANSAÇAR for support and continuous encouragement.

TABLE OF CONTENTS

1. DISCOVERY OF NEW CANDIDATES TARGETING THE SH2 DOMAINS OF SPLEEN TYROSINE KINASE (SYK) THROUGH *IN SILICO* STUDIES 1

1.1 INTRODUCTION 1
1.2 METHODOLOGY 3
1.2.1 Target Protein and Ligand Preparation 3
1.2.2 Molecular Docking 4
1.2.3 Molecular Dynamics (MD) Simulation 4
1.2.4 MM/PBSA Binding Free Energy Calculation 6
1.2.5 Drug-likeness properties and ADME Prediction 6
1.2.6 Carcinogenicity Prediction 6
1.3 RESULTS AND DISCUSSION 7
1.3.1 Docking Evaluations 7
1.3.2 Molecular Dynamics Analysis 11
1.3.3 Drug-likeness Properties, ADME and Carcinogenicity Prediction 18
1.3 CONCLUSION 20

***2.* TARGETING SH2 DOMAINS OF SYK KINASE AND EVALUATION OF BINDING BY IN *VITRO* STUDIES 22**

2.1 INTRODUCTION 22
2.1.1 Spleen tyrosine kinase (Syk) 23
2.1.2 Structure and Function of Syk 24
2.1.3 Signaling pathways and diseases involved in the Syk Network 25
2.1.4 Treatments Targeting Syk and Their Limitations 30
2.1.5 Targeting Syk SH2 Domains as a New Approach and the Aim of the Chapter 31
2.2 METHODOLOGY 31
2.2.1 Searching for target compounds for SH2 domains of Syk using the ENAMINE database 31
2.2.1.4 Drug-likeness Properties and ADME Prediction 36
2.2.5 Carcinogenicity Prediction 36
2.2.2 Expression and Purification of Recombinant SH2 Domains 37
2.2.3 Differential Scanning Fluorimetry Assay 48
2.2.4 Testing the Binding of Compounds to Syk-C-SH2 Domain by Intracellular Fluorescence Resonance Energy Transfer (FRET) Method 48
2.2.5 Statistical Analysis 50
2.3 RESULTS AND DISCUSSION 50
2.3.1 Searching for target compounds for SH2 domains of Syk using the ENAMINE database 50
2.3.2 Expression and Purification of Recombinant SH2 Domains 60
2.3.3 Testing the Binding of Compounds to C-Syk SH2 domain by Differential Scanning Fluorimetry Assay 76
2.3.4 Testing the binding of compounds to Syk SH2 domains by Intracellular Fluorescence Resonance Energy Transfer (FRET) Method 78
2.4 CONCLUSION 80

3. TARGETING OF SYK SH2 DOMAINS FOR THE TREATMENT OF ACUTE MYELOID LEUKEMIA 83

3.1 INTRODUCTION 83
3.1.1 Acute Myeloid Leukemia 83
3.1.3 AML and Deregulated Signaling Pathways 88

3.1.4 Targeting the Syk Enzyme as a Therapeutic Approach in AML *88*
3.1.5 Purpose of the Chapter *91*
3.2 METHODOLOGY 92
3.2.1 Chemicals *92*
3.2.2 Cell Culture *93*
3.2.3 In vitro Cell Viability Assay *93*
3.2.4 Cell Death Assay *94*
3.2.5 Cell Cycle Assay *94*
3.2.6 Real-Time Polymerase Chain Reaction (RT-PCR) *95*
3.2.7 Western Blotting Assay *96*
3.2.8 Statistical analyses *96*
3.3 RESULTS AND DISCUSSION 97
3.3.1 Antiproliferative Effects of Candidate Syk-SH2 Enzyme Inhibitors Z2608161550 and Z2155444005 on THP-1 and HL-60 Cells *97*
3.3.2 Effects of Candidate Syk-SH2 Enzyme Inhibitors Z2608161550 and Z2155444005 on Apoptotic Cell Death in THP-1 and HL-60 Cells *99*
3.3.3 Effects of Candidate Syk-SH2 Enzyme Inhibitors Z2608161550 and Z2155444005 on Cell Cycle in THP-1 and HL-60 Cells *102*
3.3.4 Effects of Candidate Syk-SH2 Enzyme Inhibitors Z2608161550 and Z2155444005 on Nuclear Factor-B (NF-κB) Related Genes in THP-1 and HL-60 Cells *104*
3.3.5 Investigation of the effects of Syk-CSH2 domain inhibitors Z2608161550 and Z2155444005 on apoptotic proteins by Western Blotting *106*
3.3 CONCLUSION 108
4. CONCLUSIONS AND FUTURE PROSPECTS 111
4.1 CONCLUSIONS 111
4.2 SOCIETAL IMPACT AND CONTRIBUTION TO GLOBAL SUSTAINABILITY 112
4.3 FUTURE PROSPECTS 113

LIST OF FIGURES

Figure 1.1 The structure of Syk and activation. ……..……..7

Figure 1.2 3D & 2D interaction figures of the top 5 COCONUT compounds against the C-SH2 domain of Syk….……..……....8-9

Figure 1.3 3D & 2D interaction figures of the top 5 COCONUT compounds against the N-SH2 domain of Syk. …….....…...…….....10-11

Figure 1.4 RMSD plots of the top 5 COCONUT compounds against the C-SH2 and N-SH2 domain of Syk. …….....…...……..12-13

Figure 1.5 Average Distance analysis of the top candidate compound CNP0265345 against C-SH2 (A) and N-SH2 (B) domains of Syk..……...….…....…14

Figure 1.6 Root mean square fluctuation (RMSF) and solvent-accessible surface area (SASA) results..……...…….……15

Figure 1.7 CNP0265345's superimposition over the course of the 300 ns MD simulation at 10 ns snapshots. ……...…….....…… 16

Figure 1.8 MM/PBSA results for both C-SH2 (LIGC) and N-SH2 (LIGN) domains.....18

Figure 2.1 Signal transduction often begins when SRC family kinases phosphorylate the tyrosine residues within ITAMs, which then initiates signaling through Syk……26

Figure 2.2 The role of the Spleen Tyrosine Kinase (Syk) in diseases …….28

Figure 2.3 #6144 Linear structure of pCS2-N-6x-myc-hSyk(1-635) and designed primer pairs..…….……....37

Figure 2.4 Bacterial vector for expression of proteins 6xHis-tagged at the N-terminus with a thrombin site..……..……38

Figure 2.5 Biosensor design ……..….49

Figure 2.6 2D and 3D structures of the 9 selected candidate compounds and their interaction with the C-SH2 domain (Arg175, Arg195, Arg217) are shown with the distance between the atoms in angstroms (Å)..……..52-55

Figure 2.7 Radial distribution function R175 (A), R195 (B) and R217 (C). Rg Plot of all complexes with protein during 100 ns MD Simulation (D). Hydrogen bond number plot of all complexes with protein during 100 ns MD Simulation (E)……56

Figure 2.8 (A) Time evolution of RMSD values during 100 ns simulation (protein). (B) Time evolution of RMSD values during 100 ns simulation (ligand). (C) RMSF plot of all complexes with C-SH2 domain during 100 ns MD Simulation.....57
Figure 2.9 The binding energies of the top 9 compounds are shown in the graph…….....58
Figure 2.10 A) DH5α Competent cells (B) Pet28a(+) expression vector (C) #6144 pCS2-N-6x-myc-hSyk (1-635) ……...….....…… 60
Figure 2.11 1% agarose gel results. ……..……60
Figure 2.12 Transformation of ligation results ……..……..….62
Figure 2.13 1% agarose gel results ……..63
Figure 2.14 Transformation Results ……..…..…64
Figure 2.15 Sample 1 - Sequencing results of Tandem SH2 (forward read)……....…...65
Figure 2.16 Sample 1 - Sequencing results of Tandem SH2 (reverse read)…..……...66
Figure 2.17 Sample 4 - Sequencing results of C-SH2 (forward read)……..…67
Figure 2.18 Sample 5 - Sequencing results of N-SH2 (forward read)……..…..…….68
Figure 2.19 Transformation results of positive plasmids to BL21(D3) (A) N-SH2 (B) C-SH2 (C) Tandem SH2 domains ……....…..…..…...69
Figure 2.20 Induction with 0.5 mM IPTG as final concentration for 16 hours at 18 °C….69
Figure 2.21 Coomassie Brilliant Blue Assay after IPTG Induction ……..…..…70
Figure 2.22 Coomassie Brilliant Blue Assay after IPTG Induction……..……...71
Figure 2.23 Western Blotting Results after IPTG Induction (anti-his).…….....…71-72
Figure 2.24 Results of purification of N-SH2 domain with 0.5 mM IPTG as a final concentration……72
Figure 2.25 Results of purification of Tandem SH2 domain with (A) and without IPTG (B) as a final concentration of 0.5 mM for 4 h at 37 °C. ……...……..…...73
Figure 2.26 Results of purification of C-SH2 domain with 0.5 mM IPTG as final concentration (A) and without IPTG (B) for 4 h at 37 °C. ……...…73
Figure 2.27 Fast Protein Liquid Chromatography and Coomassie Brilliant Blue Assay ……...…...75
Figure 2.28 The results of Differential Scanning Fluorimetry (DSF) Assay.……...77
Figure 2.29 Treatment of HEK293 cells with increasing doses of Z260816155 (A) and Z2155444005 (B) for 48 hours, respectively, and evaluation of the results by MTT assay.……..…..…78

Figure 2.30 HEK293 cells, from top to bottom, non-transfected cells, treated with transfection reagent only, treated with GFP-labeled plasmid (positive control) and Cytosolic Syk Biosensor (Plasmid #125729) (DIC: Differential interference contrast)…….....…..79

Figure 2.31 Change in FRET/CFP value of HEK293 cells transfected with Syk biosensor during 1 hour after addition of Z260816155 (A-B) and Z2155444005 (C-D), respectively. ……..…80

Figure 3.1 2D and 3D structures of the two selected candidate compounds and their interaction with the C-SH2 domain (Arg175, Arg195, Arg217) are shown with the distance between the atoms in angstroms (Å)……..92

Figure 3.2 Effects of Z260816155 and Z2155444005 on the proliferation of THP-1(A-B) and HL-60 (C-D) cells..……...…98

Figure 3.3 Effect of Z260816155 and Z2155444005 on THP-1 cell death. ……..….100

Figure 3.4 Effect of Z260816155 and Z2155444005 on HL-60 cell death. ……101

Figure 3.5 Effect of Z260816155 and Z2155444005 on THP-1 cell cycle progression.103

Figure 3.6 Effect of Z260816155 and Z2155444005 on HL-60 cell cycle progression..104

Figure 3.7 Measurement of the effects of Z260816155 and Z2155444005 on NF-ϰB related TNF-α and IL-1β genes in THP-1 and HL-60 cells via changes in mRNA expression levels…….106

Figure 3.8 Immunoblot analysis of Bcl-2 and Bcl-xL in Thp-1 cells in response to treatment with increasing dosages Z2608161550 and Z2155444005 for 48 hours. ……..…….107

LIST OF TABLES

Table 1.1 COCONUT NPs that are present in the top 100 in both domains…….8
Table 1.2 Drug-likeness properties, ADME and Carcinogenicity Prediction of top 5 compounds …….....19
Table 2.1 Primers designed for individual amplification of SH2 domains……..….37
Table 2.2 PCR Mixture for production of SH2 domains…….40
Table 2.3 Restriction Enzyme Digestion Mixture……..40-41
Table 2.4 Molar Ratios (vector: insert) ……41
Tablo 2.5 Ligation Mixture for N-SH2……42
Tablo 2.6 Ligation Mixture for C-SH2……42
Tablo 2.7 Ligation Mixture for Tandem SH2……...…42
Tablo 2.8 Restriction Digestion Mixture…….43
Table 2.9 Optimization of IPTG Concentration, Incubation Time and Temperature…..44
Table 2.10 Samples selected for Western Blotting after SDS-PAGE-Coomassie Brilliant Blue Assay……..…45-46
Table 2.11 26 Ligands with Highest Binding Affinity to C-SH2 Domain……..…51-52
Table 2.12 The 9 ligands selected for MD analysis and their scores (kcal/mol)……..52
Table 2.13 Drug-likeness Properties, ADME and Carcinogenicity Prediction……59
Table 2.14 Nanodrop Results of gel extraction (N-SH2, C-SH2 and Tandem SH2) and digested pET28a(+) expression vector with EcoRI and HindIII…….61
Table 2.15 Nanodrop Results after RE digestion and PCR clean-up procedure……..61
Table 2.16 NanoDrop Results after Plasmid Isolation……..64
Table 2.17 BCA Protein Concentration Assay Results……76
Table 3.1 Summary of FAB Classification……..84
Table 3.2 Comparison of AML Classification Systems Based on Updates…….85
Table 3.3 Key Differences: WHO 2022 vs. ICC 2022……86
Table 3.4 ELN 2022 Genetic Risk Classification……87
Table 3.5 Primers for RT-PCR……95
Table 3.6 Percentage concentrations of Z260816155 and Z2155444005 that inhibited cell growth by 10, 20, 30 and 50%.....98

LIST OF ABBREVIATIONS

ADME	Absorption, Distribution, Metabolism, and Excretion
AML	Acute Myeloid Leukemia
ATP	Adenosine Triphosphate
BBB	Blood-brain barrier
C-SH2	C-terminal Src homology 2
CarcinoPred-EL	Carcinogenicity Prediction using Ensembled Learning Methods
CFP	Cyan Fluorescent Protein
CHARMM	Chemistry at Harvard Macromolecular Mechanics
CLL	Chronic Lymphocytic Leukemia
COCONUT	the COlleCtion of Open NatUral producTs
COM	Average Distance heatmap plots between center of mass
DMARD	Disease-Modifying Antirheumatic Drugs
DSF	Differential Scanning Fluorimetry
FAB	French-American-British
FLVR	PheLeuValArg
FLVRES	PheLeuValArgGluSer
FPLC	Fast Protein Liquid Chromatography
FRET	Fluorescence Resonance Energy Transfer
HIA	Human Intestinal Absorption
IBD	Inflammatory Bowel Disease
IPTG	Isopropyl-β-D-thiogalactopyranoside
ITAM	Immunoreceptor Tyrosine-Based Activation Motif
ITP	Immune Thrombocytopenic Purpura
MAPK	Mitogen-Activated Protein Kinase
MD	Molecular Dynamics
MDR	Multidrug Resistance
MDS	Myelodysplastic Syndrome
MM/PBSA	Molecular Mechanics Poisson–Boltzmann Surface Area
MPN	Myeloproliferative Neoplasms
N-SH2	N-Terminal Src Homology 2

NF-κB	Nuclear Factor-B
NPs	Natural Products
NSAID	Nonsteroidal Anti-Inflammatory Drug
P-gp	P-glycoprotein
PCR	Polymerase Chain Reaction
PDAC	Pancreatic Ductal Adenocarcinoma
PI3K	phosphoinositide 3-kinase
PLCγ	phospholipase Cγ
PLI	Protein Ligand Interaction
PPI	Protein-Protein Interaction
PTK	Protein Tyrosine Kinase
pTyr	tyrosyl-phosphorylated
RA	Rheumatoid Arthritis
RCSB	The Research Collaboratory for Structural Bioinformatics
RF	Random Forest
Rg	Radius of gyration
RMSD	Root Mean Square Deviation
RMSF	Root-Mean-Square-Fluctuation
SASA	Solvent Accessible Surface Area
SDS-PAGE	sodium dodecyl sulfate–polyacrylamide gel electrophoresis
SLE	Systemic Lupus Erythematosus
SLP76	SH2 domain-containing leukocyte protein 76
SMILES	Simplified Molecular Input Line Entry System
SMINA	Scoring and Minimization with AutoDock Vina
SVM	Support Vector Machine
Syk	Spleen Tyrosine kinase
Tm	Melting Temperature
TPSA	Topological Surface Area
UCSF	University of California San Francisco
WHO	World Health Organization
XGBoost	Extreme Gradient Boosting

To everything that brought me to these days

Chapter 1

Discovery of New Candidates Targeting the SH2 Domains of Spleen Tyrosine Kinase (Syk) through *in silico* Studies

This chapter of the thesis is based on the publication "M. Şansaçar, C. Sarı, M. S. Yücel, E. B. Gencer Akçok, İ. Akçok, Discovery of New Candidates Targeting the SH2 Domains of Spleen Tyrosine Kinase (Syk) Through In Silico Studies. ChemistrySelect 2025, 10, e00547."

1.1 Introduction

Spleen tyrosine kinase (Syk) is a non-receptor tyrosine kinase which acts as a critical player in important cellular processes involving signal transduction, cell proliferation, differentiation, and phagocytosis [1], [2], [3]. Syk is a multifunctional protein that also contributes to the bone metabolism, platelet function and vascular development [3], [4]. It is mainly expressed in hematopoietic cells, neutrophils, B-lymphocytes, macrophages and myeloid-derived suppressor cells [5], [6]. Syk has a significant role in downstream signaling of both B and T cell receptors [7], [8], [9], [10]. Besides, non-immune cells like fibroblasts, epithelial and endothelial cells and neurons frequently express Syk [11], [12], [13]. Src subfamily kinases phosphorylates the immunoreceptor tyrosine-based activation motif (ITAM) domain via interaction of the receptor tyrosine phosphorylated ITAM domain with the SH2 domain of Syk protein and recruited to a signaling complex on the cell plasma membrane [14]. This activates the Syk and its direct binding to members of the VAV and phospholipase Cγ (PLCγ) families, the p85α subunit of phosphoinositide 3-kinase (PI3K), as well as SH2 domain-containing

leukocyte protein 76 (SLP76) and SLP65. This activates the downstream signaling elements, which eventually causes various cellular responses [3]. Numerous studies have reported that there is a strong correlation between Syk dysregulation and disorders such as cancer, autoimmune or allergic conditions [1], [12], [15], [16]. Therefore, Syk inhibition has recently gained attention as a potential treatment option to combat such diseases, which always require novel treatment approaches. Protein tyrosine kinase (PTK) inhibitors which target the active site of the kinase domain are used in the clinic for the treatment of many diseases, especially cancer [1], [14], [16], [17]. However, recurrence of drug resistance has emerged as a problem during the clinical use of these inhibitors [18]. In addition, structural similarity between adenosine triphosphate (ATP) binding sites is another limiting factor for low specificity of kinase inhibitors [19]. Several small-molecule ATP-competitive Syk inhibitors have been developed and evaluated, including fostamatinib, cerdulatinib, and TAK-659 [20], [21], [22]. Nevertheless, they did not show promising results in clinical studies because of low specificity and serious cytotoxicity [23]. It has been demonstrated that patients receiving fostamatinib treatment have side effects such as hypertension, diarrhea, elevation of hepatic enzymes and neutropenia [24], [25]. Moreover, other studies showed that hypertension was the most important side effect of fostamatinib use and was significantly associated with cardiovascular side effects [26], [27]. This has led researchers to investigate new generation Syk inhibitors. Entospletinib, on the other hand, is a second-generation Syk inhibitor with higher Syk specificity that shows promise in the treatment of hematological malignancies such as acute myeloid leukemia and chronic lymphoid leukemia [28]. Nonetheless, the rapid development of drug resistance to entospletinib during treatment rendered its efficacy ineffective [29]. Therefore, there is an unmet need for the development of novel Syk inhibitors that addresses drug resistance and has fewer side effects. Syk enzyme contains two SH2 domains followed by the kinase domain. [30]. SH2 domains recognize and bind to tyrosyl-phosphorylated (pTyr) peptide sequences on the target proteins, thus having an important role in mediating intracellular protein-protein interaction (PPI) [31] (Figure 1.1). SH2 domains possess conserved residue motifs and the most crucial motif for pTyr binding includes an arginine at the fifth position of βB, βB5, as part of a highly conserved " PheLeuValArg (FLVR)" or "PheLeuValArgGluSer (FLVRES)" sequence motif [32]. Several lines of evidence reported that FLVR arginine is required for SH2-pTyr binding. Studies indicate that PPI regulation and targeting is regarded as a potentially effective drug discovery approach. SH2 domains are important

targets suggesting blocking the activation of abnormal proteins that cause diseases [33].Conventional experimental methods for drug discovery and evaluation of these candidates could be expensive and time-costly. Recently, computational methods have been widely used to narrow down the larger inhibitor pools to promising candidates. Owing to methods including virtual screening, molecular docking, and MD simulations, one could filter large libraries of compounds and recognize those that are most likely to bind to a target protein with desired features [34].

In the present study, we aimed to reveal a potential inhibitor which targets both C-SH2 and N-SH2 domains of Syk enzyme using a natural product library, named COlleCtion of Open Natural ProdUcTs (COCONUT) database which consists of 406747 unique natural products (NPs), via combining over 50 open NP resources, through targeting conserved amino acid motif and examine the interactions of compounds with SH2 domains of Syk. With this purpose, a series of protocol containing molecular docking, molecular dynamics simulations, molecular mechanics Poisson-Boltzmann surface area (MM/PBSA) calculations, drug-likeness properties and carcinogenicity prediction were applied to COCONUT natural product library.

1.2 Methodology

1.2.1 Target Protein and Ligand Preparation

The crystal structure of Syk was retrieved from The Research Collaboratory for Structural Bioinformatics (RCSB) protein data bank (PDB ID: 7Q63). In this regard, SH2 domains and residues that play major role in the recognition were located via comparing the known literature review and 7Q63's sequence [35]. These residues were also used as coordinates for recognition sites of SH2 domains. By using University of California San Francisco (UCSF) Chimera, heteroatoms were removed, and missing hydrogen atoms, and charges were added by utilizing DockPrep script in accordance with AMBER ff14SB [36].

For ligand acquisition, COlleCtion of Open Natural ProdUcTs (COCONUT) database, has been used [37]. COCONUT database consists of 406747 unique natural products (NPs), via combining over 50 open NP resources. For being able to report the product of this research as possible drug candidate, database had been filtered via applying modified Lipinski's Rule of Five with the Veber extension. The above-

mentioned change extends one of Lipinski's rules, namely that the possible candidate must have a molecular weight of less than 500 AMU, to a molecular weight of less than 1000 AMU, while the remaining rules and extensions were kept unchanged.
After this filtration, around 211 thousand NPs remained in the selected database. Filtered database were separated into unique, ready-to-dock format generating 3D coordinates for each NP by while also minimizing each according to MMFF94 forcefield at maximum 1000 steps by making use of the for each step making use of the OpenBabel version 3.1.1 [38]. Chemistry at Harvard Macromolecular Mechanics (CHARMM) General Force Field (CGenFF) tool was used to automatically construct the CHARMM force field parameters for the ligands [39].

1.2.2 Molecular Docking

Molecular Docking pipeline which was adapted from Gencer Akçok et al. (2024) was applied to discover NPs that have the best binding potential to both, N and C terminal, SH2 domains. In this regard, Smina, a fork of AutoDock Vina, version 1.1.2 has been used, which specific scoring functions that utilizes energies of hydrogen bonding, hydrophobic interactions, steric hindrances, repulsion, electrostatic interactions, and internal ligand torsional constraints [40], [41]. For the C-SH2 centre coordinates of 4.5, -4.15, -2.8 with sizes of 19.4, 20.78, 20.5 and for the N-SH2 centre coordinates of -15.47, -26.05, -5.20 with sizes of 17.88, 16.33, 25.30, was used as their respective docking box. A maximum of ten conformation were allowed per NP with the rest of the parameters of Smina were set as default. The first poses of each docked-NP were selected, and these poses were ordered from lowest binding energy to highest. Hundred docked-NP which have the lowest scores were selected for each SH2 domain. Those two lists' common NPs were selected for further examination in Molecular Dynamics (MD) simulations. Interactions of docked NP for each domain were visualized by BIOVIA, D.S. 2024 Discovery Studio Visualizer.and PyMOL.

1.2.3 Molecular Dynamics (MD) Simulation

Molecular Dynamics studies were conducted using Gromacs ver. 2023.1 [42] at 300 nanoseconds (ns) for the CNP0265345 and at 100 ns for other top 4 compounds at a 300 K temperature. Protein complexes were cleaned and prepared for the simulations by using UCSF Chimera package (version 1.73.3) [36]. CHARMM36 [39] as the force field

and CHARMM-modified TIP3P3 [43] as the explicit water models were selected to describe the ensemble, and the system was solvated in a dodecahedron box with a 10 Å distance. Na^+ and Cl^- ions were added for system neutralization and the steepest descent algorithm was utilized to minimize energy, executed for a maximum of 50,000 steps.

After the system was brought to the minimum energy level, the real dynamic processes began. The equilibrium steps, NVT (constant number of particles, volume, and temperature) and NPT (constant number of particles, pressure at 1 atm, and temperature) conditions, were done separately. Each step was accomplished over a duration of 100 picoseconds. The V-rescale technique was used to regulate temperature throughout all simulations. By employing this strategy, the system's temperature undergoes a methodical and incremental adjustment, thereby reinforcing the stability of the simulated dynamics. Firstly, the complex underwent simulation within an NVT ensemble, with a time constant of 0.1 picoseconds, obtaining velocities consistent with the Maxwell–Boltzmann distribution. After that, the complex was simulated under NPT and in this one, an additional step was applied to control the system's pressure. The Brenden pressure coupling was added with time constants 2.0 picoseconds. This technique upholds pressure stability by adjusting atomic velocities proportionally to variations from the desired pressure level. Combining the V-rescale thermostat for temperature control in both NVT and NPT ensembles, alongside the Berendsen pressure coupling for the NPT ensemble, aimed for a balanced representation of the system's thermodynamic properties in molecular dynamics simulations.

The final MD simulation, conducted for a duration of 300 ns for the best compound (CNP0265345) and 100 ns for the other four compounds, utilized the leap-frog integration method with a time interval of 2 femtoseconds. The simulation was executed within three-dimensional periodic boundary conditions, a vital factor for simulating an infinite system and mitigating boundary effects. Pressure coupling was accomplished using the Parrinello-Rahman method, which ensured a constant pressure during the simulation and an altered version of the Berendsen method was used to create temperature coupling, leading to accurate temperature control within the system. The stability of each complex was determined by using the GROMACS software tools [44].

1.2.4 MM/PBSA Binding Free Energy Calculation

MM/PBSA binding free energy calculations were employed to estimate the strength of the binding interaction between ligands and receptors [45]. The computations were performed utilizing the g_mmpbsa GROMACS-compatible free energy software [46], employing a grid spacing of 0.5 Å, a salt concentration of 0.150 M, a solute dielectric constant of 2, and utilizing the solvent accessible surface area (SASA) as an estimate of the nonpolar solvation energy.

1.2.5 Drug-likeness properties and ADME Prediction

The Swiss-ADME online platform (accessible at http://www.swissadme.ch/) was employed to forecast the pharmacokinetic attributes encompassing absorption, distribution, metabolism, and excretion of the designated compounds [47]. To facilitate this process, every molecule underwent conversion into a simplified molecular input line entry system (SMILES) format and was subsequently input on the Swiss-ADME server. Following a brief processing time, the outcomes were generated, and the gathered data was utilized for constructing result tables.

1.2.6 Carcinogenicity Prediction

Carcinogenicity Prediction using Ensembled Learning Methods (CarcinoPred-EL) is a computational method to predict the potential of inducing carcinogenicity of the compound in humans and animals. This method is based on three novel ensemble classification models, Ensemble Support Vector Machine (SVM), Ensemble Random Forest (RF), and Ensemble Extreme Gradient Boosting (XGBoost) and was developed to predict carcinogenicity of compounds using seven types of molecular fingerprints and three machine learning methods based on a dataset which is included 1003 various compounds with rat carcinogenicity [48].

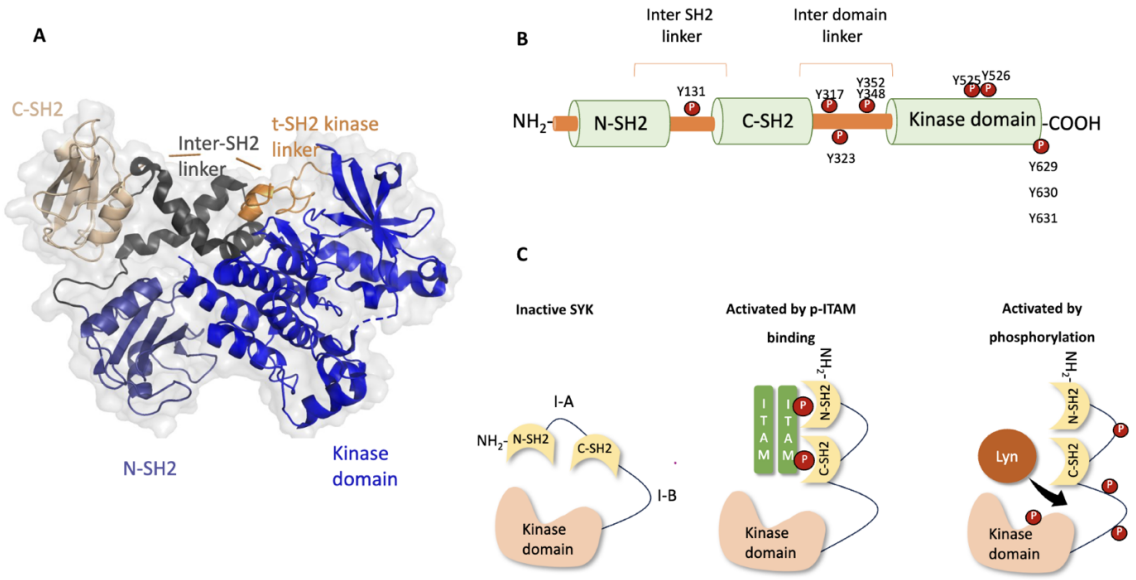


Figure 1.1 The structure of Syk and activation. (A) The representative demonstration of the domain structure of Syk. (PDB: 4FL3) (B) The showing of Syk tyrosine phosphorylation sites. (C) The activation of Syk mechanism via binding of pITAM or by the phosphorylation (autophosphorylation or through LYN kinase) IA: Inter SH2 linker, IB: Inter domain linker [49].

1.3 Results and Discussion

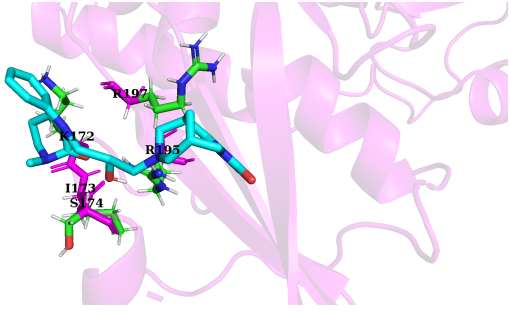
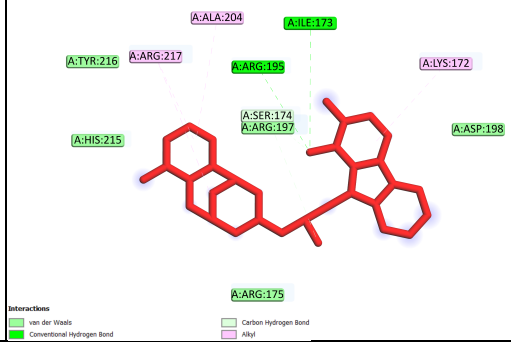
1.3.1 Docking Evaluations

The COCONUT NP database, which had over 400 thousand products, was filtered based on Lipinski's rules with the Veber extension, that ultimately resulted in just over 211 thousand compounds. Furthermore, the original Lipinski's Rule of Five is criteria for orally active compounds that examines four physicochemical parameters: molecular weight <= 500, logP <=5, H-bond donors <=5, H-bond acceptors <=10 [50]. Consequently, Veber extension to the original Lipinski's rules suggested number of rotatable bonds should be equal or less than 10 and the total polar surface area should be equal or less than 140 Angstrom squared [51]. As a result of structure-based virtual screening utilizing the SMINA, lowest energy conformers were discovered with previously stated coordinates and parameters for each SH2 domain for each compound. From these results, top 100 NPs based on the lowest energy conformers were selected for each domain and their binding affinity lies within the -9.3 kcal/mol to -9.9 kcal/mol range for N-SH2 domain while it lies within the -7.9 kcal/mol to -9.1 kcal/mol range for the C-SH2 domain which was shown in supplementary materials, Table S1.

Furthermore, from these top 100 NPs, NPs that are in both lists have been selected for further studies (Table 1.1). To test the possible targeting of both SH2 domains with the same NP, the top 5 NP were selected from the common NP list. To achieve this, the mean binding affinity of N-SH2 and C-SH2 for each NP was calculated and 5 NPs with the lowest average binding affinity were selected for further analysis. These top 5 compounds can be listed as follows for N-SH2 and C-SH2, respectively: CNP0118091 with -9.7 kcal/mol and -8.3 kcal/mol; CNP0265345 with -9.5 kcal/mol and -8.4 kcal/mol; CNP0159934 with -9.4 kcal/mol and -8.4 kcal/mol; CNP0015002 with -9.8 kcal/mol and -7.9 kcal/mol; CNP0114154 with -9.5 kcal/mol and -8.1 kcal/mol. Moreover, regarding C-SH2, almost all top 5 NP have at least one hydrogen bond with a key residue Arg195, except for CNP0114154 (Figure 1.2). On the other hand, regarding N-SH2, CNP0114154 and CNP0265345 make at least one hydrogen bond with a key residue Arg42, as well as interact with other residues such as Arg22, Lys232, Arg45, Asn46, and Thr65 (Figure 1.3).

Table 2.1 COCONUT NPs that are present in the top 100 in both domains.

COCONUT ID	N-SH2 Binding Affinity (kcal/mol)	C-SH2 Binding Affinity (kcal/mol)
CNP0265345	-9.5	-8.4
CNP0170588	-9.6	-8.0
CNP0118091	-9.7	-8.3
CNP0114154	-9.5	-8.1
CNP0015002	-9.8	-7.9
CNP0159934	-9.4	-8.4
CNP0376120	-9.4	-7.9

3D interactions	2D interactions
CNP0118091	**CNP0118091**
	

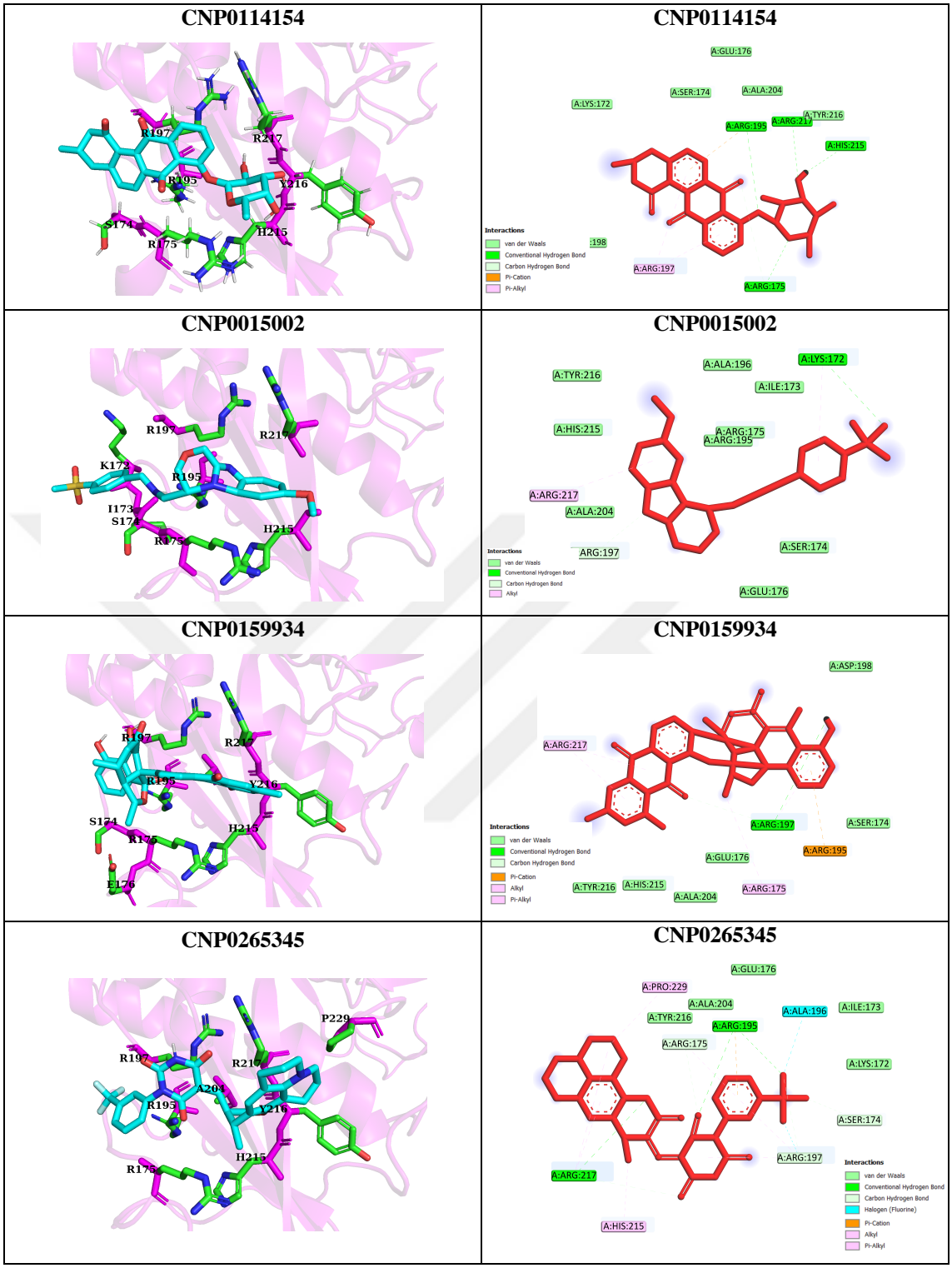
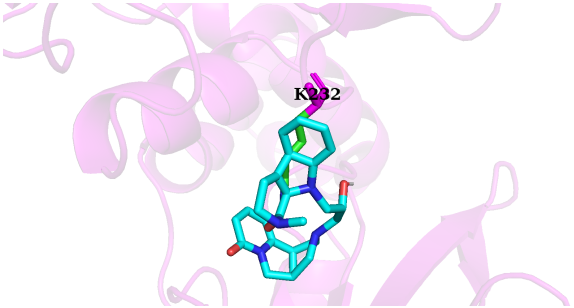
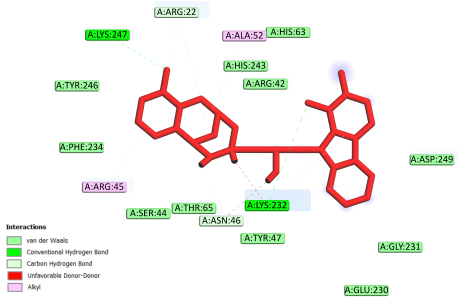
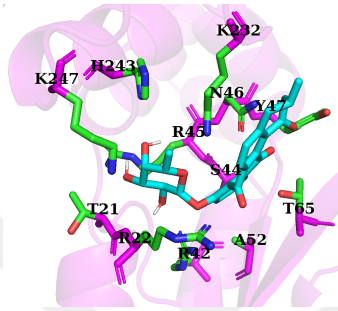
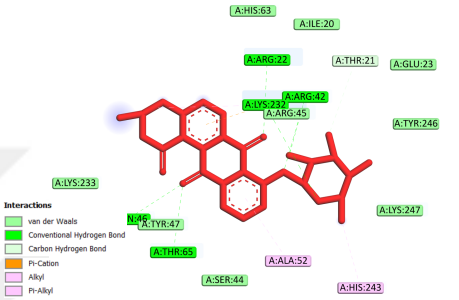
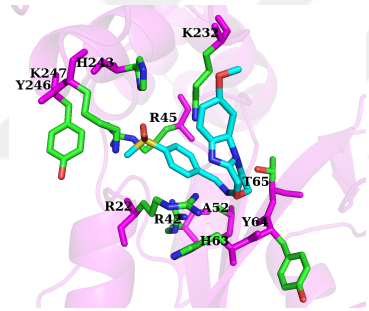
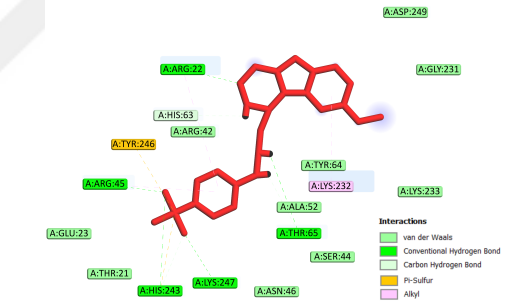
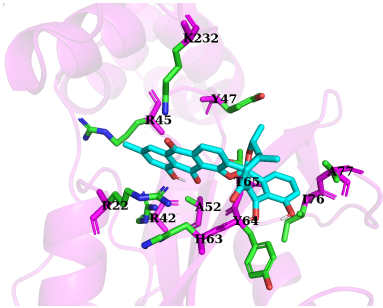
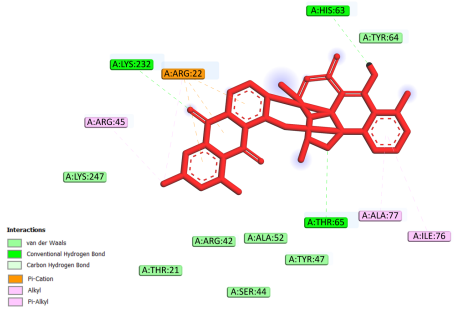


Figure 1.2 3D & 2D interaction figures of the top 5 COCONUT compounds against the C-SH2 domain of Syk. Magenta color represents the backbone atoms while cyan color represents docked compounds and side chains carbon atoms are shown in green, nitrogen atoms in blue, and oxygen atoms in red. (3D figures created by PyMOL, 2D figures are done by Discovery Studio Visualizer)

3D interactions	2D interactions
CNP0118091	**CNP0118091**
	
CNP0114154	**CNP0114154**
	
CNP0015002	**CNP0015002**
	
CNP0159934	**CNP0159934**
	
CNP0265345	**CNP0265345**

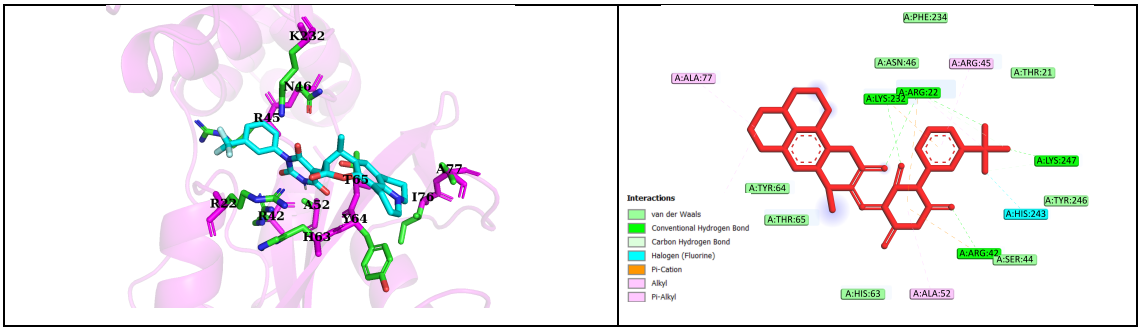


Figure 1.3 3D & 2D interaction figures of the top 5 COCONUT compounds against the N-SH2 domain of Syk. Magenta color represents the backbone atoms while the cyan color represents docked compounds and side chains carbon atoms are shown in green, the nitrogen atom in blue, the oxygen atom in red) (3D figures created by PyMOL, 2D figures are done by Discovery Studio Visualizer)

1.3.2 Molecular Dynamics Analysis

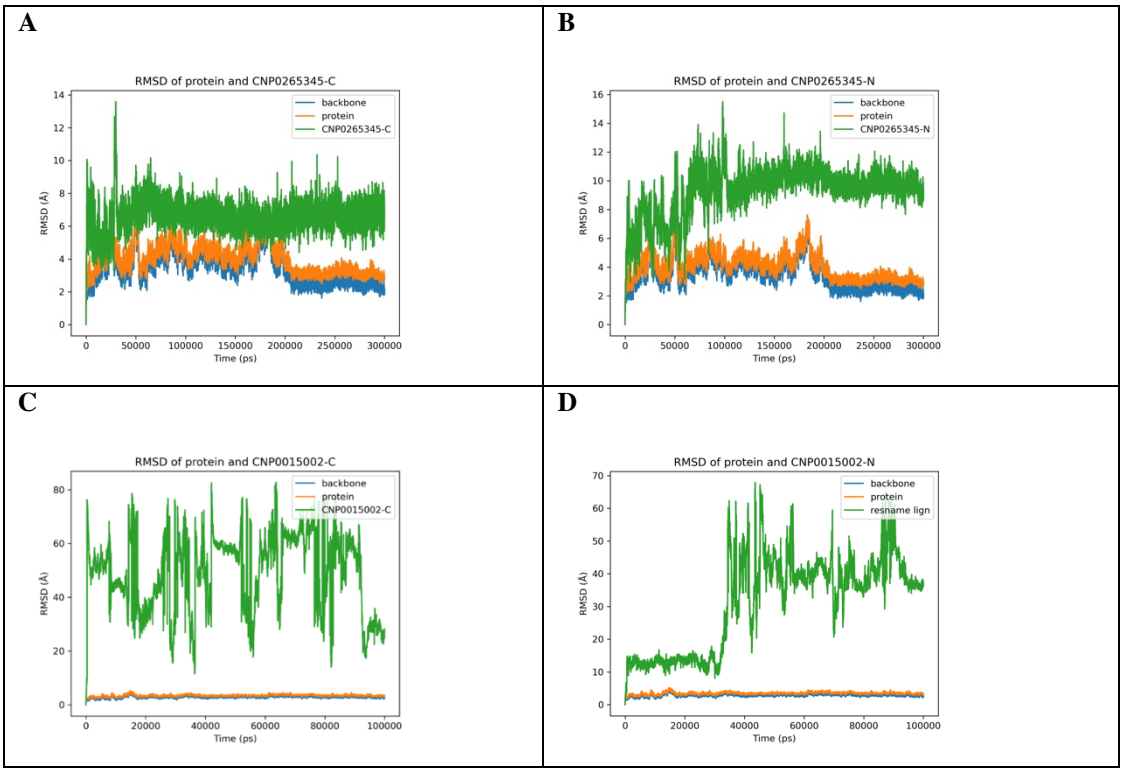
1.3.2.1 Molecular Dynamics (MD) simulations

To understand the complex stability and interaction profile of the previously selected top 5 candidate compounds for both SH2 domains of Syk protein, MD simulations were performed for the period of 100 ns. Each candidate compound was simulated simultaneously for each domain of the Syk protein. By this way, we could get information about the stability of the NP-Syk complex having the same ligand in both domains. According to the first results, simulation time MD analysis of the compound with the best binding affinity was increased to 300 ns. Root Mean Square Deviation (RMSD), Distance, Root-Mean-Square-Fluctuation (RMSF), Radius of Gyration (Rg), Solvent-Accessible Surface Area (SASA), Hydrogen-Bonds and Molecular Mechanics/Poisson-Boltzmann Surface Area (MM/PBSA) analyses were performed from the obtained MD results.

1.3.2.1 RMSD and Distance analyses

RMSD (Root Mean Square Deviation) analysis is used in molecular dynamics simulations to measure structural changes of a molecule or molecular system over time. The difference between the protein's backbone atoms in its initial and final conformations was measured using RMSD plots of 5 hit ligands' MDs. RMSD values between the ligand and protein is used for inferring the overall protein-ligand stability. Furthermore, the fluctuations seen during the simulations can be utilized for estimating the protein's stability as well as the ligand-protein complex stability. These values show how the structure of the protein changes over the simulation time. The protein RMSD is slightly higher than the backbone values in all results (Figure 1.4). Both the backbone and side

chains are considered in the protein RMSD. Basically, smaller changes during simulations led to a more stable protein structure. In Figure 1.4A, the C-SH2 - CNP0265345 complex fluctuated throughout the simulation with a range of 4 to 10 Å. It exhibited fluctuation patterns until ~50 ns, and maintained steadiness until 300 ns, with little deviations. In the same manner, the N-SH2 - CNP0265345 complex exhibits similar fluctuation patterns, with a range of 4 to 12 Å and showed stable equilibrium with approximately 10 Å from 100 ns to 300 ns (Figure 1.4B). Molecular Dynamic simulations of the docking complexes of both C-SH2 and N-SH2 with the other 4 NPs (CNP0015002, CNP0114154, CNP0159934 and CNP0118091) pointed out the severe structural instability, which can be ascertained from the elevated angstrom values of the RMSD and multiple fluctuations in them. Overall, these four compounds revealed similar RMSD values, revealing an unstable binding with both SH2 domains under given simulation conditions (Figure 1.4C-J). Average Distance heatmap plots between the center of mass (COM) of the ligand and amino acids' COM that are in the SH2 binding sites show actual interactions between the ligand and SH2 binding sites (Figure 1.5, and Supplementary materials Figure S1). The NP named as CNP0265345, showed relatively close interaction with both SH2 domains compared to the rest of the tested compounds.



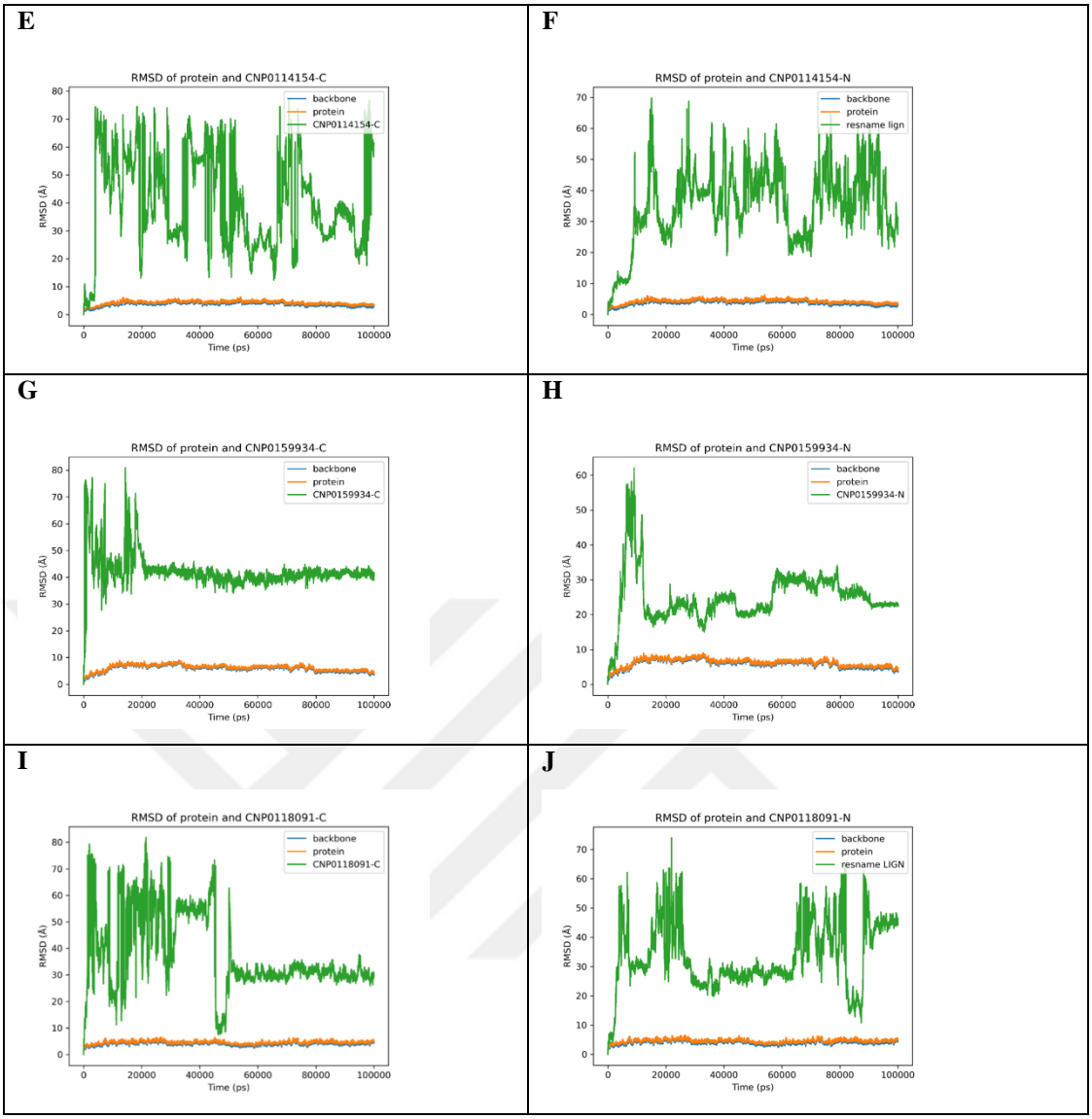


Figure 1.4 RMSD plots of the top 5 COCONUT compounds against the C-SH2 and N-SH2 domain of Syk. The green color represents the ligand, the orange color represents the protein and the blue color represents the backbone. (RMSD = Root Mean Square Deviation)

CNP0265345 exhibited average distance in the interval of 8-9 Å in the C-SH2 domain's key residue of Arg195 while also demonstrating closer interaction with another C-SH2 binding site amino acid, Arg197, in the vicinity of 5-7 Å, especially after ~28 ns to simulation end (Figure 1.5A). In the same manner, CNP0265345 displayed similar closer interaction with the N-SH2 domain relative to the rest of the tested NPs. More specifically, it displayed distance in the interval of ~8 Å between the key residue, Arg42, of N-SH2 and CNP0265345, especially after the first ~100 ns it showed no fluctuation, like C-SH2's stabilization after ~28 ns, which indicates relatively stable protein-ligand complexes in both SH2 domain of Syk. Besides, the most significant interaction of Arg22

residue (4-5 Å), especially after 115 ns, could be the main factor behind the stability of the N-SH2 - CNP0265345 complex. Meanwhile in the rest of the NPs, as it can be calculated from the RMSD values of the mentioned NPs MD simulations, all of them except for the CNP0265345 as reported previously exhibited no relatively stable complexes, meaning all of them cannot stably bind the SH2 domains, resulted in much higher than 10 Å of the heatmap's maximum threshold value (Supplementary materials, Figure S1 and Figure S2).

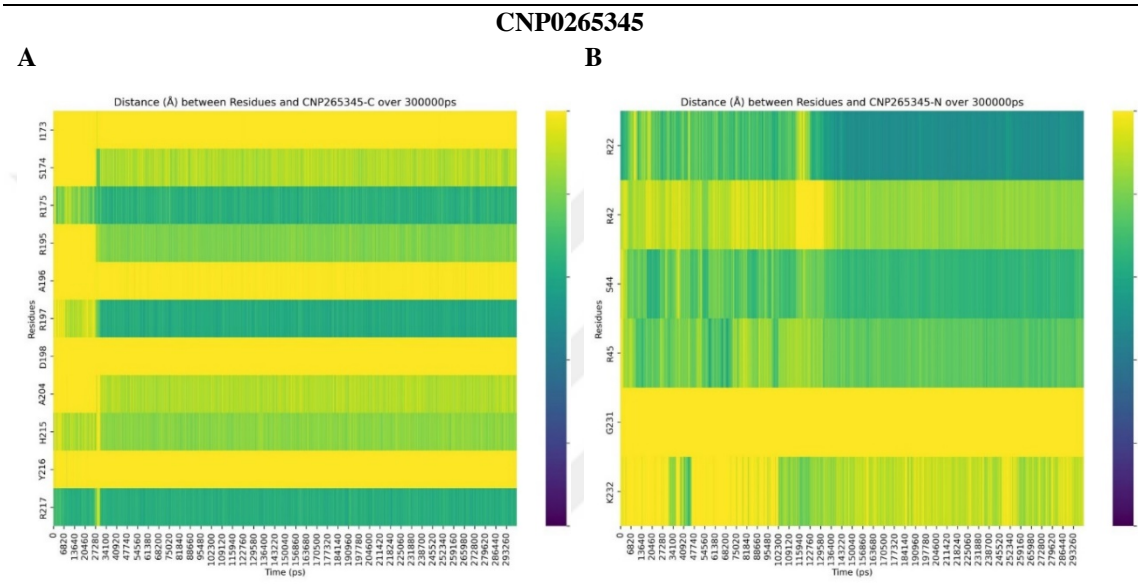


Figure 1.5 Average Distance analysis of the top candidate compound CNP0265345 against C-SH2 (A) and N-SH2 (B) domains of Syk.

1.3.2.1 RMSF, Rg, SASA, H-Bond analyses, and MM-PBSA calculations

Further, the average atomic flexibility of the SH2-docked complexes was measured using root mean square fluctuation (RMSF) analysis to determine the flexible and rigid portions of the complex. All the complexes revealed similar average RMSF values of ~3Å (Figure 1.6). Average fluctuations of all the complexes showed similar values between 1 Å and 5 Å, mostly under 4 Å. Utilizing the radius of gyration (Rg) analysis, the stabilities of the complexes were investigated to ascertain their compactness. The lowest Rg value ligands were the most stable. Rg analysis of CNP0015002, CNP0114154, CNP0159934 and CNP0118091 with complexes demonstrated similar Rg values in the range 2.05 to 2.20 nm. CNP0265345 was the most stable ligand, having an Rg value that fluctuated very little. It is evident that this complex obtained an average Rg value of approximately 2.12 Å, suggesting that, in comparison to the other complexes, the CNP0265345-SH2 has

the best compactness during 300 ns simulation (Supplementary materials, Figure S3). To support this idea, the SASA analysis was performed as part of the stability study of the top 5 ligand complex, and the SASA identification process was carried out to predict the conformational changes in proteins that water molecules would encounter during the simulation. In general, as SASA values decrease, the ligand-receptor complex's stability rises. SASA profile of the CNP0265345 complex had average values with a range of 147 nm^2 –153 nm^2 (Figure 1.6). The average SASA value of the other 4 compounds had average values with a range of 150 nm^2 –170 nm^2 and the fluctuations were observed throughout the 100 ns simulation (Figure 1.6). The SH2-CNP0265345 complex has the lowest SASA value compared to other complexes.

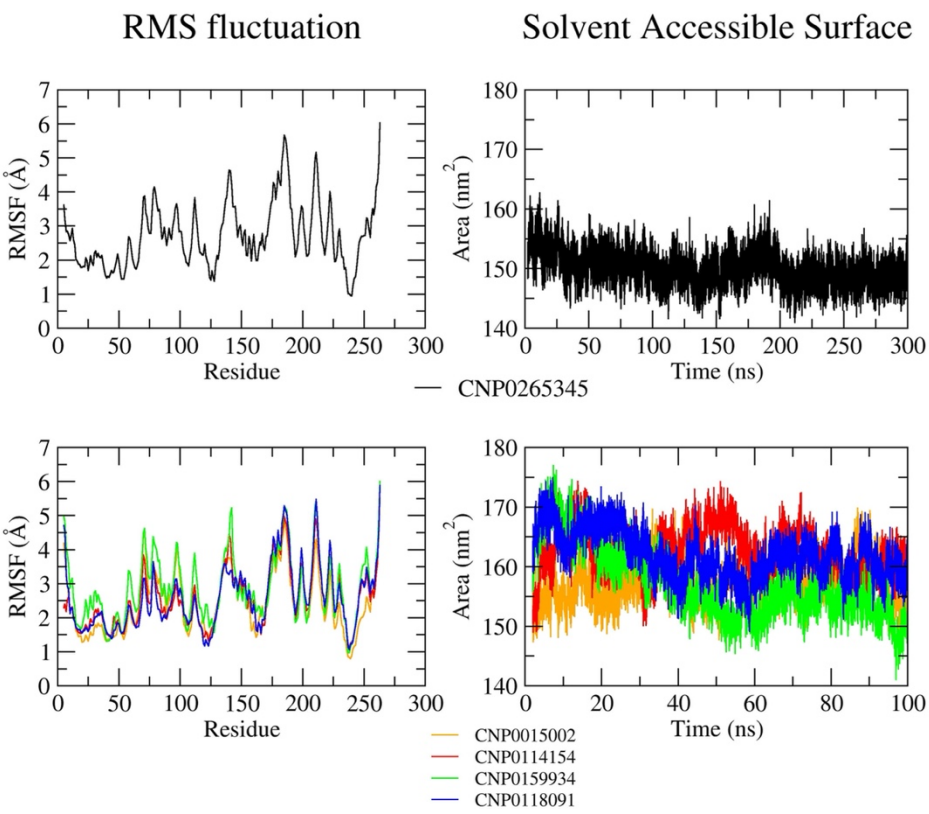


Figure 1.6 Root mean square fluctuation (RMSF) and solvent-accessible surface area (SASA) results.

The total number of bonds generated between the protein-ligand complexes was calculated by analyzing the MD trajectories for hydrogen bond monitoring to comprehend the binding affinity of NPs towards SH2 domains. Plots of hydrogen bonds indicate that every ligand has established an H-bond with the desired amino acids. Each of the five NPs could form an H-bond. However, it was noted that during the simulation, 4 out of 5

(CNP0015002, CNP0114154, CNP0118091 and CNP159934) compounds either lost their capacity to form stable H-bonds or were unable to accomplish effectively. After 100 ns of the simulation, the number of hydrogen bonds in the docked complexes CNP0015002, CNP0114154, CNP0118091, and CNP0159934 were found to be between 0-2, 0-3, 0-2, and 0-4, respectively. The number of H-bonds in the CNP0265345-Syk docked complex was found to be between 0–4 at the first 25 ns and to rise to 4–10 over the 300 ns. The maximum number of hydrogen bonds was observed in this complex, and CNP0265345 indicates it was highly stabilizing both C and N-SH2 domains. Moreover, it is observed that the amount of H-bonds remained constant throughout the simulations (Supplementary materials Figure S4).

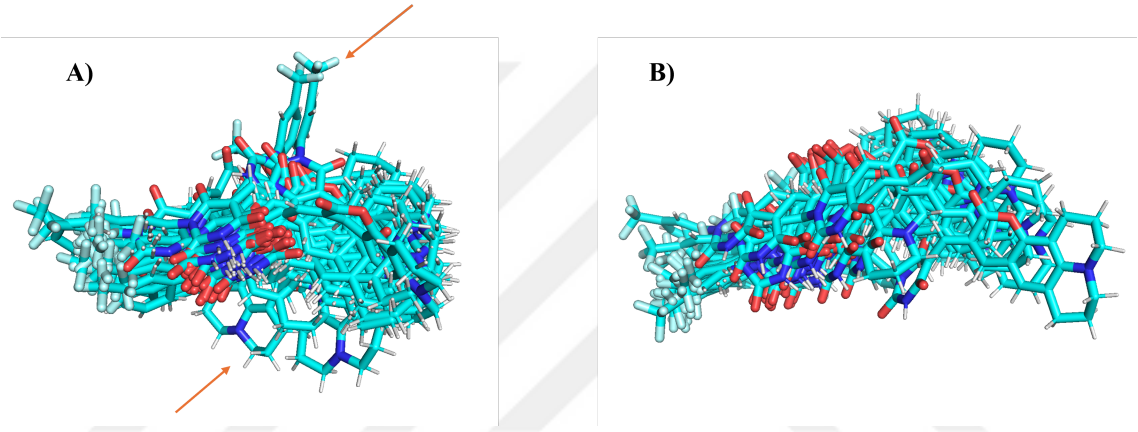


Figure 1.7 CNP0265345's superimposition over the course of the 300 ns MD simulation at 10 ns snapshots. A) CNP0265345's snapshots at the C-SH2 domain of Syk. Orange arrows indicate the first two snapshots. B) CNP0265345's snapshots at the N-SH2 domain of Syk. (MD = Molecular Dynamics)

Next, to support both RMSD and Average Distance Analysis, analysis of CNP0265345's location at the SH2 domains across the 300ns MD simulation was done by superimposing them at by 10ns intervals. As suspected from the previous analyses, CNP0265345 remained at the phosphopeptide recognition site of the SH2 domains of the Syk. Interestingly, at the C-SH2 domain of the Syk, after the first 20ns', there is an altered position of the compound in the phosphopeptide recognition site and after this change, it reasonably could be reported stable. The first 20ns' poses can be seen from the orange arrows in Figure 1.7A. However, no such change was observed in CNP0265345 docked position against the N-SH2 domain of Syk. Even though RMSD results showed relatively higher values for N-SH2 than C-SH2, there is no significant position change of the compound, which can be interpreted as the N-SH2 domain undergoing a structural change

after binding with our compound of interest. Further analysis and confirmation are needed by *in vitro* experiments to confirm this conformational change; however, this situation can explain the high RMSD values even though the ligand didn't relocate from the phosphopeptide recognition site.

Next, by using Molecular Mechanics/Poisson-Boltzmann Surface Area (MM/PBSA) analysis, we investigated the binding free energy related to protein–ligand interactions. The bar plots demonstrate the binding free energies of the top 5 compounds in Figure 1.8. From the graph, it can be seen clearly that there are not any significant average binding differences between each domain for the same compound. As it was mentioned, MD simulation analyses of the top 5 candidates were performed as 100 ns. Results showed that CNP0265345 has the best binding energy -41,78 kcal/mol and -47.75 kcal/mol for the C-SH2 domain and N-SH2 domain, respectively for 100 ns simulation time. CNP0118091 and CNP0015002 have demonstrated positive binding energies due to large polar solvation energies. The other two compounds, CNP0159934 and CNP0114154, exhibited non-significant negative binding energies, because of having relatively small van der Waals energies and low number of H-bonds. Then, the MD analysis time of the best candidate compound (CNP0265345) was prolonged to 300 ns to observe whether the stability of the complex remained or was lost. At this time, it was observed better binding energies for CNP0265345 compared to 100 ns, -44.54 kcal/mol and -55.98 kcal/mol for the C-SH2 domain and N-SH2 domain, respectively during 300 ns simulation time (Figure 1.8). The results obtained here support other analyses. When we consider and combine the data obtained in distance analysis and H-bond analysis, close interactions of the ligand and the amino acids, especially Arg residues, in the SH2 domains elucidate the stability of the complex. The stability of the NPs-Syk complexes can be also seen in MD simulations videos (see MD_videos as supplementary material). In the movies, it is observed that other NPs except CNP0265345 move from their original positions. MD movies demonstrate the high stability of the CNP0265345-Syk complex in both SH2 domains. It can be seen that CNP0265345 remains positioned in both SH2 domains.

The contribution of individual amino acid residues building each SH2 domain and the binding energies of these residues to all candidates were calculated. The results showed that the residues composing the C-SH2 domain interact with the candidate molecules with acceptable binding energies (Table S3). Although positive binding energy was calculated for the important Arg175 residue against the most promising compound

(CNP0265345), the overall binding energy for this compound was found to be -41.78 kcal/mol (Figure 1.8). Since the focus of the study is to target the phosphotyrosine binding pocket as a whole, the overall binding of the molecule is determined by the neighboring residues as well and thus the binding of the molecule is not dependent on only one single residue. Besides, the residues constructing the N-SH2 domain interact with the candidate molecules with high binding energies. Especially for the Arg42 residue, which is a conserved positively charged residue for phosphotyrosine binding of SH2 domains, all the molecules have good binding energies (Table S4). Similar to the C-SH2 domain, the N-SH2 domain's overall binding free energy was calculated as -47.75 kcal/mol for the CNP0265345 compound.

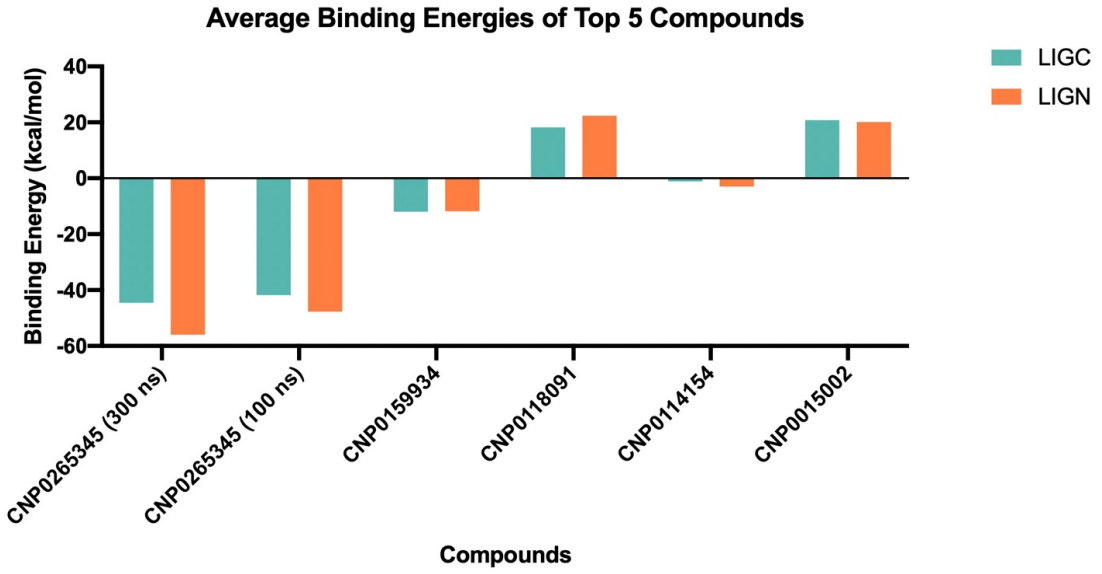


Figure 1.8 MM/PBSA results for both C-SH2 (LIGC) and N-SH2 (LIGN) domains. The average binding energies of the top 5 compounds are represented in the graph

1.3.3 Drug-likeness Properties, ADME and Carcinogenicity Prediction

The drug-likeness properties of the top 5 compounds were measured using Lipinski's rules with the Veber extension. The results indicated that three compounds (CNP0118091, CNP0114154 and CNP0015002) were found suitable for Lipinski's Rule of Five (Table 1.2). The molecular weight of two compounds (CNP0265345 and CNP0159934) slightly exceeded 500 g/mol, with 537.49 g/mol and 534.51 g/mol, respectively. Depending on Lipinski's Rule of Five, hydrogen donors and acceptors have a limit of 5 and 10, respectively. Results demonstrated that each compound was

successfully suitable for this rule. Furthermore, lipophilicities (Log Po/w) of the 5 compounds were less than 5, which also fits with Lipinski's Rule of Five. Moreover, ADME features of 5 compounds were evaluated in Table 2 and Table S5. The topological surface area (TPSA), which is a well-known indicator of drug permeability through the cell membrane, is expected to be ≤140 Å^2 according to Veber filter. Consistent with this, the TPSA value of each compound was less than 140 Å^2. Orally administered drugs are more comfortable for the patients in terms of administration. Thus, human intestinal absorption (HIA) is important for the bioavailability of the drug candidates. ADME results also showed that the candidates have high HIA except one (CNP0159934). Interestingly, the data showed that none of the top 5 compounds could cross the Blood-brain barrier (BBB) (logBB must be greater than 0.3 for proper passage across the BBB). The BBB is important when especially the drug aims to target neurological diseases such as Alzheimer's disease, Parkinson's disease, or stroke [52]. P-glycoprotein (P-gp) has a paramount role in the disposition of drugs. P-glycoproteins reduce the oral availability of drugs that are its substrates since P-gp pumps them out of cells before they can be absorbed into the bloodstream [53]. Thus, identification of permeability glycoprotein substrates is crucial during drug discovery studies for the evaluations of drug candidates. The best candidate, CNP0265345, was not P-gp substrate. Therefore, we could claim that it is not excreted out of the cell via the P-gp carrier protein. Furthermore, the results obtained from CarcinoPred-EL were summarized in Table 2. The average values of highly carcinogenic compounds depending on the calculations with the RF method are close to 1. According to carcinogenicity prediction using RF method, the average value of top 5 compounds was smaller than 0.5 and this showed each compound non-carcinogen.

Table 1.2 Drug-likeness properties, ADME and Carcinogenicity Prediction of top 5 compounds

Compound Name	CNP0265345	CNP0159934	CNP0118091	CNP0114154	CNP0015002
Molecular Weight (g/mol)	537.49	534.51	446.54	452.45	401.48
Num. H-bond acceptors	8	8	4	8	6
Num. H-bond donors	1	3	1	3	1
Log $P_{o/w}$	4.25	3.78	2.10	1.61	2.05
Number of exceptions of	1	1	0	0	0

Lipinski's Rule of Five					
TPSA	99.93 Å²	130.36 Å²	70.71 Å²	130.36 Å²	90.83 Å²
BBB	No	No	No	No	No
P-gp substrate	No	Yes	No	Yes	Yes
HIA	High	Low	High	High	High
CarcinoPred - EL Method, Random Forest (RF), (Average)	Non-carcinogen (0.33)	Non-carcinogen (0.48)	Non-carcinogen (0.37)	Non-carcinogen (0.33)	Non-carcinogen (0.42)

1.3 Conclusion

Protein-protein interactions (PPI) are very critical for many cellular processes such as cell proliferation, signal transduction, cell death mechanisms or cell differentiations. Any deviation or disruption of the PPIs results in as many diseases as cancer, neurodegenerative diseases, or autoimmune diseases. Therefore, targeting PPIs is one of the most attractive ways to uncover new drug candidates. SH2 domains are highly conserved protein units found in over 110 proteins and are important in PPIs. SH2 domains possess conserved residues like arginine at the fifth position of βB5 (N-SH2 of Syk; Arg42 and C-SH2 of Syk; Arg195) on the pTyr recognizing pocket. This specific motif facilitates the targetability of SH2 domains. One of such proteins that possess two SH2 domains is the Syk enzyme. In this study, we aim to reveal the possible Syk-SH2 domain inhibitors by using computational analysis from a natural product library which is the COCONUT database. Based on the best docking scores obtained from the molecular docking results, we were interested in the top 5 compounds for further studies including MD analysis, MM/PBSA, ADME and carcinogenicity predictions. All studies showed that compound CNP0265345 has the best binding properties towards both C-SH2 and N-SH2 of Syk enzyme with –44.54 kcal/mol and –55.98 kcal/mol binding free energies, respectively for 300 ns simulation time. CNP0265345 belongs to the class of "coumarins and derivatives". The literature studies indicate that there are studies in which coumarin or its derivatives directly target the SH2 domain when docked with proteins with SH2 domains such as Grb2 or STAT3, which are in line with our results [54], [55]. Although we could not identify any prior *in silico* study targeting SH2 domains of Syk, we found an *in-vitro* study with the same aim. In this experiment, 8,8'-disulfanediylbis(1,3-dimethyl-3,7-dihydro-1H-purine-2,6-dione) (named as compound

44 in the original article) was shown to be effective under biological conditions [56]. We did molecular docking and molecular dynamic studies of this reference compound using the same methodology. When compound 44 and CNP0265345 are compared for their docking poses, similar amino acids are found to be interacting, as can be observed from Figure S5. More importantly, CNP0265345 showed much better results in *in silico* environment than the compound 44 (Figure S5 and Figure S6), which can be observed from the RMSD results (Figure S6). This figure indicates the docking of N-SH2 and C-SH2 with compound 44 that stayed constantly above 20 Å apart from the first nanoseconds of MD simulation. Besides, the average distance analysis of compound 44, which supports the RMSD analysis displays compound 44, going 10 Å away from the phosphopeptide recognition site of both SH2 domains. These results show that CNP0265345 has stronger binding and higher stability against protein, demonstrating better stability than in every MD analysis. Since *in silico* results are an important indicator of possible interactions in biological environments, it can be said that CNP0265345 may be a much more promising drug candidate if *in-vitro* experiments support it. Because *in silico* results provide an important indicator of potential interactions in biological environments. Our molecular docking results provide initial hypotheses regarding the interaction of these natural compounds with the Syk-SH2 domains. However, these findings should be interpreted in light of limitations inherent to docking methodologies, such as scoring function inaccuracies and simplified treatment of molecular flexibility. Furthermore, the structural complexity and potential polypharmacological nature of natural compounds mean that these single-target predictions require rigorous validation. Subsequent studies using *in vitro* biochemical and functional assays are mandatory to validate predicted binding modes, affinities, and biological activities. Here, we propose a novel SH2 domain inhibitor of the Syk enzyme using computational drug discovery methods. Consequently, even though both *in vitro* and *in vivo* validations are needed, this study will help to find a way forward the development of novel drugs to target dysregulated protein-protein interactions.

Chapter 2

Targeting SH2 domains of Syk kinase and evaluation of binding by in *vitro* studies

2.1 Introduction

Spleen tyrosine kinase (Syk) is a 72 kDa non-receptor tyrosine kinase belonging to the Src kinase family. Although Syk is known as a non-receptor tyrosine kinase that is primarily involved in various functions of the immune system and also includes some non-immune biological processes, recent reports have shown that Syk also mediates other biological functions important for cellular communication, differentiation, activation, and survival. Numerous studies have reported a strong association between abnormal or overexpressed Syk and disorders such as cancer, autoimmune, or allergic conditions [1], [12], [16]. In addition to the importance of Syk in many diseases, its connections with signaling sub-pathways are also quite remarkable. Because Syk interacts with many signaling pathways and plays a major role in the activation of these pathways and many of these pathways may be disease-related. Therefore, targeting the Syk enzyme is an important step in developing new treatments.

In this context, literature studies show that some kinase inhibitors (protein tyrosine kinase inhibitor-PTKi) directly target the kinase region, which is the active site of the Syk enzyme. However, the recurrence of drug resistance has emerged as a problem during the clinical use of these inhibitors [18]. In addition, the structural similarity between the ATP-binding sites is another factor that limits the use of kinase inhibitors with low specificity [19]. Furthermore, in clinical studies, these inhibitors have not given promising results in clinical studies due to low specificity, side effects such as hypertension, diarrhea, elevation of hepatic enzymes and neutropenia in patients, and serious cytotoxicity [23].

Therefore, the development of a new type of Syk inhibitor that challenges drug resistance and has fewer side effects is an unmet need.

The Syk enzyme contains two SH2 domains, and these two domains play a very important role in protein-protein interactions. SH2 domains are 100 amino acid modular units that recognize and bind to tyrosyl-phosphorylated peptide sequences on target proteins, thus mediating intracellular protein-protein interactions. Researchers have shown that regulating and targeting protein-protein interactions is considered a promising strategy in drug discovery. When looking at the literature, recent studies suggested that SH2 domains are also important targets in addition to active kinase domains in cancer treatment methods to prevent the activation of abnormal proteins that lead to cancer [57], [58], [59], [60], [61].

Considering the role of Syk in cancer and other diseases, it is seen that it acts as a kind of "hub" together with different signaling pathways. For this reason, targeting this protein is necessary and important. In the proposed project, the inhibition of protein-protein interactions is aimed by targeting the SH2 domains of Syk. For this purpose, it is aimed to investigate new candidate inhibitors using the ENAMINE data library for the SH2 domain of Syk enzyme both *in silico* and *in vitro*. It is aimed that the findings obtained will provide a new perspective on treatment approaches and make significant contributions to the literature.

2.1.1 Spleen tyrosine kinase (Syk)

The Syk enzyme was discovered by Taniguchi and colleagues in 1991 [62]. The gene encoding human SYK is located at position q22 of chromosome 9. It is a 72 kDa non-receptor cytosolic tyrosine kinase belonging to the Src kinase family. Syk is a multifunctional protein that also contributes to bone metabolism, platelet function, and vascular development [3], [4]. It is mainly expressed in hematopoietic cells, neutrophils, B lymphocytes, macrophages, and myeloid-derived suppressor cells [5], [6]. In addition, cells outside the immune system, such as fibroblasts, epithelial and endothelial cells, and neurons, frequently express Syk [11], [12], [13]. Syk has an important role in downstream signaling of both B and T cell receptors [7], [8], [9], [10].

2.1.2 Structure and Function of Syk

Syk has a kinase domain (SH1) at the COOH-terminus and two SH2 domains at the NH2-terminus. The region between the NH2-terminal SH2 (N-SH2) and the COOH-terminal SH2 (C-SH2) is called interdomain A (IDA), while interdomain B (IDB) is located between the SH1 domain and SH2-C (Figure 1.1). The homology of N-SH2 and C-SH2-C is 36%, which may differ when specifically bound to phosphorylated tyrosine. Furthermore, IDA and the two SH2 domains have been reported to be highly conserved across species [10]. Due to alternative splicing (splicing) during transcription, there are two Syk protein isoforms in cells, called full-length Syk (Syk-L) and shortened Syk (Syk-S); the second one is missing 23 amino acids from IDB (TWSPGGIISRIK-SYSFPKPGHKK) [63]. There are 10 tyrosine residues on Syk that are capable of being autophosphorylated (Figure 1.1). These phosphorylation sites play a role in maintaining the kinase inactive, primary activation of the kinase catalytic domain, enhancement of kinase activity and docking sites for various substrates after activation. In the inactive state, Syk adopts an autoinhibitory conformation through the synergistic action of several residues from the A and B interdomains, the kinase domain and the carboxy terminus. When the upstream receptor is activated, the tandem SH2 domains bind to immunoreceptor tyrosine-based activation motifs (ITAMs), which is the key step in Syk activation [64]. The SH2 domain is a non-catalytic motif of approximately 100 amino acids and its structure consists of a β-sheet core with an antiparallel center and an α-helix on either side. The ITAM is a conserved peptide motif containing two tyrosines separated by 9–11 amino acids. When Tyr-130 is phosphorylated in interdomain A, Syk dissociates from the phosphorylated ITAM (p-ITAM) [2].

Phosphorylation of tyrosine residues in interdomain A/B leads to kinase activation even without phosphorylated ITAM binding. This evidence further suggests that Syk adopts an autoinhibitory conformation to maintain the inactive state. Activated Syk can catalyze the phosphorylation of tyrosine residues in the interdomain domain, ensuring that Syk is continuously activated, and these phosphorylated tyrosine residues provide docking sites for downstream signaling molecules and trigger downstream signaling. Upon activation, Syk further phosphorylates several signaling molecules and activates several downstream signaling pathways, such as the RAS-RAF-MAPK-AP1 signaling pathway that controls cell proliferation, the BTK-PLCγ2-IP3-NFAT signaling pathway or the BTK-PLCγ2-PKC-NF-κB signaling pathway that controls cell survival and

cytokine release, and the PI3K-AKT-mTOR signaling pathway that regulates cell growth [65]. These signaling pathways play an important role in cell growth, proliferation, and cytokine release. In recent years, there has been increasing evidence that Syk plays an important role in the pathological mechanisms of allergic reactions, autoimmune diseases, hematomas, and other diseases.

2.1.3 Signaling pathways and diseases involved in the Syk Network

Syk has an important role in the downstream signaling of both B and T cell receptors. Src subfamily kinases phosphorylate the ITAM domain through interaction of the receptor tyrosine phosphorylated ITAM domain with the SH2 domain and recruit it to a signaling complex on the cell plasma membrane [14]. This activates Syk and its direct binding to members of the VAV and phospholipase Cγ (PLCγ) families, the p85α subunit of phosphoinositide 3-kinase (PI3K), and SH2 domain-containing leukocyte protein 76 (SLP76) and SLP65. This ultimately results in the activation of downstream signaling elements that cause a variety of cellular responses. ITAMs are found in the cytoplasmic domains of immunoreceptors such as Fc receptors, T- and B-cell receptors, and NK cell receptors. Association of activating FcγRs with IgG immune complexes induces receptor cross-linking and phosphorylation of tyrosine residues in immunoreceptor tyrosine-based activation motif domains by Src family kinases, such as Lyn. Phosphorylated tyrosine residues become docking sites for Syk, which phosphorylates multiple substrates, leading to diverse signaling pathways that ultimately activate a variety of cellular responses [66]. The Syk protein also plays a role in bone metabolism, platelet function, and vascular development [67]. In addition to the importance of Syk in many diseases, its connections to signaling downstream pathways are also noteworthy (Figure 2.1 and Figure 2.2).

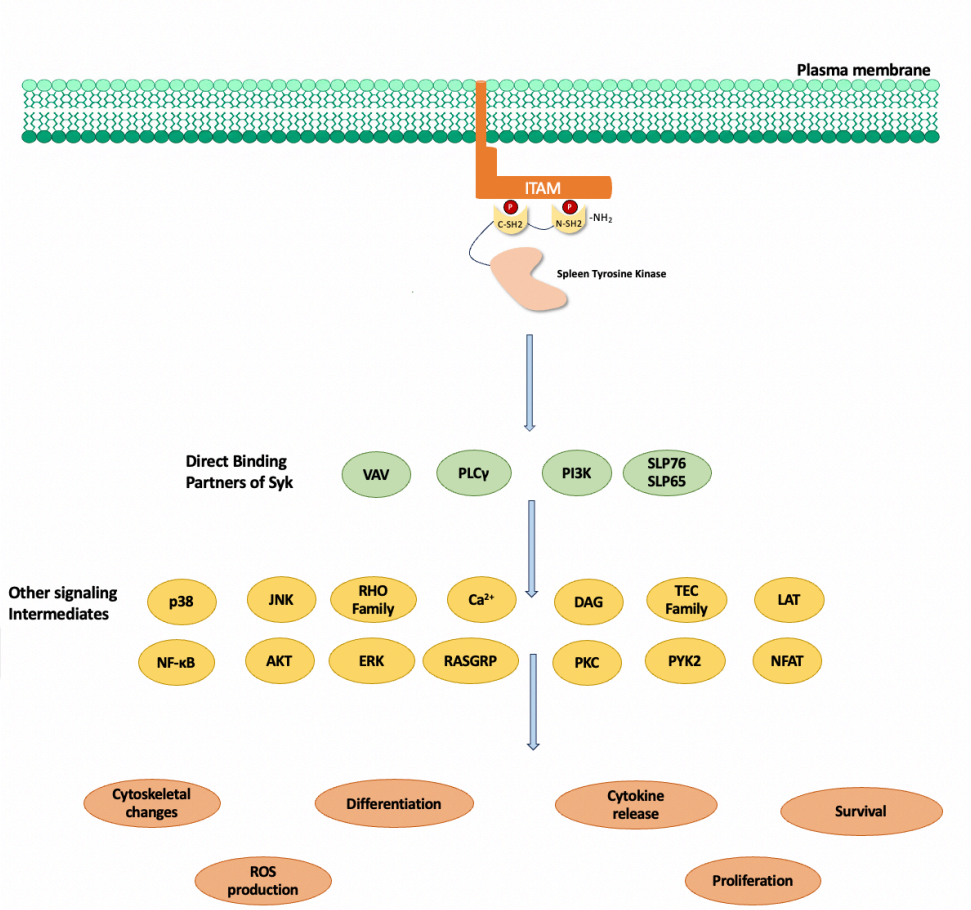


Figure 2.1 Signal transduction often begins when SRC family kinases phosphorylate the tyrosine residues within ITAMs, which then initiates signaling through Syk (Adapted from [3]).

2.1.3.1 Allergic Diseases

Allergic rhinitis, asthma and atopic dermatitis are common allergic diseases. Allergic diseases are mainly mediated by immunoglobulin E (IgE). Allergen-specific IgE recognizes and binds to allergens; then the antigen-IgE complex is cross-linked with FcεRI on mast cells and basophils, leading to an early allergic reaction mediated by degranulation [68], [69]. This early allergic response results in increased vascular permeability, smooth muscle contraction and initial inflammatory cell influx. This is then followed by degranulation and release of some inflammatory mediators such as histamine, tryptamine, 5-hydroxytryptamine (5-HT), heparin, leukotriene (LT) and prostaglandin; chemokines and inflammatory cytokines are produced that regulate late allergic responses including chronic inflammation, airway remodeling and airway hyperresponsiveness (AHR) [65].

In the FcεRI signaling process, FcεRI signals through the interaction between Syk and ITAM located on the receptor-associated transmembrane adaptors FcR-γ and other activated FcRs such as FcεRI and FcγRIIIA [70]. After the antigen-IgE complex binds to FcεRI, ITAM is phosphorylated by the Src family kinase Lyn [71]. The phosphorylated ITAM then binds to the two SH2 domains of Syk and activates Syk. Subsequently, downstream signaling molecules VAV, PLCγ, PI3Ks and SH2 domain-containing leukocyte protein-76 (SLP-76) are phosphorylated. SLP-76 is a transmembrane scaffold protein that can coordinate various downstream signaling events such as Erk-1/2, JNK and p38 activation. PLCγ activation mediates calcium mobilization and protein kinase C (PKC) activation, leading to degranulation and cytokine gene transcription. In addition, mitogen-activated protein kinases (MAPKs) regulate the production of lipid mediators such as LT and cytokines. PI3K activates Akt by recruiting PDK-1, thereby improving cell survival and also regulating FcεRI-mediated degranulation [72]. Since Syk is a key regulator of FcεRI signaling and initiates a cascade of signaling events leading to mast cell degranulation, cytokine production, and lipid media synthesis, drugs that inhibit Syk activity have potential benefits by blocking multiple pathways involved in the pathogenesis of these diseases. Syk inhibitors have demonstrated good efficacy in animal models and clinical studies of allergic diseases.

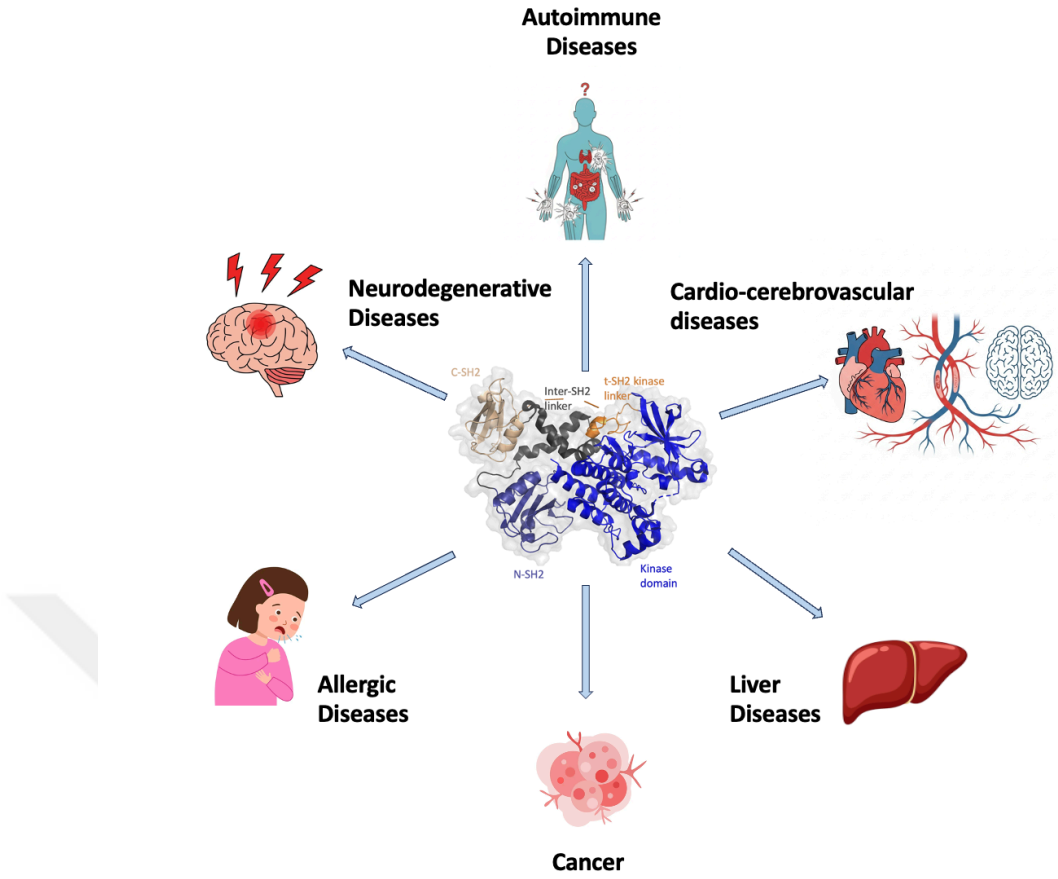


Figure 2.2 The role of the Spleen Tyrosine Kinase (Syk) in diseases [3].

2.1.3.2 Autoimmune Diseases

Syk has emerged as an important tyrosine kinase in the study of the pathogenesis of autoimmune diseases, particularly Immune Thrombocytopenic Purpura (ITP), rheumatoid arthritis (RA), systemic lupus erythematosus (SLE), and inflammatory bowel disease (IBD) [73]. The pathogenesis of ITP involves autoantibody-mediated platelet phagocytosis facilitated by activated Fc receptors on monocytes that activate Syk and bind to specific recognition sequences of ITAM. Promotion of FcγR-mediated phagocytosis via the Syk signaling pathway leads to increased platelet clearance. Inhibition of SYK prevents phagocytosis and promotes platelet survival, highlighting Syk as a therapeutic target. The Syk inhibitor fostamatinib was approved as a treatment for ITP in 2018. Fostamatinib reduces immune system damage to platelets, allowing platelet counts to increase. Based on positive results from two clinical trials, fostamatinib has been approved by the FDA for the treatment of adult patients with chronic ITP [65], [74].

RA is a progressive autoimmune and inflammatory disease characterized by pain and swelling in the foot and hand joints, which can lead to permanent joint destruction

and deformity [75]. Many immune cells and inflammatory factors such as T cells, B cells, mast cells, dendritic cells, fibroblasts, chemokines, proinflammatory factors, etc. play a role in the progression of RA [76]. Current drugs used in the treatment of RA are nonsteroidal anti-inflammatory drugs (NSAIDs), corticosteroids, and disease-modifying antirheumatic drugs (DMARDs). However, these drugs can only delay disease progression or improve inflammatory symptoms. Syk is the central molecule in B-cell receptor signaling and can regulate many downstream signaling molecules, including BTK. Syk also plays an important role in the activation and signaling of mast cells, fibroblasts, and dendritic cells. Inhibiting the activity of Syk may be an important way to treat RA [65]. In a randomized, placebo-controlled Phase II trial, patients receiving R788 (renamed fostamatinib) at 100 mg twice daily or 150 mg twice daily had ACR20 responses of 65% and 72%, respectively, compared with 38% in the placebo group. ACR50 and ACR70 responses were also reported to be significantly better than placebo, but phase III trials were disappointing [3], [67], [77]. Overall, fostamatinib is a new drug that is effective in reducing inflammation and improving clinical activity in patients with RA.

Systemic lupus erythematosus (SLE) is an autoimmune disease that affects every organ system in the body, including the joints, skin, blood vessels, liver, kidneys, and nervous system [65]. Signaling from the BCR in B cells of SLE patients appears abnormal, and significant phosphorylation and expression of Syk have been noted in B cells of SLE patients compared with healthy donors. Administration of R788 to lupus-prone mice has been reported to delay the onset of proteinuria and azotemia in lupus-prone mice, reduce renal pathology and renal infiltrates, and significantly prolong the survival of lupus-prone mice [78]. Subsequent experiments confirmed that Syk inhibition prevents the development of lupus-prone skin and significantly reduces established skin disease. There is also evidence that FcγRs play an important role in the pathogenesis of SLE. The role of FcγRs in the pathogenesis of SLE has been demonstrated in mice with lupus nephritis. In these studies, deletion of FcR-γ or FcR-γ RIII protected these mice from severe glomerulonephritis and prolonged their survival [79].

2.1.3.3 Cancer

Cancer can be divided into two main groups; hematological malignancies and solid tumors, according to their biological characteristics and site of origin. Syk is thought to have both tumor-inhibitory and tumor-promoting effects, and its effect is related to the

tumor type. Syk inhibition has been shown to suppress cell proliferation and migration in lymphomas [67]. Syk inhibitors also play a therapeutic role in multiple myeloma, chronic lymphocytic leukemia (CLL), and acute myeloid leukemia (AML) [23], [65], [67]. Syk has been reported as a potential tumor suppressor in some types of cancer. In breast cancer, SYK expression is negatively associated with the invasiveness of breast cancer cell lines [73], [80]. Wang et al. reported that increased H_2O_2 access to cervical cancer cells results in phosphorylation of Syk and activation of the PI3K-AKT signaling pathway, thereby promoting invasion and metastasis of HeLa cells [81]. Ghotra et al. found that increased Syk protein expression promotes prostate cancer progression [82]. In addition, Syk is thought to be a tumor suppressor gene in gastric cancer. Its mRNA expression level is significantly lower than that in adjacent noncancerous tissue [83]. However, Syk may act as a tumor promoter in some other cancers. In lung cancer, Syk can stimulate the growth and invasion of lung cancer cells by controlling oxidative stress [84]. Rohila et al. showed that macrophage Syk promotes the growth and metastasis of pancreatic ductal adenocarcinoma (PDAC) cells [85]. Interestingly, Syk can exert both tumor suppressor and tumor-promoting effects in the same cancer type. In hepatocyte carcinoma, Syk inhibits cancer cell migration, while the splice variant SYK-S promotes the growth and invasion of hepatocyte carcinoma cells [86]. In addition, Syk has an important role in multidrug resistance (MDR). Zhou et al. showed that SYK expression increases resistance to DNA-targeted therapies and increases resistance to poly(ADP-ribose) polymerase (PARP) inhibitors by promoting homologous recombination [87]. Among the types of oncogenic effects played by Syk, activation of signaling pathways such as Mincle/SYK/NF-κB and PI3K/Akt/mTOR plays an important role in the growth, survival, invasion, and metastasis of cancer cells. Syk is upstream of these signaling pathways, and inhibition of Syk may have greater clinical efficacy than inhibition of downstream signaling molecules. In summary, Syk is an important target for a variety of cancer therapies, and this has been confirmed by the effects of a number of drugs targeting Syk in clinical trials.

2.1.4 Treatments Targeting Syk and Their Limitations

As detailed in Section **1.1 Introduction**, the development of a new type of Syk inhibitor that challenges drug resistance and has fewer side effects is an unmet need. SH2 domains recognize and bind tyrosylphosphorylated (pTyr) peptide sequences on target proteins, thus playing an important role in mediating intracellular protein-protein

interaction (PPI) [31] SH2 domains have conserved residue motifs and the most important motif for pTyr binding involves the βB5 arginine at the fifth position of βB as part of a highly conserved "PheLeuValArg (FLVR)" or "PheLeuValArgGluSer (FLVRES)" sequence motif [32]. Several lines of evidence have reported that the FLVR arginine is essential for SH2-pTyr binding. Studies suggest that PPI editing and targeting is considered a potentially effective drug discovery approach. SH2 domains are important targets proposed to block the activation of aberrant proteins that cause diseases [33].

2.1.5 Targeting Syk SH2 Domains as a New Approach and the Aim of the Chapter

This chapter aims to discover new candidate inhibitors by targeting especially C-SH2 domain of Syk enzyme. For this purpose, binding affinity of 4,032,162 specific compounds in Enamine Screening Collection to SH2 domains of Syk protein was determined. Later, Molecular simulation dynamics (MD) of 9 candidates selected from compounds with high binding affinity were determined. According to the results, the *in vitro* validation of the 2 candidates with the best binding energy and MD (Z2155444005 and Z2608161550) was carried out using the Differential Scanning Fluorimetry (DSF) assay and intracellular Fluorescence Resonance Energy Transfer (FRET) Assay. The aim of the chapter is to identify a new candidate inhibitor by targeting the C-SH2 domain of the Syk enzyme, especially the SH2 domains, using both *in silico* and *in vitro* studies. This new inhibitor search will be the beginning of many different studies, especially considering the relationship of the Syk enzyme with diseases and other proteins and signaling pathways.

2.2 Methodology

2.2.1 Searching for target compounds for SH2 domains of Syk using the ENAMINE database

2.2.1.1 Docking Methods

Receptor and Ligand Library Preparation

The crystal structure of the Homo sapiens Spleen Tyrosine Kinase (Syk) tandem SH2 domains (PDB ID: 1A81) was obtained from the Protein Data Bank for use in this

study. The protein structure was prepared by first removing all crystallographic water molecules to eliminate potential steric hindrances during docking simulations. Polar hydrogens were then added using UCSF Chimera version 1.16 to ensure proper protonation states at physiological pH (7.4). Partial atomic charges were assigned according to the AMBER ff14SB force field to accurately model electrostatic interactions. Finally, the structure underwent energy minimization in GROMACS version 2022.4, consisting of 500 steps of steepest descent followed by 500 steps of conjugate gradient optimization, to relieve any residual steric clashes and improve structural integrity.

For the ligand library, we utilized the Enamine High-Throughput Screening (HTS) collection, comprising 1,368,049 commercially available compounds with drug-like properties compliant with Lipinski's Rule of Five. Each compound underwent thorough preparation beginning with conversion from 2D to 3D representations using RDKit version 2022.09, which generated low-energy conformations for docking. Tautomer and protonation states were enumerated. Finally, all ligands were subjected to energy minimization using the MMFF94 force field to ensure stable three-dimensional geometries prior to docking.

High-Throughput Virtual Screening of the C-SH2 Domain

Potential allosteric binding sites on the C-terminal SH2 domain (residues 168-259) were identified using the fpocket algorithm version 3.1. Among several candidate pockets, "pocket17" was selected for further analysis based on its moderate volume of 161.5 $Å^3$, which is suitable for small-molecule binding, and its lining by key residues including Arg175, His215, Tyr216, and Arg217 that could participate in polar interactions. This pocket also showed high evolutionary conservation in ConSurf analysis, suggesting functional importance.

Molecular docking was performed using smina, a fork of AutoDock Vina optimized for scoring function accuracy. The docking grid was centered at coordinates (x=55.0, y=56.2, z=100.6) with dimensions of 13.5×10.7×12.3 Å to encompass the entire binding site. An exhaustiveness value of 8 was chosen to balance computational efficiency with thoroughness of conformational sampling. The Vinardo scoring function was employed for pose prediction and scoring. From the initial library of 1,368,049 compounds, 1,147,222 (83.8%) were successfully docked into the target site.

Selectivity Docking Against the N-SH2 Domain

To evaluate binding selectivity, we conducted comparative docking studies against the N-terminal SH2 domain (residues 15-107). The binding site termed "pocket18" was characterized as having a larger volume of 234.5 Å^3 compared to pocket17, with distinct lining residues including Arg22, Arg42, Asn46, His63, Tyr64, and Lys232 that could accommodate different ligand interactions.

A subset of top-performing compounds from the initial C-SH2 screen was re-docked into pocket18 using higher precision settings. The docking grid for this site measured 15.4×13.2×11.4 Å and was centered at (x=48.1, y=81.9, z=96.4). To ensure more rigorous conformational sampling, the exhaustiveness parameter was increased to 64, and calculations were distributed across 12 CPU cores per ligand to maintain reasonable computation times.

Post-Screening Analysis and Hit Selection

Following docking, results were analyzed using a hierarchical filtering approach. The primary filter retained compounds with binding affinities of -7.2 kcal/mol or better, yielding 150 potential hits. These were then subjected to visual inspection in PyMOL to confirm formation of specific interactions with key residues such as Arg175 and His215, absence of steric clashes, and favorable hydrophobic packing within the binding site.

For selectivity assessment, binding affinities from both SH2 domains were directly compared. Compounds were classified into three categories: those showing at least 1.0 kcal/mol preference for the C-SH2 domain (C-SH2-selective), those with at least 1.0 kcal/mol preference for the N-SH2 domain (N-SH2-selective), and those with less than 1.0 kcal/mol difference between domains (dual binders).

2.2.1.2 MD Methods

System Preparation

For each of the nine selected protein-ligand complexes, we prepared the system for molecular dynamics simulations. The initial coordinates for the Spleen Tyrosine Kinase (SYK) receptor were taken from PDB ID **1A81** (chain A), while the ligand coordinates were obtained from the virtual screening docking poses.

First, the receptor and ligand PDB files were merged into a single complex structure using **PyMOL**. The subsequent preparation steps were performed using a custom script leveraging **UCSF Chimera** (--nogui mode). The script separated the protein and ligand

(designated as 'UNL') into distinct molecules. The protein structure was cleaned, and hydrogens were added. The ligand was also prepared by adding hydrogens and assigning partial atomic charges using the **AM1-BCC** method as implemented in the antechamber tool. This process yielded a cleaned protein file (protein_clean.pdb) and a hydrogenated ligand file (ligand_wH.pdb).

Force Field Parameterization

We used the **OPLS-AA** (all-atom) force field for all simulations. The protein topology was generated using the **GROMACS** pdb2gmx utility, with **SPCE** as the chosen water model. The ligand required separate parameterization. We submitted the hydrogenated ligand structure to the **LigParGen** web server to generate OPLS-AA compatible topology (.itp) and coordinate (.gro) files for the ligand, referred to as UNL.

Molecular Dynamics Simulation Protocol

All MD simulations were performed using **GROMACS 2021.2**.

1. Complex Assembly: The GROMACS-formatted coordinates for the protein and the LigParGen-generated ligand were combined into a single coordinate file (complex.gro). The main topology file (topol.top) was updated to include the ligand's topology (#include "UNL.itp"), creating the final system topology topol_PLIG.top.

2. Solvation and Ionization: The protein-ligand complex was placed in a dodecahedron simulation box using gmx editconf, ensuring a minimum distance of 1.2 nm between the complex and the box edges. The system was then solvated with SPCE water molecules using gmx solvate. To neutralize the system and achieve a physiological salt concentration of 0.15 M, water molecules were replaced with sodium (Na+) and chloride (Cl–) ions using gmx genion.

3. Energy Minimization: To remove steric clashes, the solvated and ionized system underwent energy minimization. We used the steepest descent algorithm for a maximum of 50,000 steps or until the maximum force on any atom was less than 1000 kJ $mol^{-1}nm^{-1}$.

4. Equilibration: The system was subjected to a two-phase equilibration process.

a. **NVT Equilibration:** A 100 ps simulation was performed under constant volume and temperature (NVT) conditions to stabilize the system's temperature at 300 K. We used the V-rescale thermostat. During this phase, position restraints with a force constant of 1000 kJ $mol^{-1}nm^{-2}$ were applied to the heavy atoms of both the protein and the ligand to allow the solvent to equilibrate around them.

b.**NPT Equilibration:** Following NVT, a 200 ps simulation was performed under constant pressure (1 bar) and temperature (300 K) (NPT) conditions to stabilize the system's density. The V-rescale thermostat and Parrinello-Rahman barostat were used. Position restraints on the protein and ligand were maintained.

5. Production MD: After equilibration, all position restraints were removed, and a 100 ns production MD simulation was run for each of the nine complexes. The LINCS algorithm was used to constrain bonds involving hydrogen atoms, allowing for a 2 fs time step. Long-range electrostatic interactions were calculated using the Particle Mesh Ewald (PME) method, and a cutoff of 1.2 nm was used for short-range van der Waals and Coulomb interactions. All simulations were run on a high-performance workstation with GPUs.

Trajectory Analysis

The 100 ns production trajectories were analyzed to ensure system stability and to prepare for binding free energy calculations. The GROMACS utility gmx trjconv was used for post-processing. Periodic boundary conditions (PBCs) were corrected by centering the protein-ligand complex in the simulation box and removing any rotational and translational motion of the complex as a whole. The root-mean-square deviation (RMSD) of the protein backbone and ligand heavy atoms were calculated to assess conformational stability throughout the simulation (analysis not shown in the provided script but is a standard follow-up).

2.2.1.3 Binding Free Energy Calculation (MM/PBSA)

To estimate the binding affinity of each compound, we calculated the binding free energy (ΔG_{bind}) from the simulation trajectories using the Molecular Mechanics/Poisson-Boltzmann Surface Area (**MM/PBSA**) method, as implemented in the g_mmpbsa tool.

The binding free energy is calculated as:

$$\Delta G_{bind} = \Delta E_{MM} + \Delta G_{solvation} - T\Delta S$$

Where:

- ΔE_{MM} is the change in molecular mechanics energy in the gas phase (van der Waals and electrostatic interactions).
- $\Delta G_{solvation}$ is the change in solvation free energy, composed of polar (ΔG_{PB}) and nonpolar (ΔG_{SA}) contributions.

- TΔS represents the change in conformational entropy upon binding, which was not calculated in this protocol due to its high computational cost.

For each complex, the analysis was performed on the final, stable portion of the trajectory (e.g., the last 5 ns, from 95-100 ns) to ensure the system was fully equilibrated. The g_mmpbsa script calculated the energy components by extracting snapshots from the trajectory. The final binding energy and its standard error were computed using the MmPbSaStat.py script. Additionally, a per-residue energy decomposition analysis was performed to identify the key protein residues contributing to the binding of each ligand.

2.2.1.4 Drug-likeness Properties and ADME Prediction

The Swiss-ADME online platform (accessible at http://www.swissadme.ch/) was employed to forecast the pharmacokinetic attributes encompassing absorption, distribution, metabolism, and excretion of the designated compounds [47]. To facilitate this process, every molecule underwent conversion into a simplified molecular input line entry system (SMILES) format and was subsequently input on the Swiss-ADME server. Following a brief processing time, the outcomes were generated, and the gathered data was utilized for constructing result tables.

2.2.5 Carcinogenicity Prediction

Carcinogenicity Prediction using Ensembled Learning Methods (CarcinoPred-EL) is a computational method to predict the potential of inducing carcinogenicity of the compound in humans and animals. This method is based on three novel ensemble classification models, Ensemble Support Vector Machine (SVM), Ensemble Random Forest (RF), and Ensemble Extreme Gradient Boosting (XGBoost) and was developed to predict carcinogenicity of compounds using seven types of molecular fingerprints and three machine learning methods based on a dataset which is included 1003 various compounds with rat carcinogenicity [48].

2.2.2 Expression and Purification of Recombinant SH2 Domains

2.2.2.1 Design of Primers and Vector

The #6144 pCS2-N-6x-myc-hSyk (1-635) insert, which will be required for the production of SH2 domains (single N-SH2, single C-SH2 and tandem N-SH2+C-SH2) by recombinant DNA technology, was obtained by Prof. Dr. Oliver HANTSCHEL from Philipps University of Marburg. Primers were designed using the Benchling web tool (https://www.benchling.com/) according to the pET28a(+) expression vector and restriction sites. EcoRI and HindIII restriction enzyme sites were added to our primer pairs to cut and amplify SH2 domains (Figure 2.3 and Figure 2.4) (single N-SH2, C-SH2 and tandem N-SH2+C-SH2).

Table 2.1 Primers designed for individual amplification of SH2 domains

Primers:	
N-SH2 forward	5’ gcGAATTCATGGCTGACAGCGCCAACCACC 3’
N-SH2 reverse	5’gcAAGCTTCCGGTTGAAGGGCTTCTTGAGGAGGC3’
C-SH2 forward	5’gcgcgcgGAATTCatgCATGAAAAAATGCCTTGGTTCC3’
C-SH2 reverse	5’gcgcgcAAGCTTCGGCCTCCAAAATTAACATTTCCCTG3’

Note: For tandem SH2 domain, N-SH2 forward and C-SH2 reverse primer pairs were used.

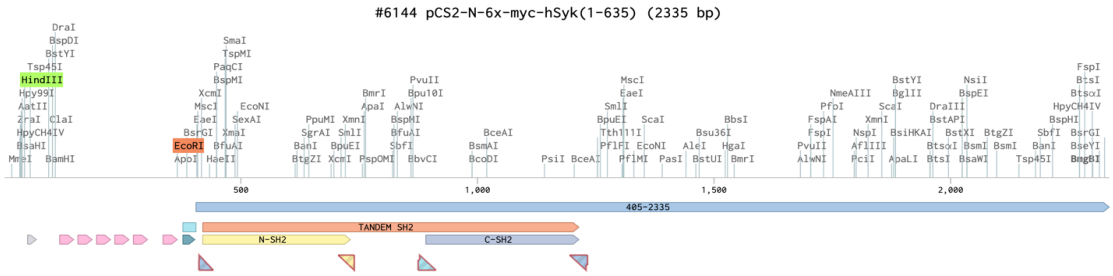


Figure 2.3 #6144 Linear structure of pCS2-N-6x-myc-hSyk(1-635) and designed primer pairs (https://www.benchling.com/).

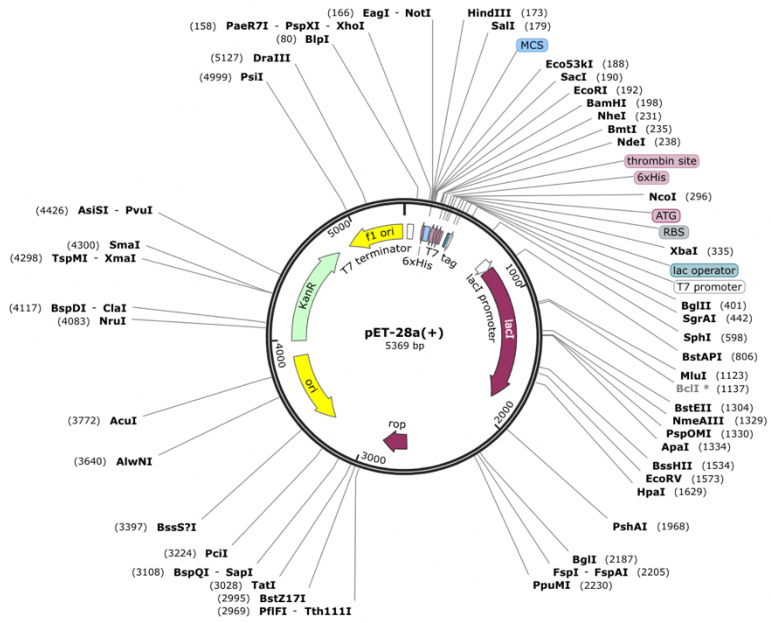


Figure 2.4 Bacterial vector for expression of proteins 6xHis-tagged at the N-terminus with a thrombin site.

2.2.2.2 Production of Competent Cells for Transformation

Escherichia coli DH5-α and *Escherichia coli* BL21(DE3) strains were obtained from Abdullah Gül University FİDAN laboratory. *E. coli* DH5α and BL21(DE3) strains were streaked onto a LB (Luria-Bertani) agar plate and *E. coli* strains were cultured at 37 °C, 220 rpm overnight by picking a single colony in 3 ml of LB. In the morning, 2 ml of overnight culture was added to 100 ml of LB in a 200 ml volumetric flask and the culture was cultured at 37 °C until the OD600 reached 0.35-0.4. The culture was transferred to a sterile centrifuge tube and centrifuged at 6000 rpm at 4 °C for 8 min to collect the cells and discard the supernatant. Cells were resuspended in 20 ml of iced 100 mM $CaCl_2$ and the suspended cells were incubated on ice for 20 min and centrifuged at 6,000 rpm for 8 min at 4 °C. For long-term storage of cells as frozen stock, cells were resuspended in 2 ml of cold 100 mM $CaCl_2$ containing 10% glycerol (2 ml of 100 mM $CaCl_2$ + 1 ml of 50% glycerol + 1 ml of sterile water). Then, 150 µL of competent cells were distributed into Eppendorfs and stored frozen at −80 °C for later use.

2.2.2.3 Transformation of Pet28a(+) Expression Vector and Plasmid Isolation

Pet28a(+) expression vector was obtained from Abdullah Gül University FİDAN Lab. First, DH5α competent cells were thawed on ice and incubated with 1 µL of Pet28a(+) and 150 µL of DH5α competent cells on ice in a biosafety cabinet for 25 min. Then, the cells were heat shocked at 42°C for 30 s and incubated on ice for 1 min, and then 250 µl of LB was added to the cells. Cells were incubated in a 37°C shaking incubator for 25 min. The transformation mixture was spread on an LB kanamycin (+) plate and allowed to dry in a biosafety cabinet for approximately 15 min. They were incubated at 37°C overnight and the plates were checked the next morning, parafilmed and stored at 4°C for further use. When a plasmid was needed, a colony was picked and grown overnight in 5 ml LB kanamycin (+) at 250 rpm and 37°C. Plasmid isolation was performed with the "Bioanalysis NucleoSpin DNA/RNA isolation kit (cat no: 740588.50)". 10 mL of saturated *E. coli* LB cultures were used according to the manufacturer's instructions and microcentrifuged at 11,000 × g for 30 s. The supernatant was discarded and as much liquid as possible was removed. The cell pellet was completely resuspended with 500 µL of Buffer A1 by pipetting up and down until no cell clumps remained before adding Buffer A2. 500 µL of Buffer A2 was added and the tube was gently mixed by inverting 6–8 times and incubated at room temperature for up to 5 min. Then, 600 µL of Buffer A3 was added and the tube was mixed thoroughly by inverting 6–8 times. The tube was centrifuged at 11,000 x g for 10 min at room temperature and the supernatant was transferred to a NucleoSpin® Plasmid Column. The supernatant was transferred to a NucleoSpin® Plasmid Column and the bottom liquid was discarded and the NucleoSpin® Plasmid Column was placed back into the collection tube. The tube was centrifuged at 11,000 x g for 2 min and the collection tubes were discarded and the NucleoSpin® Plasmid Column was placed in a 1.5 mL microcentrifuge tube and 50 µL of Buffer AE preheated to 70 °C was added. The tube was incubated at 70 °C for 2 min and centrifuged at 11,000 x g for 1 min and stored at −20 °C for further studies.

2.2.2.4 Polymerase Chain Reaction (PCR) Amplification of SYK Domains and Recovery of PCR Products from Gel Using Gel Purification Kit

25 µl total PCR mixture was prepared by adding 2 µL (50 ng) template DNA, forward and reverse primers at 0.2 µM final concentration, 2.5 µl Taq polymerase buffer, 1.6 µl dNTP at 200 µM final concentration, 0.125 and completed to 25 µl with nuclease-free water (Table 2.2). Thermal cycling started with initial denaturation at 95°C for 30 s. Then,

denaturation at 94°C for 30 s and Primer Annealing at 72°C for 1 min were continued. After annealing, the samples were extended at 68°C for 1 min. Denaturation, annealing and extension steps were repeated 30 times. Samples were incubated at 68°C for 5 min for final extension. PCR products were run on a 1% agarose gel at 140 V for 40 min. Results were visualized using Gel Imaging Systems - Bio-Rad. For Gel Extraction, PCR products were also removed with the help of a razor blade. PCR product was extracted the with MN NucleoSpin Gel and PCR Cleanup Kit. The manufacturing manual was followed for gel extraction (cat no: 740609.50).

Table 2.2 PCR Mixture for production of SH2 domains

Nuclease free H_2O	17.37 µl
10x Taq polymerase Buffer	2.5 µl
dNTPs	0.5 µl
template DNA	2 µl
Taq DNA polymerase	0.2 µl
Forward Primer	0.5 µl
Reverse Primer	0.5 µl
Total	***25 µl***

2.2.2.5 Digestion of the Vector and Insert DNA with Restriction Enzymes and PCR Clean-up Procedure

Expression vector pET28a(+) and inserts (SH2 domains -N-SH2, C-SH2, TANDEM SH2- obtained by gel purification) were digested with EcoRI and HindIII, respectively, according to the manufacturer's instructions. 500 ng of template DNA was added to the total digestion mixture depending on the concentrations (Table 2.3). Initially, the digestion mixture was incubated with EcoRI for 2 h at 37 °C and after 2 h, the second enzyme was added to the reaction at 37 °C for 2 h. The reaction was inactivated by heat inactivation by incubating the mixture at 80 °C for 20 min. In addition to double digestion, we also wanted to check the digestion capacity of our enzymes separately. For this purpose, we digested pET28a(+) only with EcoRI and only with HindIII separately.

Table 2.3 Restriction Enzyme Digestion Mixture

	pET28a(+)	**N-SH2**	**C-SH2**	**Tandem SH2**
500 ng DNA	7.14 µl	2.6 µl	2.11 µl	2.18 µl
10X NEBuffer	2.5 µl	2.5 µl	2.5 µl	2.5 µl
EcoRI	0.5 µl	0.5 µl	0.5 µl	0.5 µl

HindIII*	0.5 µl	0.5 µl	0.5 µl	0.5 µl
Nuclease free H_2O	14.36 µl	18.9 µl	19.39 µl	19.32 µl
Total	25 µl	25 µl	25 µl	25 µl

* HindIII was added to the reaction after 2 hours at 37 °C.

In order to avoid problems in enzymatic reactions in subsequent processes, PCR clean-up protocol (Bioanalysis NucleoSpin) was applied after restriction enzyme digestion with EcoRI and HindIII. Digested samples were mixed with twice the amount of each NTI buffer (for example, by adding 100 µL of NTI buffer to 50 µL of sample). The resulting mixtures were transferred to PCR cleanup columns and centrifuged at 11,000 g for 1 minute. In addition, the supernatant was removed and 700 µL of NT3 buffer was added to the columns. Then, the columns were centrifuged at 11,000 g for 1 minute. Then, the supernatant was discarded and the columns were centrifuged empty at 11,000 g for 1 minute. Then, the columns were incubated at 70°C for 5 minutes to completely remove the NT3 buffer. Then, the columns were transferred to new labeled Eppendorf tubes and 30 µL of NE buffer was added. Finally, the tubes and columns were incubated at room temperature for 1 minute and centrifuged at 11,000 g for 1 minute. The samples in the Eppendorf tubes to be used in future studies were stored at -20 °C. During our experiments, we encountered empty plasmid problems after RE digestion. We later eliminated this problem by adding this process to our experimental plan.

2.2.2.6 Ligation of PCR Products with Pet28a(+) Expression Vector and Transformation of Ligation Tube into DH5α Competent Cells

The following reaction was set up in a PCR tube on ice for ligation of PCR products and expression vector. NEBioCalculator was used to calculate the molar ratios in Table 2.4 below. Each domain was ligated with a vector:insert ratio of 5:1, 7:1, 10:1. Details are listed in Tables 2.5-7. The ligation mixtures were incubated at 16 °C overnight and heat inactivated at 65 °C for 10 min.

Table 2.4 Molar Ratios (vector: insert)

50 ng vector DNA	**5:1**	**7:1**	**10:1**
N-SH2	15.37 ng	21.52 ng	30.64 ng
C-SH2	16.82 ng	23.55 ng	33.64 ng
Tandem SH2	38.32 ng	53.64 ng	76.64 ng

Tablo 2.5 Ligation Mixture for N-SH2

N-SH2	5:1	7:1	10:1
vector DNA (50 ng)	1.5 µl	1.5 µl	1.5 µl
Insert DNA	0.29 µl	0.44 µl	0.57 µl
T4 DNA Ligase Buffer (10X)	1 µl	1 µl	1 µl
T4 DNA Ligase	0.5 µl	0.5 µl	0.5 µl
Nuclease free H_2O	6.71 µl	6.6 µl	6.43 µl
Total	10 µl	10 µl	10 µl

Tablo 2.6 Ligation Mixture for C-SH2

C-SH2	5:1	7:1	10:1
vector DNA (50 ng)	1.5 µl	1.5 µl	1.5 µl
Insert DNA	0.34 µl	0.48 µl	0.68 µl
T4 DNA Ligase Buffer (10X)	1 µl	1 µl	1 µl
T4 DNA Ligase	0.5 µl	0.5 µl	0.5 µl
Nuclease free H_2O	6.7 µl	6.5 µl	6.3 µl
Total	10 µl	10 µl	10 µl

Tablo 2.7 Ligation Mixture for Tandem SH2

TANDEM SH2	5:1	7:1	10:1
vector DNA (50 ng)	1.5 µl	1.5 µl	1.5 µl
Insert DNA	0.76 µl	1.07 µl	1.52 µl
T4 DNA Ligase Buffer (10X)	1 µl	1 µl	1 µl
T4 DNA Ligase	0.5 µl	0.5 µl	0.5 µl
Nuclease free H_2O	6.2 µl	6 µl	5.5 µl
Total	10 µl	10 µl	10 µl

150 µl of DH5α competent cells were thawed on ice and mixed with 10 µL of ligation mix. The mixture was incubated on ice in a biosafety cabinet for 25 min. The mixture was then heat shocked at 42°C for 30 s and then incubated on ice for 1 min. 250 µl of LB was then added to the cells and incubated on a 37°C shaker for 25 min. The transformation mix was spread onto an LB+ kanamycin agar plate and allowed to dry in a biosafety cabinet for approximately 15 min. It was incubated overnight at 37°C and the plates and colony formation were checked the following morning, parafilmed, and stored at 4°C for later use.

2.2.2.7 Checking the Correct Plasmid using Restriction Enzymes and Selecting the Correct Colony and Transforming into the DH5α Competent Cells

One colony was picked and grown overnight at 37°C at 220 rpm in LB-kanamycin. Two colonies were selected for plasmid isolation and restriction enzyme digestion from the 5:1 ratio plate for each SH2 domain (N-SH2, C-SH2 and Tandem). Plasmid isolation was performed as previously mentioned. The concentration of the isolated plasmid was measured by nanodrop. Depending on the concentrations, 500 ng of DNA template was added to the total cutting mixture (Table 2.8). Initially, the digestion mixture was incubated with EcoRI at 37°C for 2 hours and after the second enzyme was added to the reaction at 37°C for 2 hours. The reaction was inactivated by heat incubation the mixture at 80°C for 20 minutes. The positive colonies that were identified and selected after restriction digestion were transformed into DH5a competent cells. Incubated overnight at 37°C and the plates were checked for colony formation the next morning, parafilmed and stored at 4°C for later use.

Tablo 2.8 Restriction Digestion Mixture

	N-SH2 (1)	**N-SH2 (2)**	**C-SH2 (1)**	**C-SH2 (2)**	**Tandem (1)**	**Tandem (2)**
500 ng DNA	11.7µl	12.3 µl	10.2 µl	13.1µl	14.5 µl	12.7
10X NEBuffer	2.5 µl	2.5 µl	2.5 µl	2.5 µl	2.5 µl	2.5 µl
EcoRI	0.5 µl	0.5 µl	0.5 µl	0.5 µl	0.5 µl	0.5 µl
HindIII*	0.5 µl	0.5 µl	0.5 µl	0.5 µl	0.5 µl	0.5 µl
Nuclease free H_2O	10.3 µl	9.2 µl	11.3 µl	8.4 µl	7.5 µl	8.8
Total	25 µl	25 µl	25 µl	25 µl	25 µl	25 µl

2.2.2.8 Confirmation of Cloning by Sequencing

Six plasmids, consisting of two different samples from each SH2 domain, confirmed by restriction digestion, were sent to the “Izmir Institute of Technology Biotechnology and Bioengineering Research and Application Center” for DNA sequencing. The sequencing results were confirmed that the constructs have no unwanted mutations.

2.2.2.9 Transformation of Correct Colonies into Expression host, BL21(D3), and Induction with Isopropyl-β-D-thiogalactopyranoside (IPTG)

Plasmids confirmed by DNA sequencing were transformed into BL21(D3) cells for expression. Transformation of positive plasmids into BL21(D3) was performed as previously mentioned above (**Section 2.2.2.3**). Then, one colony was picked into 10 ml of LB-kanamycin (+) and incubated at 37 °C with shaking at 220 rpm. 2 ml of preculture was inoculated into 100 ml with kanamycin and incubated at 37 °C with shaking at 220 rpm until OD600 nm reached 0.8. When OD600 reached 0.8, the reaction was induced with 0.5 mM IPTG at 18 °C for 16 h at 220 rpm. In the morning, cells were harvested by centrifugation at 6000 g for 15 min at 4 °C. The cell pellet was resuspended with binding buffer (20 mM sodium phosphate, 0.5 M NaCl, 20 mM imidazole, pH 7.4) at a ratio of 5:1. The solution was sonicated 5 times for 30 s and centrifuged at 20,000 g for 20 min at 4 °C.

Second Induction and optimizations

One colony was picked into 10 ml of LB-kanamycin and incubated at 37°C with shaking at 220 rpm. 5 ml of preculture was inoculated into 50 ml with kanamycin and incubated at 37°C with shaking at 220 rpm until OD600 nm reached 0.8. When OD600 reached 0.8, the reaction was induced with 0.1, 0.5 and 0.5 mM IPTG at different temperature ranges (20°C, 28°C and 37°C at 220 rpm for 4-16 hours) (Table 2.9). Cells were collected in the morning and centrifuged at 6000 g for 15 minutes at 4°C. The cell pellet was resuspended with binding buffer (20 mM sodium phosphate, 0.5 M NaCl, 20 mM imidazole, pH 7.4) at a ratio of 5:1. The solution was sonicated 5 times for 30 s and centrifuged at 20,000 g, 4 °C for 20 min.

Table 2.9 Optimization of IPTG Concentration, Incubation Time and Temperature

Sample ID
NSH2 20 ^{0}C IPTG negative (12h)
NSH2 20 ^{0}C IPTG 0.1 mM (12h)
NSH2 20 ^{0}C IPTG 0.4 mM (12h)
NSH2 20 ^{0}C IPTG 0.5 mM (12h)
CSH2 28 ^{0}C IPTG negative (4h)
CSH2 28 ^{0}C IPTG 0.1 mM (4h)
CSH2 28 ^{0}C IPTG 0.4 mM (4h)
CSH2 28 ^{0}C IPTG 0.5 mM (4h)
TANDEM 37 ^{0}C IPTG negative (4h)

TANDEM 37 ^{0}C IPTG 0.1 mM (4h)
TANDEM 2 37 ^{0}C IPTG 0.4 mM (4h)
TANDEM 37 ^{0}C IPTG 0.5 mM (4h)

2.2.2.10 Confirmation of Results by SDS-PAGE (sodium dodecyl sulfate–polyacrylamide gel electrophoresis)-Coomassie Brilliant Blue Assay and Western Blotting

SDS-PAGE-Coomassie Brilliant Blue Assay

Total protein concentration was determined by Bradford Assay. Cell lysates were loaded at 25 µg protein concentration into each well and separated by SDS-Gel electrophoresis (15% acrylamide gels). The gel was incubated with Coomassie Brilliant Blue reagent for 30 min on a shaker at room temperature. The gel was gently washed 3 times with tap water and de-stain solution (30% methanol and 10% glacial acetic acid) was applied to the gel on a shaker at room temperature overnight. The signal was detected by ChemiDocTM (Biorad).

Western Blotting

After confirming protein expression and IPTG induction by SDS-PAGE Coomassie Brilliant Blue assay, we checked the expression level of anti-His tag antibody since our plasmid contained 6-His-taq. Selected samples (Table 2.10) were prepared as mentioned before. Total protein concentration was determined by Bradford Assay. Cell lysates were loaded at 25 µg protein concentration into each well and separated by SDS-Gel electrophoresis (15% acrylamide gels). Trans-Blot Turbo Transfer System (Biorad, München) was used to transfer the gel to PVDF membrane for 5 min. The membrane was blocked using 5% dried milk in 1x TBST buffer (0.15 M NaCl, 0.02 M Tris pH 7.6 and 0.1% Tween20) for 1 h at room temperature. Then the membrane was incubated with primary antibody Purified anti-His tag, Mouse IgG1 (1:1000, cat no: 652502, Biolegend) for 12 hours at 4 ^{o}C followed by conjugation with secondary antibody for 1 hour at room temperature. The signal was detected by PierceTM ECL Western Blotting Substrate with ChemiDocTM (Biorad).

Table 2.10 Samples selected for Western Blotting after SDS-PAGE-Coomassie Brilliant Blue Assay

Sample ID
NSH2 20 ^{0}C IPTG negative (12h)
NSH2 20 ^{0}C IPTG 0.1 mM (12h)
CSH2 28 ^{0}C IPTG negative (4h)
CSH2 28 ^{0}C IPTG 0.5 mM (4h)
TANDEM 18 ^{0}C IPTG negative (16h)
TANDEM 18 ^{0}C IPTG 0.5 mM(16h)
TANDEM 37 ^{0}C IPTG negative (4h)
TANDEM 37 ^{0}C IPTG 0.5 mM(4h)

2.2.2.11 Purification of Recombinant SH2 Domains using HisPur™ Ni-NTA Superflow Agarose

HisPur™ Ni-NTA Superflow Agarose Kit via Batch Method was used (cat no: 25214) to purify SH2 domains.

• One colony was picked and grown in 10 ml LB supplemented with kanamycin and incubated at 37 °C with shaking at 220 rpm.

• 2 ml pre-culture was inoculated into 100 ml with LB medium (supplemented with kanamycin) and incubated at 37 °C with shaking at 220 rpm until OD600 at 600 nm reached 0.8.

• When OD600 reached 0.8, expression was induced with 0.5 mM IPTG 37 °C for 4 h at 220 rpm.

• Then, cells were collected by centrifugation at 2750 g for 15 min at 4 °C.

• The cell pellet was resuspended with binding buffer (10 mM sodium phosphate, 0.3 M NaCl, 20 mM imidazole, pH 7.4) at a ratio of 5:1.

• After resuspension, the solution was sonicated 5 times for 30 seconds and 100 µl of the sample was stored for SDS-PAGE (1: After Sonication).

• After 1 h of incubation on ice, the lysate was centrifuged at 5300 rpm for 20 minutes at 4 °C.

• For the purification step, 50 µl of Ni-NTA Superflow Agarose was used for 5 ml of protein extract. First, 50 µl of Ni-NTA Superflow Agarose was centrifuged at 700 x g for 2 minutes and the supernatant was carefully removed and discarded.

• Then 2.5 ml of Equilibration Buffer (10 mM sodium phosphate, 0.3 M NaCl, 20 mM imidazole, pH 7.4) was added and mixed until the resin was completely resuspended after centrifugation at 700 x g for 2 min.

• Then the supernatant was carefully removed and discarded. Then the resin was mixed with the protein extract and gently mixed on an end-to-end rotary mixer overnight.

• After the incubation period, the mixture was centrifuged at 700 x g for 2 min and the supernatant was carefully removed. The supernatant was saved for the next steps because we wanted to control the unbound protein fraction (supernatant after overnight incubation with Ni-NTA agarose).

• To continue purification, the resin was washed with 200 µl Wash Buffer (20 mM sodium phosphate, 0.3 M NaCl, 20 mM imidazole, pH 7.4) and centrifuged at 700 x g for 2 min and the supernatant was carefully discarded.

• The supernatant was saved for downstream analysis, referred to as Wash 1, 2 and 3 samples. This process was repeated three times.

• In the final step, His-tagged proteins were eluted by resuspending the beads with 200 µl Elution Buffer (20 mM sodium phosphate, 0.3 M NaCl, 300 mM imidazole, pH 7.4).

• After mixing, the solution was stirred to keep the resin suspended It was stirred slowly for 10 minutes. Then the solution was centrifuged at 700xg for 2 minutes and the supernatant was carefully removed. The supernatant was stored for analysis called Elution (1,2 and 3). This process was repeated 3 times. The results were confirmed by SDS-PAGE-Coomassie Brilliant Blue Test.

2.2.2.12 Purification of Recombinant SH2 domains using Ni-NTA Affinity Purification Method with Fast Protein Liquid Chromatography (FPLC) and BCA Protein Quantification Assay

One colony was picked into 100 ml of LB-kanamycin and incubated at 37°C with shaking at 220 rpm. 20 ml of preculture was inoculated into 1000 ml with kanamycin and incubated at 37°C with shaking at 220 rpm until OD600 nm reached 0.8. When OD600 reached 0.8, the reaction was induced with 0.5 mM IPTG at 28°C for 4 h at 220 rpm. In the morning, cells were collected and centrifuged at 6000 g for 15 min at 4°C. The cell pellet was resuspended with binding buffer (20 mM sodium phosphate, 0.5 M NaCl, 20 mM imidazole, pH 7.4) at a ratio of 5:1. The solution was sonicated 5 times for 30 seconds and centrifuged at 20,000 g, 4 °C for 20 minutes and passed through the filter into the device and eluted using ÄKTA pure™ protein purification system. The results were

confirmed by SDS-PAGE-Coomassie Brilliant Blue Assay. The concentration of purified proteins was measured DC (detergent compatible) Protein Quantification Assay (cat no: 5000111).

2.2.3 Differential Scanning Fluorimetry Assay

Differential Scanning Fluorimetry (DSF) is a demonstration of the thermal denaturation of proteins in the presence of a fluorescent dye (SYPRO Orange) using a typical real-time PCR instrument. Fluorescence intensity is plotted as a function of temperature, and this function generates a sigmoidal curve defined by a two-state transition. The inflection point (Tm) of the transition curve is calculated using the Boltzmann equation. Each sample was repeated three times for the experiment. Here, in order to check the binding capacity of our drug candidates, we performed a Differential Scanning Fluorimetry assay using SYPRO Orange dye. 5 µM of Z2155444005 and Z2608161550 was treated with recombinantly purified C-SH2 domain of Syk (10 µg) for 1h at room temperature. After, SYPRO Orange dye was added to the tubes at 5X concentration. Fluorescence intensity was measured between 20°C and 95 °C at 0.5 °C for 15 seconds using FRET channel using a PCR instrument (BioRad CFX96). The inflection point (Tm) of the transition curve was calculated using the Boltzmann equation.

2.2.4 Testing the Binding of Compounds to Syk-C-SH2 Domain by Intracellular Fluorescence Resonance Energy Transfer (FRET) Method

2.2.3.1 Transfection of Syk Biosensor into HEK-293 Cells

Transfection was performed using Turbofect transfection agent (cat no: R0531, Thermo Scientific™). In a 24-well plate, 5×10^5 cells were seeded into each well in 1 mL of growth medium 24 h before transfection. 0.5 µg of Syk biosensor was added to 100 µL of serum-free RPMI-1640 growth medium. 2 µL of transfection agent (Turbofect) was added to the diluted DNA and mixed immediately by pipetting and incubated for 15–20 min at room temperature. 100 µL of transfection reagent/DNA mixture was added dropwise to each well. Immediately after adding the transfection reagent, the plate was gently shaken to ensure even distribution of the complexes and incubated at 37 °C in a CO_2 incubator. Transfection was analyzed and confirmed with the help of a fluorescence microscope after 24-48 hours.

2.2.3.2 Testing the Binding of Candidate Compounds to the Syk C-SH2 Domain by Intracellular FRET method

In this part, we tested candidate inhibitors using Cytosolic Syk Biosensor (Plasmid #125729) [88]. According to the above-mentioned transfection method, the transfected cells were treated with G418 (Geneticin) for 48 hours and Syk biosensor positive cells were distinguished. The applied dose (400 µM) was determined by looking at the literature studies [89]. Then, the cells were counted using hematocytometer and trypan blue and re-seeded in 96-well black plates with 30,000 cells per well. Candidate inhibitors were prepared with Hank's Balanced Salt Solution (HBSS) at certain concentrations in 3 replicates (25 µM, 50 µM, 75 µM and 100 µM). After 24 hours, the medium of the cells was collected and washed once with 100 µL of PBS. HBSS was added on it. The plate was placed in the microplate reader and measured by setting an imaging protocol such that both CFP (excitation 433±10 nm, emission 476±10 nm) and FRET (excitation 433±10 nm, emission 527±10 nm) channels were obtained for each well. Then, the prepared drugs were added and measured with the above settings for 1 hour. The results were analyzed using the following formula.

$$\text{Yellow to Cyan Emission Ratio} = \frac{\text{FRET Channel Emission Intensity} - \text{FRET Channel Emission Intensity of Background}}{\text{CFP Channel Emission Intensity} - \text{CFP Channel Emission Intensity of Background}} \quad \textbf{(2.1)}$$

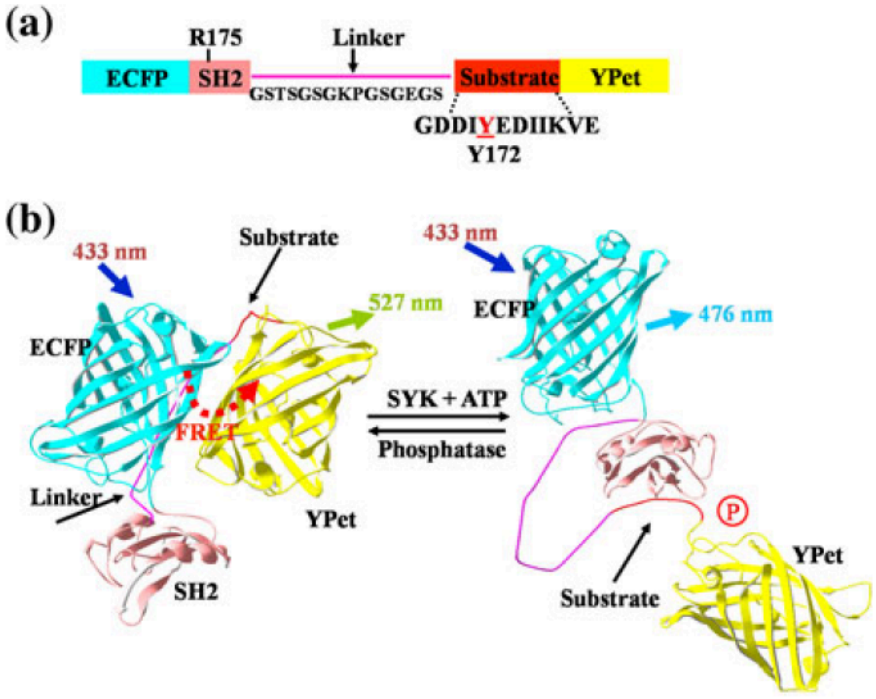


Figure 2.5 Biosensor design (a) SYK kinase biosensor consists of ECFP, SH2 domain, a flexible linker, SYK kinase substrate peptide and YPet. (b) Schematics showing the principle of reporting SYK activity by FRET-based biosensor. Phosphorylation of the substrate peptide induces its binding to the SH2 domain, resulting in a negative confirmation for FRET [88].

2.2.5 Statistical Analysis

The statistical analysis will be performed by GraphPad Prism 8. The comparations of two experiments will set done by 2-Way ANOVA with Dunnett's Multiple Comparation test and Unpaired t test and the level of significance will be determinate $P<0.05$.

2.3 Results and Discussion

2.3.1 Searching for target compounds for SH2 domains of Syk using the ENAMINE database

2.3.1.1 Docking Evaluations

Virtual Screening Identifies Potent Binders for the C-SH2 Domain

The compounds from Enamine High-Throughput Screening (HTS) collection, comprising 1,368,049, were screened for the C-SH2 domain using our *in-silico* studies. The top 26 ligands with the best binding affinity (kcal/mol) are listed in Table 2.11. The atomic interactions and bonds of these 26 ligands with the C-SH2 domain were investigated based on their 2D-3D structures and their interactions with the C-SH2 domain (Table 2.11), and it was observed that the compounds exhibited strong hydrogen bonds with residues such as Arg175, Arg195, and Arg217. The 9 most suitable of these, considering the aforementioned properties (Arg175, Arg195, and Arg217), were selected for the next step, Molecular Dynamics simulations (Table 2.12 and Figure 2.6). The high-throughput virtual screening campaign against the C-SH2 domain successfully identified 150 compounds with binding affinities of -7.2 kcal/mol or better. The top-ranked compound, Z2155444005, demonstrated an exceptional docking score of -8.2 kcal/mol. Analysis of binding modes revealed this compound forms two hydrogen bonds with Arg175 and participates in π-stacking interactions with Tyr216. Among the top hits, 89%

were found to engage His215 through hydrogen bonding, indicating the importance of this residue for ligand recognition. The chemical diversity of the hit compounds spanned eight distinct scaffold classes, including benzimidazoles and quinazolines, suggesting multiple avenues for further optimization.

Cross-Docking Reveals Ligand Selectivity for N-SH2 vs. C-SH2 Domains

The selectivity screening against the N-SH2 domain revealed distinct binding preferences among the top compounds. Several ligands showed marked preference for the N-SH2 domain, including Z1440129633 which bound with -8.9 kcal/mol compared to its -7.5 kcal/mol affinity for the C-SH2 domain. This compound formed salt bridges with Arg42 and Lys232 in the N-SH2 site. Another notable example was Z2734746070, which showed stronger binding to the N-SH2 domain (-8.0 kcal/mol) compared to the C-SH2 domain (-7.3 kcal/mol).

Interestingly, some compounds demonstrated relatively balanced binding to both domains. The initial top hit from the C-SH2 screen, Z2155444005, maintained strong binding to the N-SH2 domain (-8.7 kcal/mol) while retaining its high affinity for the C-SH2 domain (-8.2 kcal/mol). Similarly, Z296110126 showed only slightly weaker binding to the C-SH2 domain (-7.3 kcal/mol) compared to its strong N-SH2 binding (-8.6 kcal/mol).

A smaller subset of compounds exhibited preference for the C-SH2 domain, with Z1823944531 being the most notable example. This compound bound to the C-SH2 domain with -8.0 kcal/mol affinity while showing weaker binding (-7.7 kcal/mol) to the N-SH2 domain. Analysis of the structural features revealed that N-SH2-preferential compounds tended to be larger (molecular weight > 400 Da), taking advantage of the expanded volume of pocket18. In contrast, C-SH2-selective hits were typically more rigid and planar, while dual binders often contained flexible linkers and balanced hydrophobic character.

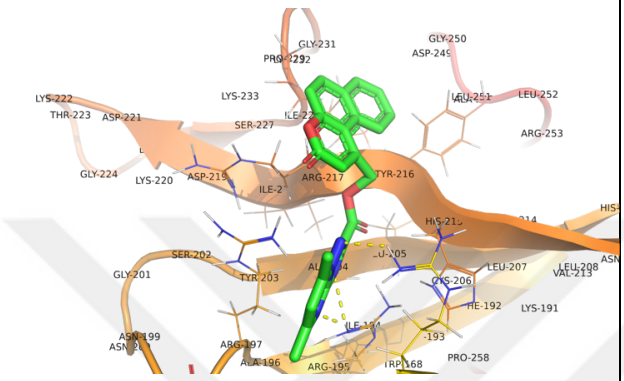
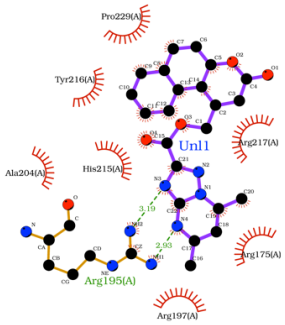
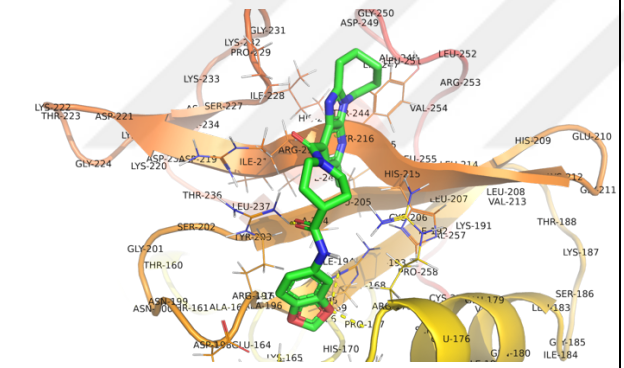
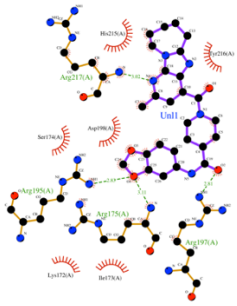
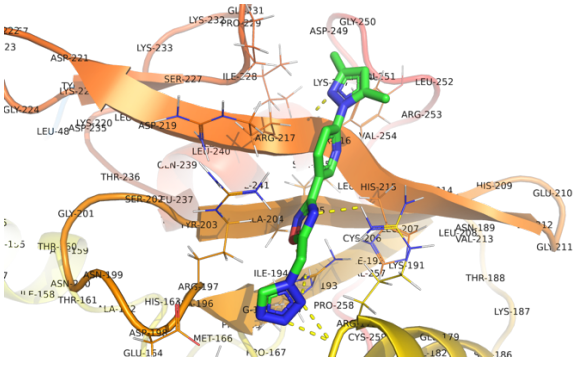
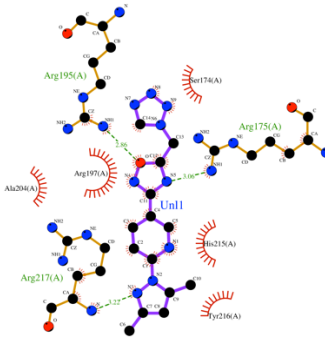
Table 2.11 26 Ligands with Highest Binding Affinity to C-SH2 Domain

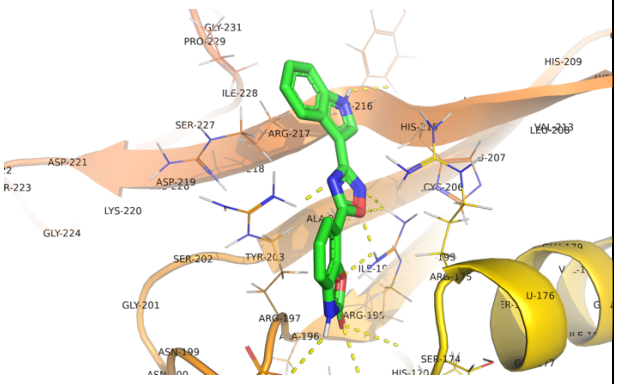
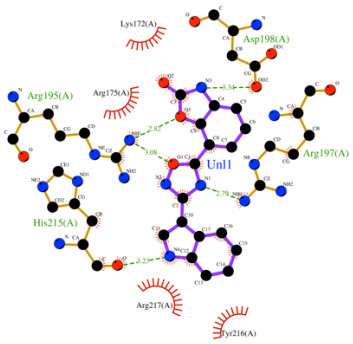
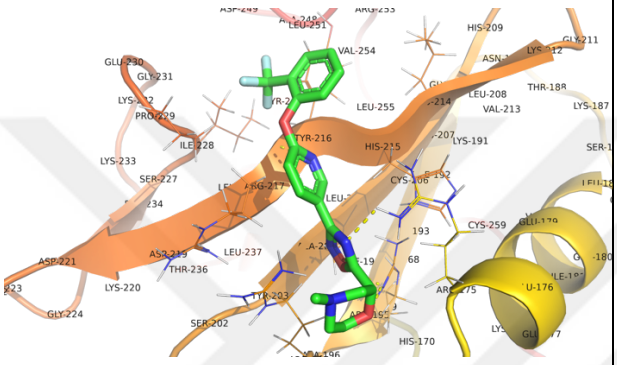
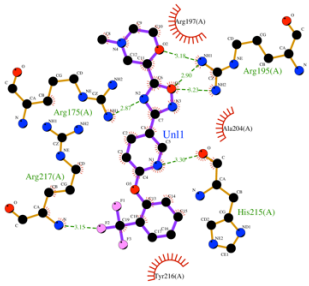
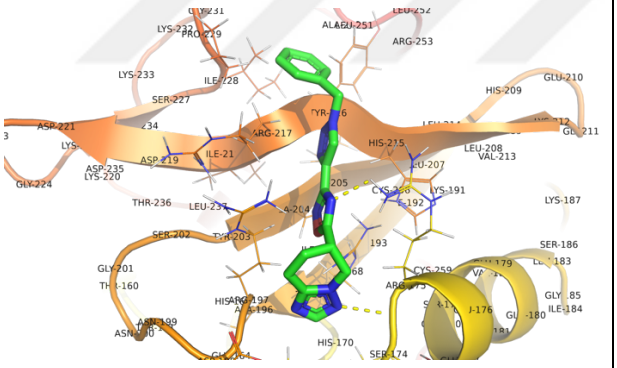
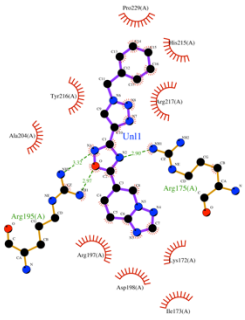
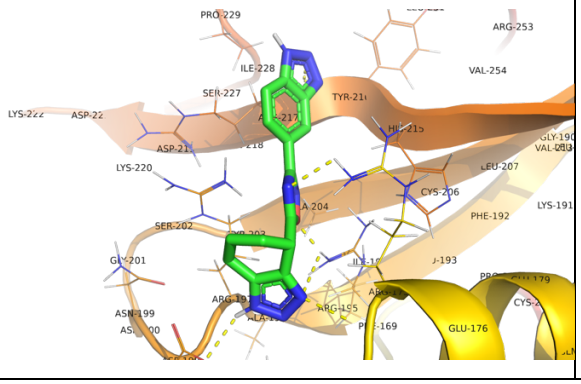
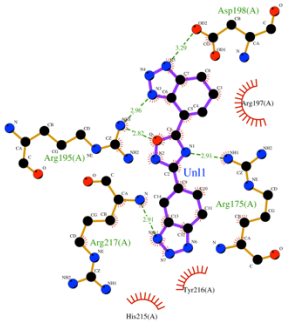
ENAMINE ID	Binding Affinity (kcal/mol)	ligfile
Z2155444005	-8.2	enamine/bin_900000_1000000/z2155444005_rdkit3d.pdb
Z2155444005	-8.2	enamine/bin_900000_1000000/z2155444005_rdkit3d.pdb

Z1823944531	-8.0	enamine/bin_1000000_1100000/z1823944531_rdkit3d.pdb
Z2617132396	-8.0	enamine/bin_1200000_1300000/z2617132396_rdkit3d.pdb
Z2900718100	-7.7	enamine/bin_1200000_1300000/z2900718100_rdkit3d.pdb
Z2179654268	-7.7	enamine/bin_900000_1000000/z2179654268_rdkit3d.pdb
Z1170162000	-7.7	enamine/bin_700000_800000/z1170162000_rdkit3d.pdb
Z1824400326	-7.5	enamine/bin_100000_200000/z1824400326_rdkit3d.pdb
Z1440129633	-7.5	enamine/bin_1000000_1100000/z1440129633_rdkit3d.pdb
Z3016339129	-7.5	enamine/bin_1300000_1400000/z3016339129_rdkit3d.pdb
Z1170175138	-7.5	enamine/bin_700000_800000/z1170175138_rdkit3d.pdb
Z2608161550	-7.4	enamine/bin_1200000_1300000/z2608161550_rdkit3d.pdb
Z1890760807	-7.4	enamine/bin_1100000_1200000/z1890760807_rdkit3d.pdb
Z3377781892	-7.4	enamine/bin_1300000_1400000/z3377781892_rdkit3d.pdb
Z2900718145	-7.4	enamine/bin_1200000_1300000/z2900718145_rdkit3d.pdb
Z2976508786	-7.4	enamine/bin_1300000_1400000/z2976508786_rdkit3d.pdb
Z3290576805	-7.3	enamine/bin_1300000_1400000/z3290576805_rdkit3d.pdb
Z2734746070	-7.3	enamine/bin_1200000_1300000/z2734746070_rdkit3d.pdb
Z3268495886	-7.3	enamine/bin_1300000_1400000/z3268495886_rdkit3d.pdb
Z1170087494	-7.3	enamine/bin_300000_400000/z1170087494_rdkit3d.pdb
Z2755766932	-7.3	enamine/bin_1200000_1300000/z2755766932_rdkit3d.pdb
Z2755766934	-7.3	enamine/bin_1200000_1300000/z2755766934_rdkit3d.pdb
Z1080834340	-7.3	enamine/bin_100000_200000/z1080834340_rdkit3d.pdb
Z2900718031	-7.3	enamine/bin_1200000_1300000/z2900718031_rdkit3d.pdb
Z1778577157	-7.3	enamine/bin_1000000_1100000/z1778577157_rdkit3d.pdb
Z2998021664	-7.3	enamine/bin_1300000_1400000/z2998021664_rdkit3d.pdb
Z296110126	-7.3	enamine/bin_300000_400000/z296110126_rdkit3d.pdb
Z220405186	-7.3	enamine/bin_700000_800000/z220405186_rdkit3d.pdb

Table 2.12 The 9 ligands selected for MD analysis and their scores (kcal/mol)

Enamine ID	**C-SH2 Binding Affinity** (kcal/mol)
Z2155444005	-8.2
Z3016339129	-7.5
Z1170175138	-7.5
Z2608161550	-7.4
Z1890760807	-7.4
Z3377781892	-7.4
Z2734746070	-7.3
Z296110126	-7.3
Z19573081	-7.4

3D Interactions	2D Interactions
Z19573081	**Z19573081**
	
Z296110126	**Z296110126**
	
Z1170175138	**Z1170175138**
	

Z1890760807	**Z1890760807**
	
Z3377781892	**Z3377781892**
	
Z2155444005	**Z2155444005**
	
Z2608161550	**Z2608161550**
	

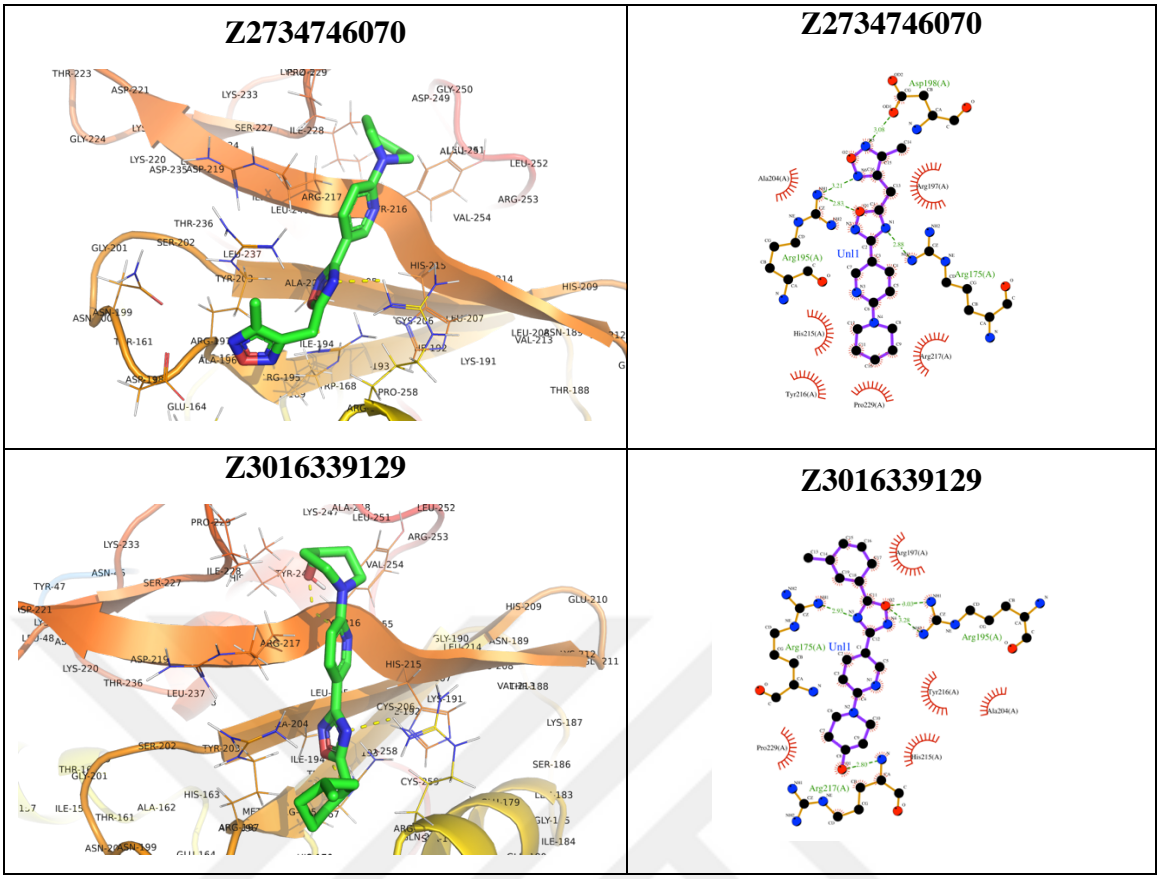


Figure 2.6 2D and 3D structures of the 9 selected candidate compounds and their interaction with the C-SH2 domain (Arg175, Arg195, Arg217) are shown with the distance between the atoms in angstroms (Å).

2.3.1.2 Molecular Dynamics Analysis of Candidates Targeted to the C-SH2 Domain of Syk

The radial distribution function represents the average distribution of atoms around any atom in the system. The structure of water molecules at the protein interface can be described by the radial distribution function (RDF), and the calculated distance of the first minimum in the RDF can be thought of as the thickness of the hydration layer around a given location. pTyr (tyrosyl phosphopeptides) is stabilized by a dense network of hydrogen bonds and ionic interactions contributed by SH2 domain residues, which form the pTyr binding pocket, a deep cavity. Most notably, a universally conserved arginine residue (Arg βB5--N-SH2-R42 and C-SH2 R195--) at the center and base of the cavity forms a bidentate ionic interaction with the two oxygens of the phosphate group. Therefore, the binding pocket was determined based on R42 (N-SH2) and R195 (C-SH2) using PyMOL. In the case of C-SH2, we specifically focused on the interaction of the

selected ligands on residue R195 of the C-SH2 domain. Molecular docking studies also revealed that the selected ligands also had strong interactions with R175 and R217. Therefore, we wanted to examine the radial distribution function due to R175, R195, and R217 for the nine selected ligands (Figure 2.7). When R175 was selected as the reference, the results showed that z2608161550 (z260) was preferred among the nine selected ligands. z2155444005 (z215) was also the second preferred ligand. Next, z2734746070 (z273) preferred to interact with R195 compared to the other eight ligands. Second, z260 strongly interacted with R195. Finally, R217 was selected as the reference. Among the 9 ligands selected, z215 was more preferred and z260 was second preferred (Figure 2.7).

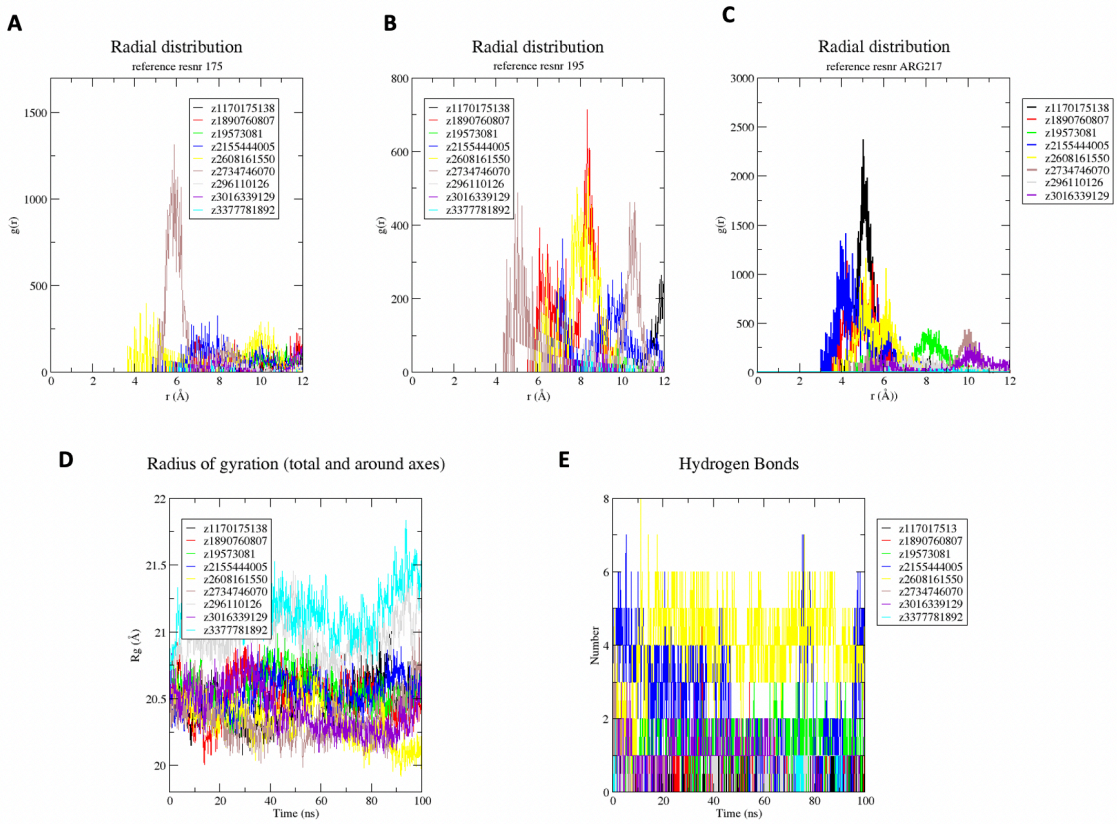


Figure 2.7 Radial distribution function R175 (A), R195 (B) and R217 (C). Rg Plot of all complexes with protein during 100 ns MD Simulation (D). Hydrogen bond number plot of all complexes with protein during 100 ns MD Simulation (E).

Radius of gyration (radius of inertia - radius of gyration - radius of gyration):

The radius of gyration (Rg) is defined as the distribution of a protein's atoms around its axis. Rg represents the distance between the point of rotation and the point where energy transfer has the maximum effect. The radius of gyration measures the compactness of a protein structure. Analysis of the Rg plot showed that the protein remained compact

upon binding of z3016339129 (z301), z1170175138, z260, z1890760807 (z189), z2734746070 (z273), z19573081 (z195), and z215 during the 100 ns simulation period. The results indicate that binding these seven ligands significantly stabilizes the protein structure. In contrast, variable compactness was observed in the Rg plots of compounds z3377781892 (z337) and z296110126 (z337) (Figure 2.7D).

Hydrogen Bonding Interactions:

Hydrogen bonds play a crucial role in stabilizing protein-ligand complexes, so we analyzed the evolution of H-bonds over time to assess the folding dynamics of the C-SH2 domain in the complexes. The plot showed a strong increase in hydrogen bonding with z260 and z215 in the C-SH2 domain (Figure 2.7E).

Root-mean-square deviation (RMSD):

RMSD is used to determine the backbone differences between the initial conformations and the final position. Stability is determined by the deviation produced in the MD simulation. A smaller deviation indicates a more stable complex structure. The results showed that the reference ligand Z189 was more stable compared to the other eight ligands. On the other hand, when using the protein as a reference, the seven ligands, except for Z286 and Z337, had similar RMSD values (2-3 Å) (Figure 2.8A-B).

Root-mean-square fluctuation (RMSF):

RMSF is often used to assess the flexibility of a protein or ligand, specifically how much the molecule's atoms fluctuate over time in the simulated orbit. A lower RMSF value indicates less movement of the protein or ligand atoms, indicating a more rigid region, while a higher RMSF value indicates a more flexible region. The average atomic fluctuation showed similar binding patterns except at z296 and z337. This suggests that the average atomic fluctuation of the C-SH2 residue showed similar binding patterns, and that, except at z296 and z337, the seven ligands stabilize the protein in the conformation they adopt for inhibition (Figure 2.8C).

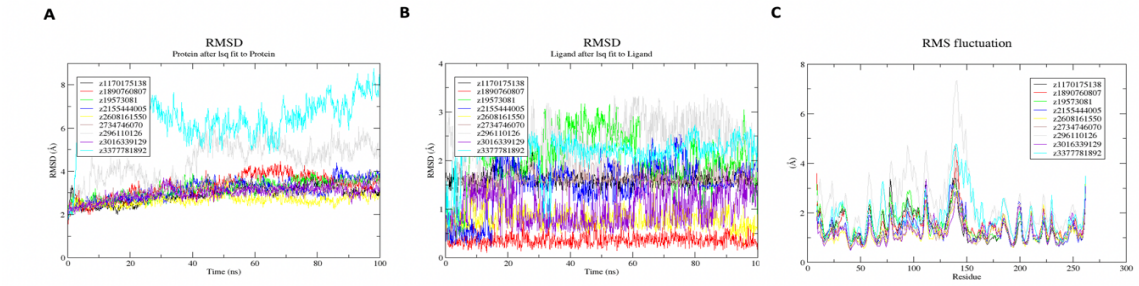


Figure 2.8 (A) Time evolution of RMSD values during 100 ns simulation (protein). (B) Time evolution of RMSD values during 100 ns simulation (ligand). (C) RMSF plot of all complexes with C-SH2 domain during 100 ns MD Simulation.

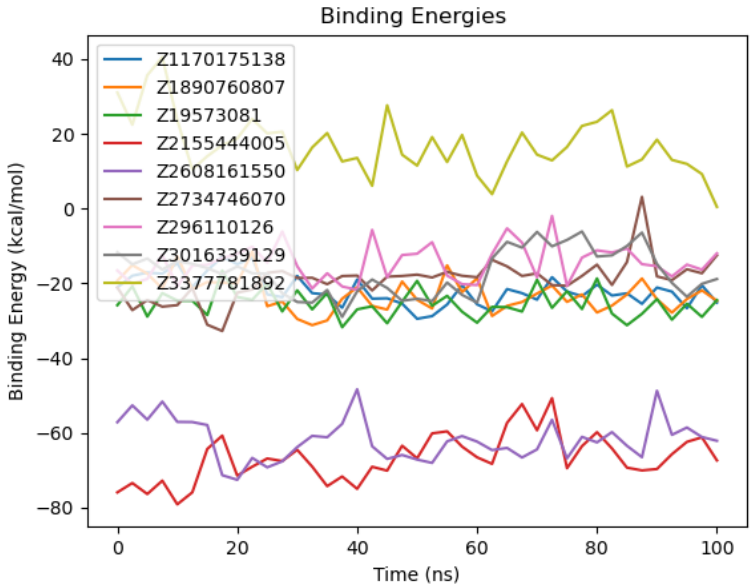


Figure 2.9 The binding energies of the top 9 compounds are shown in the graph.

Furthermore, z215 and z260 have the best binding energies of -279.424 kJ (-66.782 kcal/mol) and -258.564 kJ (-61.79 kcal/mol), respectively (Figure 2.9).

2.3.1.3 Drug-likeness Properties, ADME and Carcinogenicity Prediction

The drug-like properties of the candidate compounds were measured using Lipinski filter. The results showed that both the compounds were found to comply with the Lipinski Rule of Five (Table 2.13). The molecular weight of the two compounds does not exceed 500 g/mol with 348.36 g/mol and 308.30 g/mol, respectively. Based on the Lipinski Rule of Five, hydrogen donors and acceptors have a limit of 5 and 10, respectively. Our results showed that each compound successfully complied with this

rule. Also, the lipophilicities (Log Po/w) of 5 compounds were less than 5. This was also in accordance with the Lipinski Rule of Five. Also, the ADME properties of the candidate compounds are evaluated in Table 4.8. The topological surface area (TPSA) is expected to be ≤140 Å², which is a good indicator of drug permeation through the cell membrane. The TPSA value of each compound was below 140 Å². The administration of orally administered drugs is more comfortable for patients. Therefore, human intestinal absorption (HIA) was important for the bioavailability of drug candidates. Our ADME results also showed that our candidates had high intestinal absorption. Interestingly, our data showed that none of the candidates had the ability to cross the Blood-brain barrier (BBB) (logBB must be greater than 0.3 for proper passage through the BBB). BBB is especially important when the purpose of the drug is to target neurological diseases such as Alzheimer's disease, Parkinson's disease or stroke. P-glycoprotein (P-gp) has a very important role in the absorption and distribution of drugs. Therefore, it is very important to identify permeation glycoprotein substrates during drug discovery studies for the evaluation of drug candidates. Two of our candidates were not P-gp substrates. Therefore, we can claim that they were not excreted out of the cell via the P-gp carrier protein. In addition, the results obtained from CarcinoPred-EL are summarized in Table 4.9. The average values of highly carcinogenic compounds according to the calculations made by the RF method are close to 1. According to the carcinogenicity estimation using the RF method, the average value of each compound is less than 0.5, indicating that each compound is not carcinogenic.

Table 2.13 Drug-likeness Properties, ADME and Carcinogenicity Prediction

Compound Name	CNP0265345	CNP0159934	CNP0118091	CNP0114154	CNP0015002
Molecular Weight (g/mol)	537.49	534.51	446.54	452.45	401.48
Num. H-bond acceptors	8	8	4	8	6
Num. H-bond donors	1	3	1	3	1
Log $P_{o/w}$	4.25	3.78	2.10	1.61	2.05
Number of exceptions of Lipinski's Rule of Five	1	1	0	0	0
TPSA	99.93 Å²	130.36 Å²	70.71 Å²	130.36 Å²	90.83 Å²
BBB	No	No	No	No	No
P-gp substrate	No	Evet	No	Evet	Evet

HIA	High	Low	High	High	High
CarcinoPred - EL Method, Random Forest (RF), (Average)	Non-carcinogen (0.33)	Non-carcinogen (0.48)	Non-carcinogen (0.37)	Non-carcinogen (0.33)	Non-carcinogen (0.42)

2.3.2 Expression and Purification of Recombinant SH2 Domains

2.3.2.1 Production of Competent Cells and Transformation of Pet28a(+) Expression Vectors and #6144 pCS2-N-6x-myc-hSyk (1-635) insert

Competent cells were successfully obtained mentioned procedure and stored at -80 ºC. Pet28a(+) expression vector was grown on Kanamycin (+) agar plate for plasmid isolation. Template DNA containing the human SYK gene (**#6144 pCS2-N-6x-myc-hSyk (1-635)**) was successfully grown on ampicillin agar and one colony was isolated and made ready for PCR amplification (Figure 2.10).

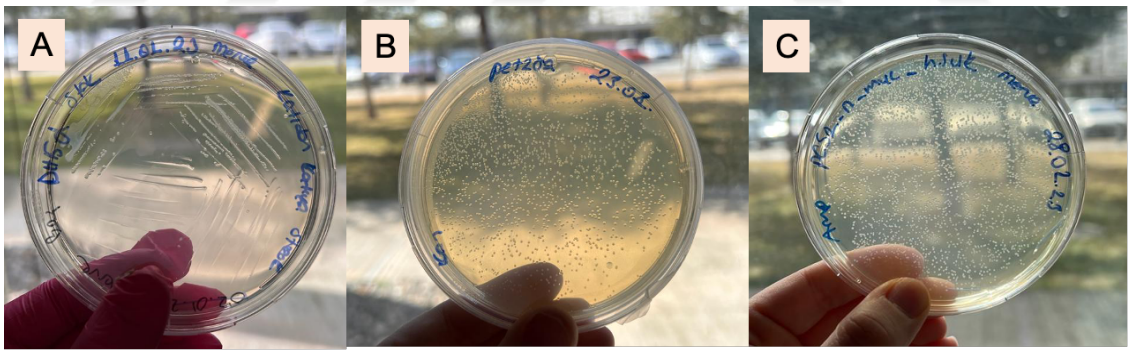


Figure 2.10 (A) DH5α Competent cells (B) Pet28a(+) expression vector (C) #6144 pCS2-N-6x-myc-hSyk (1-635)

2.3.2.2 PCR Amplification of SYK Domains and Recovery of PCR Products from Gel Using Gel Purification Kit

The agarose electrophoresis results showed that N-SH2 (312 bp) domain, C-SH2 (324 bp) and Tandem SH2 (795 bp) were successfully amplified using PCR method. The bands were cut and extracted from the gel with the help of MN NucleoSpin Gel and PCR Cleanup Kit (Figure 2.11 and Table 2.14).

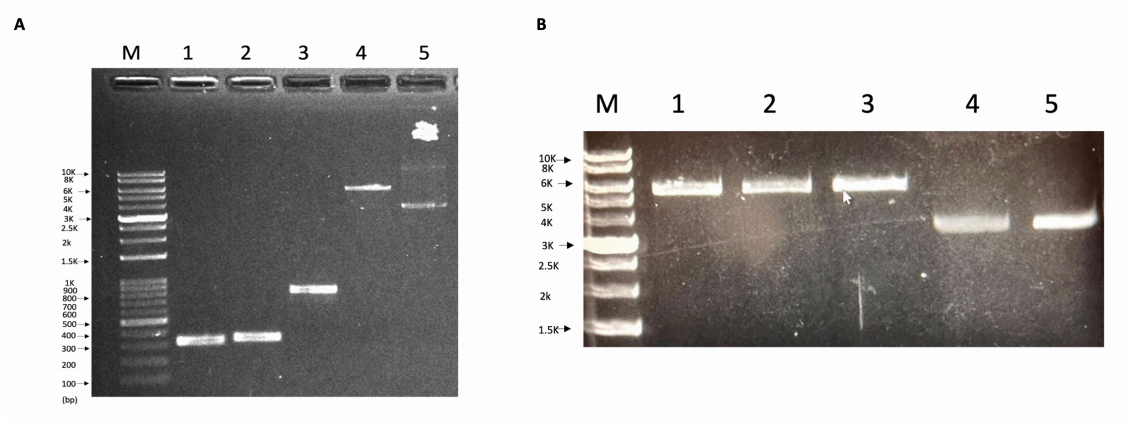


Figure 2.11 1% agarose gel results. **(A)** M:Marker. Band 1: N-SH2 (312 bp) domain PCR product, Band 2: C-SH2 (324 bp) domain PCR product Band 3: Tandem SH2 (795 bp) domain PCR product Band4: EcoRI/HindIII cut Pet28a(+) Band 5: uncut circular Pet28a(+) **(B)** Band 1: Cut Pet28a(+) with EcoRI only, Band 2: Cut Pet28a(+) with HindIII only and Band 3: Cut Pet28a(+) with EcoRI/HindIII together, Band 4-5: uncut circular Pet28a(+).

2.3.2.3 Digestion of the Vector and Insert DNA with Restriction Enzymes and PCR Clean-up Procedure

The length of the pET28a(+) expression vector was approximately 3000 bp before digestion with EcoRI and HindIII, but increased to a linear length of 5369 bp after digestion. This confirmed that the pET28a(+) expression vector was cut (Figure 2.11). In addition to the double cut, we also wanted to check the folding capacity of our enzymes separately. For this purpose, we digested pET28a(+) only with EcoRI and only with HindIII (Figure 2.11). pET28a(+) was successfully cleared and absorbance was measured using Nanodrop (Table 2.15).

Table 2.14 Nanodrop Results of gel extraction (N-SH2, C-SH2 and Tandem SH2) and digested pET28a(+) expression vector with EcoRI and HindIII

Sample Name	Concentration (ng/ µL)
pET28a(+)	69.9
N-SH2	191.5
C-SH2	236.1
Tandem SH2	229.5

Table 2.15 Nanodrop Results after RE digestion and PCR cleanup procedure

Sample Name	Concentration (ng/ µL)
pET28a(+)	52.9
N-SH2	52.9
C-SH2	48.8

Tandem SH2	50.1

2.3.2.4 Ligation of PCR Products with Pet28a(+) Expression Vector, Transformation of the Ligation Tube into DH5α Competent cells and Checking the Correct Plasmid using Restriction Digestion Enzymes

Transformation results are presented in Figure 2.12 and colonies were observed in all of them. In Figure 2.13A, we saw that approximately 800 bp of DNA was present in the Tandem SH2 (795 bp) section in band 1. This was consistent with our 795 bp insert DNA. Band 2 has a length between 300-400 bp and this band represented N-SH2 (312 bp). We also cut the empty vector as a control in band 3. Then, in Figure 2.13B, we digested two C-SH2, Tandem SH2 and N-SH2, respectively. In band 1, we did not see any band in the C-SH2 site digestion. This was considered as an empty vector. In band 2, we detected a band between 300-400 bp. This band was identified as our C-SH2 insert (324 bp). Also, digestion of Tandem SH2 with EcoRI and HindIII gave positive results with a band close to 800 bp at the actual site in Figure 2.13B at band 3. Finally, we saw a band at 300-400 bp in band 4 (Figure 2.13B). This band confirmed the NSH2 domain of 312 bp. Since we could not see a positive control in C-SH2 in Figure 2.13B, we repeated this experiment for the C-SH2 domain in order to obtain another positive colony (Figure 2.13C). C-SH2 was successfully digested with EcoRI and HindIII and a band of 300-400 bp similar to the length of CSH2 in band 2 was detected. We also did not see any band in the empty vector in band 1 (Figure 2.13C).

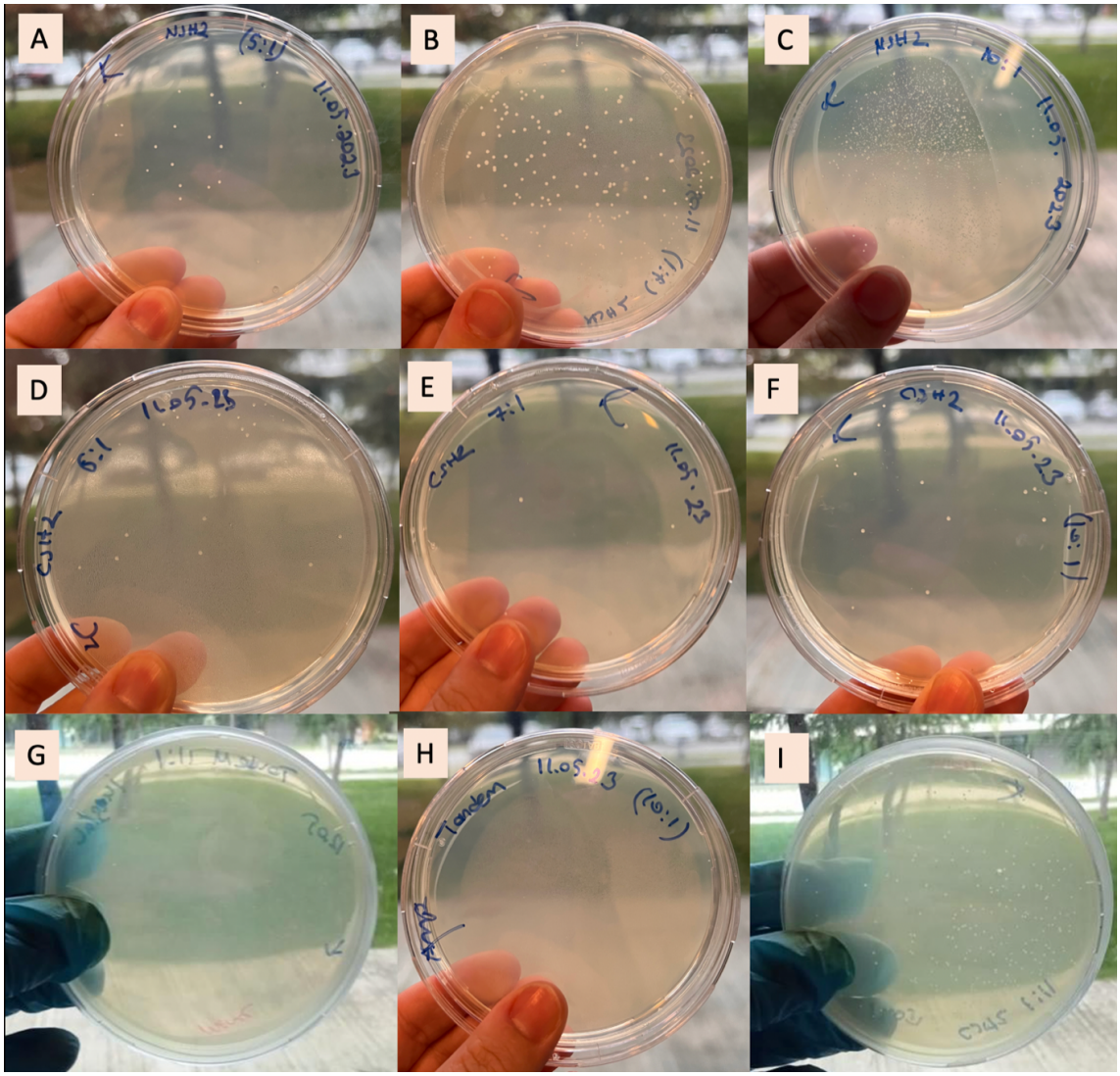


Figure 2.12 Transformation of ligation results (A) N-SH2 5:1 ratio (B) N-SH2 7:1 ratio (C) N-SH2 10:1 ratio (D) C-SH2 5:1 ratio (E) C-SH2 7:1 ratio (F) C-SH2 10:1 ratio (G) TANDEM SH2 5:1 ratio (H) TANDEM SH2 7:1 ratio (I) TANDEM SH2 10:1 ratio

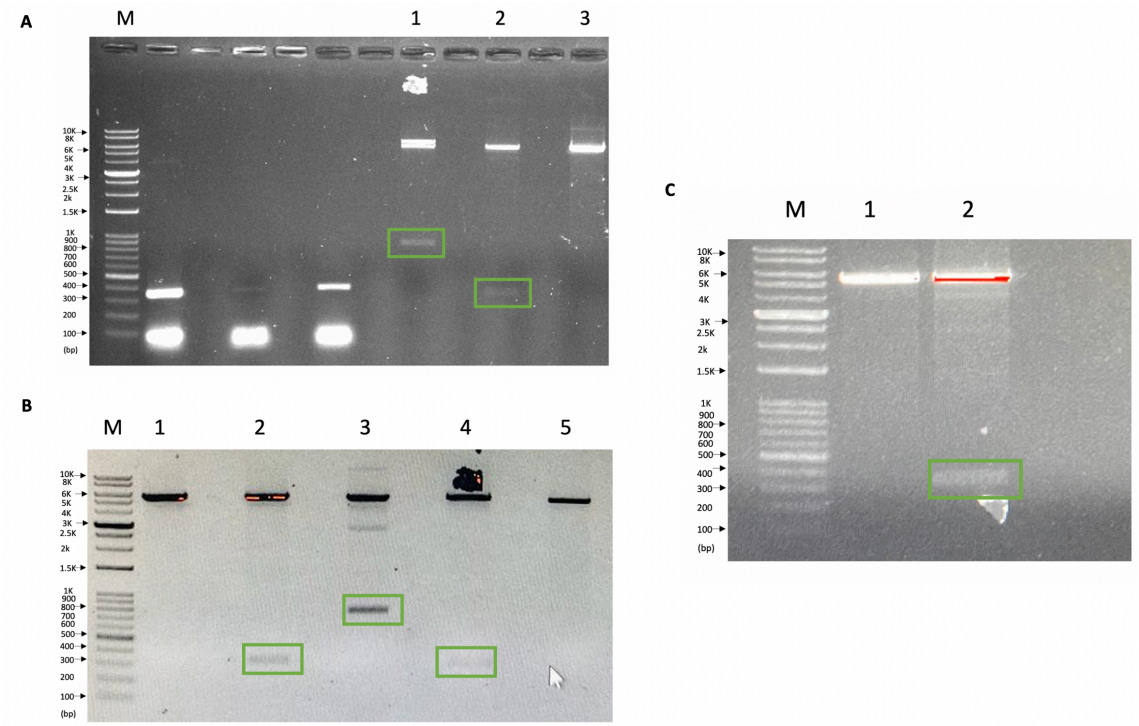


Figure 2.13 1% agarose gel results **(A)** restriction enzyme digestion with EcoRI and HindIII enzymes: Band 1: Tandem SH2 (795 bp) site, Band 2: N-SH2 (312 bp) site, Band 3: empty vector (Pet28a(+)). **(B)** Restriction enzyme digestion with EcoRI and HindIII enzymes: Band 1-2: C-SH2 (324 bp) site, Band 3: Tandem SH2 (795 bp) site, Band 4: N-SH2 (312 bp) site, Band 5: empty vector (Pet28a(+)). **(C)** Restriction enzyme digestion with EcoRI and HindIII enzymes: Band 1: empty vector (Pet28a(+)) and Band 2: C-SH2 (324 bp) site.

2.3.2.5 Selection of the Correct Colony, Transformation into DH5α Competent Cells and Plasmid Isolation

The positive colonies identified and selected, which were proven by restriction digestion, were transformed into DH5a competent cells. They were incubated overnight at 37°C and the plates and colony formation were checked the next morning, parafilmed and stored at 4°C for later use (Figure 2.14). One colony was selected from each plate mentioned in Figure 2.12 and isolation was carried out as mentioned earlier. The concentration was measured by Nanodrop (Table 2.15).

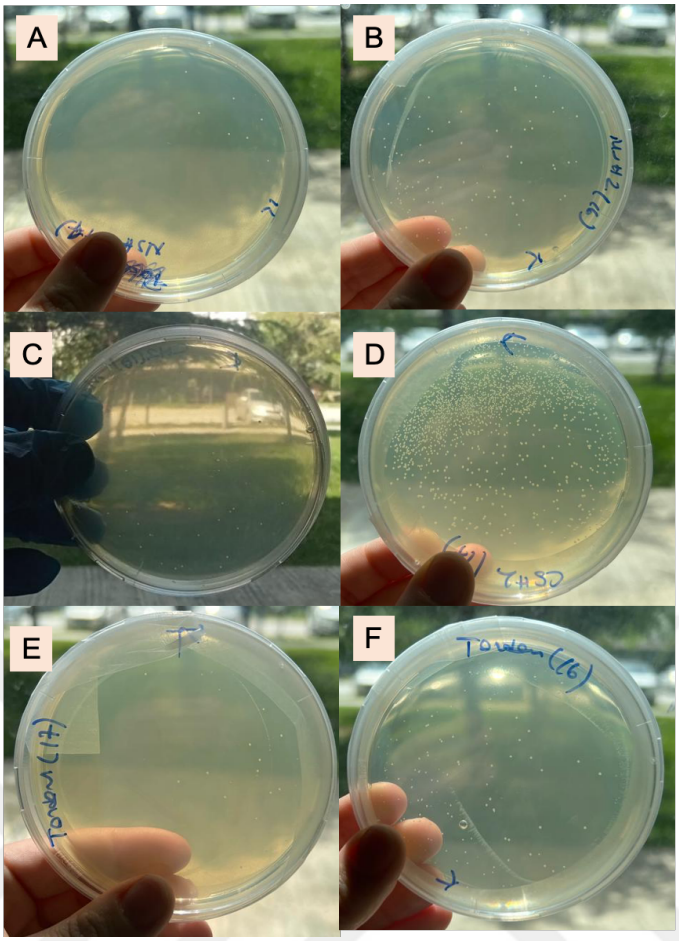


Figure 2.14 Transformation Results (A) N-SH2 (1) (B) N-SH2 (2) (C) C-SH2 (1) (D) C-SH2 (2) (E) Tandem SH2 (1) (F) Tandem SH2 (2)

Table 2.16 NanoDrop Results after Plasmid Isolation

Sample Name		Concentration (ng/µL)
Sample 1	TANDEM SH2	26.3
Sample 2	TANDEM SH2	19.3
Sample 3	C-SH2	22
Sample 4	C-SH2	15.3
Sample 5	N-SH2	21.1
Sample 6	N-SH2	8.1

2.3.2.6 Confirmation of Cloning by Sequencing

Six plasmids consisting of two different samples confirmed by restriction digestion from each SH2 domain were sent to "Izmir Institute of Technology Biotechnology and Bioengineering Research and Application Center" for DNA sequencing. Especially Tandem-SH2 was sequenced both forward and reverse. Since the reading capacity of the device is 500 bp, reverse reading was done again for the parts after 500 bp. Sequence

results, sample 1, sample 4 and sample 5 are given as Tandem-forward SH2 (Figure 2.15), Tandem-reverse SH2 (Figure 2.16), C-SH2 (Figure 2.17) and N-SH2 (Figure 2.18), respectively. For further studies, sample 1 (tandem SH2), sample 4 (C-SH2) and sample 5 (N-SH2) were selected for protein expression and purification experiments.

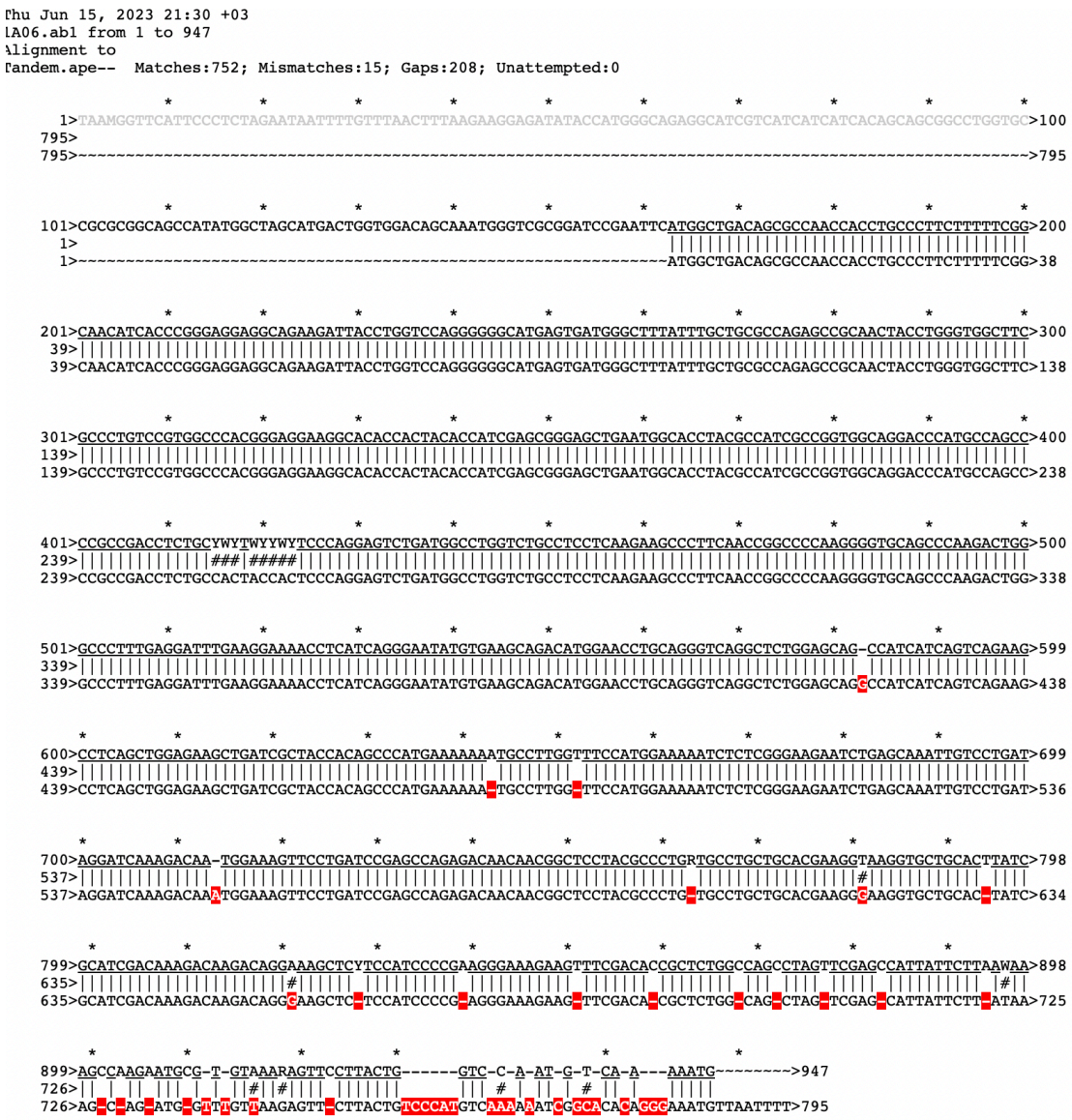


Figure 2.15 Sample 1 - Sequencing results of Tandem SH2 (forward read)

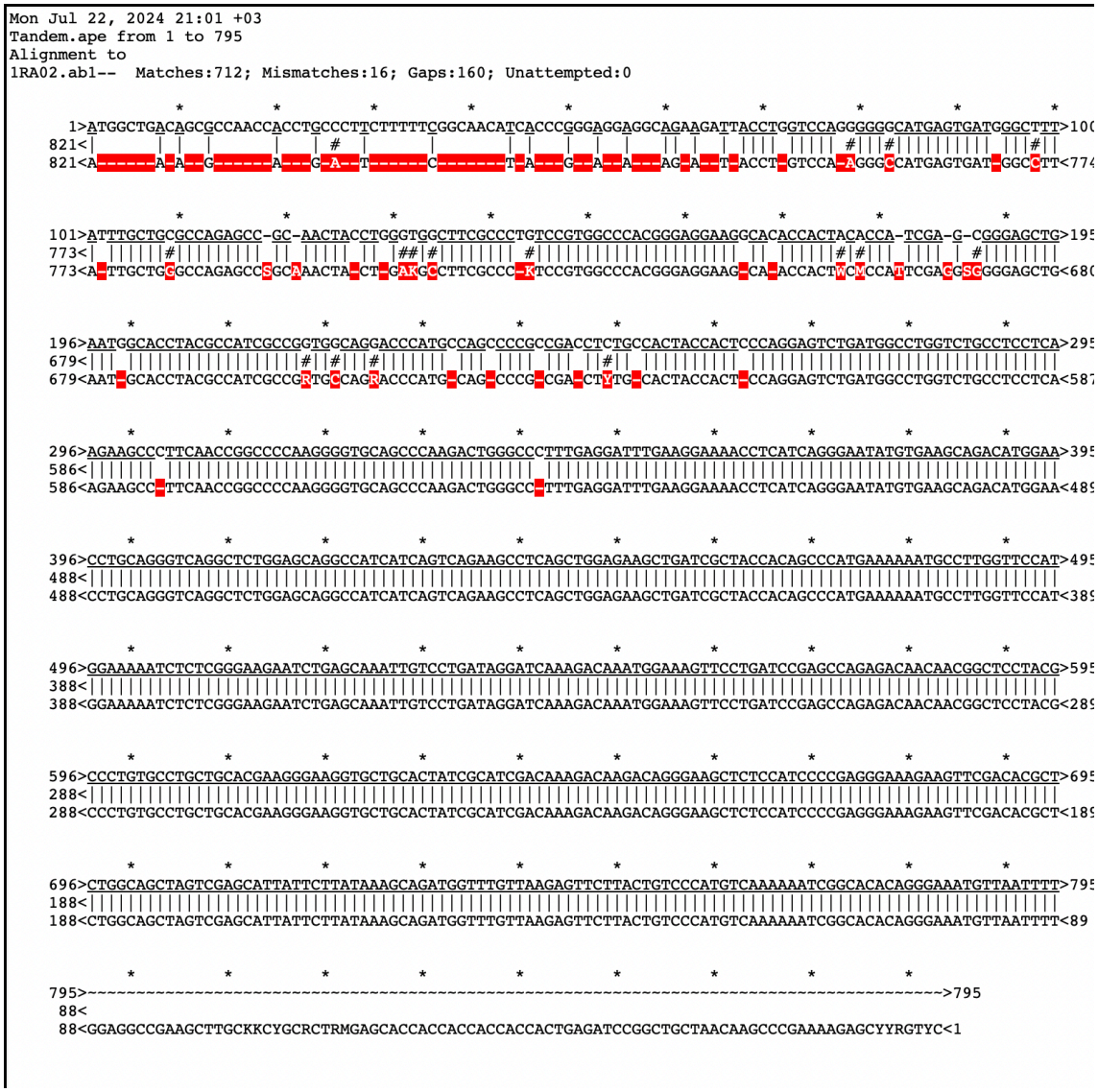


Figure 2.16 Sample 1 - Sequencing results of Tandem SH2 (reverse read)

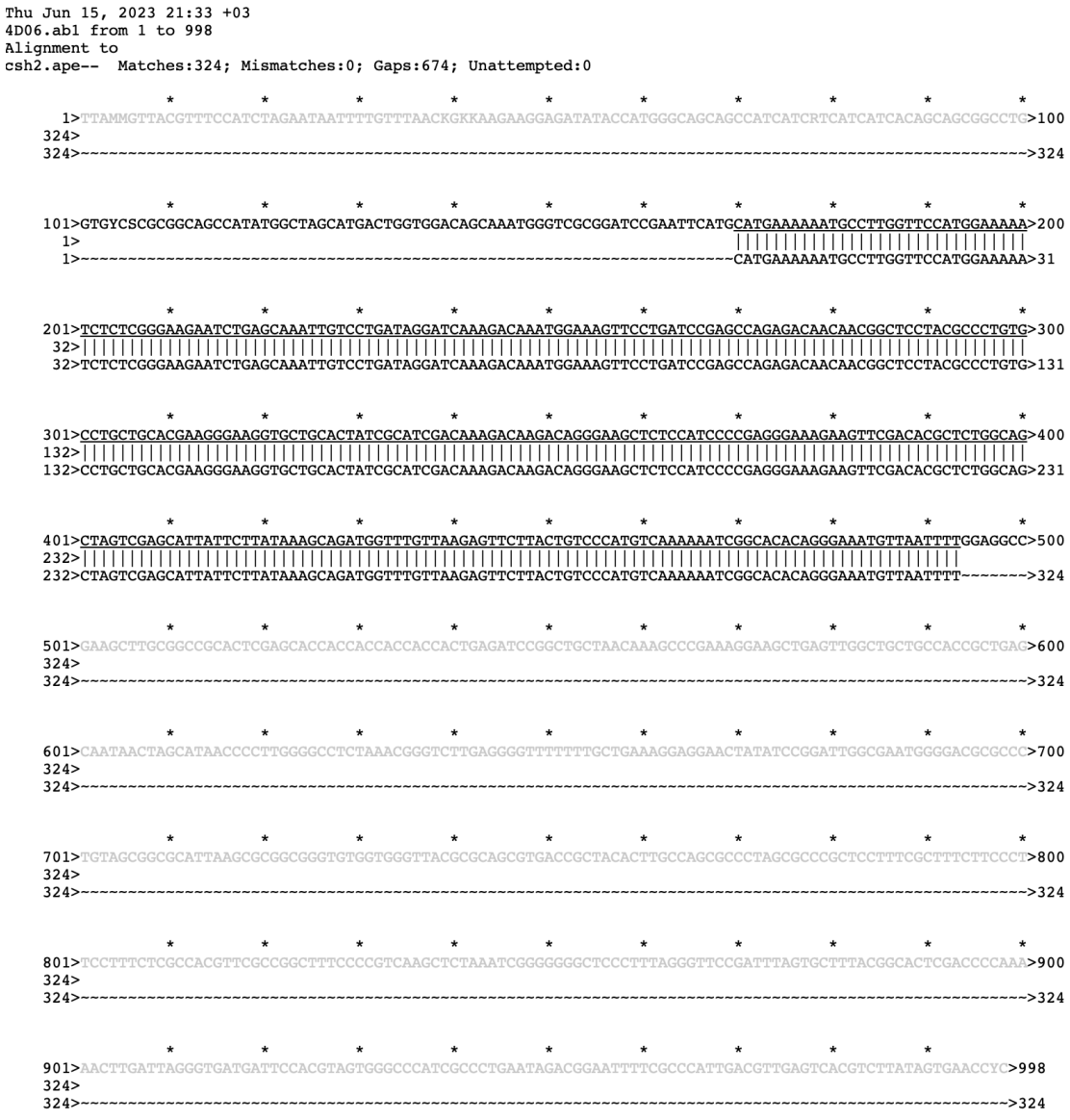


Figure 2.17 Sample 4 - Sequencing results of C-SH2 (forward read)

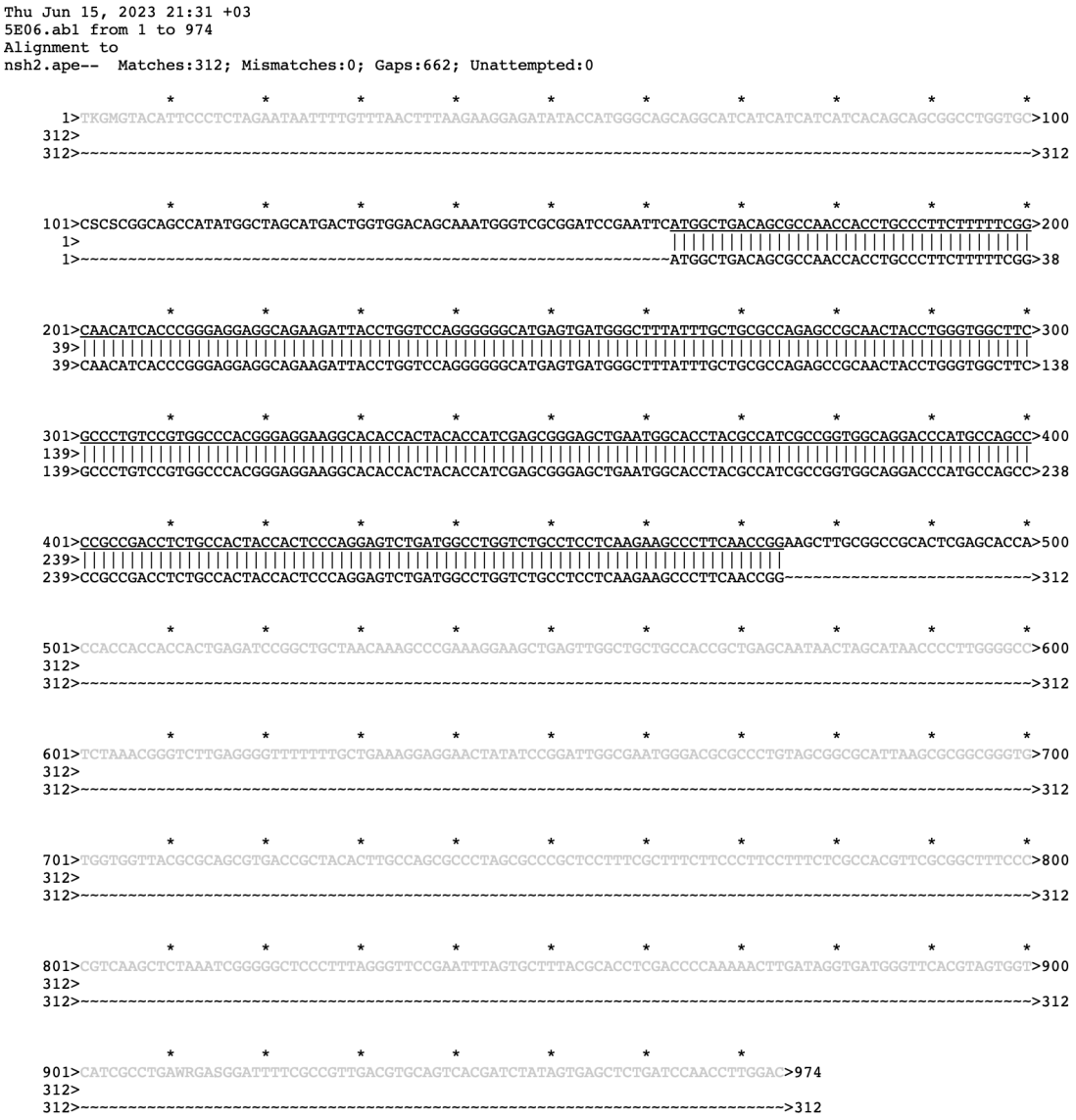


Figure 2.18 Sample 5 - Sequencing results of N-SH2 (forward read)

2.3.2.7 Transformation of Correct Colonies into Expression Host BL21(D3), Induction with Isopropyl-β-D-thiogalactopyranoside (IPTG) and Confirmation of Results by SDS-PAGE-Coomassie Brilliant Blue Assay and Western Blotting

Plasmids confirmed by sequencing were transformed into BL21(D3) cells for expression. Transformation of positive plasmids into BL21(D3) was carried out as

mentioned earlier. The results showed that colonies were formed and transformation into BL21(D3) was successful (Figure 2.19).

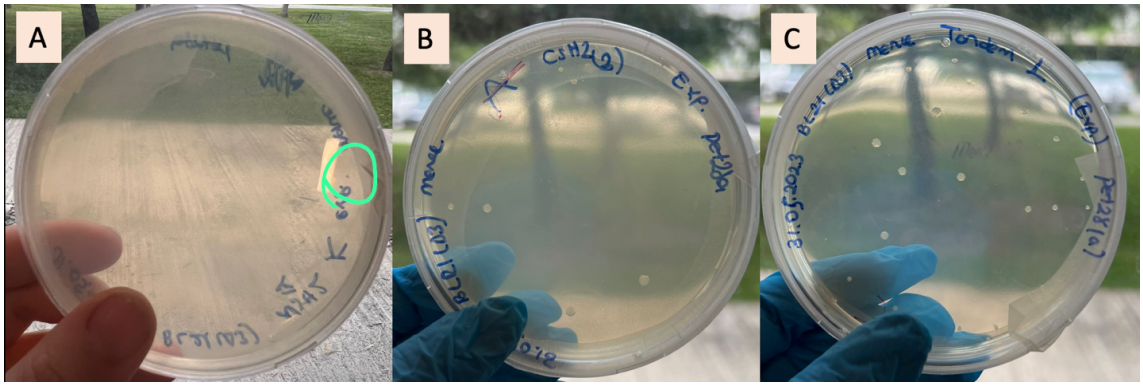


Figure 2.19 Transformation results of positive plasmids to BL21(D3) (A) N-SH2 (B) C-SH2 (C) Tandem SH2 domains

IPTG Induction:

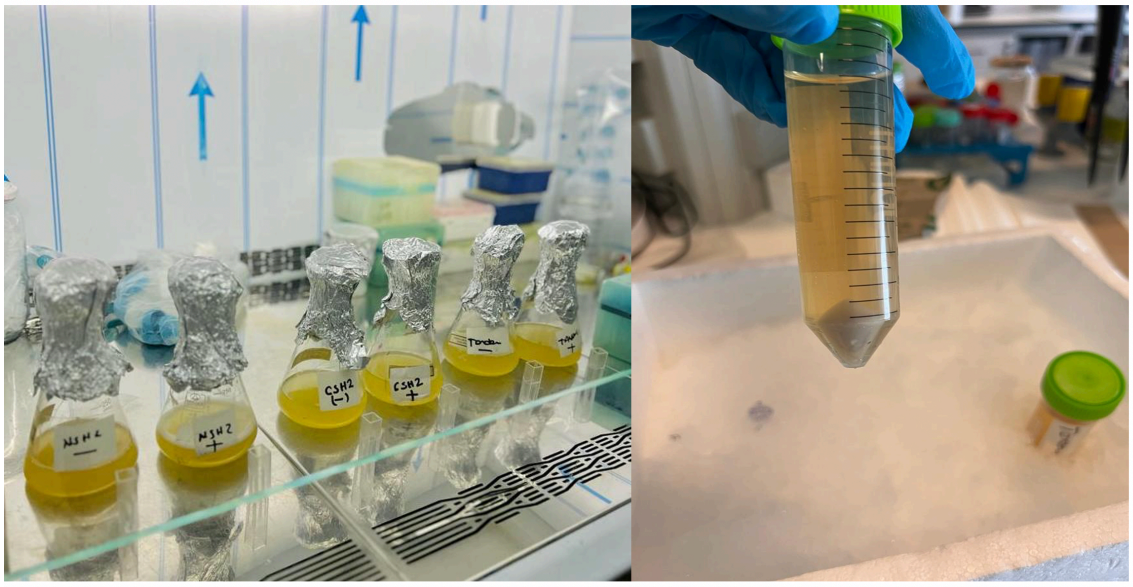


Figure 2.20 Induction with 0.5 mM IPTG as final concentration for 16 hours at 18 ºC.

First Induction:

First, the confirmed (positive plasmids) N-SH2, C-SH2 and Tandem SH2 were induced with a final IPTG concentration of 0.5 mM. In Figure 2.21, a strong band at 30 kDa was observed in band 6 after staining with SDS-PAGE-Coomassie Brilliant Blue Assay. This indicated that it was our protein since the molecular weight of Tandem-SH2 was 29921.86 Da compared to the negative control (band 5). On the other hand, we did not see strong induction of any protein after IPTG induction approached 12 kDa or 13 kDa in N-SH2 and C-SH2, respectively.

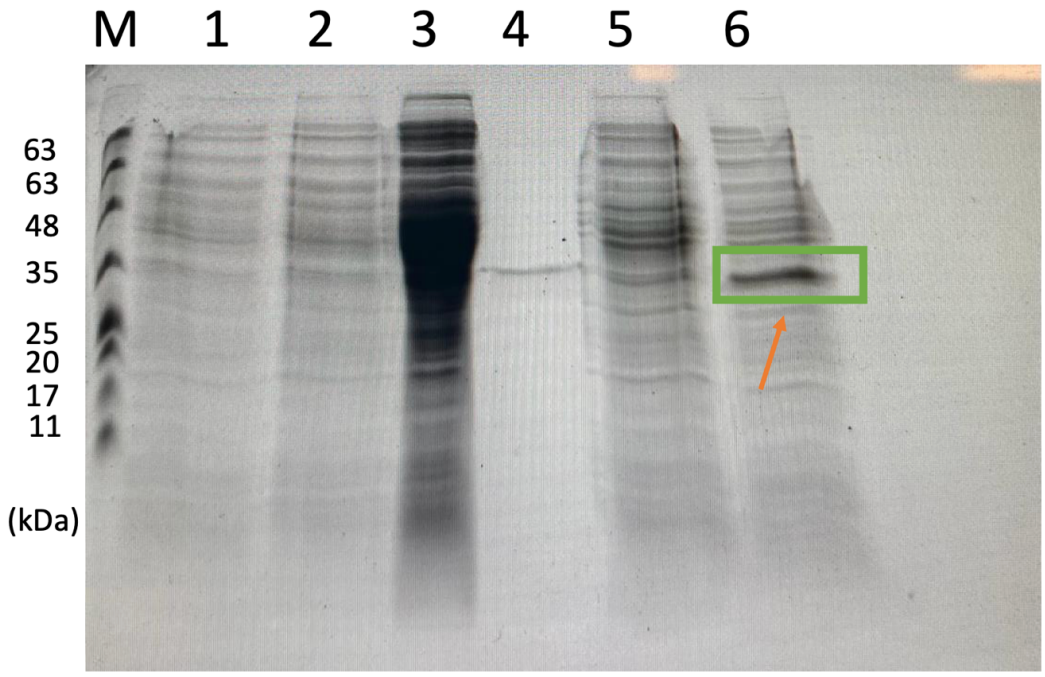


Figure 2.21 Coomassie Brilliant Blue Assay after IPTG Induction. Band 1: N-SH2 18 ^{0}C IPTG negative (16h), Band 2: N-SH2 18 ^{0}C IPTG 0.5 mM(16h), Band 3: C-SH2 18 ^{0}C IPTG negative (16h), Band 4: C-SH2 18 ^{0}C IPTG 0.5 mM(16h), Band 5: Tandem 18 ^{0}C IPTG negative (16h), Band 6: Tandem 18 ^{0}C IPTG 0.5 mM(16h). N-SH2 (11582.86 Da), CSH2 (12384.21 Da), Tandem (29921.86 Da)

Second Induction:

Since we could not see a significant band in the first induction, we repeated this experiment by changing the final concentration and temperature of IPTG in order to find the optimal state of our proteins. For this purpose, we performed an experiment with 50 ml of BL21(DE) culture. When we checked the results, we detected a strong band close to 11 kDa in band 2,3,4 in Figure 2.22A. Since our N-SH2 domain is 11582.86 Da, we estimated that it was N-SH2 domain expression. Especially band 2 in Figure 2.22A is strongly expressed, so we chose this sample for western blotting confirmation. On the other hand, C-SH2 was strongly expressed in bands 6,7,8 in Figure 2.22A. We examined the high expression levels of different bands compared to the negative control after IPTG induction in Tandem SH2 in Figure 2.22B. However, this band was close to 17 kDa, not 30 kDa. Later, by western blotting results, we observed that this band was close to 30 kDa (Figure 2.23). Our results showed that no band was detected in the negative control of IPTG (bands 1, 3, 5, 7) in Figure 2.23. On the other hand, we saw strong bands at 11 kDa,

16 kDa, 30 kDa and 30 kDa in the positive controls (bands 2, 4, 6, 8) respectively. As a result, western blot results revealed that our protein domains were produced after IPTG induction.

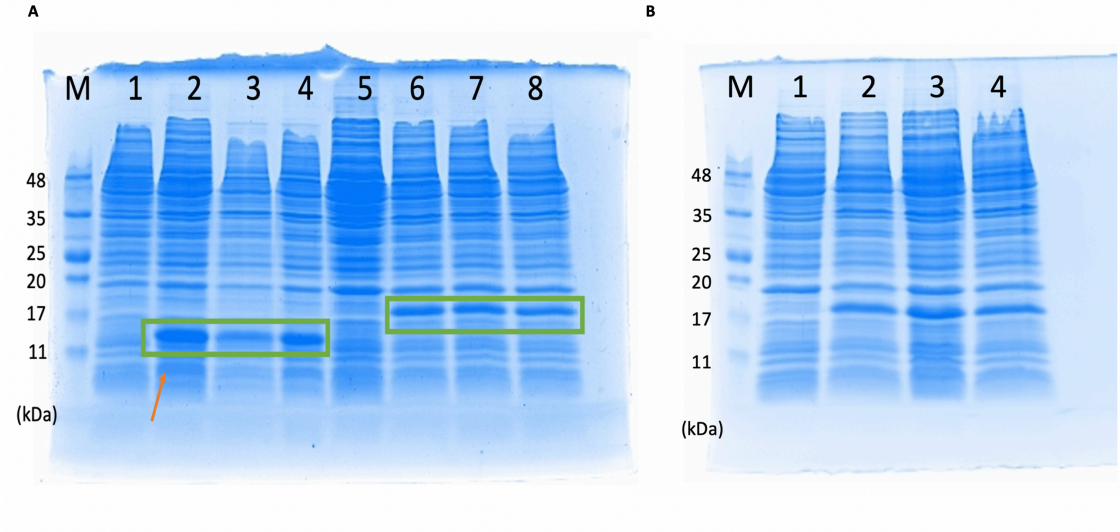


Figure 2.22 Coomassie Brilliant Blue Assay after IPTG Induction. **(A)** Band 1: N-SH2 20 ^{0}C IPTG negative (12h), Band 2: N-SH2 20 ^{0}C IPTG 0.1 mM (12h), Band 3: N-SH2 20 ^{0}C IPTG 0.4 mM (12h), Band 4: N-SH2 20 ^{0}C IPTG 0.5 mM (12h), Band 5: C-SH2 28 ^{0}C IPTG negative (4h), Band 6: C-SH2 28 ^{0}C IPTG 0.1 mM (4h), Band 7: CSH2 28 ^{0}C IPTG 0.4 mM (4h), Band 8: C-SH2 28 ^{0}C IPTG 0.5 mM (4h). **(B)** Bant 1: Tandem SH2 37 ^{0}C IPTG negative (4h), Bant 2: Tandem SH2 37 ^{0}C IPTG 0.1 mM (4h), Bant 3: TANDEM 37 ^{0}C IPTG 0.4 mM (4h), Bant 4: TANDEM 37 ^{0}C IPTG 0.5 mM (4h). N-SH2 (11582.86 Da), C-SH2(12384.21 Da), Tandem SH2 (29921.86 Da).

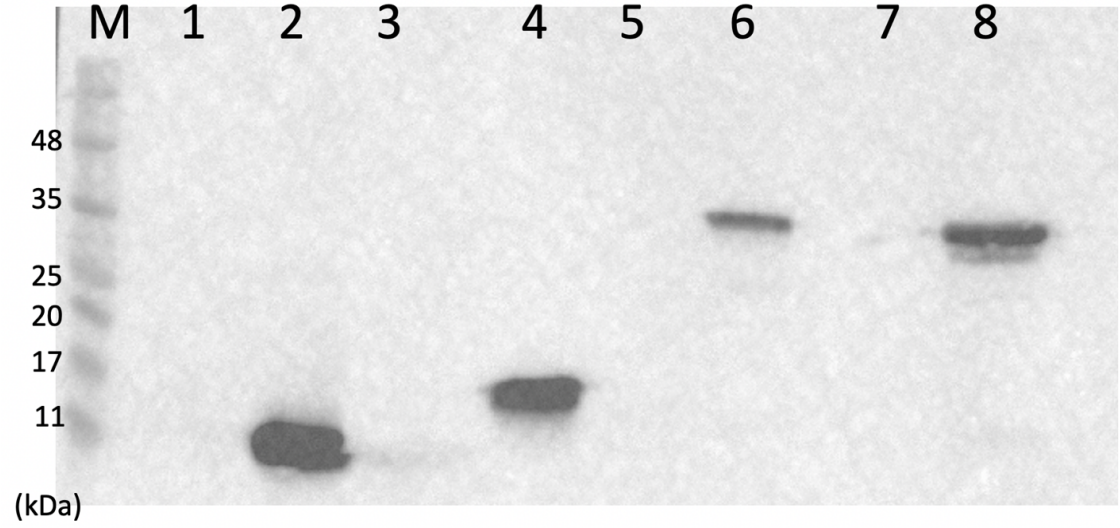


Figure 2.23 Western Blotting Results after IPTG Induction. Band 1: N-SH2 20 0C IPTG negative (12h), Band 2: N-SH2 20 ^{0}C IPTG 0.4 mM (12h), Band 3:C-SH2 28 ^{0}C IPTG negative (4h), Band 4: C-SH2 28 ^{0}C IPTG 0.5 mM (4h), Band 5: Tandem SH2 18 ^{0}C

IPTG negative (16h), Band 6: Tandem SH2 18 ^{0}C IPTG 0.5 mM (16h). Band 7: Tandem SH2 37 ^{0}C IPTG negative (4h), Band 8: Tandem SH2 37 ^{0}C IPTG 0.5 mM (4h). N-SH2 (11582.86 Da), CSH2 (12384.21 Da) and Tandem (29921.86 Da), (Purified anti-His tag, Mouse IgG1, (cat no: 652502, Biolegend))

2.3.2.8 Purification of Recombinant SH2 Domains using HisPur™ Ni-NTA Superflow Agarose and SDS-PAGE-Coomassie Brilliant Blue Assay

When we checked the results, a strong band with a molecular weight around 11 kDa was observed in Figure 2.24 after elution 1, 2 and 3. Since our N-SH2 domain is 11582.86 Da, the observed band belongs to N-SH2 domain and this indicated successful expression and purification. Also, for tandem SH2 domain, a strong band around 30 kDa after elution 1, 2 and 3 in Figure 2.25 represents tandem-SH2 domain. Similarly, C-SH2 was successfully purified and in Figure 2.26, there is a strong band between 11 and 17 kDa after elution 1, 2 and 3, indicating C-SH2.

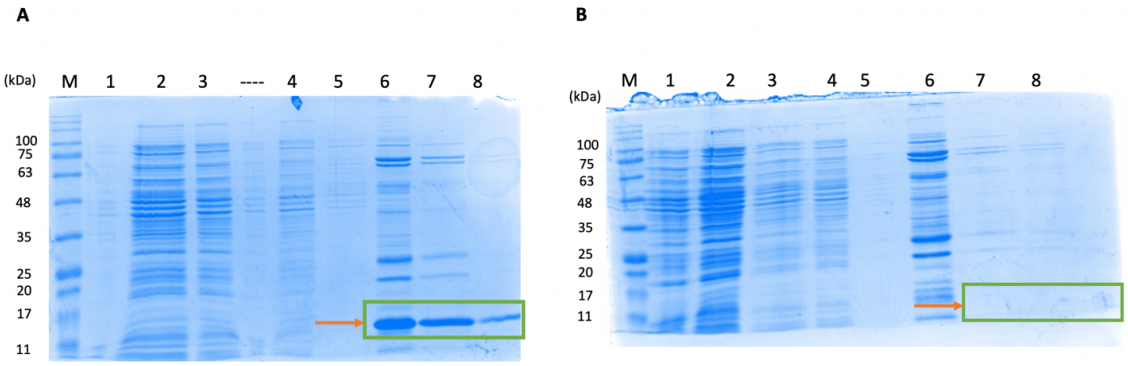


Figure 2.24 Results of purification of N-SH2 domain with 0.5 mM IPTG as a final concentration (A) and without IPTG (B) for 4 h at 37 ^{o}C. 1: After sonication, 2: After overnight incubation with Ni-NTA agarose (supernatant), 3: Wash 1 (supernatant), 4: Wash 2 (supernatant), 5: Wash 3 (supernatant), 6: Elution 1 (supernatant), 7: Elution 2 (supernatant) and 8: Elution 3 (N-SH2 11582.86 Da).

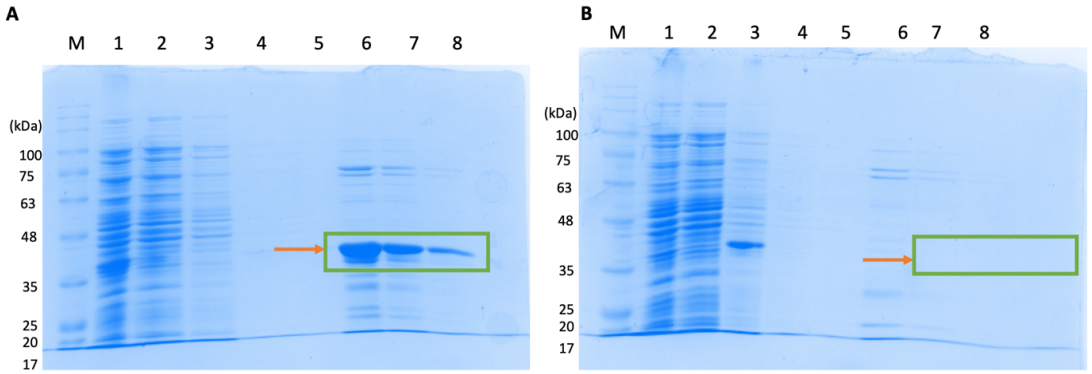


Figure 2.25 Results of purification of Tandem SH2 domain with (A) and without IPTG (B) as a final concentration of 0.5 mM for 4 h at 37 ºC. 1: After sonication, 2: After overnight incubation with Ni-NTA agarose (supernatant), 3: Wash 1 (supernatant), 4: Wash 2 (supernatant), 5: Wash 3 (supernatant), 6: Elution 1 (supernatant), 7: Elution 2 (supernatant), and 8: Elution 3 (Tandem SH2 29921.86 Da).

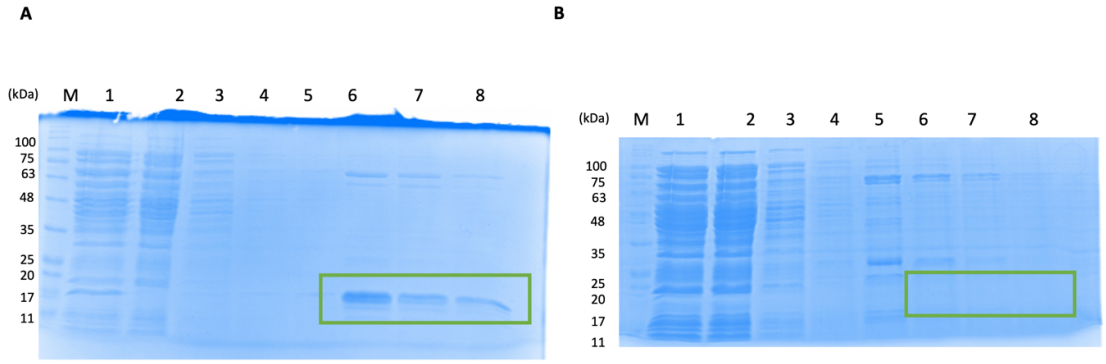


Figure 2.26 Results of purification of C-SH2 domain with 0.5 mM IPTG as final concentration (A) and without IPTG (B) for 4 h at 37 ºC. 1: After sonication, 2: After overnight incubation with Ni-NTA agarose (supernatant), 3: Wash 1 (supernatant), 4: Wash 2 (supernatant), 5: Wash 3 (supernatant), 6: Elution 1 (supernatant), 7: Elution 2 (supernatant), and 8: Elution 3 (C-SH2 12384.21 Da).

2.3.2.9 Purification of Recombinant SH2 domains using Ni-NTA Affinity Purification Method with Fast Protein Liquid Chromatography (FPLC) and BCA Protein Quantification Assay

Purification of SH2 domains was successfully carried out by Ni-NTA affinity purification method by Fast Protein Liquid Chromatography (FPLC) (Figure 2.27) and confirmed by SDS-PAGE-Coomassie Brilliant Blue Assay (Figure 2.28). The concentration of purified proteins is shown in Table 2.17.

The results showed that there was a strong band around 30 kDa molecular weight in well 1 in Figure 2.28 after purification. This observed band having 30 kDa belongs to Tandem SH2 domain since our Tandem SH2 domain. This showed that Tandem SH2 domain was expressed and purified successfully. Also, for C-SH2 domain, a strong band around 12 kDa in row 2 represents C-SH2 domain. We also observed strong bands at 11 kDa in rows 3-6 in Figure 2.28. This also represented the purification of N-SH2 domain of Syk enzyme.

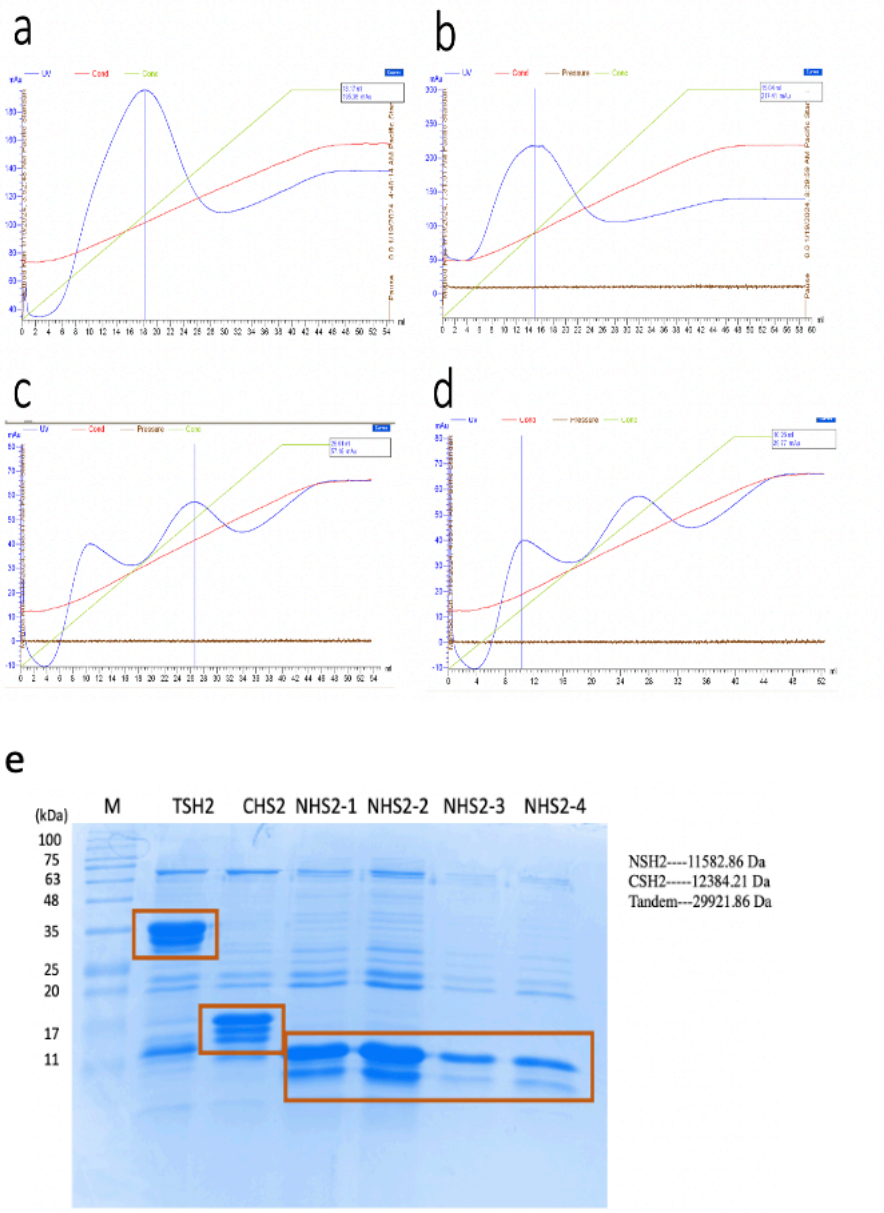


Figure 2.27 Fast Protein Liquid Chromatography and Coomassie Brilliant Blue Assay. Chromatogram Graphs of Syk Domains Obtained from FPLC a) C-SH2 domain of Syk protein b) Tandem SH2 domain of Syk protein c) N-SH2 domain of Syk protein d) N-SH2 domain of Syk protein e) Total Protein of Syk domains in SDS-PAGE-Coomassie Brilliant Blue Assay

Table 2.17 BCA Protein Concentration Assay Results

Sample Name	Concentration (mg/ mL)
TANDEM SH2	2.091004341
C-SH2 SH2	1.507259392
N-SH2-1	3.093234546
N-SH2-2	4625461757
N-SH2-3	0.407301302
N-SH2-4	0.719503068

As a result, N-SH2, C-SH2 and Tandem SH2 were successfully purified and made ready for "Differential Scanning Fluorimetry and Intracellular FRET assay".

2.3.3 Testing the Binding of Compounds to C-Syk SH2 domain by Differential Scanning Fluorimetry Assay

Differential Scanning Fluorimetry (DSF) is a biophysical technique used to rapidly and efficiently measure the thermal stability of a protein. The method monitors the change in fluorescence of a dye (such as SYPRO Orange) as it binds to the hydrophobic regions of a protein while the temperature of the solution is slowly increased. In its native, folded state, a protein's hydrophobic regions are hidden in its core. As the temperature rises, the protein begins to denature (lose its folded structure), exposing these hydrophobic regions. The dye then binds to these newly exposed areas, causing a sharp increase in the fluorescence signal. This abrupt rise in signal identifies a thermal transition point, known as the protein's **melting temperature (Tm)**. DSF is particularly useful in drug discovery and biochemistry to determine if a ligand (a small molecule) binds to a protein. When a ligand binds to a protein, it typically stabilizes its structure. This stabilization requires a higher temperature to cause the protein to denature.

Therefore, we can conclude:

- The Tm of a protein without a ligand represents its baseline thermal stability.
- The Tm of a protein with a bound ligand increases, proportional to the stabilizing effect of the ligand.

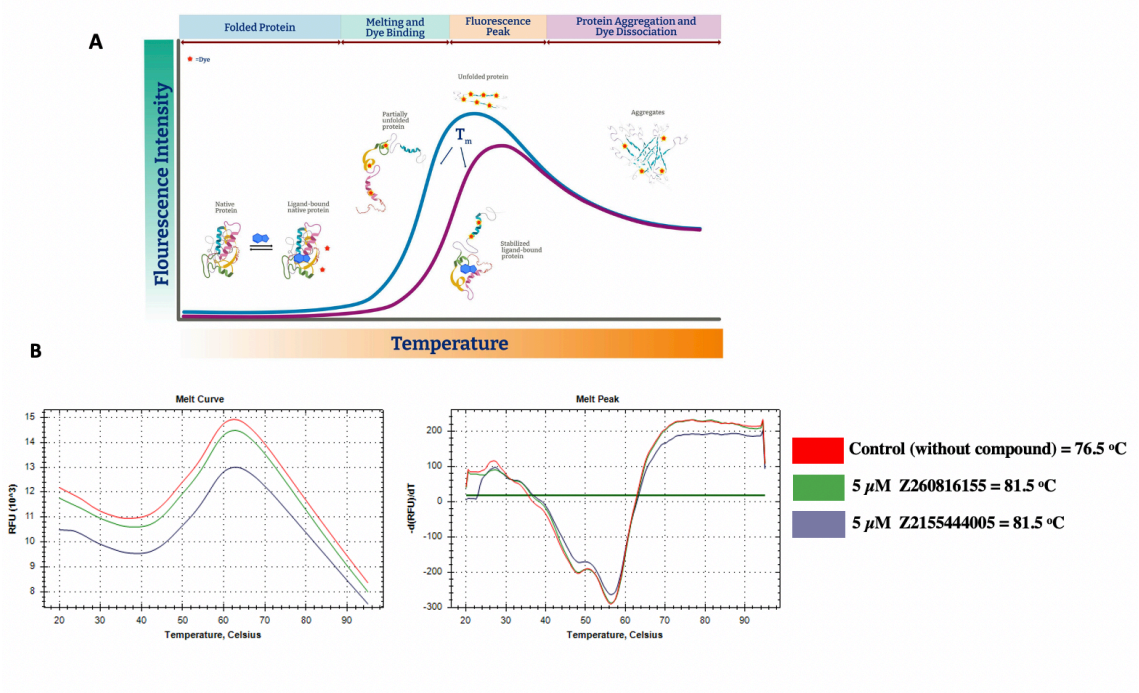


Figure 2.28 The results of Differential Scanning Fluorimetry (DSF) Assay (A) The thermal stability of a protein is quantified by its melting temperature (Tm), defined as the temperature at which the populations of folded and unfolded protein are equal. This value is determined from the inflection point of a thermal denaturation curve. Ligand binding stabilizes the protein's native state, increasing its resistance to heat-induced unfolding and thus resulting in an elevated Tm. (B) Protein ligand interaction (PLI) monitoring using Differential Scanning Fluorimetry (DSF) Assay (n=2).

The increase in the Tm value, known as **ΔTm**, is a measure of how tightly the ligand binds to the protein and how much it stabilizes it. A larger ΔTm value generally indicates a stronger binding affinity.

From this data, it's clear that both compounds bind to and stabilize the protein (Figure 2.28).

- For Z260816155, the ΔTm=81.5°C–76.5°C=5°C.
- For Z2155444005, the ΔTm=81.5°C–76.5°C=5°C.

Both compounds cause a significant 5°C increase in the protein's thermal stability, which provides clear evidence of a protein-ligand interaction. The identical ΔTm values suggest that both compounds have a similar binding affinity and stabilizing effect on the protein at the tested concentration of 5 μM. Both are promising candidates for further investigation.

2.3.4 Testing the binding of compounds to Syk SH2 domains by Intracellular Fluorescence Resonance Energy Transfer (FRET) Method

Fluorescence resonance energy transfer (FRET) is defined as a non-radiative energy transfer process occurring between the electronically excited states of a donor and an acceptor fluorophore. This phenomenon is highly dependent on the intermolecular distance, becoming efficient when the molecules are separated by approximately 1 to 10 nm, thereby leading to the sensitized emission of the acceptor. Consequently, FRET proves invaluable for real-time investigation of molecular dynamics within the intricate cellular milieu. Here, we tested candidate compounds using Cytosolic Syk Biosensor (Plasmid #125729).

The G418 dose was determined as 400 ug/ml from the literature for HEK293 cells [89]. First, in order to determine the correct dose, the cells were subjected to the MTT test and an approximate GI50 value was determined for both drugs. According to the MTT results, 75 µM was accepted as the approximate GI50 value for both drugs (Figure 2.29). Then, depending on the concentration, different concentrations of both drugs (25-200 µM) were prepared in HBSS and the fluorescence intensity of the cells was measured first without drug and then with drug addition, every 5 min for 1 h by adjusting an imaging protocol to obtain both CFP (excitation 433±10 nm, emission 476±10 nm) and FRET (excitation 433±10 nm, emission 527±10 nm) channels for each well. The results are presented in Figure 2.30 and 2.31. According to the results, increasing concentrations of both drugs showed that the FRET/CFP ratio decreased after drug administration. This indicates that the inhibitors successfully bound to the C-SH2 domain. Because a rather dramatic decrease was detected at increasing doses at the end of 1 hour.

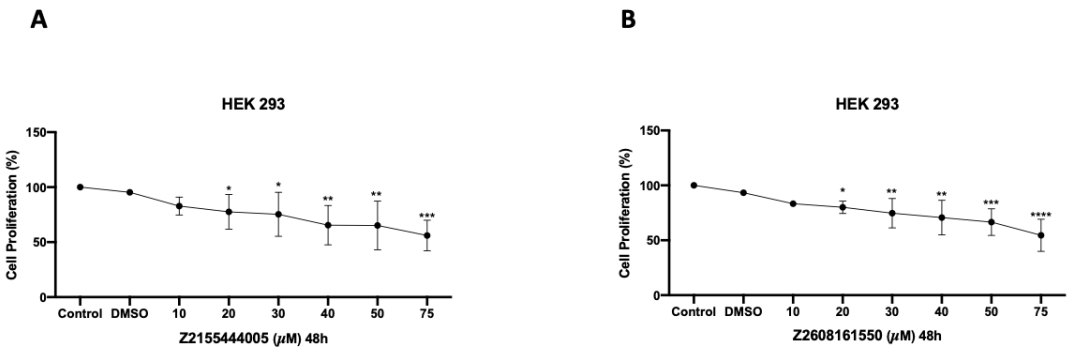


Figure 2.29 Treatment of HEK293 cells with increasing doses of Z2155444005 (A) and Z260816155 (B) for 48 hours, respectively, and evaluation of the results by MTT assay.

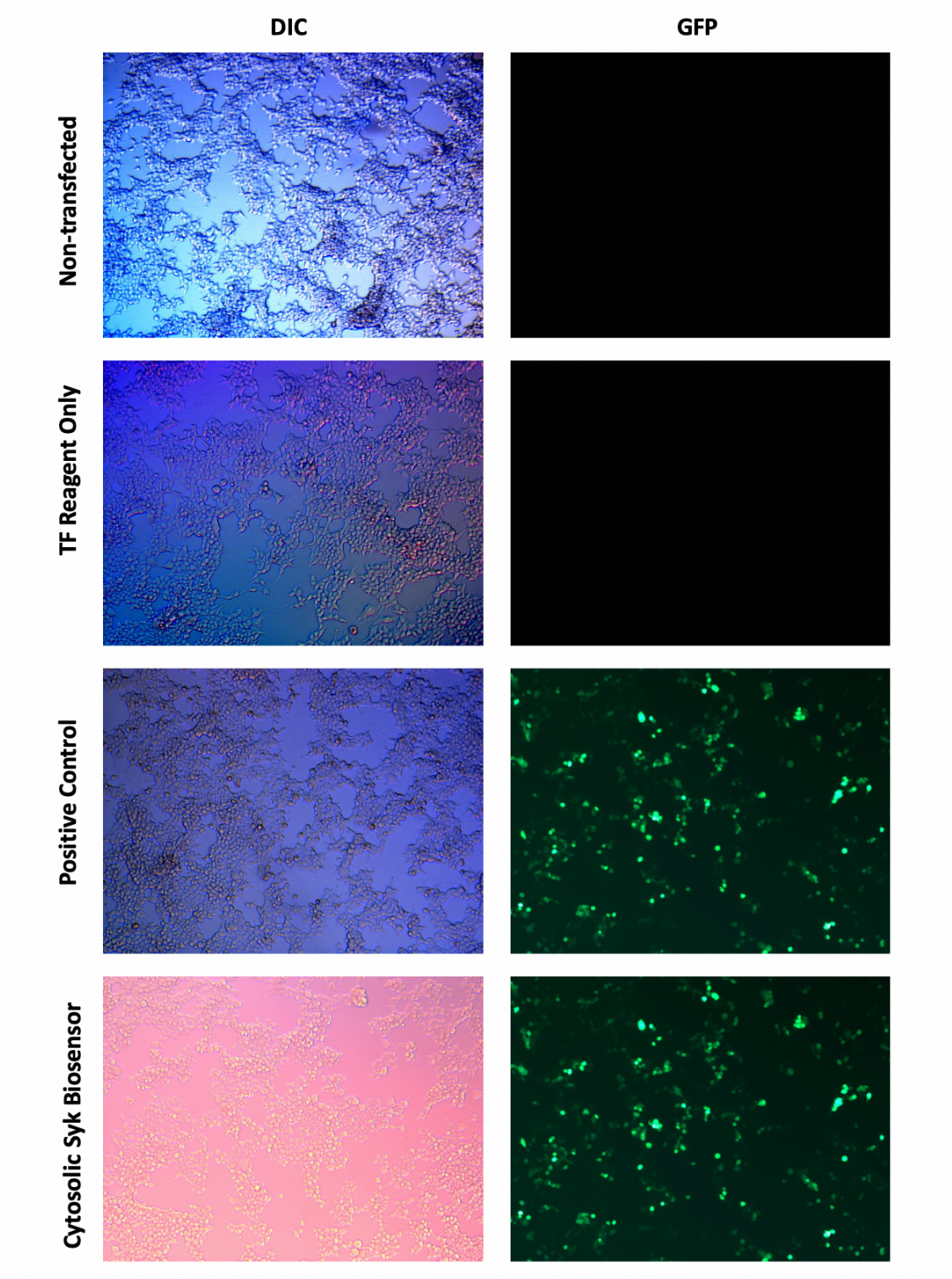


Figure 2.30 HEK293 cells, from top to bottom, non-transfected cells, treated with transfection reagent only, treated with GFP-labeled plasmid (positive control) and Cytosolic Syk Biosensor (Plasmid #125729) (DIC: Differential interference contrast)

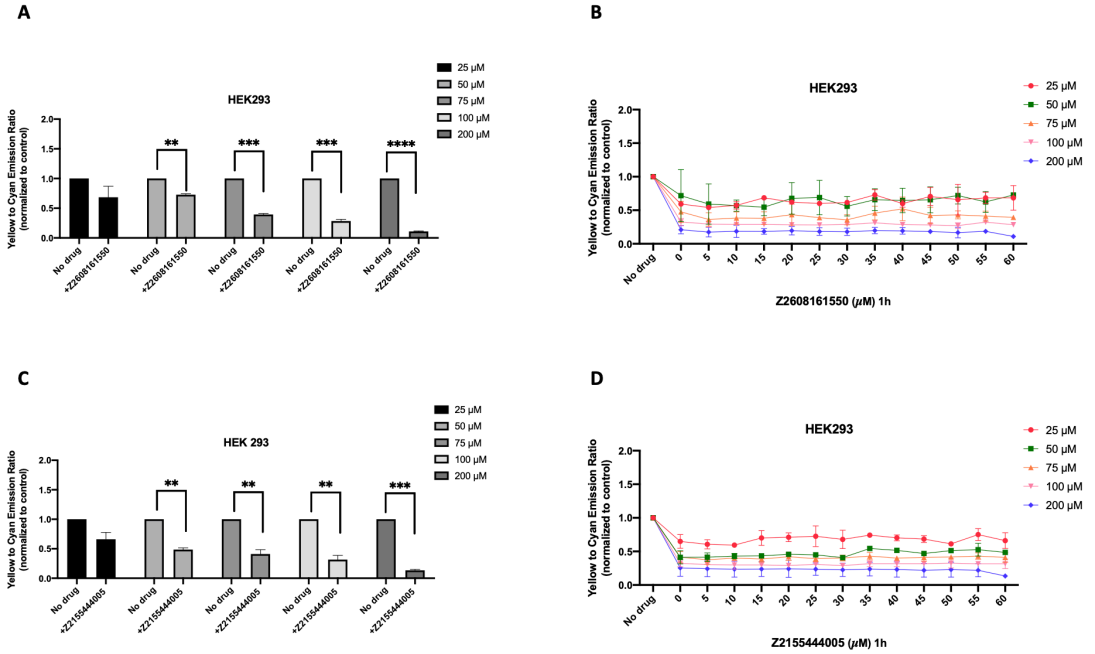


Figure 2.31 Change in FRET/CFP value of HEK293 cells transfected with Syk biosensor during 1 hour after addition of Z260816155 (A-B) and Z2155444005 (C-D), respectively. Fluorescence intensity was measured using spectrophotometer and normalized to No drug control cells. Standard deviation was done on the number of replicates of 8 wells per treatment and the experiment was repeated 2 times independently (n = 2). Statistical analyses were performed by Unpaired t test. The significance level was set at $P < 0.0001$. All data are presented as mean ± s.d. Calculations were performed using GraphPad Prism 8.

2.4 Conclusion

In this chapter, *in silico* studies were performed using the ENAMINE database, which contains a large database of available inhibitors. MD analyses showed that Z2155444005 and Z260816155 had the best binding energies of -279.424 kJ (-66.782 kcal/mol) and -258.564 kJ (-61.79 kcal/mol), respectively. These results were quite promising. These compounds were purchased and their binding to the C-SH2 domain was confirmed *in vitro* using "Differential Scanning Fluorimetry Assay" and "Intracellular FRET Methods".

Differential Scanning Fluorimetry (DSF) rapidly assesses protein thermal stability, crucial for protein-ligand binding studies. It works by heating a protein with a fluorescent

dye; as the protein unfolds, the dye binds to exposed hydrophobic regions, increasing fluorescence. This allows us to determine the protein's melting temperature (Tm). When a ligand binds to a protein, it typically stabilizes the protein, causing a shift to a higher Tm. This ΔTm indicates ligand binding strength, making DSF invaluable for high-throughput screening of drug candidates and understanding molecular interactions in drug discovery. For this purpose, we designed a Differential Scanning Fluorimetry (DSF) in order to test binding of our candidate inhibitors to C-SH2 domain of Syk enzyme. First, the C-SH2 domain was produced recombinantly and cloning was confirmed by sequencing, then the purification of the protein was validated by Coomassie Bright Blue Assay and Western Blotting. DSF results indicated that both compounds cause a significant 5°C increase in the protein's thermal stability, which provides clear evidence of a protein-ligand interaction.

Live-cell compound screening with genetically encoded fluorescence- or bioluminescence-based biosensors offers a potentially powerful approach to identify novel regulators of a signaling event of interest. In particular, the additional advantage of compound screening in living cells is that the entire signaling network remains intact, and therefore, screening is not performed solely against a single molecule of interest, but rather against any molecule within the signaling network that could modulate the specific signaling event reported by the biosensor in use. One class of such biosensors is fluorescence resonance energy transfer (FRET)-based biosensors, which can detect the complex spatiotemporal dynamics of second messengers, enzyme activation activities, and protein-protein interactions in living cells. A genetically encoded FRET-based biosensor was developed by Xiang and colleagues to study the dynamics of Syk activities at the subcellular level in living cells. This sensor contains an N-terminal ECFP, an SH2 domain, a peptide derived from the SYK substrate VAV2, and a C-terminal YPET. Upon specific phosphorylation by Syk *in vitro,* the biosensor substrate peptide binds to the intramolecular SH2 domain to reduce FRET efficiency [88]. Therefore, we wanted to use this biosensor to verify intracellular SH2 domain binding. HEK293 cells were transfected with this biosensor, and intracellular binding of Z260816155 and Z2155444005 was tested. The results were quite promising. Both inhibitors strongly bound to the R175 region of the SH2 domain of the biosensor, inhibiting the FRET response and increasing the CFP ratio. This demonstrated that our candidates bind strongly to the SH2 domain *in vitro.*

Although further validation is needed, we propose two novel C-SH2 domain inhibitors of the Syk enzyme using computational drug discovery methods and *in vitro* validation. Future studies can confirm these results by conducting further validation tests. Furthermore, these inhibitors can be used to investigate various diseases, particularly cancer, and specifically the pathways and proteins involving Syk. We believe our research represents a significant milestone in the field of protein-protein interactions and will pave the way for new research, particularly on the SH2 domain, contributing to researchers interested in this area.

Chapter 3

Targeting of Syk SH2 domains for the Treatment of Acute Myeloid Leukemia

3.1 Introduction

3.1.1 Acute Myeloid Leukemia

Acute myeloid leukemia (AML) is a heterogeneous malignancy that is a clonal disorder of hematopoietic stem and progenitor cells, characterized by uncontrolled growth and impaired differentiation ability of immature myeloid precursors [90]. AML is the most common type of acute leukemia in adults, and its incidence increases with age. The median age at diagnosis is around 68–69 years[91], [92], [93]. AML can occur de novo, as well as from hematological disorders such as previous myelodysplastic syndrome (MDS) or myeloproliferative neoplasms (MPN), after cytotoxic therapy (chemotherapy/radiotherapy) (treatment-related AML - t-AML) or on the basis of hereditary (germline) genetic predisposition.

3.1.2 Classification of AML

AML classification has evolved from the French-American-British (FAB) Classification, based on morphology and cytochemistry, to more complex systems such as the World Health Organization (WHO) Classification and the International Consensus Classification (ICC), which integrate immunophenotyping, cytogenetics, and molecular

genetic data. Technological advances such as next-generation sequencing (NGS) have increased the importance of genetic markers. The first modern classification system, the French-American-British (FAB) Classification, was based on morphology and cytochemistry. The FAB classification divided AML into eight subtypes, from M0 to M7, based on the normal bone marrow elements that the leukemic cells resemble [94]:

Table 3.1 Summary of FAB Classification

FAB Subtype	Name	Key Morphological Features	Key Cytochemical Findings
M0	Minimally Differentiated AML	No obvious myeloid morphology, agranular blasts	<3% MPO/SBB+, NSE-
M1	AML without Maturation	Blasts with few granules, Auer rods may be present, <10% maturing granulocytic cells	≥3% MPO/SBB+, NSE-
M2	AML with Maturation	Blasts with variable granulation, Auer rods common, ≥10% maturing granulocytic cells	≥3% MPO/SBB+, NSE-
M3	Acute Promyelocytic Leukemia (APL)	Abnormal promyelocytes dominant, heavy granulation, frequent Auer rods (faggot cells)	Strong MPO+, NSE+/-
M4	Acute Myelomonocytic Leukemia (AMML)	Both granulocytic and monocytic differentiation (≥20% each)	≥3% MPO/SBB+, NSE+ (monocytic component)
M5	Acute Monocytic Leukemia (AMoL)	≥80% monocytic lineage (M5a: monoblastic, M5b: monocytic)	MPO+/- (often weak/negative), Strong NSE+
M6	Acute Erythroid Leukemia	≥50% erythroid precursors, ≥30% blasts in non-erythroid cells (FAB 1985 definition)	Variable MPO/SBB/NSE
M7	Acute Megakaryoblastic Leukemia	Megakaryoblasts dominant, morphology variable, cytoplasmic budding may be present	MPO/SBB-, NSE-

**Note: NSE: Non-Specific Esterase. MPO/SBB percentages refer to blast cells.*

The World Health Organization (WHO) Classification was introduced in 2001 and updated in 2008, 2017 and 2022. It offers an approach that integrates morphology, immunophenotyping, genetic and clinical information. The blast threshold for AML diagnosis has been reduced from 30% to 20% in the WHO classification [95], [96]. The

2022 version emphasizes genetic factors more strongly and the category "AML with Definitive Genetic Abnormalities (AML-DGA)" takes precedence over other categories. The ≥20% blast threshold has been removed for many AML-DGA subtypes. The International Consensus Classification (ICC) 2022 was developed simultaneously with WHO 2022, and genetic abnormalities are prioritized here. It generally requires ≥10% blasts for the diagnosis of AML in the presence of defining genetic abnormalities. It added a new main category for AML with TP53 mutations. It created a new intermediate category (10-19% blasts) called MDS/AML [97].

Table 3.2 Comparison of AML Classification Systems Based on Updates

Feature	FAB (1976/1985)	WHO 2017 (Revised 4th Ed.)	WHO 2022 (5th Ed.)	ICC 2022
Core Criteria	Morphology, Cytochemistry	Morphology, Immunophenotype, Cytogenetics, Molecular Genetics (limited), Clinical	Morphology, Immunophenotype, Genetics (primary), Clinical	Morphology, Immunophenotype, Genetics (primary), Clinical
General Blast Threshold	≥30% (initially)	≥20%	≥20% (general); No threshold for most DGA	≥20% (general); ≥10% for most RGA
Genetic Integration	None	Separate categories for certain recurrent abnormalities (RGA) and mutations (NPM1, CEBPA, RUNX1 provisional); Cytogenetics in MRC	Defining genetic abnormalities (DGA) as main category; Genetics/cytogenetics mandatory for MR; RUNX1 removed	Recurrent genetic abnormalities (RGA) as main category; Separate categories for MR genetics/cytogenetics; AML-TP53 new category; RUNX1 in MR gene mutations
MDS-Related AML	None (concept of preleukemia/ MDS existed)	AML-MRC: Defined by history, cytogenetics OR morphology (dysplasia)	AML-MR: Defined by history OR cytogenetics OR MR-gene mutations; morphology alone insufficient	AML-MR-Cytogenetic / AML-MR-Gene Mutations: Defined by cytogenetics OR MR-gene mutations; history is a qualifier

10-19% Blasts (No Genetics)	MDS (RAEB/RAEB -t)	MDS-EB2	MDS-IB2	MDS/AML (new intermediate category)
Treatment-Related/Germline	None	t-MN / Germline Predisposition (separate categories/subtypes)	Secondary Myeloid Neoplasms (MN-pCT, Germline Predisposition MN under main category)	Diagnostic Qualifiers (added to primary diagnosis)

Table 3.3 Key Differences: WHO 2022 vs. ICC 2022

Feature	WHO 2022 Approach	ICC 2022 Approach
Genetic AML Blast Threshold (General)	No threshold for most DGA	≥10% blasts for most RGA
BCR::ABL1 Blast Threshold	≥20% blasts	≥20% blasts
CEBPA Mutated AML Blast Threshold	≥20% blasts	≥10% blasts
CEBPA Mutation Definition	Biallelic (biCEBPA) OR single bZIP region (smbZIP-CEBPA)	In-frame bZIP CEBPA mutations (mono- or biallelic)
Myelodysplasia-Related (MR) AML	Single category: AML-MR (Defined by History OR Cytogenetics OR MR-Gene Mutations)	Two categories: AML-MR-Cytogenetic / AML-MR-Gene Mutations (Defined by Cytogenetics OR MR-Gene Mutations; History is a qualifier)
RUNX1 Mutated AML	Removed as a defining entity	Included in AML-MR-Gene Mutations category
AML with Mutated TP53	No separate main category (generally under AML-MR or AML-DBD)	New main category (≥20% blasts, VAF>10%), takes precedence over AML-MR
10-19% Blasts (No Defining Genetics)	MDS-IB2 (MDS subtype)	MDS/AML (new intermediate category)
Treatment-Related/Germline/Prior MDS History	Secondary Myeloid Neoplasms main category (MN-pCT, Germline); Prior MDS history contributes to AML-MR definition	Diagnostic Qualifiers (added to primary diagnosis); Prior MDS history not a classifier for AML-MR
Terminology Examples	AML-DGA (Defining Genetic Abnormalities); AML-DBD (Defined By Differentiation)	AML-RGA (Recurrent Genetic Abnormalities); AML-NOS (Not Otherwise Specified)

The European Leukemia Network (ELN) 2022 Risk Classification divides AML patients into Good, Intermediate, and Poor risk groups based on their genetic abnormalities at diagnosis and is used to guide treatment intensity and prognostic expectations. Initial risk assignment may change based on measurable residual disease (MRD) analysis during treatment [98].

Table 3.4 ELN 2022 Genetic Risk Classification

Risk Category	Defining Genetic Abnormalities (Cytogenetic and Molecular)
Favorable Risk	t(8;21)(q22;q22.1) / RUNX1::RUNX1T1
	inv(16)(p13.1q22) or t(16;16)(p13.1;q22) / CBFB::MYH11
	Mutated NPM1 (in the absence of FLT3-ITD)
	Mutated CEBPA (in-frame bZIP)
Intermediate Risk	Mutated NPM1 (in the presence of FLT3-ITD)
	Wild-type NPM1 and FLT3-ITD (without adverse-risk genetic lesions)
	t(9;11)(p21.3;q23.3) / MLLT3::KMT2A
	Other cytogenetic/molecular abnormalities not classified as favorable or adverse risk
Adverse Risk	t(6;9)(p23.3;q34.1) / DEK::NUP214
	t(v;11q23.3) / KMT2A-rearranged (excluding t(9;11))
	t(9;22)(q34.1;q11.2) / BCR::ABL1
	inv(3)(q21.3q26.2) or t(3;3)(q21.3;q26.2) / GATA2, MECOM
	-5 or del(5q)
	-7
	-17/abn(17p)
	Complex karyotype (≥3 abnormalities)
	Monosomal karyotype
	Mutated ASXL1
	Mutated BCOR
	Mutated EZH2
	Mutated RUNX1

	Mutated SF3B1
	Mutated SRSF2
	Mutated STAG2
	Mutated U2AF1
	Mutated ZRSR2
	Mutated TP53 (pathogenic, VAF≥10%)

3.1.3 AML and Deregulated Signaling Pathways

It has been demonstrated that abnormalities in intracellular signaling pathways play an important role in the pathogenesis of AML by controlling important cellular processes such as proliferation, survival, and differentiation [99], [100]. Dysregulations in these pathways are a common consequence of various genetic and epigenetic alterations found in AML. Therefore, it is important to understand the signaling pathways that play a role in the background of AML, the proteins involved in these pathways, and the interactions and relationships of these proteins with other proteins. Activation of one pathway often leads to activation of many other downstream pathways (e.g., PI3K/AKT, MAPK, JAK/STAT, Wnt) [99]. This network complexity underlies AML heterogeneity and contributes to therapeutic resistance. For example, inhibition of a single node may lead to compensatory signaling through another pathway, explaining why single-agent targeted therapies may have limited efficacy or encounter rapid resistance. Understanding this interactive nature is essential to developing effective therapeutic strategies. Recent studies have shown that Spleen Tyrosine Kinase (Syk), a non-receptor kinase, intersects with important signaling pathways involved in the pathogenesis of AML, such as the PI3K, NFκB, and JAK/STAT signaling pathways [2].

3.1.4 Targeting the Syk Enzyme as a Therapeutic Approach in AML

Studies have shown that Syk enzyme activation, which plays an important role in AML phenotype and pathogenesis, is associated with direct or indirect signaling pathways [101], [102]. Overexpression of Hox and Meis1 genes triggers leukemia formation and is associated with high-risk AML. Mohr et al., in their study, showed that the transcription factor Meis1 increases protein expression and activation of Syk.

Moreover, Syk inhibition resulted in prolonged survival of mice with Hoxa9/Meis1-mediated leukemia, thus emphasizing that Syk is a key regulator of Hoxa9/Meis1-mediated AML and a prime candidate for clinical testing of Syk inhibitors in the treatment of AML [103]. Another study by Miller et al. showed that inhibition of Syk at the gene level or via small molecules abolished leukemia cell growth in the MLL-AF9 mouse model containing human leukemia cells. In addition, they found that integrin beta 3 (Itgb3) is a critical molecule for leukemic growth and that Syk phosphorylation is the main mediator of Itgb3 activity in AML. Moreover, it was shown that silencing of Itgb3 or Syk at the gene level resulted in decreased leukemia stem cell gene expression levels [104].

FLT3 receptor tyrosine kinase mutations occur in approximately 30% of all AML cases, supporting FLT3 as one of the most frequently mutated genes in AML [22]. Puissant et al. have shown that Syk phosphorylates several receptors involved in leukemogenesis, including Flt3, PDGFRα, and KIT. Syk protein has been implicated as a critical regulator of FLT3 in AML, and high expression of Syk protein has been shown to trigger transformation in AML and resistance mechanism to FLT3-ITD targeted therapies [101]. Furthermore, Weisberg and colleagues found that the combination of Midostaurin and the dual Flt3/Syk inhibitors tR406 (tamatinib) and R788 (fostamatinib) inhibited Syk in cell-based models of FLT3-ITD [105]. Furthermore, a novel signaling relationship between the tyrosine phosphatase, Shp2, and the tyrosine kinase, Syk, in FLT3-ITD+ AML was demonstrated by Richine et al. This finding provided evidence that multiple targeting of this pathway may provide a novel therapeutic benefit for the treatment of patients with FLT3-ITD+ AML [106]. In this context, literature studies show some kinase inhibitors (protein tyrosine kinase inhibitor-PTK) and their direct targeting to the kinase domain, which is the active site of the Syk enzyme. When looking at their working principles, they bind to the ATP binding pocket of Syk and inhibit kinase activity as an ATP competitive inhibitor [23]. PTKs are used in the clinic for the treatment of many diseases, especially cancer [17], [18]. However, recurrence of drug resistance has emerged as a problem during the clinical use of these inhibitors [18]. Although it was initially assumed that resistance to chemotherapeutic agents was due to the induction of mutations that initially led to the resistant phenotype, it is now clear that drugs that selectively target PTKs result in mutational changes and the acquisition of resistance to inhibition. Since kinase inhibitors act by targeting a specific kinase or set of kinases, there is a strong selective pressure to develop mutations that prevent drug binding but preserve

the catalytic activity of these enzymes [107]. In addition, the structural similarity between the ATP binding sites is another factor that limits the use of kinase inhibitors with low specificity [19]. Some of these inhibitors are: R406 (active metabolite of fostamatinib), cerdulatinib (PRT062070), entospletinib (GS-9973) [20], [21], [22]. A number of small molecule ATP-competitive Syk inhibitors, such as fostamatinib, cerdulatinib, and TAK-659, have therefore been developed and evaluated [20], [21], [22]. However, they have not shown promising results in clinical trials due to low specificity and severe cytotoxicity [23]. Patients receiving fostamatinib treatment have been shown to have side effects such as hypertension, diarrhea, elevated hepatic enzymes, and neutropenia [24], [25]. In addition, another study has shown that hypertension is the most important side effect of fostamatinib use and is significantly associated with cardiovascular side effects [26], [27]. This has led researchers to investigate new generation Syk inhibitors. Entospletinib is a second-generation Syk inhibitor with higher Syk specificity that promises to treat hematological malignancies including acute myeloid leukemia (AML) and chronic lymphoid leukemia [28]. However, rapidly developing drug resistance to entospletinib during treatment has rendered it ineffective [29]. Therefore, the development of a new type of Syk inhibitor that challenges drug resistance and has fewer side effects is an unmet need. In addition, there is no Syk inhibitor approved by the FDA for the treatment of AML yet. Since AML has a very heterogeneous prognosis, it is important to investigate new approaches because new treatment methods are always needed. The Syk enzyme contains two SH2 domains, and these two domains play a very important role in protein-protein interactions. SH2 domains are 100 amino acid modular units that recognize and bind to tyrosyl-phosphorylated peptide sequences on target proteins, thereby mediating intracellular protein-protein interactions. Researchers have shown that regulating and targeting protein-protein interactions is considered a promising strategy in drug discovery. When looking at the literature, recent studies suggested that SH2 domains are an important target in addition to active kinase domains in cancer treatment methods to prevent the activation of abnormal proteins that lead to cancer. In studies, Grb7 [60], STAT3 and STAT5 SH2 [59], [61] domains have been targeted with peptides and peptide mimetics and their importance for cancer treatment has been revealed. In a recent study, it has been reported that targeting the SH2 domain of c-Src may represent a promising therapeutic target for triple negative breast cancer (TNBC) patients with very poor prognosis and may represent a new treatment strategy [58]. Manoharan et al. revealed that the STAT3 protein is continuously activated in tumor cells and therefore can be

studied as a strong target for cancer prevention. For this purpose, the best 10 inhibitors were selected from 191 selected inhibitor compounds from the SELLECK database using molecular dynamics simulation method and were nominated to target the SH2 domain of STAT3 [57]. In addition, STAT3 SH2 inhibitor STATTIC significantly reduced the growth of HNSCC (head and neck squamous cell carcinoma) tumors in a mouse orthotopic xenograft and analysis of tumor lysates confirmed the decrease of STAT3 phosphorylation [108]. Another study showed that subcutaneous injection of STAT3 SH2 inhibitor STATTIC into mouse xenografts of human colorectal cancer significantly increased chemo/radiotherapy sensitivity and reduced tumor progression [109]. Considering the role of Syk in cancer and other diseases, it seems to act as a "hub" together with different signaling pathways. For this reason, targeting this protein is necessary and important. In the chapter, the aim is to inhibit protein-protein interactions by targeting the SH2 domains of Syk. Our motivation for this study is the fact that Syk protein is at the intersection of important signaling pathways that play a role in the pathogenesis of AML, and therefore, Syk may be a potential target for AML treatment. Many studies suggest that inhibition of Syk may inhibit leukemic growth and pave the way for cancer-specific treatments.

3.1.5 Purpose of the Chapter

In this chapter, we aimed to investigate the cytotoxic effects of targeting the C-SH2 domain to disrupt Syk enzyme activity on AML cells. HL-60 and THP-1 AML cells were selected for the study because they are the cells with the highest Syk expression levels according to the Human Protein Atlas Database. The data show that HL-60 and THP-1 have nTPM (Transcripts Per Million) of 107.5 and 77.9, respectively. This study is the first to study SH2 inhibition using HL-60 and THP-1 cells, demonstrating the originality and innovative approach of the study. We assume that finding new targets for the SH2 domain of Syk enzyme will reveal a new therapeutic approach for AML patients by disrupting protein-protein interactions. Cases of multidrug resistance to drugs and low treatment response to chemotherapeutic agents reveal the need for new and more effective therapeutic approaches for AML. Here, we propose a new strategy for AML patients. We also think that the study may provide an insight into the molecular mechanisms leading to the pathogenesis of AML. In this context, it is hoped that inhibition by targeting the SH2 domains of Syk enzyme will open the door to a more specific treatment resulting in the elimination of AML.

3.2 Methodology

3.2.1 Chemicals

The chemicals used within the scope of the chapter are as follows: RPMI medium (Diagnovum, D840), FBS (Gibco, A5256801), Penicillin/streptomycin (Gibco, 15140-122-100ml), Inhibitors were dissolved in DMSO and their stocks were prepared as 1 mM stock and stored at -20°.

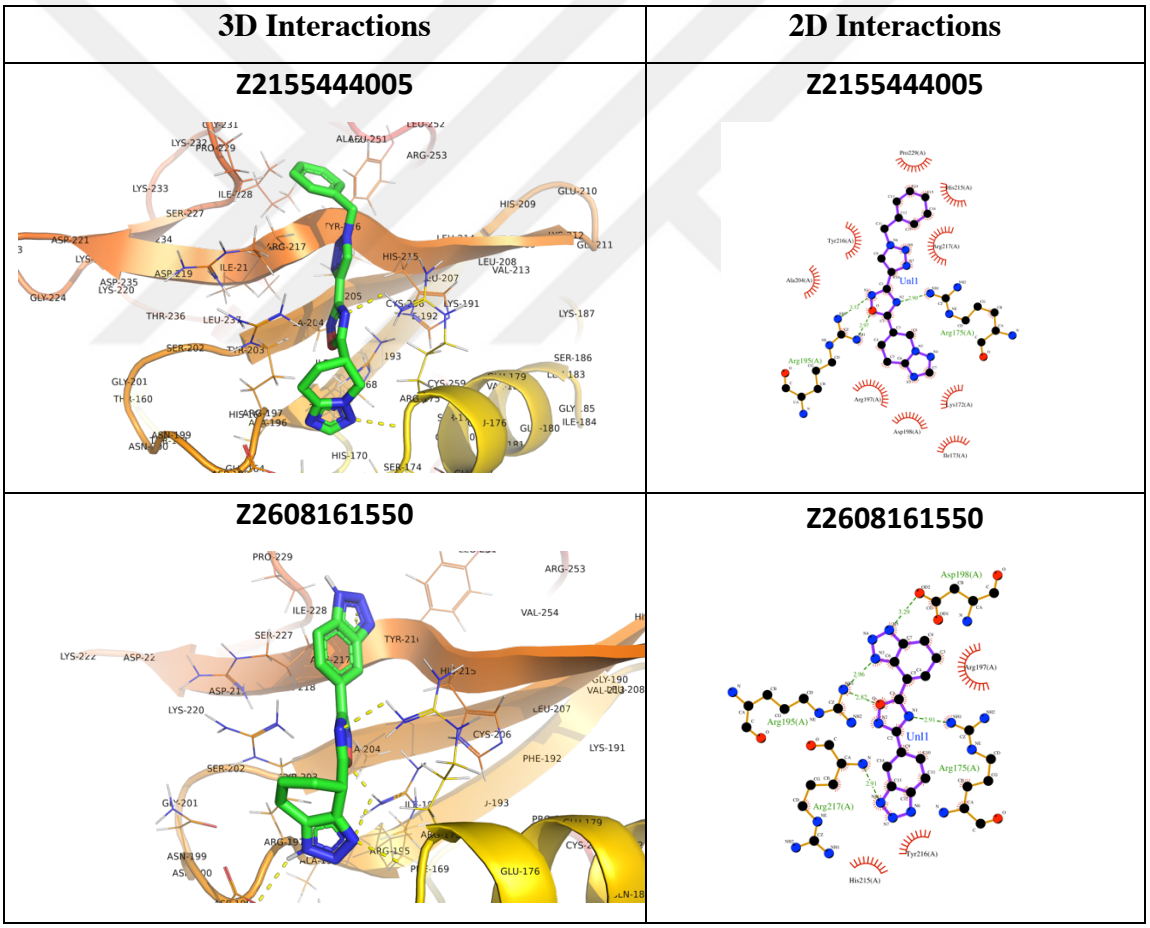


Figure 3.1 2D and 3D structures of the two selected candidate compounds and their interaction with the C-SH2 domain (Arg175, Arg195, Arg217) are shown with the distance between the atoms in angstroms (Å).

MTT solution (Sigma Aldrich, M2128), DMSO (Panreacapplichem, 67-68-5-250 ml), Propidium Iodide staining solution (Cayman, 10008351) Triton-X (Merck Millipore,

1.08603.1000), RNase (Sigma Aldrich, R5503). The following experimental kits were used in the chapter: ElabScience E-CK-A211 Annexin V-FITC/PI Apoptosis Kit, EZ-10 SPIN COLUMN TOTAL RNA MINI-PREPS KIT, (Biobasic Canada, BS1361), BlasTaq 2X qPCR MasterMix, (G891, Abmgood). OneScript® Plus cDNA Synthesis Kit (G236, Abmgood), NucleoSpin® RNA Set for NucleoZOL™ (Macherey nagel, 740406.50).

3.2.2 Cell Culture

THP-1 and HL-60 AML cell lines were maintained and grown using RPMI medium (Diagnovum, D840) supplemented with 10% FBS and 100 U/mL penicillin/streptomycin and incubated at 37°C with 5% CO_2. THP-1 and HL-60 cells were seeded in $5x10^6$ cells/10 mL/96mm x 21mm tissue culture plates. When they reached 60-70% confluency, cells were passaged every 2-3 days. Collected cells were centrifuged at 700 rpm for 5 minutes. Following the centrifugation step, the supernatant was removed and the cell pellet was dissolved with fresh medium. Cells were seeded in 100 mm tissue culture plates (Axycell, 704-001).

3.2.3 *In vitro* Cell Viability Assay

Cell proliferation assay was used to determine the cytotoxic effects of two Syk-CSH2 candidate inhibitors, Z2608161550 and Z2155444005, which were previously determined by *in silico* studies, on THP-1 and HL-60 AML cell lines. After drug application, cell proliferation was calculated by 3-(4,5-dimethylthiazol-2-yl)-2,5-diphenyl-2H-tetrazolium bromide Cell Viability Assay (MTT). MTT assay is a colorimetric assay and is used to calculate and determine cellular viability (growth and survival). For this purpose, relevant inhibitors were added to 10,000 cells and incubated for 48 hours. At the end of incubation, 10 µl of MTT reagent was added to each well and incubated for 2 hours at 37°C in an incubator containing 5% CO_2. At the end of the incubation period, 96-well plates were centrifuged at 1800 rpm for 10 minutes and the formed formazan crystals were dissolved with 100 µl dimethylsulfoxide (DMSO). The plates were incubated on a shaker for 15 minutes to homogenize the formazan crystals and DSMO mixture, and then formazan concentrations were measured by absorbance at 570 nm wavelength in a spectrophotometer with a Varioskan™ LUX multi-mode microplate reader (Thermo Scientific™).

According to the spectrophotometric results, cell proliferation graph was created and the concentrations of GI10, GI20, GI30 and GI50 (inhibiting cell growth by 10%,

20%, 30% and 50%) were calculated for the indicated inhibitors. As a result, the cytotoxic effects of the relevant agents on both cell lines were determined [110]. GI20 and GI50 values obtained from these experiments were used as inhibitor concentrations in the subsequent work packages.

3.2.4 Cell Death Assay

THP-1 and HL-60 AML cells were treated separately with Z2608161550 and Z2155444005, and the amounts and localization of phosphatidyl serine were determined by flow cytometry using the Annexin V/Propidium iodide double staining method. For this purpose, $1x10^5$ cells were incubated with inhibitors for 48 hours. After 48 hours of incubation with drugs, cells were collected and then centrifuged at 300 g for 5 minutes at 4°C. Cells were washed twice with 1XPBS and centrifuged after each wash. After the last wash, PBS was removed and the cell pellet was dissolved in 500 µl of 1X Annexin binding solution (diluted 1:10 with ultrapure water). Then, 2 µl Annexin V and 4 µl propidium iodide were added to this mixture and incubated for 15 minutes at room temperature in the dark. Control cells that were not exposed to any treatment were dissolved in 400 µl 1X binding buffer and divided into PI+ /FITC+, PI- /FITC-. Samples were mixed with vortex and incubated for 15 minutes at room temperature in the dark. Then, cells were analyzed on BD LSRFortessa (Becton Dickinson) flow cytometry [110].

3.2.5 Cell Cycle Assay

In THP-1 and HL-60 cells treated with Z2608161550 and Z2155444005, cell cycle analyses were performed using flow cytometry [110]. $1x10^6$ cells were incubated with the relevant inhibitor for 48 hours. At the end of 48 hours, cells were collected and centrifuged at 260 G for 10 minutes at 4 °C. After centrifugation, the supernatant was removed and the cells were lysed with 1 mL of cold 1XPBS. After centrifugation at 260 G for 10 minutes at 4 °C, the supernatant was discarded and the pellet was washed with 1 mL of 1XPBS twice. After centrifugation, cells were lysed with 1 mL of cold 1XPBS and 4 mL of cold ethanol (70%) was added to the centrifuge tube. The mixture contained cells and PBS and the added ethanol was homogenized by vortexing. The mixture was incubated overnight at -20 °C for cell fixation. After 24 h of incubation, cells were centrifuged at 260 G for 10 min at 4 °C and the supernatant was completely removed. Cells were solubilized with 1 mL of cold 1XPBS and centrifuged at 260 G for 10 min at 4 °C, the supernatant was discarded after centrifugation. The pellet was homogenized

with a mixture of 1 mL of 0.1% Triton-X (Merck Millipore 1.08603.1000) and 100 µL of RNase (200µg/mL) (Sigma R5503) in 1XPBS and incubated at 37 °C for 30 min in the dark. Samples were individually added with 25 µL of PI (1 mg/mL) and stained with untreated control PI. After 15 min of incubation at room temperature, samples were analyzed with the BD FACSAria III Cell Analyzer flow cytometer.

3.2.6 Real-Time Polymerase Chain Reaction (RT-PCR)

In THP-1 and HL-60 cells treated with Z2608161550 and Z2155444005, TNF-α and IL-1β mRNA levels were measured by Real-time Polymerase Chain Reaction (RT-PCR) method. For this purpose, cells were first treated with candidate inhibitors for 48 h and RNA was extracted using EZ-10 SPIN COLUMN TOTAL RNA MINI-PREPS KIT, (Biobasic Canada, BS1361). However, nanodope results showed that there was genomic DNA contamination and RNA concentration was low. Therefore, RNA was isolated as B strand with NucleoSpin® RNA Set for NucleoZOL™ (Macherey nagel, 740406.50). cDNA synthesis was performed using OneScript® Plus cDNA Synthesis Kit (G236, Abmgood) from a concentration of 1µg total RNA, and PCR was performed at an annealing temperature of 62.5°C for TNF-α (Tumor Necrosis Factor Alpha) and IL-1β (Interleukin 1 Beta) for 32 cycles. For quantitative SYBR-Green real-time PCR, samples were run in duplicate at 3.5 µl cDNA per well and detected using the CFX Connect Real-Time PCR Detection System (BIORAD). Expression in cDNA samples was assessed using SYBR-green labeling. The results obtained were normalized to 18s RNA, and relative quantification was assessed by the comparative threshold cycle method. mRNA gene expression was presented as fold increase calculated relative to untreated cells after normalization against 18S RNA[111].

Table 3.5 Primers for RT-PCR

Gene Name	Forward Primer	Reverse Primer
IL-1β	5'-GGCATCCAGCTACGAATCTC-3'	5'-TCGTTATCCCATGTGTCGAA-3' [112]
TNF-α	5'-AGGCAGTCAGATCATCTTC-3'	5'-TTATCTCTCAGCTCCACG-3' [113]
18S RNA	5'AAACGGCTACCACATCCAAG'3	5'CCTCCAATGGATCCTCGTTA'3 [114]

3.2.7 Western Blotting Assay

The cells were seeded into 6-well plates with a density of $5x10^6$ cells/mL and treated with the above-mentioned drugs for 48 hours. Then, the cells were harvested and lysed in 1X RIPA lysis buffer (50 mM Tris-HCl, pH 8.0, with 150 mM sodium chloride, 1.0% Igepal CA-630 (NP-40), 0.5% sodium deoxycholate, and 0.1% sodium dodecyl sulfate) including the protease (cat no: A32925, Thermo Scientific™) and phosphatase inhibitors (cat no: A32957, Thermo Scientific™). Total protein concentration was determined by the DC Protein quantification Kit (cat no: 5000111, Biorad). The whole cell lysates were loaded at a protein concentration of 20 µg per well, separated by SDS-Gel electrophoresis (10-12% acrylamide gel) and transferred to PVDF membrane for 7 min by using Trans-Blot Turbo Transfer System (Biorad). The membrane was blocked by using 5% dried milk in 1X TBST buffer (5M NaCI, 2M Tris pH 7.5 and 10% Tween20) for 1h at room temperature. After the membrane was incubated overnight at 4 ^oC with primary antibodies, it was incubated with secondary antibody for 1h at room temperature. The signal was detected by PierceTM ECL Western Blotting Substrate with ChemiDocTM (Biorad). Protein quantification was analyzed via Image Lab Software (Biorad). In western blotting following antibodies were used; LC3B (Cell Signaling) and GAPDH (Cell Signaling).

3.2.8 Statistical analyses

Results are presented as mean ± standard deviation (SD). Statistical analyses were performed using two-way ANOVA for inhibitor treatments for cell lines. The significance level was set at $P < 0.0001$. Statistical significance was determined using a one-way analysis of variance (ANOVA) for Dunnett's assay compared to untreated controls for cell cycle analyses.

3.3 Results and Discussion

3.3.1 Antiproliferative Effects of Candidate Syk-SH2 Enzyme Inhibitors Z2608161550 and Z2155444005 on THP-1 and HL-60 Cells

The binding affinity of 1,368,049 compounds in the Enamine High Throughput Screening (HTS) collection to the SH2 domains of the Syk protein was determined and molecular simulation dynamics (MD) determination of 9 candidates selected among the compounds with high binding affinity was performed. According to the results, in order to determine the biological activities of Z2608161550 and Z2155444005 with the best binding energy and MD on HL-60 and THP-1, their antiproliferative effects were first examined by MTT cell viability test. For this purpose, firstly, dose optimizations of Z2608161550 and Z2155444005 were made in THP-1 and HL-60 cell lines. Then, cell proliferation graphs were determined for both cell lines with 3 independent experiments in the appropriate dose range, respectively (Figure 3.2). At the end of this study, it was observed that both Z2608161550 and Z2155444005 were effective at low micromolar concentrations (1-25 μM) on both cell lines. We treated THP-1 and HL-60 AML cell lines by increasing the drug concentration (1-25 μM) for 48 hours. Our results showed that both drug candidates successfully reduced the proliferation of cells at a statistically significant level in a dose-dependent manner for 48 hours (Figure 3.2). The growth percentage concentrations that inhibited cell growth by 10, 20, 30 and 50% were calculated using GraphPad Prism 8 and are given in Table 3.6.

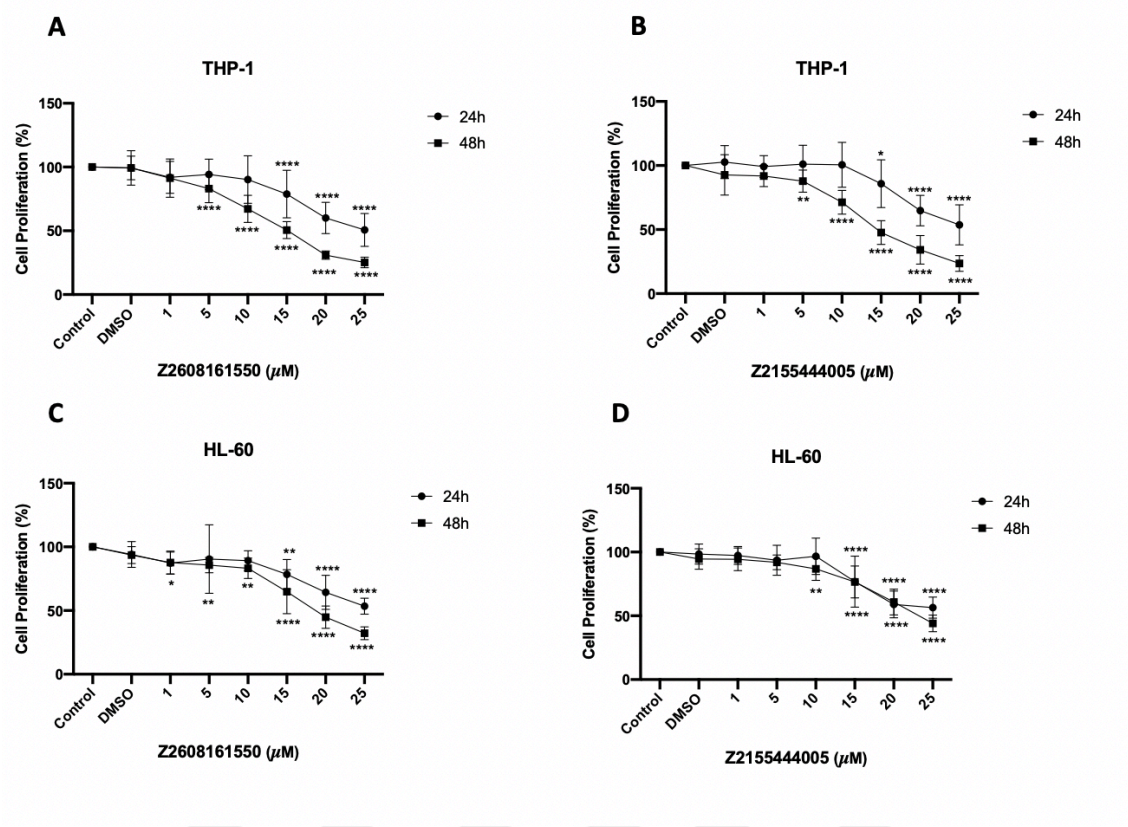


Figure 3.2 Effects of Z260816155 and Z2155444005 on the proliferation of THP-1(A-B) and HL-60 (C-D) cells. Standard deviation was done on the number of replicates of 3 wells per treatment and the experiment was repeated 3 times independently (n = 3). Statistical analyses were performed by two-way ANOVA. The significance level was set at $P < 0.0001$. All data are presented as mean ± s.d. Calculations were performed using GraphPad Prism 8.

Table 3.6 Percentage Concentrations of Z260816155 and Z2155444005 that Inhibited Cell Growth by 10, 20, 30 and 50%.

	THP-1	
	Z2608161550 (μM)	**Z2155444005 (μM)**
GI50	12.78	12.26
GI10	6.919	6.926
GI20	8.678	8.551
GI30	10.09	9.836
	HL-60	
	Z2608161550 (μM)	**Z2155444005 (μM)**
GI50	13.87	15.36
GI10	7.99	8,421
GI20	9.794	10.51
GI30	11.21	12.18

3.3.2 Effects of Candidate Syk-SH2 Enzyme Inhibitors Z2608161550 and Z2155444005 on Apoptotic Cell Death in THP-1 and HL-60 Cells

Syk enzyme has a complex role in the apoptosis process, playing both pro-apoptotic and anti-apoptotic roles depending on the cell type, cellular context and environmental stimuli[115]. Syk has been observed to be constitutively active or overexpressed in many B-cell malignancies (e.g., chronic lymphocytic leukemia (CLL), diffuse large B-cell lymphoma (DLBCL), mantle cell lymphoma) [116], [117]. In these cases, Syk contributes to the escape of apoptosis and the development of resistance to chemotherapy in cancer cells. Syk supports tumor progression by providing a continuous survival signal in these cells. Therefore, it is important to investigate the effects of Z260816155 and Z2155444005 on apoptotic cell death in THP-1 and HL-60 cells. For this purpose, we treated THP-1 and HL-60 cell lines with different doses of relevant inhibitors for 48 hours and evaluated apoptotic cell death by Annexin-V double staining method using flow cytometry. Our results showed that GI50 value and 18 μM Z260816155 concentration caused 2-fold and 4-fold increase in apoptotic cell death compared to control cells, respectively. Moreover, there was a 5-fold increase in late apoptotic cell death in THP-1 cells compared to untreated control at 18 μM Z260816155 concentration. Similarly, 18 μM Z2155444005 concentration increased apoptotic cell death approximately 5-fold compared to control cells (Figure 3.3). On the other hand, HL-60 cells significantly increased apoptosis compared to control cells after 25 μM concentration for both drugs (Figure 3.4). However, an approximately 5-fold increase in the amount of early apoptotic cells was observed in HL-60 cells treated with 20 μM and 25 μM Z260816155. In conclusion, both inhibitor candidates caused dose-dependent changes in the amount of total apoptosis in both cells.

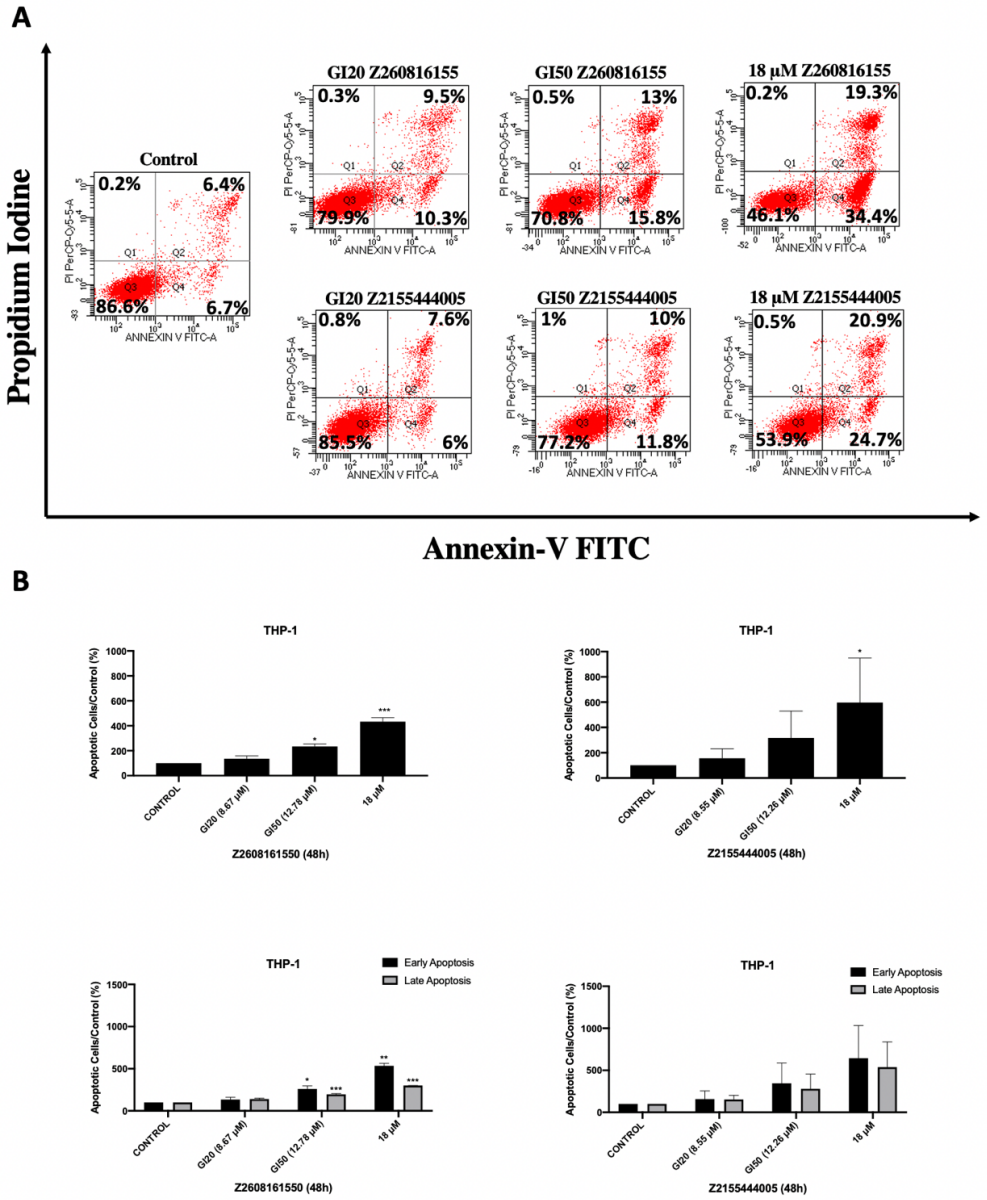


Figure 3.3 Effect of Z260816155 and Z2155444005 on THP-1 cell death. Stained cells were analyzed by flow cytometry to determine the percentage of apoptotic cells. Representative histograms are shown (A). Cells in the lower right (Q4; Annexin V-FITC+/PI−) and upper right (Q2; Annexin V-FITC+/PI+) quadrants indicate early and late apoptosis, respectively. The graphs in the lower panel (B) showed the percentages of apoptotic cells. The upper graph shows the total number of apoptotic cells (Q2+Q4), while the lower graph shows the early (Q4) and late (Q2) apoptotic cell populations separately. Statistical analyses were performed using two-way ANOVA. (ns=P > 0.05, *= P≤ 0.05, **= P ≤ 0.01, ***= P ≤ 0.001, ****= P≤ 0.0001).

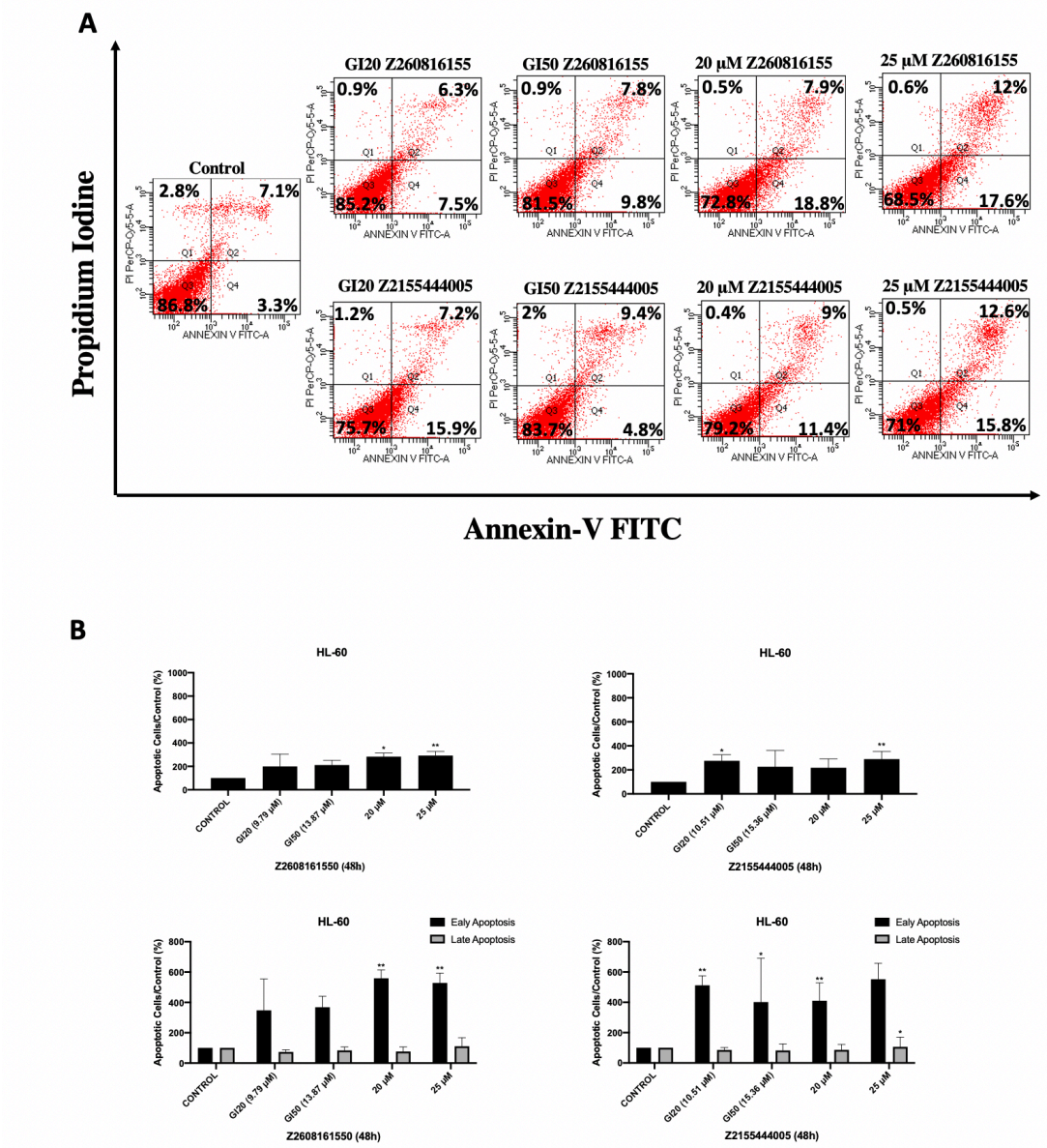


Figure 3.4 Effect of Z260816155 and Z2155444005 on HL-60 cell death. Stained cells were analyzed by flow cytometry to determine the percentage of apoptotic cells. Representative histograms are shown (A). Cells in the lower right (Q4; Annexin V-FITC+/PI−) and upper right (Q2; Annexin V-FITC+/PI+) quadrants indicate early and late apoptosis, respectively. The graphs in the lower panel (B) showed the percentages of apoptotic cells. The upper graph shows the total number of apoptotic cells (Q2+Q4), while the lower graph shows the early (Q4) and late (Q2) apoptotic cell populations separately. Statistical analyses were performed using two-way ANOVA. (ns=P > 0.05, *= P≤ 0.05, **= P ≤ 0.01, ***= P ≤ 0.001, ****= P≤ 0.0001).

3.3.3 Effects of Candidate Syk-SH2 Enzyme Inhibitors Z2608161550 and Z2155444005 on Cell Cycle in THP-1 and HL-60 Cells

It has been shown that Syk plays various roles at different stages of the cell cycle and these roles are generally mediated by the signaling pathways and target proteins it interacts with. In many cell types, especially in immune cells such as B lymphocytes, Syk is known to promote the transition from G1 to S phase [118]. Activated by stimulation of receptors such as the B cell receptor (BCR), Syk triggers downstream signaling pathways such as PI3K/Akt and MAPK/ERK [116]. These pathways increase the expression and activity of cyclin D (especially cyclin D2 and D3) and cyclin E, which play important roles in the G1 phase. Cyclin D-CDK4/6 and cyclin E-CDK2 complexes phosphorylate and inactivate retinoblastoma protein (Rb). Inactivation of Rb results in the release of E2F transcription factors and the initiation of transcription of genes required for S phase (e.g. DNA polymerase, thymidine kinase). Syk can also facilitate the G1/S transition by reducing the levels or activities of CDK inhibitors p27Kip1 and p21Cip1[119], [120]. Therefore, we wanted to investigate the effects of drug candidates on the cell cycle distribution of THP-1 and HL-60 cell lines. For this purpose, we treated cells with both drugs for 48 hours and analyzed the results by flow cytometry. We observed that Z260816155 and Z2155444005 caused G0/G1 phase arrest in THP-1 cells after application of GI20 and 18 μM drug concentrations (Figure 3.5). On the other hand, Z260816155 caused S phase arrest in HL-60 cells, while Z2155444005 at 25 μM caused G0/G1 phase arrest in HL-60 cells compared to the control (Figure 3.6). These data suggest that candidate inhibitors may have a significant effect on cell cycle arrest for both AML cells. In particular, the knowledge that Syk promotes the transition from G1 to S phase supported our findings of G0/G1 phase arrest in our cells.

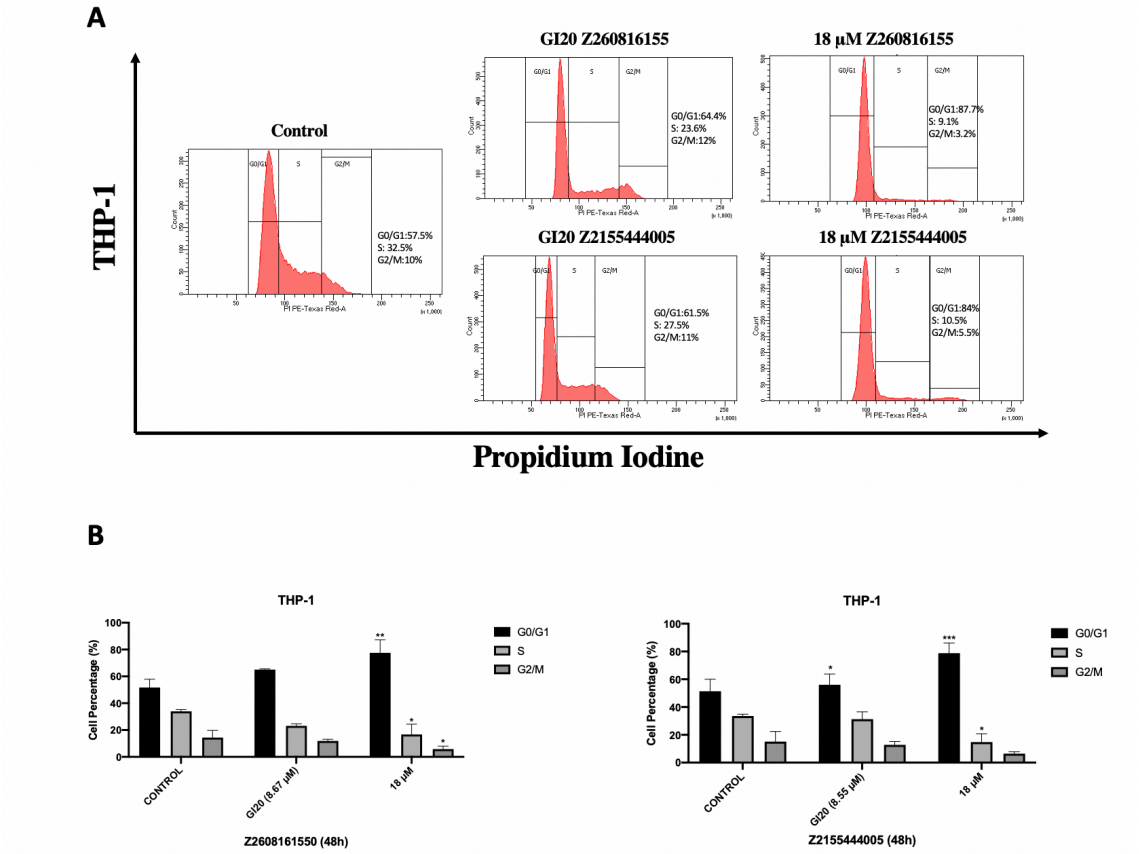


Figure 3.5 Effect of Z260816155 and Z2155444005 on THP-1 cell cycle progression. Inhibitors were applied to THP-1 cells for 48 h, cells were collected, fixed, and stained with propidium iodide. Cells were then analyzed by flow cytometry. Three independent experiments were performed, combined and analyzed. Statistical analyses were performed using two-way ANOVA. (ns=P > 0.05, *= P≤ 0.05, **= P≤ 0.01, ***= P≤ 0.001, ****= P≤ 0.0001).

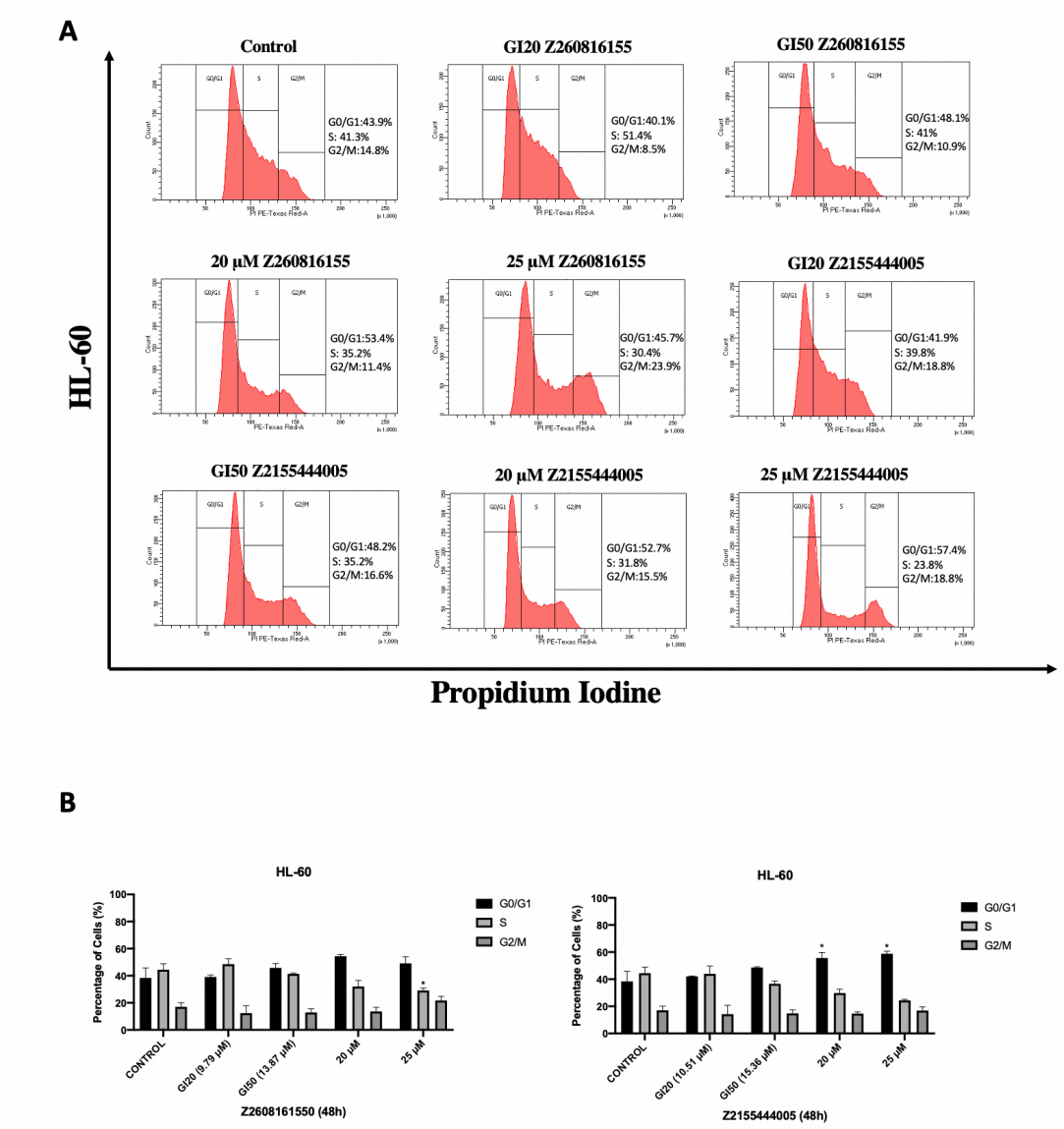


Figure 3.6 Effect of Z260816155 and Z2155444005 on HL-60 cell cycle progression. Inhibitors were applied to HL-60 cells for 48 h, cells were collected, fixed, and stained with propidium iodide. Cells were then analyzed by flow cytometry. Three independent experiments were performed, combined, and analyzed. Statistical analyses were performed using two-way ANOVA. (ns=P > 0.05, *= P≤ 0.05, **= P ≤ 0.01, ***= P ≤ 0.001, ****= P≤ 0.0001).

3.3.4 Effects of Candidate Syk-SH2 Enzyme Inhibitors Z2608161550 and Z2155444005 on Nuclear Factor-B (NF-κB) Related Genes in THP-1 and HL-60 Cells

Nuclear Factor-B (NF-κB) is known as a transcription factor that regulates the gene expression of cytokine receptors and adhesion molecules, and also controls cell apoptosis, adaptive immunity, cell growth, and senescence [121]. The NF-κB signaling pathway is induced by TLR4 with the upstream molecules, Syk and Src tyrosine kinases, being sequentially activated. As a result of Syk and Src activation, NF-κB signaling molecules,

including phosphoinositide-3-kinase (PI3K)/p85, phosphoinositide-dependent kinase-1 (PDK1), protein kinase B (Akt), IκB kinase (IKK)α/β, and IκBα are phosphorylated, and the phosphorylation of these molecules is required for the trafficking of transcriptional factors to the nucleus [122]. Activated NF-κB upregulates the gene expression of many chemokines, including TNF-α and IL-1β [121]. TNF-α expression has been shown to be associated with a higher rate of blasts, extramedullary infiltration, and poor prognosis in AML [123], [124]. It has been demonstrated that the levels of IL-1β and IL-1 receptors are increased in AML patients, and silencing of the IL-1 receptor leads to significant suppression of clonogenicity and disease progression *in vivo* [113]. Syk enzyme is involved in the activation of the NF-κB signaling pathway [125], and many studies have also demonstrated that impaired NF-κB pathway causes the development of AML [123]. The relationship between NF-κB and both the Syk enzyme and the pathogenesis of AML reveals the importance of examining the NF-κB pathway [126]. In this context, the effects of inhibiting the activity of Syk on the level of TNF-α and IL-1β mRNA gene expression via the NF-κB pathway, which has an important role in the pathogenesis of AML, were examined. The results showed that Z260816155 and z2155444005 significantly reduced both TNF-α and IL-1β mRNA gene expression in THP-1 cells at increasing doses (Figure 3.7A and Figure 3.7B). On the other hand, there was a significant decrease in TNF-α mRNA gene expression level in HL-60 cells treated with GI20 (9.79 μM) and 25 μM Z260816155 (Figure 3.7C). A significant decrease in IL-1β mRNA gene expression level was observed in HL-60 cells treated with GI50 (13.87 μM) and 25 μM Z2155444005 (Figure 3.7C). Interestingly, a decrease in TNF-α and IL-1β mRNA gene expression was observed in HL-60 cells treated with GI20 and GI50 value of z2155444005, while increasing the dose by 25 μM reversed the decrease in TNF-α and IL-1β mRNA gene expression levels compared to GI20 and GI50 of z2155444005 (Figure 3.7D). This may indicate that the drugs are dose-dependent. In particular, the fact that Z260816155 caused a decrease in TNF-α and IL-1β mRNA gene expression levels with increasing dose is an important finding in terms of our results. In conclusion, our experiments showed that different biological regulations in two AML cells with different genetic mutations may lead to different responses to the same inhibitors.

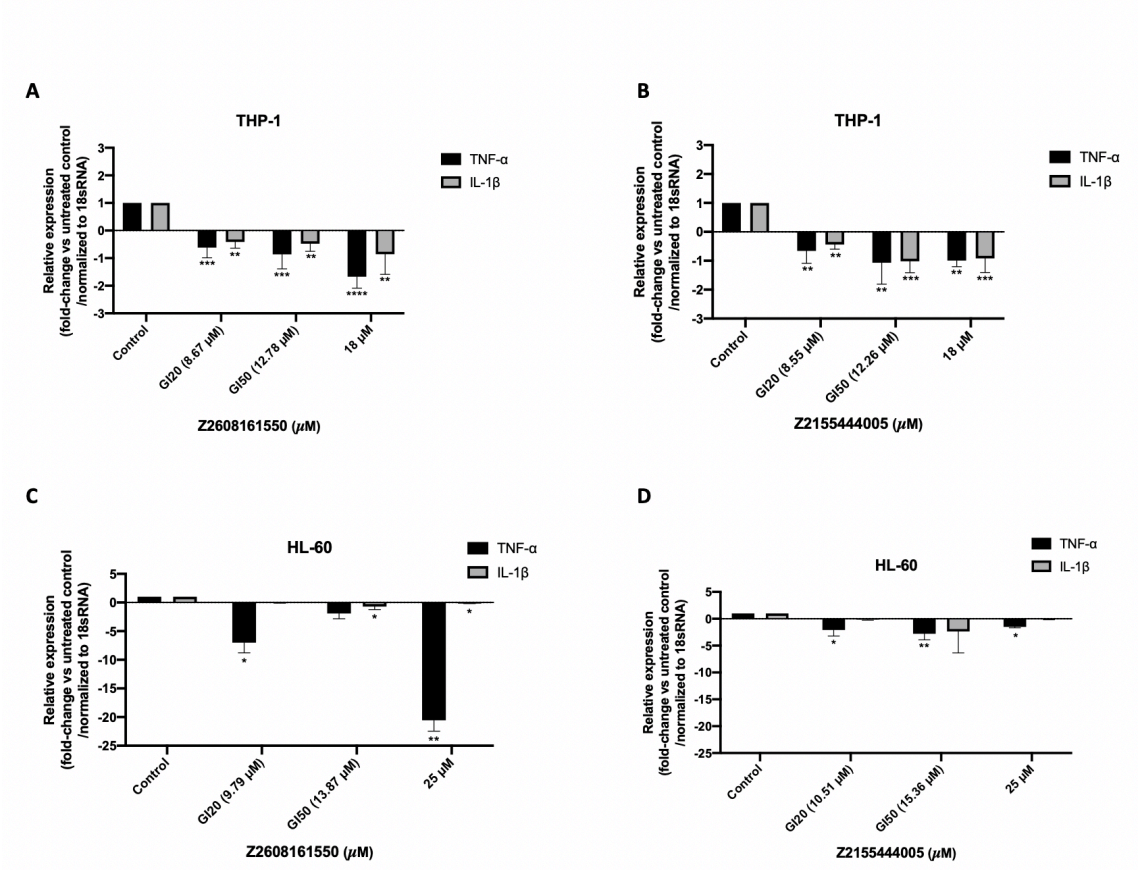


Figure 3.7 Measurement of the effects of Z260816155 and Z2155444005 on NF-κB related TNF-α and IL-1β genes in THP-1 and HL-60 cells via changes in mRNA expression levels. RT-PCR analysis shows the changes in the relative expression of TNF-α and IL-1β genes compared to the reference (housekeeping) 18s RNA gene. Fold change of each gene of interest was calculated by Quigen, Genelglobe (n=3). Statistical analyses were performed using two-way ANOVA. (ns=P > 0.05, *= P≤ 0.05, **= P ≤ 0.01, ***= P ≤ 0.001, ****= P≤ 0.0001).

3.3.5 Investigation of the effects of Syk-CSH2 domain inhibitors Z2608161550 and Z2155444005 on apoptotic proteins by Western Blotting

Constitutive Syk activity can drive cellular proliferation and resistance to apoptosis by activating key downstream pathways, including PI3K/Akt and NF-κB. These pathways converge on the transcriptional regulation of anti-apoptotic proteins, most notably the B-cell lymphoma 2 (Bcl-2) family [115]. Proteins such as Bcl-2 and Bcl-xL are pivotal gatekeepers of the intrinsic apoptotic pathway, and their overexpression is a common mechanism by which cancer cells evade cell death. Therefore, it is hypothesized that the pharmacological inhibition of Syk will disrupt this pro-survival axis, leading to

the transcriptional repression and subsequent downregulation of Bcl-2 and Bcl-xL protein levels, thereby sensitizing cells to apoptosis. To investigate the impact of Syk inhibition on key anti-apoptotic regulators, THP-1 cells were treated with Z260816155 and Z2155444005, at increasing concentrations. The protein expression levels of Bcl-2 and Bcl-xL were subsequently assessed by Western Blot analysis. The results indicated that treatment with both Z260816155 and Z2155444005 induced a clear, dose-dependent reduction in the expression of Bcl-2 protein (Figure 3.8 A, B1). This finding strongly indicates that the expression of Bcl-2 in THP-1 cells is highly dependent on constitutive Syk signaling. The effective suppression of Bcl-2 by both inhibitors validates the hypothesis that targeting Syk disrupts a critical survival pathway mediated by this anti-apoptotic protein. On the other hand, the results suggested that a slight reduction in Bcl-xL levels upon treatment with Z260816155, whereas a clear effect was not apparent for Z2155444005 (Figure 3.8 A, B2). These data suggest that Bcl-xL expression in THP-1 cells is less sensitive to Syk inhibition than Bcl-2 expression. This differential regulation may imply that Bcl-xL is co-regulated by Syk-independent pathways or that the transcriptional and post-transcriptional control of BCL2L1 (the gene encoding Bcl-xL) is distinct from that of BCL2 in this cellular context.

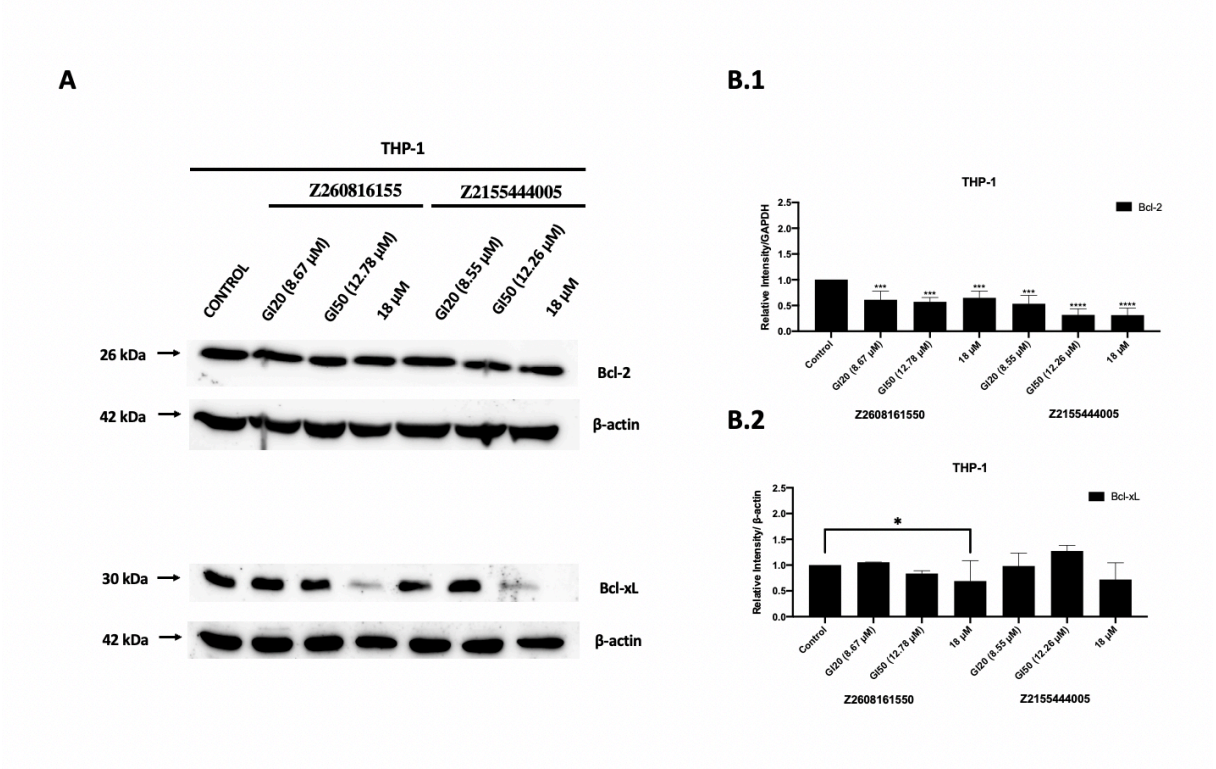


Figure 3.8 Immunoblot analysis of Bcl-2 and Bcl-xL in Thp-1 cells in response to treatment with increasing dosages Z2608161550 and Z2155444005 for 48 hours. The

relative density of proteins after normalization with β-actin is plotted. The untreated negative control group was taken as 1.0 and the drug-treated groups were compared to the negative control, and the fold difference was indicated in panel B.

3.3 Conclusion

Syk has been identified as a cytoplasmic, non-receptor protein tyrosine kinase that plays a central role in immune receptor signaling primarily in hematopoietic cells [3]. Its functions include B cell development, differentiation, antibody production, and activation of other immune cells such as mast cells and macrophages [5], [6]. However, recent studies have revealed that Syk extends beyond these traditional roles to perform surprisingly complex and often opposing functions in cancer biology, including a wide variety of solid tumors. In the context of cancer, Syk acts as a double-edged sword; in some cancers it plays an oncogenic role, promoting tumor growth, cell survival, and metastasis, while in others it acts as a tumor suppressor, inhibiting cell proliferation, inducing apoptosis, and inhibiting angiogenesis [115]. This dual nature makes Syk a challenging and attractive molecule in cancer research and in the development of targeted therapy strategies. Many studies have reported that overexpression or activation of Syk is associated with poor prognosis and increased drug resistance AML subtypes [14], [101], [102]. Syk contributes to cancer progression by activating survival and proliferation pathways such as PI3K/Akt/mTOR and NF-κB, as well as by integrating survival signals from the microenvironment. Therefore, the strategy of targeting Syk is particularly attractive for the treatment of leukemia types such as AML. However, although some inhibitors targeting the kinase domain of Syk have been found in the literature, the SH2 domain has not been targeted before. When looking at the literature, recent studies suggested in cancer treatment methods to prevent the activation of abnormal protein that leads to cancer have revealed that SH2 domains are also an important target in addition to active kinase domains [57], [58], [59], [60], [61]. For this purpose, the binding affinity of the compounds from Enamine High-Throughput Screening (HTS) collection, comprising 1,368,049, to the SH2 domains of the Syk protein was determined and molecular simulation dynamics (MD) determination of 9 candidates selected from the compounds with high binding affinity was performed. According to the results, the biological activities of Z2608161550 and Z2155444005, which have the best binding energy and MD, on HL-60 and THP-1 were determined for the first time in this project.

Our results revealed that both candidate drugs statistically significantly reduced cell viability in THP-1 and HL-60 cells at low micromolar levels (25 μM). These results particularly paved the way for other biological activity tests to be conducted and the GI values determined here were later used for further studies in the study.

Especially considering that Syk triggers downstream signaling pathways of the PI3K/Akt pathway [116], PI3K/Akt signaling prevents the expression of pro-apoptotic proteins, reduces tissue apoptosis and increases the survival rate of cancer cells [127], [128]. Therefore, Syk inhibition is expected to increase apoptosis in line with this situation. According to our results, the candidate inhibitors induced apoptosis in a dose-dependent manner, consistent with the above network. Syk kinase inhibitors such as fostamatinib, entospletinib, TAK-659, serdulatinib, RO9021, BAY 61-3606 consistently shows concentration-dependent anti-proliferative effects in primary AML cells and AML cell lines and have been shown to induce apoptosis [14], [29], [129]. Our results are consistent with kinase inhibitors.

Disruptions in cell cycle checkpoints may provide growth and survival advantages to cancer cells. Therefore, it is important to control the effects of candidate inhibitors on the cell cycle. It was shown that Z260816155 and Z2155444005 caused G0/G1 phase arrest in THP-1 cells after application of GI20 and 18 μM drug concentrations (Figure 3.5), while Z260816155 caused S phase arrest in HL-60 cells, Z2155444005 at 25 μM resulted in G0/G1 phase arrest in HL-60 cells compared to the control (Figure 3.6). Studies have shown that Syk inhibition blocks the G1-S transition and causes cell cycle arrest in DLBHL cells. It was found that the effect of Syk inhibition on PLCγ2 and AKT rather than ERK1/2 is responsible for cell cycle arrest. This suggests that Syk relies on specific downstream signaling pathways to regulate G1/S progression [118]. In addition, studies have shown that Syk depletion by RNA interference or treatment with a chemical Syk inhibitor prevented nocodazole-treated B-lineage lymphoid and non-lymphohematopoietic cells from activating the G2 checkpoint via CDC25C S216 phosphorylation, resulting in polyploidy [130]. These results may be explained by the cancer-specific role of Syk.

Considering the role of Syk enzyme in the activation of NF-κB signaling pathway [123], [125] and the relationship between NF-κB pathway disorders and AML development [123], it is of great importance to examine this pathway [126]. Accordingly, the effects of inhibiting Syk activity on TNF-α and IL-1β mRNA gene expression levels via NF-κB pathway, which plays a critical role in AML pathogenesis, were investigated.

Our results showed that Z260816155 and Z2155444005 caused a statistically significant decrease in TNF-α and IL-1β mRNA gene expression levels, especially in THP-1 cells, depending on the increasing dose. On the other hand, there was an approximately 20-fold decrease in the level of TNF-α mRNA gene expression in HL-60 cells treated with 25 μM Z260816155. While a decrease in both TNF-α and IL-1β mRNA gene expression was observed in HL-60 cells treated with GI20 and GI50 values of Z2155444005 (3.7D), increasing the dose by 25 μM reversed the decrease in TNF-α and IL-1β mRNA gene expression levels. This may indicate that the candidate inhibitors do not affect the biological activities differently depending on the dose. Studies have shown that one-hour treatment of THP-1 cells with 10 μmol/L Syk kinase inhibitor R406 caused a significant decrease in the expression of adhesion molecule ICAM-1, proinflammatory cytokines TNF-α and IL-1β, and phosphorylated signaling proteins ERK2, JNK, p-38, and IκBα, and significantly reduced the release of TNF-α in infected H292 cells [131]. Studies have also shown that R406 significantly inhibited IL-1β gene expression [132]. These results highly support our results.

This study tested the hypothesis that Syk kinase activity promotes cell survival by upregulating the anti-apoptotic proteins Bcl-2 and Bcl-xL. To this end, THP-1 cells were treated with two different Syk inhibitors, Z260816155 and Z2155444005. The results demonstrated that both inhibitors potently decreased Bcl-2 protein levels in a dose-dependent manner. This finding confirms that Bcl-2 expression in THP-1 cells is highly dependent on the Syk signaling pathway.

In contrast, the effect on Bcl-xL was weaker and inconsistent. This suggests that in these cells, Bcl-xL is co-regulated by other, Syk-independent mechanisms and is therefore less sensitive to Syk inhibition than Bcl-2.In conclusion, our experiments have shown that two AML cells with different genetic mutations may have different biological responses to the same inhibitors. In light of all the results, despite the need for further research, targeting the SH2 domain of the Syk enzyme in AML cells with Z2608161550 and Z2155444005 may be a good start to pave the way for a new option for patients suffering from AML.

Chapter 4

Conclusions and Future Prospects

4.1 Conclusions

In the Chapter 1, we aim to reveal the possible Syk-SH2 domain inhibitors by using computational analysis from a natural product library which is the COCONUT database. Based on the best docking scores obtained from the molecular docking results, we were interested in the top 5 compounds for further studies including MD analysis, MM/PBSA, ADME and carcinogenicity predictions. All studies showed that compound CNP0265345 has the best binding properties towards both C-SH2 and N-SH2 of Syk enzyme with –44.54 kcal/mol and –55.98 kcal/mol binding free energies, respectively for 300 ns simulation time.

In the Chapter 2, *in silico* studies were performed using the ENAMINE database, which contains a large database of available inhibitors. MD analyses showed that Z2155444005 and Z260816155 had the best binding energies of -279.424 kJ (-66.782 kcal/mol) and -258.564 kJ (-61.79 kcal/mol), respectively. These results were quite promising. These compounds were purchased and their binding to the C-SH2 domain was successfully confirmed *in vitro* using "Differential Scanning Fluorimetry Assay" and "Intracellular FRET Methods".

In the Chapter 3, in light of all the results, despite the need for further research, targeting the SH2 domain of the Syk enzyme in AML cells with Z2608161550 and Z2155444005 may be a good start to pave the way for a new option for patients suffering from AML. Ultimately, it is hoped that this inhibition will lead to more specific targeted therapy resulting in the eradication of AML.

4.2 Societal Impact and Contribution to Global Sustainability

This thesis, which combines *in vitro* and *in vivo* approaches with molecular docking studies to combat devastating diseases like Acute Myeloid Leukemia (AML), not only contributes to the body of scientific knowledge but also holds the potential to offer significant broader societal impacts and contributions to global sustainability goals. AML is an aggressive blood cancer that causes severe morbidity and mortality worldwide, and current treatment options are often characterized by limited efficacy, high toxicity, and substantial costs. This thesis directly focuses on improving human health by supporting efforts to develop more effective new treatment strategies with fewer side effects.

The discovery of new and safer drugs can improve patients' quality of life while also reducing long-term healthcare costs. Traditional drug development processes are extremely time-consuming and expensive; integrating computational methods like molecular docking optimizes this process by accelerating the identification of potential drug candidates. This allows for more efficient use of resources and ensures that new treatments reach patients more quickly. Especially in low and middle-income countries, the development of accessible and affordable treatment options provides a critical contribution to reducing health inequalities and achieving global health justice.

From a global sustainability perspective, this thesis is directly linked to the United Nations Sustainable Development Goals (SDGs). Specifically, **SDG 3: Good Health and Well-being** is targeted by developing new and effective AML treatments. Improving human health increases the productivity of societies and lays the groundwork for economic development. Furthermore, the use of advanced technology-based research methods like molecular docking also serves the goals of **SDG 9: Industry, Innovation, and Infrastructure**. Promoting scientific and technological innovation strengthens a country's research and development capacity, increases international collaborations, and supports the transition to a knowledge economy.

The *in vitro* and *in vivo* phases of the study also have the potential to minimize the environmental impact of drugs. If the developed drug candidates are more specific, effective at lower doses, or produce fewer toxic metabolites, it can help reduce environmental pollution and potential negative impacts on ecosystems. This aligns with the principles of **SDG 12: Responsible Consumption and Production**. Finally, the knowledge generated by this thesis provides a foundation for future research, leaving a

lasting legacy for the scientific community and, consequently, all of humanity. This also supports the principle of **SDG 17: Partnerships for the Goals** through the sharing and dissemination of knowledge. In short, this thesis not only promises hope for AML patients but also helps us take concrete steps towards a healthier, more sustainable, and more equitable world.

4.3 Future Prospects

Our current study has successfully demonstrated that our novel SH2-domain-targeting Syk inhibitors, Z260816155 and Z2155444005, induce potent anti-leukemic effects in AML cells, including reduced viability, apoptosis induction, and downregulation of Bcl-2 family proteins. While these phenotypic outcomes are promising, the critical next step is to comprehensively delineate the molecular mechanisms by which these effects are mediated. Future investigations should therefore focus on mapping the impact of these inhibitors on the key downstream signaling pathways regulated by Syk. This study has provided promising initial data suggesting that targeting the SH2 domain of the Syk enzyme could be a potential strategy in the treatment of AML. Based on these findings, future research can pursue various avenues to explore this area more deeply and take steps towards clinical application. Firstly, investigating potential resistance mechanisms (e.g., SYK mutations, bypass pathways) in AML cell lines or primary patient samples that develop treatment resistance is critically important. Secondly, future work should focus on AML heterogeneity by comparing the efficacy of SH2 domain targeting across different AML subtypes with varying genetic mutations or phenotypes (e.g., FLT3-ITD, NPM1-mutated AML); this can help determine which patient groups might benefit more from the targeted therapy. Thirdly, combination therapies should be investigated by *in vitro* and *in vivo* evaluation of synergistic interactions between Syk SH2 domain inhibitors and existing AML chemotherapeutics or other targeted agents (e.g., FLT3 inhibitors); this could offer potential for higher efficacy at lower doses or overcoming resistance. Finally, *in vivo* validation of the anti-tumor efficacy and toxicity profiles of SH2 domain inhibitors in AML xenograft or genetically engineered mouse models is crucial. Additionally, pharmacokinetic and pharmacodynamic studies should be conducted to evaluate the bioavailability, distribution, metabolism, and excretion of potential candidate molecules, as well as target engagement and *in vivo* pharmacodynamic effects. These studies will contribute to a

better understanding of the potential therapeutic role of compounds targeting the Syk SH2 domain in AML, ultimately helping to advance this strategy towards clinical use.

BIBLIOGRAPHY

[1] N. Cooper, W. Ghanima, Q. A. Hill, P. L. Nicolson, V. Markovtsov, and C. Kessler, "Recent advances in understanding spleen tyrosine kinase (SYK) in human biology and disease, with a focus on fostamatinib," *Platelets*, vol. 34, no. 1, Dec. 2023, doi: 10.1080/09537104.2022.2131751.

[2] R. O. de Castro, "Regulation and Function of Syk Tyrosine Kinase in Mast Cell Signaling and Beyond," *J Signal Transduct*, vol. 2011, pp. 1–9, May 2011, doi: 10.1155/2011/507291.

[3] A. Mócsai, J. Ruland, and V. L. J. Tybulewicz, "The SYK tyrosine kinase: a crucial player in diverse biological functions," *Nat Rev Immunol*, vol. 10, no. 6, pp. 387–402, Jun. 2010, doi: 10.1038/nri2765.

[4] F. Yanaga *et al.*, "Syk interacts with tyrosine-phosphorylated proteins in human platelets activated by collagen and cross-linking of the Fc γ -IIA receptor," *Biochemical Journal*, vol. 311, no. 2, pp. 471–478, Oct. 1995, doi: 10.1042/bj3110471.

[5] Y.-S. Yi, Y.-J. Son, C. Ryou, G.-H. Sung, J.-H. Kim, and J. Y. Cho, "Functional Roles of Syk in Macrophage-Mediated Inflammatory Responses," *Mediators Inflamm*, vol. 2014, pp. 1–12, 2014, doi: 10.1155/2014/270302.

[6] N. Ozaki *et al.*, "Syk-dependent signaling pathways in neutrophils and macrophages are indispensable in the pathogenesis of anti-collagen antibody-induced arthritis," *Int Immunol*, vol. 24, no. 9, pp. 539–550, Sep. 2012, doi: 10.1093/intimm/dxs078.

[7] S. Latour, M. Fournel, and A. Veillette, "Regulation of T-Cell Antigen Receptor Signalling by Syk Tyrosine Protein Kinase," *Mol Cell Biol*, vol. 17, no. 8, pp. 4434–4441, Aug. 1997, doi: 10.1128/MCB.17.8.4434.

[8] J. A. Ackermann, J. Nys, E. Schweighoffer, S. McCleary, N. Smithers, and V. L. J. Tybulewicz, "Syk Tyrosine Kinase Is Critical for B Cell Antibody Responses and Memory B Cell Survival," *The Journal of Immunology*, vol. 194, no. 10, pp. 4650–4656, May 2015, doi: 10.4049/jimmunol.1500461.

[9] R. J. Cornall, A. M. Cheng, T. Pawson, and C. C. Goodnow, "Role of Syk in B-cell development and antigen-receptor signaling," *Proceedings of the National Academy of Sciences*, vol. 97, no. 4, pp. 1713–1718, Feb. 2000, doi: 10.1073/pnas.97.4.1713.

[10] M. Westbroek and R. Geahlen, "Modulation of BCR Signaling by the Induced Dimerization of Receptor-Associated SYK," *Antibodies*, vol. 6, no. 4, p. 23, Dec. 2017, doi: 10.3390/antib6040023.

[11] W. Wang *et al.*, "Inhibition of Syk promotes chemical reprogramming of fibroblasts via metabolic rewiring and H_2S production," *EMBO J*, vol. 40, no. 11, Jun. 2021, doi: 10.15252/embj.2020106771.

[12] H. Ennerfelt *et al.*, "SYK coordinates neuroprotective microglial responses in neurodegenerative disease," *Cell*, vol. 185, no. 22, pp. 4135-4152.e22, Oct. 2022, doi: 10.1016/j.cell.2022.09.030.

[13] S. Yanagi, R. Inatome, T. Takano, and H. Yamamura, "Syk Expression and Novel Function in a Wide Variety of Tissues," *Biochem Biophys Res Commun*, vol. 288, no. 3, pp. 495–498, Nov. 2001, doi: 10.1006/bbrc.2001.5788.

[14] S. Bartaula-Brevik, M. K. Lindstad Brattås, T. H. A. Tvedt, H. Reikvam, and Ø. Bruserud, "Splenic tyrosine kinase (SYK) inhibitors and their possible use in acute

myeloid leukemia," *Expert Opin Investig Drugs*, vol. 27, no. 4, pp. 377–387, Apr. 2018, doi: 10.1080/13543784.2018.1459562.

[15] G.-M. Deng, V. C. Kyttaris, and G. C. Tsokos, "Targeting Syk in Autoimmune Rheumatic Diseases," *Front Immunol*, vol. 7, Mar. 2016, doi: 10.3389/fimmu.2016.00078.

[16] C. Navara, "The Spleen Tyrosine Kinase (Syk) in Human Disease, Implications for Design of Tyrosine Kinase Inhibitor Based Therapy," *Curr Pharm Des*, vol. 10, no. 15, pp. 1739–1744, Jun. 2004, doi: 10.2174/1381612043384493.

[17] K. S. Bhullar *et al.*, "Kinase-targeted cancer therapies: progress, challenges and future directions," *Mol Cancer*, vol. 17, no. 1, p. 48, Dec. 2018, doi: 10.1186/s12943-018-0804-2.

[18] S. A. Rosenzweig, "Acquired Resistance to Drugs Targeting Tyrosine Kinases.," *Adv Cancer Res*, vol. 138, pp. 71–98, 2018, doi: 10.1016/bs.acr.2018.02.003.

[19] S. L. Kinnings and R. M. Jackson, "Binding Site Similarity Analysis for the Functional Classification of the Protein Kinase Family," *J Chem Inf Model*, vol. 49, no. 2, pp. 318–329, Feb. 2009, doi: 10.1021/ci800289y.

[20] S. Braselmann *et al.*, "R406, an Orally Available Spleen Tyrosine Kinase Inhibitor Blocks Fc Receptor Signaling and Reduces Immune Complex-Mediated Inflammation," *Journal of Pharmacology and Experimental Therapeutics*, vol. 319, no. 3, pp. 998–1008, Dec. 2006, doi: 10.1124/jpet.106.109058.

[21] P. A. Hamlin *et al.*, "Phase 2a Study of the Dual SYK/JAK Inhibitor Cerdulatinib (ALXN2075) As Monotherapy or in Combination with Rituximab in Patients with Relapsed/Refractory Follicular Lymphoma," *Blood*, vol. 138, no. Supplement 1, pp. 2423–2423, Nov. 2021, doi: 10.1182/blood-2021-148313.

[22] K. W. Pratz *et al.*, "A phase Ib trial of mivavotinib (TAK-659), a dual SYK/FLT3 inhibitor, in patients with relapsed/refractory acute myeloid leukemia," *Haematologica*, vol. 108, no. 3, pp. 705–716, Oct. 2022, doi: 10.3324/haematol.2022.281216.

[23] D. Liu and A. Mamorska-Dyga, "Syk inhibitors in clinical development for hematological malignancies," *J Hematol Oncol*, vol. 10, no. 1, p. 145, Dec. 2017, doi: 10.1186/s13045-017-0512-1.

[24] J. W. Friedberg *et al.*, "Inhibition of Syk with fostamatinib disodium has significant clinical activity in non-Hodgkin lymphoma and chronic lymphocytic leukemia," *Blood*, vol. 115, no. 13, pp. 2578–2585, Apr. 2010, doi: 10.1182/blood-2009-08-236471.

[25] J. Bussel *et al.*, "Fostamatinib for the treatment of adult persistent and chronic immune thrombocytopenia: Results of two phase 3, randomized, placebo-controlled trials," *Am J Hematol*, vol. 93, no. 7, pp. 921–930, Jul. 2018, doi: 10.1002/ajh.25125.

[26] M. Z. Farooq *et al.*, "A Systematic Review and Meta-Analysis of Cardio-Vascular Side Effects with Fostamatinib a Spleen Tyrosine Kinase Inhibitor," *Blood*, vol. 134, no. Supplement_1, pp. 3465–3465, Nov. 2019, doi: 10.1182/blood-2019-132151.

[27] Y. Chen, H. Liu, Y. Huang, S. Lin, G. Yin, and Q. Xie, "The Cardiovascular Risks of Fostamatinib in Patients with Rheumatoid Arthritis: A Systematic Review and Meta-Analysis," *Front Pharmacol*, vol. 12, Jul. 2021, doi: 10.3389/fphar.2021.632551.

[28] J. Sharman and J. Di Paolo, "Targeting B-cell receptor signaling kinases in chronic lymphocytic leukemia: the promise of entospletinib," *Ther Adv Hematol*, vol. 7, no. 3, pp. 157–170, Jun. 2016, doi: 10.1177/2040620716636542.

[29] A. Cremer *et al*., "Resistance Mechanisms to SYK Inhibition in Acute Myeloid Leukemia," *Cancer Discov*, vol. 10, no. 2, pp. 214–231, Feb. 2020, doi: 10.1158/2159-8290.CD-19-0209.

[30] K. Sada, T. Takano, S. Yanagi, and H. Yamamura, "Structure and Function of Syk Protein-Tyrosine Kinase," *J Biochem*, vol. 130, no. 2, pp. 177–186, Aug. 2001, doi: 10.1093/oxfordjournals.jbchem.a002970.

[31] J. Ding *et al*., "Distinctive Functions of Syk N-Terminal and C-Terminal SH2 Domains in the Signaling Cascade Elicited by Oxidative Stress in B Cells," *J Biochem*, vol. 127, no. 5, pp. 791–796, May 2000, doi: 10.1093/oxfordjournals.jbchem.a022671.

[32] R. Jaber Chehayeb and T. J. Boggon, "SH2 Domain Binding: Diverse FLVRs of Partnership," *Front Endocrinol (Lausanne)*, vol. 11, Sep. 2020, doi: 10.3389/fendo.2020.575220.

[33] A. Diop *et al*., "SH2 Domains: Folding, Binding and Therapeutical Approaches," *Int J Mol Sci*, vol. 23, no. 24, p. 15944, Dec. 2022, doi: 10.3390/ijms232415944.

[34] E. B. Gencer Akçok, H. Güner, and İ. Akçok, "Determination of promising inhibitors for N-SH2 domain of SHP2 tyrosine phosphatase: an in silico study," *Mol Divers*, May 2024, doi: 10.1007/s11030-024-10880-2.

[35] K. Fütterer, J. Wong, R. A. Grucza, A. C. Chan, and G. Waksman, "Structural basis for syk tyrosine kinase ubiquity in signal transduction pathways revealed by the crystal structure of its regulatory SH2 domains bound to a dually phosphorylated ITAM peptide," *J Mol Biol*, vol. 281, no. 3, pp. 523–537, Aug. 1998, doi: 10.1006/jmbi.1998.1964.

[36] E. F. Pettersen *et al*., "UCSF Chimera—A visualization system for exploratory research and analysis," *J Comput Chem*, vol. 25, no. 13, pp. 1605–1612, Oct. 2004, doi: 10.1002/jcc.20084.

[37] M. Sorokina, P. Merseburger, K. Rajan, M. A. Yirik, and C. Steinbeck, "COCONUT online: Collection of Open Natural Products database," *J Cheminform*, vol. 13, no. 1, p. 2, Dec. 2021, doi: 10.1186/s13321-020-00478-9.

[38] N. M. O'Boyle, M. Banck, C. A. James, C. Morley, T. Vandermeersch, and G. R. Hutchison, "Open Babel: An open chemical toolbox," *J Cheminform*, vol. 3, no. 1, p. 33, Dec. 2011, doi: 10.1186/1758-2946-3-33.

[39] K. Vanommeslaeghe *et al*., "CHARMM general force field: A force field for drug-like molecules compatible with the CHARMM all-atom additive biological force fields," *J Comput Chem*, vol. 31, no. 4, pp. 671–690, Mar. 2010, doi: 10.1002/jcc.21367.

[40] D. R. Koes, M. P. Baumgartner, and C. J. Camacho, "Lessons Learned in Empirical Scoring with smina from the CSAR 2011 Benchmarking Exercise," *J Chem Inf Model*, vol. 53, no. 8, pp. 1893–1904, Aug. 2013, doi: 10.1021/ci300604z.

[41] O. Trott and A. J. Olson, "AutoDock Vina: Improving the speed and accuracy of docking with a new scoring function, efficient optimization, and multithreading," *J Comput Chem*, vol. 31, no. 2, pp. 455–461, Jan. 2010, doi: 10.1002/jcc.21334.

[42] M. Abraham *et al*., "GROMACS 2023 Source code," Feb. 2023, *Zenodo*. doi: 10.5281/zenodo.7588619.

[43] P. Mark and L. Nilsson, "Structure and Dynamics of the TIP3P, SPC, and SPC/E Water Models at 298 K," *J Phys Chem A*, vol. 105, no. 43, pp. 9954–9960, Nov. 2001, doi: 10.1021/jp003020w.

[44] J. Lemkul, "From Proteins to Perturbed Hamiltonians: A Suite of Tutorials for the GROMACS-2018 Molecular Simulation Package [Article v1.0]," *Living J Comput Mol Sci*, vol. 1, no. 1, 2019, doi: 10.33011/livecoms.1.1.5068.

[45] N. Homeyer and H. Gohlke, "Free Energy Calculations by the Molecular Mechanics Poisson–Boltzmann Surface Area Method," *Mol Inform*, vol. 31, no. 2, pp. 114–122, Feb. 2012, doi: 10.1002/minf.201100135.

[46] R. Kumari, R. Kumar, and A. Lynn, "*g_mmpbsa* —A GROMACS Tool for High-Throughput MM-PBSA Calculations," *J Chem Inf Model*, vol. 54, no. 7, pp. 1951–1962, Jul. 2014, doi: 10.1021/ci500020m.

[47] A. Daina, O. Michielin, and V. Zoete, "SwissADME: a free web tool to evaluate pharmacokinetics, drug-likeness and medicinal chemistry friendliness of small molecules," *Sci Rep*, vol. 7, no. 1, p. 42717, Mar. 2017, doi: 10.1038/srep42717.

[48] L. Zhang *et al*., "CarcinoPred-EL: Novel models for predicting the carcinogenicity of chemicals using molecular fingerprints and ensemble learning methods," *Sci Rep*, vol. 7, no. 1, p. 2118, May 2017, doi: 10.1038/s41598-017-02365-0.

[49] J. L. Capener *et al*., "Development of SYK NanoBRET cellular target engagement assays for gain–of–function variants," *Frontiers in Chemical Biology*, vol. 3, Jul. 2024, doi: 10.3389/fchbi.2024.1447622.

[50] C. A. Lipinski, "Lead- and drug-like compounds: the rule-of-five revolution," *Drug Discov Today Technol*, vol. 1, no. 4, pp. 337–341, Dec. 2004, doi: 10.1016/J.DDTEC.2004.11.007.

[51] A. Caminero Gomes Soares, G. H. Marques Sousa, R. L. Calil, and G. H. Goulart Trossini, "Absorption matters: A closer look at popular oral bioavailability rules for drug approvals," *Mol Inform*, vol. 42, no. 11, p. e202300115, Nov. 2023, doi: 10.1002/MINF.202300115.

[52] F. M. G. Cornelissen *et al*., "Explaining Blood-Brain Barrier Permeability of Small Molecules by Integrated Analysis of Different Transport Mechanisms," *J Med Chem*, vol. 66, no. 11, pp. 7253–7267, Jun. 2023, doi: 10.1021/ACS.JMEDCHEM.2C01824/SUPPL_FILE/JM2C01824_SI_001.PDF.

[53] J. H. Lin and M. Yamazaki, "Role of P-Glycoprotein in Pharmacokinetics," *Clin Pharmacokinet*, vol. 42, no. 1, pp. 59–98, 2003, doi: 10.2165/00003088-200342010-00003.

[54] G. Cai *et al*., "Discovery of fluorescent coumarin-benzo[b]thiophene 1, 1-dioxide conjugates as mitochondria-targeting antitumor STAT3 inhibitors," *Eur J Med Chem*, vol. 174, pp. 236–251, Jul. 2019, doi: 10.1016/j.ejmech.2019.04.024.

[55] K. Sanches *et al*., "Grb2 dimer interacts with Coumarin through SH2 domains: A combined experimental and molecular modeling study," *Heliyon*, vol. 5, no. 11, p. e02869, Nov. 2019, doi: 10.1016/j.heliyon.2019.e02869.

[56] F. M. Bashore *et al*., "Characterization of covalent inhibitors that disrupt the interaction between the tandem SH2 domains of SYK and FCER1G phospho-ITAM," *PLoS One*, vol. 19, no. 2, p. e0293548, Feb. 2024, doi: 10.1371/journal.pone.0293548.

[57] S. Manoharan, A. Balakrishnan, V. Hemamalini, and E. Perumal, "Screening of potent STAT3-SH2 domain inhibitors from JAK/STAT compound library through molecular dynamics simulation," *Mol Divers*, vol. 27, no. 3, pp. 1297–1308, Jun. 2023, doi: 10.1007/s11030-022-10490-w.

[58] V. Mayoral-Varo *et al*., "The Relevance of the SH2 Domain for c-Src Functionality in Triple-Negative Breast Cancer Cells," *Cancers (Basel)*, vol. 13, no. 3, p. 462, Jan. 2021, doi: 10.3390/cancers13030462.

[59] S. Haftchenary, M. Avadisian, and P. T. Gunning, "Inhibiting aberrant Stat3 function with molecular therapeutics," *Anticancer Drugs*, vol. 22, no. 2, pp. 115–127, Feb. 2011, doi: 10.1097/CAD.0b013e328341185b.

[60] O. Giricz, V. Calvo, S. C. Pero, D. N. Krag, J. A. Sparano, and P. A. Kenny, "GRB7 is required for triple-negative breast cancer cell invasion and survival," *Breast Cancer Res Treat*, vol. 133, no. 2, pp. 607–615, Jun. 2012, doi: 10.1007/s10549-011-1822-6.

[61] K. Matsuno *et al*., "Identification of a New Series of STAT3 Inhibitors by Virtual Screening," *ACS Med Chem Lett*, vol. 1, no. 8, pp. 371–375, Nov. 2010, doi: 10.1021/ml1000273.

[62] T. Taniguchi *et al*., "Molecular cloning of a porcine gene syk that encodes a 72-kDa protein-tyrosine kinase showing high susceptibility to proteolysis.," *J Biol Chem*, vol. 266, no. 24, pp. 15790–6, Aug. 1991.

[63] S. Latour, "A unique insert in the linker domain of Syk is necessary for its function in immunoreceptor signalling," *EMBO J*, vol. 17, no. 9, pp. 2584–2595, May 1998, doi: 10.1093/emboj/17.9.2584.

[64] P. Draber, I. Halova, I. Polakovicova, and T. Kawakami, "Signal transduction and chemotaxis in mast cells," *Eur J Pharmacol*, vol. 778, pp. 11–23, May 2016, doi: 10.1016/j.ejphar.2015.02.057.

[65] Z. Wang *et al*., "Review and prospects of targeted therapies for Spleen tyrosine kinase (SYK)," *Bioorg Med Chem*, vol. 96, p. 117514, Dec. 2023, doi: 10.1016/j.bmc.2023.117514.

[66] C. Rosales, "Fcγ Receptor Heterogeneity in Leukocyte Functional Responses," *Front Immunol*, vol. 8, Mar. 2017, doi: 10.3389/fimmu.2017.00280.

[67] Y. Shao, S. Zhang, Y. Zhang, and Z. Liu, "Recent advance of spleen tyrosine kinase in diseases and drugs," *Int Immunopharmacol*, vol. 90, p. 107168, Jan. 2021, doi: 10.1016/j.intimp.2020.107168.

[68] A. M. Gilfillan and J. Rivera, "The tyrosine kinase network regulating mast cell activation," *Immunol Rev*, vol. 228, no. 1, pp. 149–169, Mar. 2009, doi: 10.1111/j.1600-065X.2008.00742.x.

[69] S. J. Galli, M. Tsai, and A. M. Piliponsky, "The development of allergic inflammation," *Nature*, vol. 454, no. 7203, pp. 445–454, Jul. 2008, doi: 10.1038/nature07204.

[70] M. Daëron, "F <scp>c</scp> RECEPTOR BIOLOGY," *Annu Rev Immunol*, vol. 15, no. 1, pp. 203–234, Apr. 1997, doi: 10.1146/annurev.immunol.15.1.203.

[71] S. Lin, C. Cicala, A. M. Scharenberg, and J. P. Kinet, "The FcεRIβ Subunit Functions as an Amplifier of FcεRIγ-Mediated Cell Activation Signals," *Cell*, vol. 85, no. 7, pp. 985–995, Jun. 1996, doi: 10.1016/S0092-8674(00)81300-8.

[72] R. P. Siraganian, R. O. de Castro, E. A. Barbu, and J. Zhang, "Mast cell signaling: The role of protein tyrosine kinase Syk, its activation and screening methods for new pathway participants," *FEBS Lett*, vol. 584, no. 24, pp. 4933–4940, Dec. 2010, doi: 10.1016/J.FEBSLET.2010.08.006.

[73] S. Zhang, L. Wang, Y. Lu, C. Guo, T. Zhang, and L. Zhang, "Targeting spleen tyrosine kinase (SYK): structure, mechanisms and drug discovery," *Drug Discov Today*, vol. 30, no. 1, p. 104257, Jan. 2025, doi: 10.1016/j.drudis.2024.104257.

[74] A. Markham, "Fostamatinib: First Global Approval," *Drugs*, vol. 78, no. 9, pp. 959–963, Jun. 2018, doi: 10.1007/s40265-018-0927-1.

[75] J. S. Smolen, D. Aletaha, and I. B. McInnes, "Rheumatoid arthritis," *The Lancet*, vol. 388, no. 10055, pp. 2023–2038, Oct. 2016, doi: 10.1016/S0140-6736(16)30173-8.

[76] M. Kaur, M. Singh, and O. Silakari, "Inhibitors of switch kinase 'spleen tyrosine kinase' in inflammation and immune-mediated disorders: A review," *Eur J Med Chem*, vol. 67, pp. 434–446, Sep. 2013, doi: 10.1016/J.EJMECH.2013.04.070.

[77] V. Kyttaris, “Kinase inhibitors: a new class of antirheumatic drugs,” *Drug Des Devel Ther*, p. 245, Sep. 2012, doi: 10.2147/DDDT.S25426.
[78] G. Deng, L. Liu, F. R. Bahjat, P. R. Pine, and G. C. Tsokos, “Suppression of skin and kidney disease by inhibition of spleen tyrosine kinase in lupus-prone mice,” *Arthritis Rheum*, vol. 62, no. 7, pp. 2086–2092, Jul. 2010, doi: 10.1002/art.27452.
[79] B. R. Wong, E. B. Grossbard, D. G. Payan, and E. S. Masuda, “Targeting Syk as a treatment for allergic and autoimmune disorders,” *Expert Opin Investig Drugs*, vol. 13, no. 7, pp. 743–762, 2004, doi: 10.1517/13543784.13.7.743.
[80] P. J. P. Coopman *et al.*, “The Syk tyrosine kinase suppresses malignant growth of human breast cancer cells,” *Nature*, vol. 406, no. 6797, pp. 742–747, Aug. 2000, doi: 10.1038/35021086.
[81] L. Wang, E. Devarajan, J. He, S. P. Reddy, and J. Le Dai, “Transcription Repressor Activity of Spleen Tyrosine Kinase Mediates Breast Tumor Suppression,” *Cancer Res*, vol. 65, no. 22, pp. 10289–10297, Nov. 2005, doi: 10.1158/0008-5472.CAN-05-2231.
[82] V. P. S. Ghotra *et al.*, “SYK Is a Candidate Kinase Target for the Treatment of Advanced Prostate Cancer,” *Cancer Res*, vol. 75, no. 1, pp. 230–240, Jan. 2015, doi: 10.1158/0008-5472.CAN-14-0629.
[83] P. Karimi, F. Islami, S. Anandasabapathy, N. D. Freedman, and F. Kamangar, “Gastric Cancer: Descriptive Epidemiology, Risk Factors, Screening, and Prevention,” *Cancer Epidemiology, Biomarkers & Prevention*, vol. 23, no. 5, pp. 700–713, May 2014, doi: 10.1158/1055-9965.EPI-13-1057.
[84] S. Narayanan *et al.*, “The Spleen Tyrosine Kinase Inhibitor, Entospletinib (GS-9973) Restores Chemosensitivity in Lung Cancer Cells by Modulating ABCG2-mediated Multidrug Resistance,” *Int J Biol Sci*, vol. 17, no. 10, pp. 2652–2665, 2021, doi: 10.7150/ijbs.61229.
[85] D. Rohila *et al.*, “Syk Inhibition Reprograms Tumor-Associated Macrophages and Overcomes Gemcitabine-Induced Immunosuppression in Pancreatic Ductal Adenocarcinoma,” *Cancer Res*, vol. 83, no. 16, pp. 2675–2689, Aug. 2023, doi: 10.1158/0008-5472.CAN-22-3645.
[86] J. Hong *et al.*, “Expression of Variant Isoforms of the Tyrosine Kinase SYK Determines the Prognosis of Hepatocellular Carcinoma,” *Cancer Res*, vol. 74, no. 6, pp. 1845–1856, Mar. 2014, doi: 10.1158/0008-5472.CAN-13-2104.
[87] Q. Zhou *et al.*, “Syk-dependent homologous recombination activation promotes cancer resistance to DNA targeted therapy,” *Drug Resistance Updates*, vol. 74, p. 101085, May 2024, doi: 10.1016/j.drup.2024.101085.
[88] X. Xiang, J. Sun, J. Wu, H.-T. He, Y. Wang, and C. Zhu, “A FRET-Based Biosensor for Imaging SYK Activities in Living Cells,” *Cell Mol Bioeng*, vol. 4, no. 4, pp. 670–677, Dec. 2011, doi: 10.1007/s12195-011-0211-x.
[89] C. Guo, F. K. Fordjour, S. J. Tsai, J. C. Morrell, and S. J. Gould, “Choice of selectable marker affects recombinant protein expression in cells and exosomes.,” *J Biol Chem*, vol. 297, no. 1, p. 100838, Jul. 2021, doi: 10.1016/j.jbc.2021.100838.
[90] H. Döhner, D. J. Weisdorf, and C. D. Bloomfield, “Acute Myeloid Leukemia,” *New England Journal of Medicine*, vol. 373, no. 12, pp. 1136–1152, Apr. 2015, doi: 10.1056/NEJMra1406184.
[91] M. S. Thein, W. B. Ershler, A. Jemal, J. W. Yates, and M. R. Baer, “Outcome of older patients with acute myeloid leukemia,” *Cancer*, vol. 119, no. 15, pp. 2720–2727, Aug. 2013, doi: 10.1002/cncr.28129.
[92] L. F. Ocias, T. S. Larsen, H. Vestergaard, L. S. Friis, N. Abildgaard, and H. Frederiksen, “Trends in hematological cancer in the elderly in Denmark, 1980–

2012," *Acta Oncol (Madr)*, vol. 55, no. sup1, pp. 98–107, Jan. 2016, doi: 10.3109/0284186X.2015.1115124.

[93] R. M. Shallis, R. Wang, A. Davidoff, X. Ma, and A. M. Zeidan, "Epidemiology of acute myeloid leukemia: Recent progress and enduring challenges," *Blood Rev*, vol. 36, pp. 70–87, Jul. 2019, doi: 10.1016/j.blre.2019.04.005.

[94] J. M. Bennett *et al.*, "Proposals for the Classification of the Acute Leukaemias F <scp>rench</scp> -A <scp>merican</scp> -B <scp>ritish</scp> (FAB) C <scp>o-operative</scp> G <scp>roup</scp>," *Br J Haematol*, vol. 33, no. 4, pp. 451–458, Aug. 1976, doi: 10.1111/j.1365-2141.1976.tb03563.x.

[95] J. D. Khoury *et al.*, "The 5th edition of the World Health Organization Classification of Haematolymphoid Tumours: Myeloid and Histiocytic/Dendritic Neoplasms," *Leukemia*, vol. 36, no. 7, pp. 1703–1719, Jul. 2022, doi: 10.1038/s41375-022-01613-1.

[96] D. A. Arber *et al.*, "The 2016 revision to the World Health Organization classification of myeloid neoplasms and acute leukemia," *Blood*, vol. 127, no. 20, pp. 2391–2405, May 2016, doi: 10.1182/blood-2016-03-643544.

[97] D. A. Arber *et al.*, "International Consensus Classification of Myeloid Neoplasms and Acute Leukemias: integrating morphologic, clinical, and genomic data," *Blood*, vol. 140, no. 11, pp. 1200–1228, Sep. 2022, doi: 10.1182/blood.2022015850.

[98] H. Döhner *et al.*, "Diagnosis and management of AML in adults: 2022 recommendations from an international expert panel on behalf of the ELN," *Blood*, vol. 140, no. 12, pp. 1345–1377, Sep. 2022, doi: 10.1182/blood.2022016867.

[99] J. L. Carter *et al.*, "Targeting multiple signaling pathways: the new approach to acute myeloid leukemia therapy," *Signal Transduct Target Ther*, vol. 5, no. 1, p. 288, Dec. 2020, doi: 10.1038/s41392-020-00361-x.

[100] A. C. B. da C. Rodrigues, R. G. A. Costa, S. L. R. Silva, I. R. S. B. Dias, R. B. Dias, and D. P. Bezerra, "Cell signaling pathways as molecular targets to eliminate AML stem cells," *Crit Rev Oncol Hematol*, vol. 160, p. 103277, Apr. 2021, doi: 10.1016/j.critrevonc.2021.103277.

[101] A. Puissant *et al.*, "SYK Is a Critical Regulator of FLT3 in Acute Myeloid Leukemia," *Cancer Cell*, vol. 25, no. 2, pp. 226–242, Feb. 2014, doi: 10.1016/j.ccr.2014.01.022.

[102] J. Carnevale *et al.*, "SYK regulates mTOR signaling in AML.," *Leukemia*, vol. 27, no. 11, pp. 2118–28, Nov. 2013, doi: 10.1038/leu.2013.89.

[103] S. Mohr *et al.*, "Hoxa9 and Meis1 Cooperatively Induce Addiction to Syk Signaling by Suppressing miR-146a in Acute Myeloid Leukemia.," *Cancer Cell*, vol. 31, no. 4, pp. 549-562.e11, Apr. 2017, doi: 10.1016/j.ccell.2017.03.001.

[104] P. G. Miller *et al.*, "In Vivo RNAi Screening Identifies a Leukemia-Specific Dependence on Integrin Beta 3 Signaling," *Cancer Cell*, vol. 24, no. 1, pp. 45–58, Jul. 2013, doi: 10.1016/j.ccr.2013.05.004.

[105] E. L. Weisberg *et al.*, "Characterization of midostaurin as a dual inhibitor of FLT3 and SYK and potentiation of FLT3 inhibition against FLT3-ITD-driven leukemia harboring activated SYK kinase.," *Oncotarget*, vol. 8, no. 32, pp. 52026–52044, Aug. 2017, doi: 10.18632/oncotarget.19036.

[106] B. M. Richine *et al.*, "Syk kinase and Shp2 phosphatase inhibition cooperate to reduce FLT3-ITD-induced STAT5 activation and proliferation of acute myeloid leukemia," *Leukemia*, vol. 30, no. 10, pp. 2094–2097, Oct. 2016, doi: 10.1038/leu.2016.131.

[107] R. Krishnamurty and D. J. Maly, "Biochemical Mechanisms of Resistance to Small-Molecule Protein Kinase Inhibitors," *ACS Chem Biol*, vol. 5, no. 1, pp. 121–138, Jan. 2010, doi: 10.1021/cb9002656.
[108] M. Adachi, C. Cui, C. T. Dodge, M. K. Bhayani, and S. Y. Lai, "Targeting STAT3 inhibits growth and enhances radiosensitivity in head and neck squamous cell carcinoma," *Oral Oncol*, vol. 48, no. 12, pp. 1220–1226, Dec. 2012, doi: 10.1016/j.oraloncology.2012.06.006.
[109] M. Spitzner *et al*., "STAT3 inhibition sensitizes colorectal cancer to chemoradiotherapy *in vitro* and *in vivo*," *Int J Cancer*, vol. 134, no. 4, pp. 997–1007, Feb. 2014, doi: 10.1002/ijc.28429.
[110] M. Şansaçar, H. Sağır, and E. B. Gencer Akçok, "Inhibition of PI3K-AKT-mTOR pathway and modulation of histone deacetylase enzymes reduce the growth of acute myeloid leukemia cells," *Medical Oncology*, vol. 41, no. 1, p. 31, Dec. 2023, doi: 10.1007/s12032-023-02247-8.
[111] N. Aktas Pepe, B. Acar, G. Erturk Zararsiz, S. Ayaz Guner, and A. Sen, "Role of Long Non-Coding RNA X-Inactive-Specific Transcript (XIST) in Neuroinflammation and Myelination: Insights from Cerebral Organoids and Implications for Multiple Sclerosis," *Noncoding RNA*, vol. 11, no. 3, p. 31, Apr. 2025, doi: 10.3390/ncrna11030031.
[112] J. K. Kim *et al*., "Mycoplasma hyorhinis infection promotes TNF-α signaling and SMAC mimetic-mediated apoptosis in human prostate cancer," *Heliyon*, vol. 9, no. 10, p. e20655, Oct. 2023, doi: 10.1016/j.heliyon.2023.e20655.
[113] A. Carey *et al*., "Identification of Interleukin-1 by Functional Screening as a Key Mediator of Cellular Expansion and Disease Progression in Acute Myeloid Leukemia," *Cell Rep*, vol. 18, no. 13, pp. 3204–3218, Mar. 2017, doi: 10.1016/j.celrep.2017.03.018.
[114] M. Şansaçar, N. A. Pepe, E. B. Gencer Akçok, and M. El Khatib, "Efficacy of combinatorial inhibition of Hedgehog and autophagy pathways on the survival of AML cell lines," *Biochem Biophys Res Commun*, vol. 775, p. 152034, Aug. 2025, doi: 10.1016/j.bbrc.2025.152034.
[115] M. O. Krisenko and R. L. Geahlen, "Calling in SYK: SYK's dual role as a tumor promoter and tumor suppressor in cancer," *Biochimica et Biophysica Acta (BBA) - Molecular Cell Research*, vol. 1853, no. 1, pp. 254–263, Jan. 2015, doi: 10.1016/j.bbamcr.2014.10.022.
[116] L. Chen *et al*., "SYK inhibition modulates distinct PI3K/AKT- dependent survival pathways and cholesterol biosynthesis in diffuse large B cell lymphomas.," *Cancer Cell*, vol. 23, no. 6, pp. 826–38, Jun. 2013, doi: 10.1016/j.ccr.2013.05.002.
[117] M. Buchner *et al*., "Spleen Tyrosine Kinase Is Overexpressed and Represents a Potential Therapeutic Target in Chronic Lymphocytic Leukemia," *Cancer Res*, vol. 69, no. 13, pp. 5424–5432, Jul. 2009, doi: 10.1158/0008-5472.CAN-08-4252.
[118] S. Cheng *et al*., "SYK inhibition and response prediction in diffuse large B-cell lymphoma," *Blood*, vol. 118, no. 24, pp. 6342–6352, Dec. 2011, doi: 10.1182/blood-2011-02-333773.
[119] C. Bertoli, J. M. Skotheim, and R. A. M. de Bruin, "Control of cell cycle transcription during G1 and S phases," *Nat Rev Mol Cell Biol*, vol. 14, no. 8, pp. 518–528, Aug. 2013, doi: 10.1038/nrm3629.
[120] Y. Dai, F. Jin, W. Wu, and S. K. Kumar, "Cell cycle regulation and hematologic malignancies," *Blood Science*, vol. 1, no. 1, pp. 34–43, Aug. 2019, doi: 10.1097/BS9.0000000000000009.

[121] T. Liu, L. Zhang, D. Joo, and S.-C. Sun, "NF-κB signaling in inflammation," *Signal Transduct Target Ther*, vol. 2, no. 1, p. 17023, Jul. 2017, doi: 10.1038/sigtrans.2017.23.
[122] E. Schweighoffer, J. Nys, L. Vanes, N. Smithers, and V. L. J. Tybulewicz, "TLR4 signals in B lymphocytes are transduced via the B cell antigen receptor and SYK," *Journal of Experimental Medicine*, vol. 214, no. 5, pp. 1269–1280, May 2017, doi: 10.1084/jem.20161117.
[123] X. Zhou *et al.*, "Transmembrane TNF-α preferentially expressed by leukemia stem cells and blasts is a potent target for antibody therapy," *Blood*, vol. 126, no. 12, pp. 1433–1442, Sep. 2015, doi: 10.1182/blood-2015-01-624833.
[124] S. Verma *et al.*, "Serum Tumor Necrosis Factor-Alpha Levels in Acute Leukemia and Its Prognostic Significance," *Cureus*, May 2022, doi: 10.7759/cureus.24835.
[125] C. Tang and G. Zhu, "Classic and Novel Signaling Pathways Involved in Cancer: Targeting the NF-κB and Syk Signaling Pathways," *Curr Stem Cell Res Ther*, vol. 14, no. 3, pp. 219–225, Apr. 2019, doi: 10.2174/1574888X13666180723104340.
[126] B. Di Francesco *et al.*, "NF-κB: A Druggable Target in Acute Myeloid Leukemia.," *Cancers (Basel)*, vol. 14, no. 14, Jul. 2022, doi: 10.3390/cancers14143557.
[127] S. Darici, H. Alkhaldi, G. Horne, H. G. Jørgensen, S. Marmiroli, and X. Huang, "Targeting PI3K/Akt/mTOR in AML: Rationale and Clinical Evidence," *J Clin Med*, vol. 9, no. 9, p. 2934, Sep. 2020, doi: 10.3390/jcm9092934.
[128] S. Park *et al.*, "Role of the PI3K/AKT and mTOR signaling pathways in acute myeloid leukemia.," *Haematologica*, vol. 95, no. 5, pp. 819–28, May 2010, doi: 10.3324/haematol.2009.013797.
[129] K. Boros *et al.*, "Increased SYK activity is associated with unfavorable outcome among patients with acute myeloid leukemia.," *Oncotarget*, vol. 6, no. 28, pp. 25575–87, Sep. 2015, doi: 10.18632/oncotarget.4669.
[130] F. M. Uckun, H. Ma, Z. Ozer, P. Goodman, J. Zhang, and S. Qazi, "A PREVIOUSLY UNKNOWN UNIQUE CHALLENGE FOR INHIBITORS OF SYK ATP-BINDING SITE: ROLE OF SYK AS A CELL CYCLE CHECKPOINT REGULATOR.," *EBioMedicine*, vol. 1, no. 1, pp. 16–28, Nov. 2014, doi: 10.1016/j.ebiom.2014.10.019.
[131] A. Alhazmi, J. Choi, and M. Ulanova, "Syk inhibitor R406 downregulates inflammation in an in vitro model of *Pseudomonas aeruginosa* infection," *Can J Physiol Pharmacol*, vol. 96, no. 2, pp. 182–190, Feb. 2018, doi: 10.1139/cjpp-2017-0307.
[132] D. W. Kurniawan *et al.*, "Therapeutic inhibition of spleen tyrosine kinase in inflammatory macrophages using PLGA nanoparticles for the treatment of non-alcoholic steatohepatitis," *Journal of Controlled Release*, vol. 288, pp. 227–238, Oct. 2018, doi: 10.1016/j.jconrel.2018.09.004.

APPENDIX

Supplementary Material

Table of Content

Content	Page
Table S1 Docking Evaluations of Syk kinase domain against filtered COCONUT database	**3 – 6**
Figure S1 Contact Angle Analysis of the CNP0015002 and CNP0114154 against C-SH2 (left panel) and N-SH2 (right panel) domains of Syk	**7**
Figure S2 Contact Angle Analysis of the CNP0159934 and CNP0118091 against C-SH2 (left panel) and N-SH2 (right panel) domain of Syk	**8**
Figure S3 Radius of gyration results of the top 5 COCONUT compounds	**9**
Figure S4 Hydrogen bond analysis of the top 5 COCONUT compounds with C-SH2 and N-SH2 domains of Syk	**10**
Table S2 Average binding energies of top 5 compounds	**11**
Figure S5 2D & 3D interactions figures of the compound 44 against both C-SH2 and N-SH2 domains of Syk. A and B refers to 2D interactions figures dotted lines representing hydrogen bonds. C and D refers to 3D interactions figures of compound 44 against C-SH2 and N-SH2 domains of Syk.	**11**
Fig. S6. Molecular Dynamics simulation results of 8,8'-disulfanediylbis(1,3-dimethyl-3,7-dihydro-1H-purine-2,6-dione) (named as compound 44).	**12**
Table S3. The contribution of individual amino acid residues of C-SH2 domain of Syk for binding of Natural Products (NPs) across 100 snapshots from MD simulations.	**13**
Table S4. The contribution of individual amino acid residues of N-SH2 domain of Syk for binding of Natural Products (NPs) across 100 snapshots from MD simulations.	**13-14**
Table S5. ADME and toxicity prediction of top 5 compounds	**14-15**

Table S1. Docking Evaluations of Syk kinase domain against filtered COCONUT database

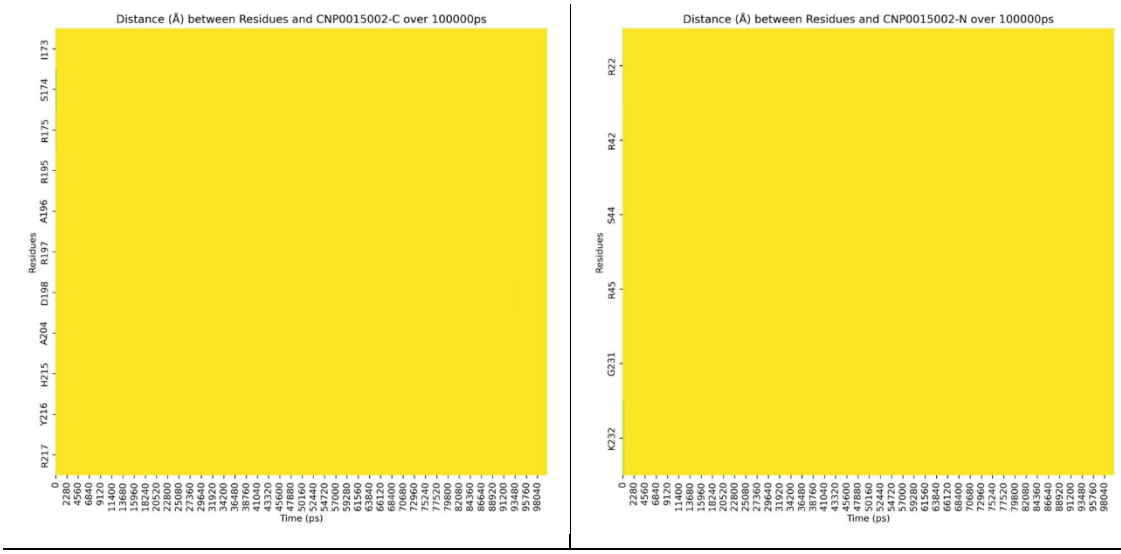
COCONUT ID	N-SH2 Binding Affinity (kcal/mol)	No	COCONUT ID	C-SH2 Binding Affinity (kcal/mol)
CNP0379208	-9.9	**1**	CNP0182771	-9.1
CNP0190435	-9.9	**2**	CNP0152233	-9
CNP0155587	-9.9	**3**	CNP0246334	-9
CNP0119644	-9.8	**4**	CNP0138873	-8.9
CNP0015002	-9.8	**5**	CNP0394479	-8.8
CNP0440242	-9.8	**6**	CNP0219593	-8.7
CNP0269189	-9.8	**7**	CNP0074462	-8.7
CNP0364080	-9.8	**8**	CNP0224067	-8.7
CNP0100482	-9.7	**9**	CNP0362624	-8.7
CNP0239141	-9.7	**10**	CNP0245328	-8.6
CNP0306746	-9.7	**11**	CNP0395373	-8.6
CNP0253675	-9.7	**12**	CNP0396052	-8.6
CNP0431820	-9.7	**13**	CNP0085668	-8.5
CNP0066470	-9.7	**14**	CNP0223323	-8.5
CNP0340443	-9.7	**15**	CNP0394519	-8.5
CNP0193284	-9.7	**16**	CNP0200944	-8.5
CNP0118091	-9.7	**17**	CNP0159934	-8.4
CNP0197395	-9.7	**18**	CNP0265345	-8.4
CNP0170588	-9.6	**19**	CNP0229183	-8.4
CNP0388938	-9.6	**20**	CNP0211375	-8.4
CNP0164152	-9.6	**21**	CNP0386115	-8.4
CNP0173966	-9.6	**22**	CNP0168905	-8.3
CNP0382270	-9.6	**23**	CNP0019876	-8.3
CNP0301777	-9.6	**24**	CNP0394224	-8.3
CNP0365987	-9.6	**25**	CNP0231286	-8.3
CNP0122736	-9.6	**26**	CNP0118091	-8.3
CNP0411292	-9.6	**27**	CNP0338161	-8.3

CNP0405760	-9.5	**28**	CNP0115623	-8.3
CNP0342754	-9.5	**29**	CNP0310383	-8.2
CNP0265345	-9.5	**30**	CNP0289633	-8.2
CNP0130240	-9.5	**31**	CNP0399453	-8.2
CNP0118697	-9.5	**32**	CNP0166249	-8.2
CNP0176512	-9.5	**33**	CNP0174609	-8.2
CNP0309801	-9.5	**34**	CNP0288609	-8.2
CNP0265219	-9.5	**35**	CNP0175643	-8.2
CNP0396323	-9.5	**36**	CNP0242904	-8.2
CNP0410114	-9.5	**37**	CNP0350933	-8.2
CNP0154797	-9.5	**38**	CNP0236239	-8.2
CNP0411214	-9.5	**39**	CNP0435444	-8.1
CNP0186352	-9.5	**40**	CNP0134697	-8.1
CNP0448933	-9.5	**41**	CNP0078408	-8.1
CNP0078190	-9.5	**42**	CNP0198058	-8.1
CNP0114154	-9.5	**43**	CNP0054113	-8.1
CNP0131030	-9.5	**44**	CNP0449002	-8.1
CNP0347629	-9.5	**45**	CNP0395403	-8.1
CNP0299942	-9.5	**46**	CNP0293045	-8.1
CNP0465809	-9.4	**47**	CNP0114154	-8.1
CNP0159934	-9.4	**48**	CNP0232905	-8.1
CNP0363154	-9.4	**49**	CNP0274118	-8.1
CNP0447450	-9.4	**50**	CNP0147238	-8.1
CNP0450319	-9.4	**51**	CNP0391300	-8.1
CNP0350880	-9.4	**52**	CNP0346209	-8.1
CNP0027635	-9.4	**53**	CNP0227785	-8
CNP0016015	-9.4	**54**	CNP0115894	-8
CNP0302344	-9.4	**55**	CNP0170588	-8
CNP0368105	-9.4	**56**	CNP0092034	-8
CNP0384464	-9.4	**57**	CNP0152605	-8

CNP0376120	-9.4	**58**	CNP0294932	-8
CNP0380860	-9.4	**59**	CNP0193917	-8
CNP0341372	-9.4	**60**	CNP0071487	-8
CNP0390193	-9.4	**61**	CNP0392028	-8
CNP0327321	-9.4	**62**	CNP0322906	-8
CNP0390716	-9.4	**63**	CNP0329209	-8
CNP0125134	-9.4	**64**	CNP0161523	-8
CNP0180541	-9.4	**65**	CNP0198866	-8
CNP0217080	-9.4	**66**	CNP0120176	-8
CNP0371459	-9.4	**67**	CNP0411168	-8
CNP0256536	-9.4	**68**	CNP0261806	-8
CNP0337301	-9.4	**69**	CNP0461617	-8
CNP0327469	-9.4	**70**	CNP0189894	-8
CNP0047685	-9.4	**71**	CNP0124989	-8
CNP0337719	-9.4	**72**	CNP0453096	-8
CNP0264053	-9.4	**73**	CNP0228220	-8
CNP0406136	-9.3	**74**	CNP0277886	-8
CNP0390813	-9.3	**75**	CNP0452071	-8
CNP0367339	-9.3	**76**	CNP0094669	-7.9
CNP0445454	-9.3	**77**	CNP0375487	-7.9
CNP0005875	-9.3	**78**	CNP0451130	-7.9
CNP0414778	-9.3	**79**	CNP0392858	-7.9
CNP0272093	-9.3	**80**	CNP0177714	-7.9
CNP0198979	-9.3	**81**	CNP0362082	-7.9
CNP0414407	-9.3	**82**	CNP0385380	-7.9
CNP0267016	-9.3	**83**	CNP0147584	-7.9
CNP0134553	-9.3	**84**	CNP0271877	-7.9
CNP0357927	-9.3	**85**	CNP0386262	-7.9
CNP0333598	-9.3	**86**	CNP0131707	-7.9
CNP0261449	-9.3	**87**	CNP0142069	-7.9

CNP0297731	-9.3	**88**	CNP0459267	-7.9
CNP0386184	-9.3	**89**	CNP0376120	-7.9
CNP0412859	-9.3	**90**	CNP0000004	-7.9
CNP0179280	-9.3	**91**	CNP0188167	-7.9
CNP0349342	-9.3	**92**	CNP0035741	-7.9
CNP0377279	-9.3	**93**	CNP0241884	-7.9
CNP0405042	-9.3	**94**	CNP0015002	-7.9
CNP0269927	-9.3	**95**	CNP0402401	-7.9
CNP0380371	-9.3	**96**	CNP0259748	-7.9
CNP0410858	-9.3	**97**	CNP0071339	-7.9
CNP0301998	-9.3	**98**	CNP0284211	-7.9
CNP0028704	-9.3	**99**	CNP0441616	-7.9
CNP0308937	-9.3	**100**	CNP0220554	-7.9

CNP0015002



CNP0114154

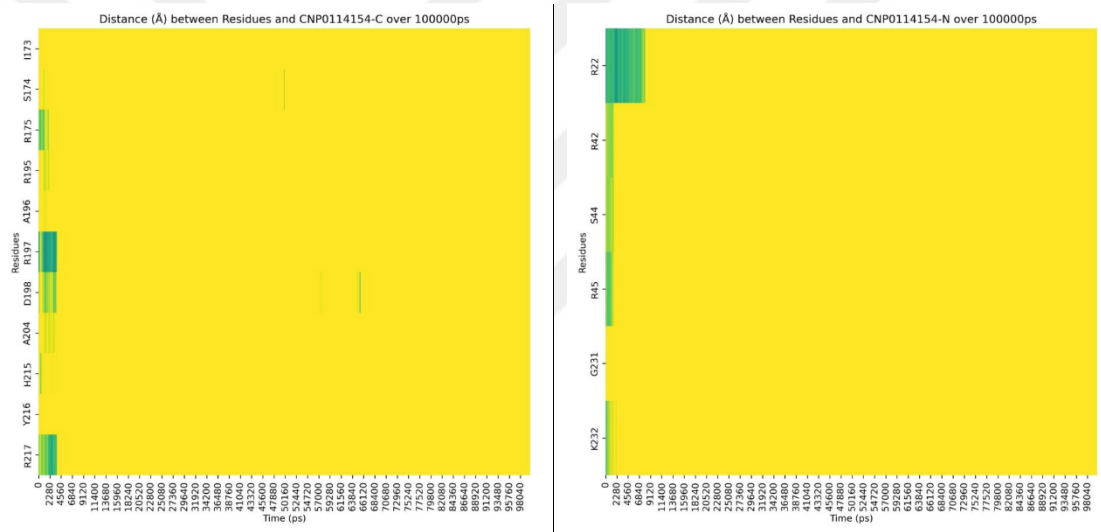
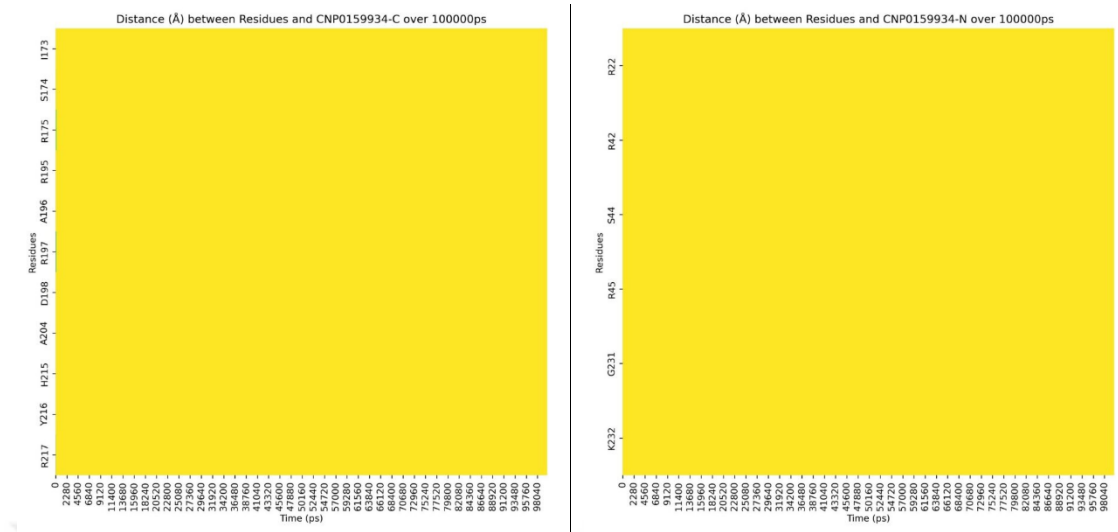


Figure S1. Contact Angle Analysis of the CNP0015002 and CNP0114154 against C-SH2 (left panel) and N-SH2 (right panel) domains of Syk

CNP0159934



CNP0118091

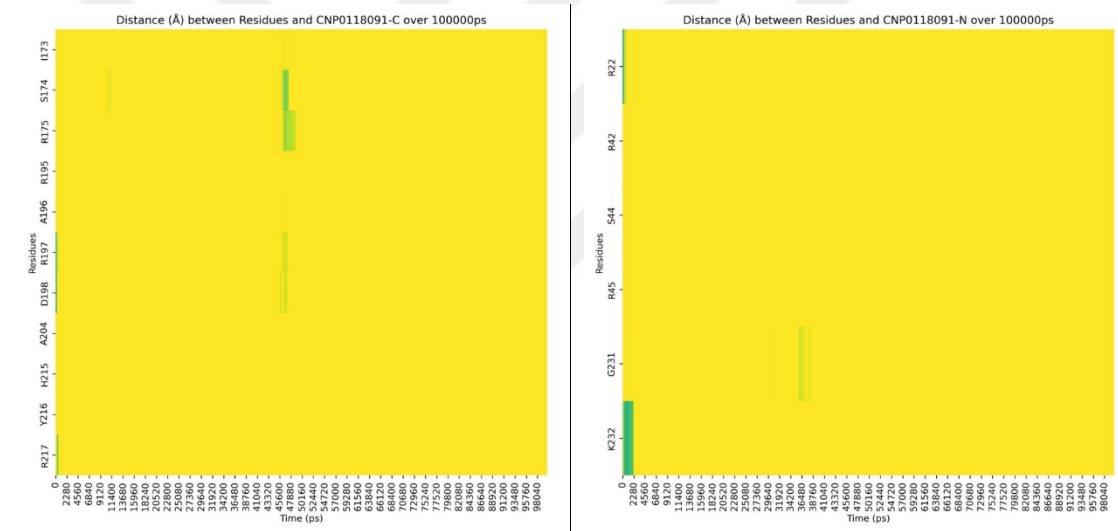
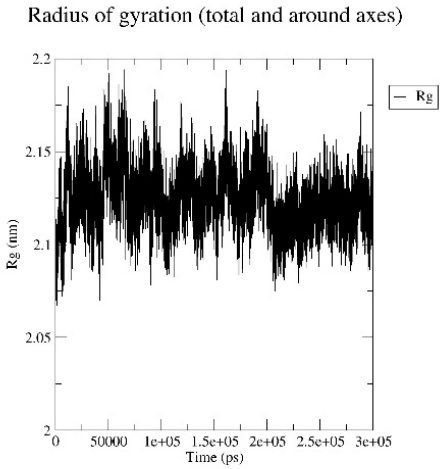
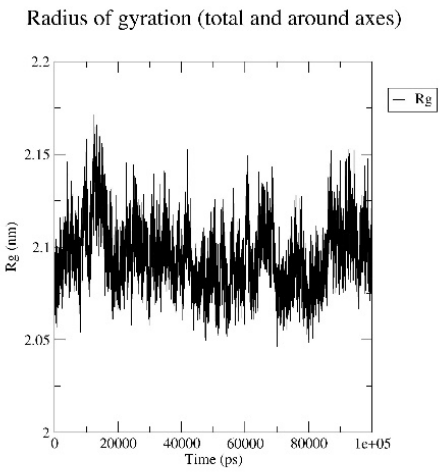


Figure S2 .Contact Angle Analysis of the CNP0159934 and CNP0118091 against C-SH2 (left panel) and N-SH2 (right panel) domain of Syk

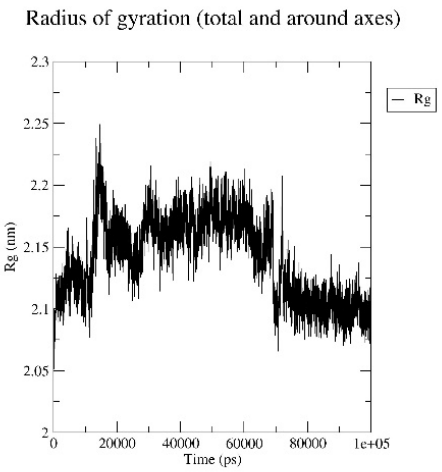
CNP0265345



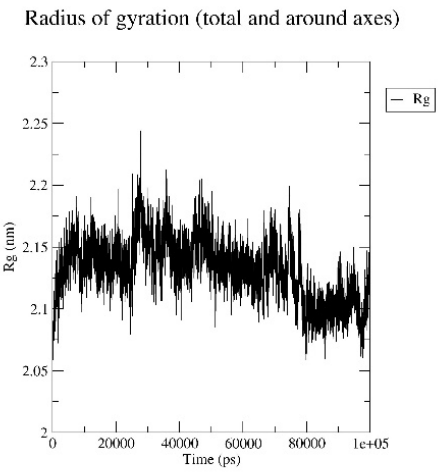
CNP0015002



CNP0114154



CNP0159934



CNP0118091

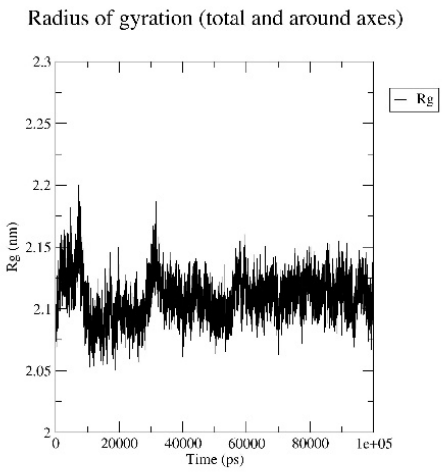
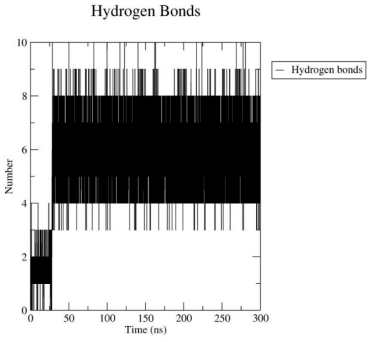
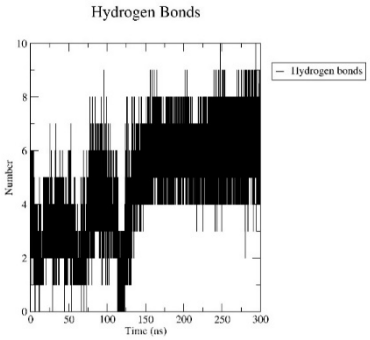


Figure S3. Radius of gyration results of the top 5 COCONUT compounds

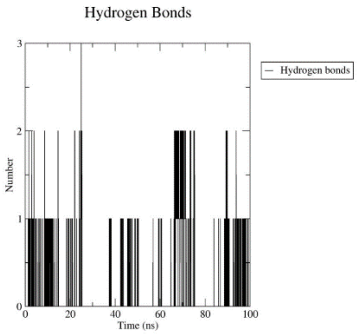
CNP0265345-C-SH2



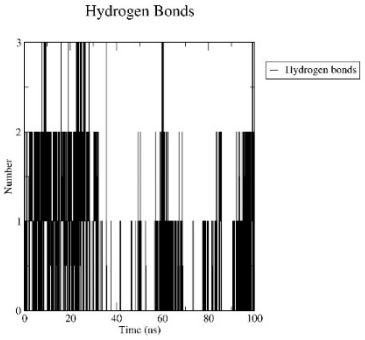
CNP0265345-N-SH2



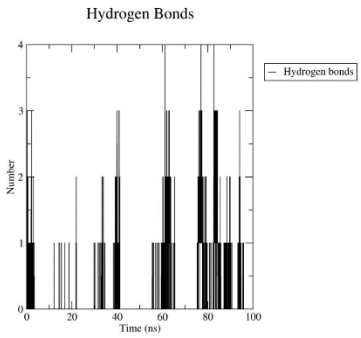
CNP0015002-C-SH2



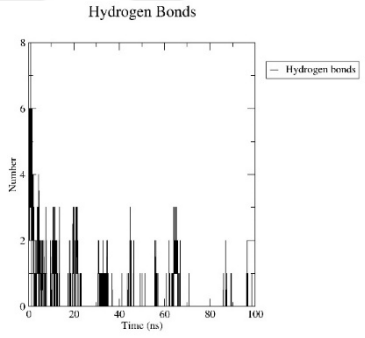
CNP0015002-N-SH2



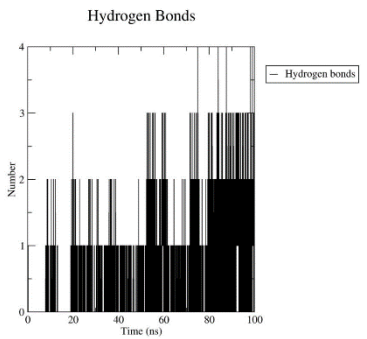
CNP0114154-C-SH2



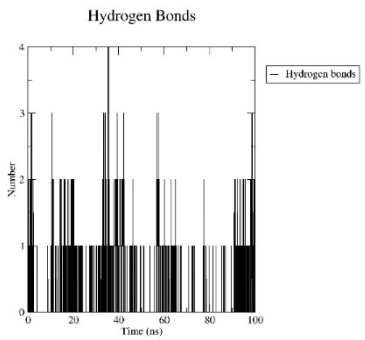
CNP0114154-N-SH2



CNP0159934-C-SH2



CNP0159934-N-SH2



CNP0118091-C-SH2

CNP0118091-N-SH2

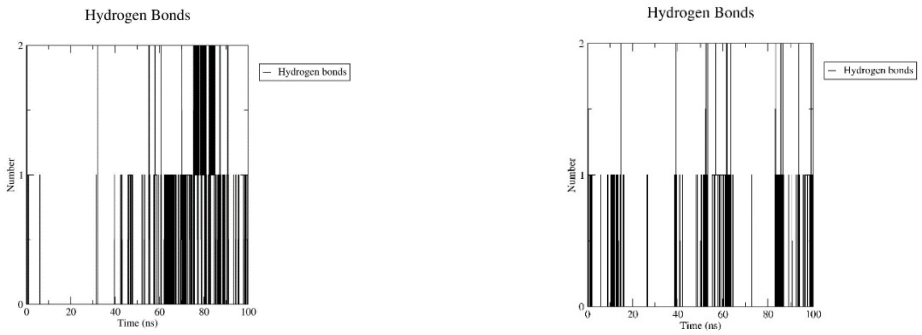


Figure S4. Hydrogen bond analysis of the top 5 COCONUT compounds with C-SH2 and N-SH2 domain of Syk

Table S2. Average binding energies of top 5 compounds

COCONUT ID	LIGC (kcal/mol)	LIGN (kcal/mol)
CNP0265345 (300 ns)	-44.54	-56.98
CNP0265345 (100 ns)	-41.78	-47.75
CNP0159934	-11.96	-11.78
CNP0118091	18.21	22.34
CNP0114154	-1.12	-2.96
CNP0015002	20.81	20.10

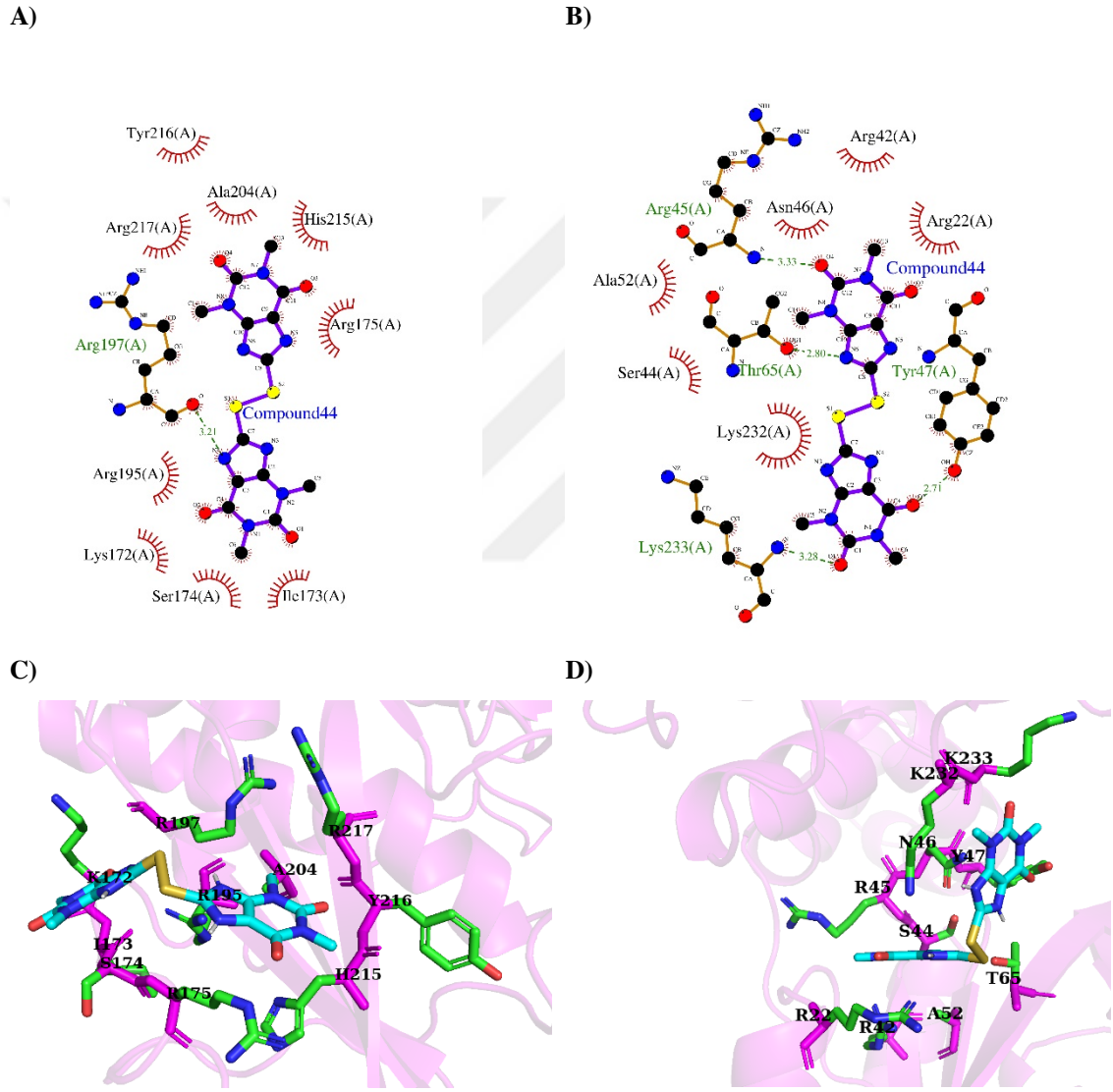


Figure S5. 2D & 3D interactions figures of the compound 44 against both C-SH2 and N-SH2 domains of Syk. A and B refers to 2D interactions figures dotted lines representing hydrogen bonds. C and D refers to 3D interactions figures of compound 44 against C-SH2 and N-SH2 domains of Syk. Magenta represents the backbone atoms while cyan color represents docked compounds and side chains carbon atoms shown in green, nitrogen atom in blue, oxygen atom in red.

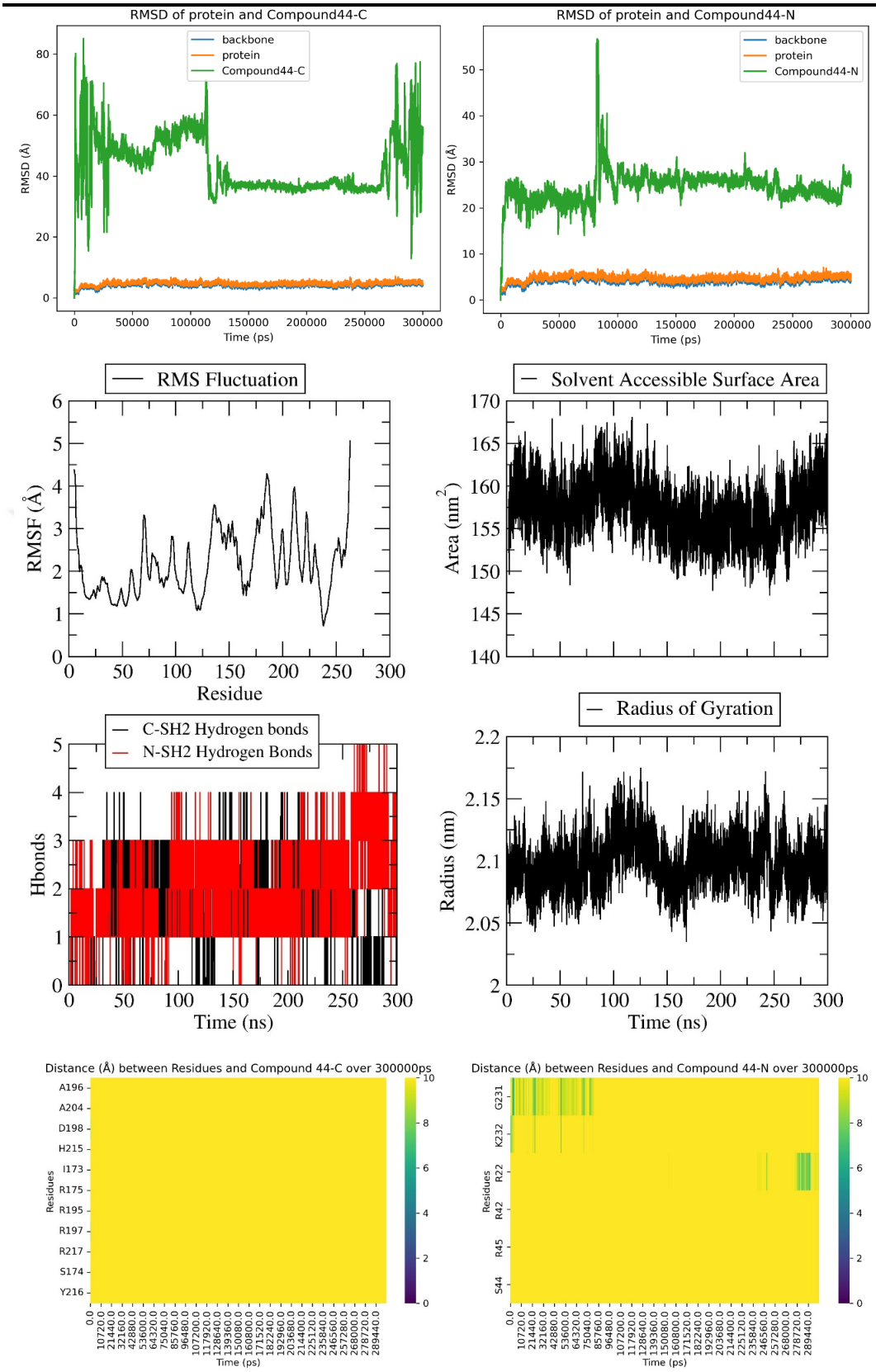


Figure S6 . Molecular Dynamics simulation results of 8,8'-disulfanediylbis(1,3-dimethyl-3,7-dihydro-1H-purine-2,6-dione) (named as compound 44).

Table S3. The contribution of individual amino acid residues of C-SH2 domain of Syk for binding of Natural Products (NPs) across 100 snapshots from MD simulations.

C-SH2 (kcal/mol)					
RESIDUE	CNP0265345	CNP0015002	CNP0114154	CNP0118091	CNP0159934
I173	5.530049	-1.91297	0.058899	-2.97628	0.032077
S174	-0.22939	-0.00822	-0.00122	-0.01087	0.001696
R175	6.001651	-1.84394	0.060356	-2.40623	0.028088
R195	0.030023	-0.01108	-0.00069	-0.02966	0.005756
A196	-0.12766	-0.00726	-0.03103	0.046264	-0.01295
R197	-0.09205	0.011608	-0.00119	0.047124	0.003941
D198	0.049871	0.005422	0.004395	-0.03232	0.005302
A204	-0.03872	-0.01574	-0.00702	0.001218	-0.00182
H215	5.953858	-2.44445	0.042873	-2.57789	0.015191
Y216	-4.14467	2.656565	0.07483	2.892234	-0.00841
R217	3.863645	-2.87179	0.066805	-2.44788	0.044831
P229	-3.78466	2.906517	-0.0198	2.318478	-0.03031

Table S4. The contribution of individual amino acid residues of N-SH2 domain of Syk for binding of Natural Products (NPs) across 100 snapshots from MD simulations.

N-SH2 (kcal/mol)					
RESIDUE	CNP0265345	CNP0015002	CNP0114154	CNP0118091	CNP0159934
T21	-0.20679	0.026679	-0.00518	0.016313	-0.00155
R22	6.240544	-2.70018	0.249881	-2.37322	0.034155
R42	0.332951	0.028948	0.03566	0.008121	0.005446
S44	0.034489	-0.02802	-0.01467	0.021711	-0.56086
R45	-0.03318	0.007404	-0.00428	-0.00048	-0.14111
N46	-0.05579	0.027324	-0.01044	0.002627	-0.03473
A52	-0.04376	-0.01493	-0.00616	0.002699	-0.00048
Y64	-3.80685	3.200298	-0.039	2.320962	0.488082
I76	-2.72005	2.903914	-0.02429	2.030764	0.055054
A77	-0.06824	0.026679	-0.00748	0.031743	-0.02013
G231	4.986269	-3.02857	0.093962	-2.56843	0.405561
K232	0.136071	0.004228	0.016409	-0.02692	-0.03224
H243	-8.44595	2.395482	-0.17276	2.751554	-0.01851
Y246	-0.14598	0.012468	-0.0118	-0.03544	-0.00514
K247	0.04464	-0.00779	-0.0026	-0.08649	-0.00521

Table S5. ADME and toxicity prediction of top 5 compounds

Property	CNP0265345	CNP0159934	CNP0118091	CNP0114154	CNP0015002
Physicochemical Properties					
Num. heavy atoms	39	40	33	33	28
Num. arom. heavy atoms	16	18	15	12	15
Fraction Csp3	0.29	0.22	0.46	0.4	0.35
Num. rotatable bonds	3	0	4	2	6
Molar Refractivity	146.87	142.14	135.27	115.39	106.23
Lipophilicity					
Log $P_{O/W}$ (iLOGP)	3.4	2.98	3.71	2.2	2.65
Log $P_{O/W}$ (XLOGP3)	4.4	4.6	1.57	1.74	1.14
Log $P_{O/W}$ (WLOGP)	4.39	4.4	2.37	1.43	3.09
Log $P_{O/W}$ (MLOGP)	3.84	1.84	2.02	0.02	1.28
Log $P_{O/W}$ (SILICOS-IT)	5.21	5.06	2.04	2.65	2.1
Consensus Log $P_{O/W}$	4.25	3.78	2.1	1.61	2.05
Water Solubility					
Log *S* (ESOL)	-6.05	-6.38	-3.67	-3.88	-3.05
Solubility	4.79e-04 mg/ml;8.91e-07 mol/l	2.20e-04 mg/ml;4.12e-08 mol/l	9.55e-02 mg/ml;2.14e-04 mol/l	5.99e-02 mg/ml;1.32e-04 mol/l	3.60e-01 mg/ml;8.96e-03 mol/l
Class	Poorly soluble	Poorly soluble	Soluble	Soluble	Soluble
Log *S* (Ali)	-6.22	-7.06	-2.67	-4.09	-2.64
Solubility	3.27e-04 mg/ml;6.09e-07 mol/l	4.63e-05 mg/ml;8.67e-08 mol/l	9.65e-01 mg/ml;2.16e-03 mol/l	3.64e-02 mg/ml;8.05e-05 mol/l	9.16e-01 mg/ml;2.28e-03 mol/l
Class	Poorly soluble	Poorly soluble	Soluble	Moderately sol.	Soluble
Log *S* (SILICOS-IT)	-8.37	-8.07	-4.82	-4.65	-6.17
Solubility	2.29e-06 mg/ml;4.27e-09 mol/l	4.57e-06 mg/ml; 8.55e-09 mol/l	6.70e-03 mg/ml;1.50e-05 mol/l	1.02e-02 mg/ml;2.24e-05 mol/l	2.75e-04 mg/ml;6.84e-07 mol/l
Class	Poorly soluble	Poorly soluble	Moderately sol.	Moderately sol.	Poorly soluble
Pharmacokinetics					
CYP1A2 inhibitor	No	No	No	No	Yes
CYP2C19 inhibitor	Yes	No	No	No	No

CYP2C9 inhibitor	Yes	Yes	No	No	No
CYP2D6 inhibitor	No	No	Yes	No	Yes
CYP3A4 inhibitor	No	No	No	No	Yes
Log *K*p (skin perm.)	-6.45 cm/s	-6.29 cm/s	-7.91 cm/s	-7.82 cm/s	-7.94 cm/s
Druglikeness					
Ghose	No; 2 violations: MW>480 MR>130	No; 2 violations: MW>480 MR>130	No; 1 violation: MR>130	Yes; 0 violation	Yes; 0 violation
Veber	Yes	Yes	Yes	Yes	Yes
Egan	Yes	Yes	Yes	Yes	Yes
Muegge	Yes	No; 1 violation #rings>7	Yes	Yes	Yes
Bioavailability Score	0.55	0.56	0.55	0.55	0.55
Medicinal Chemistry					
PAINS	1 alert: ene_six_het_A	1 alert: quinone_A	0 alert	1 alert: quinone_A	0 alert
Brenk	3 alerts: cumarine, michael_acceptor_1, michael_acceptor_4	0 alert	0 alert	0 alert	0 alert
Leadlikeness	No; 2 violations: MW>350, XLOGP3>3.5	No; 2 violations: MW>350, XLOGP3>3.5	No; 1 violation: MW>350	No; 1 violation: MW>350	No; 1 violation: MW>350
Synthetic accessibility	4.2	6.41	5.15	5.32	3.7

CURRICULUM VITAE

2012 – 2016	B.Sc., Molecular Biology and Genetics, Erzurum Technical University, Erzurum, TURKEY
2017-Present	Research Assistant, Genetics and Bioengineering, Alanya Alaaddin Keykubat University, Alanya, Antalya, TURKEY
2017-2025	Research Assistant, Bioengineering, Abdullah Gül University, Kayseri, TURKEY
2017 – 2019	M.Sc., Bioengineering, Abdullah Gül University, Kayseri, TURKEY
2022	Bursary, FEBS Young Scientist Travel Grant for 43th FEBS Congress, PORTUGAL
2023	Bursary, FEBS Young Scientist Travel Grant for 44th FEBS Congress, FRANCE
2019-2025	Ph.D., Bioengineering, Abdullah Gül University, Kayseri, TURKEY

SELECTED PUBLICATIONS AND PRESENTATIONS

J1) A.Üstün A.Saygılı F. Bostan M.Sansacar, Genetiği Değiştirilmiş Organizmalar ve Biyogüvenlik, Türkiye'de GDO'lara Toplumsal Bakış, Ankara, Turkey, April 2017 (National).

J2) Şansaçar, M., Sağır, H. & Gencer Akçok, E.B. Inhibition of PI3K-AKT-mTOR pathway and modulation of histone deacetylase enzymes reduce the growth of acute myeloid leukemia cells. Med Oncol 41, 31 (2024).

J3) Şansaçar, M., & Gencer Akçok, E. B. (2024). Measurement of Autophagic Activity in Cancer Cells with Flow Cytometric Analysis Using Cyto-ID Staining. Methods in molecular biology (Clifton, N.J.), 10.1007/7651_2024_526.

J4) Şansaçar, M., Pekin, Ö., & Gencer Akcok, E. B. Targeting HDAC enzymes by SAHA enhances the cytotoxic effects of cisplatin on acute myeloid leukemia cells. Journal of Experimental and Clinical Medicine, 41(3), 524-529 (2024).

J5) Şansaçar, M., Pepe, N. A., Gencer Akçok, E. B., & El Khatib, M. (2025). Efficacy of combinatorial inhibition of Hedgehog and autophagy pathways on the survival of AML

cell lines. Biochemical and biophysical research communications, 775, 152034. Advance online publication.

J6) Şansaçar, M., Sarı, C., Yücel, M. S., Gencer Akçok, E. B., & Akçok, İ., (2025). Discovery of New Candidates Targeting the SH2 Domains of Spleen Tyrosine Kinase (Syk) Through In Silico Studies. ChemistrySelect , 10, e00547.

J7) Şansaçar, M., and Gencer Akçok, E.B. The Anti-leukemic Effect of the Inhibition of Spleen Tyrosine Kinase and Histone Deacetylase Enzyme on the FLT3-ITD(+) Acute Myeloid Leukemia Cells (2025), Erciyes Unviversity Journal of Institute of Science and Technology, 41(2), 708 – 721.

C1) N. Aktas, M. Sansacar, M. El Khatib, "The Fine Tuning of The Hedgehog and Autophagy Pathways to Combat Acute Myeloid Leukemia" 5. Uluslararası Katılımlı Deneysel Hematoloji Kongresi, Malatya Turkey, 27-29 April 2018.

C2) M. Şansaçar, E. G.Akçok, "The Inhibition of Histone Deacetylase Enzyme and Spleen Tyrosine Kinase (SYK) on the FLT3(+) Acute Myeloid Cells" 12th Drug Chemistry Congress, 7-10 March 2024.

C3) N.A. Pepe, B. Acar, M. Şansaçar, E. G. Akçok, A. Şen, "The Effects of Cinnamic Acid and Autophagy Inhibition on Myelination of Co-cultured Cells" 12th Drug Chemistry Congress, 7-10 March 2024.

C4) Abdullah Keskin, Merve Şansaçar, Kutay İçöz, Zeliha Soran Erdem, "Protein-immobilized magnetic nanoparticles for biomedical applications" 18th International Nanoscience and Nanotechnology Conference, İstanbul/Türkiye, August 26-28, 2024.

C5) M.Şansaçar, C.Sarı, M.S.Yücel, E.G.Akçok, İ.Akçok "In silico evaluation of potential natural product inhibitors from COCONUT database targeting SH2 domains of Spleen Tyrosine Kinase (Syk)" 13th Drug Chemistry Congress,6-9 February 2025, Antalya, Turkey.

C6) M.Sansacar, S.Sahin, A.G. Kurt, "CRISPR/Cas9 Teknolojisi ve Gen Terapi " The 6. Ulusal Moleküler Biyoloji ve Biyoteknoloji Kongresi, Adana, Turkey, 5-7 October, 2017.

C7) S.Sahin, M.Sansacar, A.G. Kurt, "Kanser Biyobelirteç Tespitinde Elektrokimyasal İmpedimetrik İmmunosensörler", 6. Ulusal Moleküler Biyoloji ve Biyoteknoloji Kongresi, Adana, Turkey, 5-7 October 2017.

C8) N. Aktas, M. Sansacar, H. Sagır, M. El Khatib, "The Fine Tuning of The Hedgehog and Autophagy Pathways to Combat Cholangiocarcinoma" 6. Uluslararası Katılımlı Deneysel Hematoloji Kongresi, Gaziantep Turkey, 19-21 April 2019.

C9) M.Sansacar, N. Aktas, E.Gencer Akcok, M. El Khatib "The Effect of Hedgehog Pathway Inhibition and Autophagy Modulation on the Proliferation and Survival of AML Cell Lines" 3rd international Eurasian Conference on Biological and Chemical Sciences, Ankara Turkey, 19-21 March 2020.

C10) M. Sansacar, E. G.Akcok, H. Sagir "Investigation of the Antitumor Effect of Targeting PI3K-AKT-mTOR Pathway and Histone Deacetylase Enzymes on Acute Myeloid Leukemia Cells," in the Proceedings of the Society of Hematologic Oncology Ninth Annual Meeting, Houston ,Texas ,8-11 September, 2021.

C11) M. Sansacar, E. G.Akcok, "The effect of the combination of PI3K-AKT- mTOR pathway and Histone Deacetylase enzymes on cell cycle and cell death in CMK and MOLM-13 AML cell lines," in the Proceedings of 46th European Federation of Biochemistry Societies (FEBS) Congress, Lisbon, Portugal ,9-14 July, 2022.

C12) M. Şansaçar, Ö.Pekin, E. G.Akçok, "Cisplatin and SAHA combination inhibits cell viability of FLT3-ITD-positive AML cells via induction of apoptosis" 47th European Federation of Biochemistry Societies (FEBS) Congress, Tours, France, 8-12 July, 2023.

C13) M. Şansacar, H. Güner, İ. Akçok, E. G. Akçok, "Targeting the C-SH2 domain of the Syk kinase by virtual drug screening to identify potential anticancer candidates" 9th International BAU Drug Design Congress, İstanbul, Turkey, November 29 – December 02, 2023.

C14) M. Şansacar, H. Güner, İ. Akçok, E. G. Akçok, "Investigation of SH2 domain of Spleen Tyrosine Kinase (Syk) Enzyme using Drug Screening Studies to Combat Cancer" EMBO|FEBS Lecture Course, Molecular mechanisms in signal transduction and cancer, 18 – 26 August 2024 | Spetses, Greece.

C15) D. Akcan, M. Şansaçar, Z. S. Erdem, E.G.Akçok, "Green synthesized nanoparticles against human liver cancer", 11. Biyomalzeme Günleri, 9-10 December 2024, İzmir, Turkey.

C16) B.Demirsoy, M. Şansaçar, A.Eken, E.G.Akçok, "Investigation Of The Cytotoxic Effect Of α-Tocopheryl Succinate (α-TOS) And SAHA Combination Treatment On SH-SY5Y Neuroblastoma cells" 9th International Congress, September 12-14, 2024. İzmir, Turkey.